Simulation and Stability of Milling Processes

vorgelegt von
Dipl.-Ing. Oliver Rott
aus Augustdorf

Von der Fakultät V
Verkehrs– und Maschinensysteme
der Technischen Universität Berlin
zur Erlangung des akademischen Grades
Doktor-Ingenieur
Dr.-Ing.

genehmigte Dissertation

Promotionsausschuss:

Vorsitzender: Prof. Dr. rer. nat. Wolfgang H. Müller
Berichter: Prof. Dr. rer. nat. Dietmar Hömberg
Berichter: Prof. Dr.-Ing. Utz von Wagner

Tag der wissenschaftlichen Aussprache: 25.10.2011

Berlin 2011
D83

Acknowledgements

This thesis is the result of more than six years research at the Weierstrass Institute in Berlin in close cooperation with the Department of Production Technology and Factory Management (IWF) of Technische Universität Berlin. Above all, I want to thank my supervisor Dietmar Hömberg for matchless support and his steady encouragement whenever difficulties occurred.

Many thanks go to my colleagues Daniela Kern, Thomas Petzold, Kevin Sturm, Natalia Togobytska and to Anke Giese from Weierstrass Institute. In particular, I would like to mention Timo Streckenbach who patiently helped me with all kind of programming issues and especially those concerning *pdelib2*, Wolf Weiss who was always open for discussion related to modelling questions and who gave me a lot of moral support, Christian Meyer who helped me with mathematical problems and who shared the office with me for two long years and Klaus Krumbiegel who shared the office with me as well and who always was ready to talk about private and professional matters.

In addition, I would like to thank Elias Jarlebring from the K. U. Leuven for the fruitful joint work on non linear eigenvalue problems and Patrick Rasper from the IWF who supported me during the cooperation project for the last three years.

Furthermore, I want to thank Prof. Utz von Wagner for all the helpful comments about this work.

Beyond the Weierstrass Institute, great thanks go, of course to my family, to all my friends, in particular to Thomas Böhme, to Carmina and especially to Lucia for their support and help finishing this thesis.

Zusammenfassung

Bei der Optimierung von Fräsprozessen, die in der Massenproduktion genutzt werden, ist die Hauptaufgabe, das Zeitspanvolumen zu steigern und gleichzeitig die Produktqualität sicherzustellen. Die Erhöhung des Zeitspanvolumens ist jedoch durch die verfügbare Spindelleistung und durch den Verlust der Prozessstabilität begrenzt. Die Entwicklung von optimierten Designvorgaben für neue Werkzeugmaschinen ist daher eine der Hauptaufgaben der Forschung. Für bestehende Werkzeugmaschinen und Prozesse müssen die Effizienz und die Zuverlässigkeit der Stabilitätsanalyseverfahren weiter gesteigert werden.

Um diesen Anforderungen gerecht zu werden, wird in der vorliegenden Arbeit ein neues Fräsmodell zusammen mit einem speziell dafür entwickelten, numerischen Lösungsverfahren vorgestellt. Neben der Maschinendynamik wird das Werkstückverhalten in dem neuen Modell berücksichtigt. Ein komplexes Mehrkörpersystem, das zur detaillierten Maschinenbeschreibung verwendet wird, ermöglicht es, Optimierungspotentiale in der Maschinenstruktur aufzudecken. Die Modellierung des Werkstücks als dreidimensionaler, thermoelastischer Festkörper erlaubt eine Untersuchung der Werkstückeinflussfaktoren und die Analyse verschiedener Geometrien. Mit Hilfe eines Dexel-basierten Materialabtrennungsmodells kann darüber hinaus, auch für (thermo–)elastische Werkstückmodelle, die erzeugte Werkstückoberfläche und damit der Regenerativeffekt simuliert werden. Das numerische Lösungsverfahren basiert auf einer schnellen Methode zum Aufbau der Gleichungen des Mehrkörpersystems und einer Ortsdiskretisierung der Werkstückgleichungen mit Hilfe der Finiten Elemente Methode. Die effiziente Lösung des gekoppelten Systems im Zeitbereich wird durch ein implizites Zeitintegrationsverfahren gewährleistet. Ein weiterer Bestandteil der Arbeit ist ein neu entwickeltes, effizientes Verfahren zur Stabilitätsanalyse von periodischen Delaydifferentialgleichungen. Solche Systeme beschreiben das Stabilitätsverhalten komplexer Fräsmodelle oder repräsentieren dynamische Systeme, die von Modalanalysedaten realer Maschinen abgeleitet wurden. Das neue Verfahren basiert auf der Lösung von nichtlinearen Eigenwertproblemen und der konsquenten Ausnutzung von Modellreduktionstechniken.

Die Arbeit ist wie folgt strukturiert: Im Anschluss an die Einleitung folgt ein Kapitel in dem das neue Verfahren zur Stabilitätsanalyse, einige Anwendungsbeispiele und die Modellreduktion erläutert werden. Kapitel 3 deckt die Entwicklung des komplexen Fräsmodells sowie eine detaillierte Beschreibung der Kopplungsterme ab. Kapitel 4 beschäftigt sich mit den Diskretisierungsansätzen und dem Zeitintegrationsverfahren. Die Präsentation der Simulationsergebnisse erfolgt in Kapitel 5 und Kapitel 6 behandelt die experimentelle Verifizierung. Der letzte Abschnitt enthält einige abschließende Bemerkungen.

Abstract

The main optimisation goal for milling operations in mass production is to increase the material removal rate while maintaining an optimal product quality. In addition to the spindle power available, the loss of process stability imposes an upper boundary to the increase of the material removal rate. The challenges in research are therefore to formulate optimal design directives for new machines on the one hand and on the other to improve the reliability and the efficiency of stability prediction methods for given machines and processes.

In order to address these issues, a new coupled model for milling processes is presented in the following together with a tailored numerical simulation algorithm. The model incorporates the machine dynamics and thermo–mechanical work piece effects. While the detailed representation of the machine structure provided by means of a multi body system gives useful information to discover structure optimisation potentials, the work piece representation as a 3D thermo–elastic solid guarantees high flexibility as a large range of possible geometries fits into this framework. The regenerative effect is incorporated by a new Dexel based material removal model that allows a realistic simulation of the generated work piece surface even for (thermo–)elastic work piece models. A newly developed algorithm based on a finite element discretisation of the work piece equations and a fast method for the assembly of the equations of motion for the multi body system guarantees a robust and effective numerical solution of the coupled system due to a fully implicit time integration scheme. Another novelty is related to the need for an efficient and reliable stability analysis method for large systems of periodic delay differential equations (PDDEs). Such systems arise either from the afore mentioned complex milling system involving a machine model and the discrete elasticity equations in 3D describing the work piece dynamics or even from complex dynamical systems representing the modal analysis data of a real milling machine in time domain. The key concepts to achieve this goal are, on the one hand, a new stability analysis approach based on the solution of non linear eigenvalue problems and, on the other hand, the consequent use of recently developed model reduction techniques.

The work is organised as follows: The introduction is followed by a chapter dealing with the stability analysis for PDDEs, its applications with focus on coupled systems and the exploitation of model reduction techniques. Chapter 3 covers the development of a coupled milling system including a detailed description of the coupling terms involved. Chapter 4 is devoted to the discussion of discretisation schemes and the presentation of the time integration algorithm. The simulation results are presented in Chapter 5 while Chapter 6 covers the experimental verification. The last section is devoted to some closing remarks.

Contents

Chapter 1

Introduction

1.1 Preface

The present work is a result of the research activities related to a cooperation project between the Weierstrass Institute of Applied Analysis and Stochastics (WIAS) and the Department of Production Technology and Factory Management (IWF) of Technische Universität Berlin entitled '*Development of a Stability Prediction Tool for the Identification of stable Milling Processes'*, supported by Deutsche Forschungsgemeinschaft (DFG) within the framework of the priority program 1180[1]. The objective of the research project was the investigation of several experimental and theoretical issues arising from the development of a simulation tool to describe the effects related to the process structure interaction in milling. The experimental studies have been carried out in close cooperation with the IWF. As a consequence, the results being discussed in the present work have already partly been published in the research articles [24, 43, 75, 79–81, 102, 103].

1.2 State of research in the modelling and the stability analysis of metal cutting processes

The optimisation of production chains and particular processes is an important issue in industry and economy. In production technology, for example, the research engineers carefully analyse each step of the product development to discover optimisation potentials. In order to reduce the costs arising from extensive experimental stud-

[1]For a detailed review of the mathematical methods in production technology see e.g. [28]. In particular, the authors consider the Priority Program 1180 and point out that 'In order to better understand and to predict the relations between the production process, the machine behaviour and the resulting work piece properties, in 2005 the Priority Program 1180 *"Prediction and Manipulation of Interactions between Structure and Process"* has been established by the Deutsche Forschungsgemeinschaft. In this research program, designed for a total of six years, approx. 50 researcher throughout Germany from the fields of production engineering, mechanics, mathematics and materials sciences work interdisciplinary together. Across the field borders innovative approaches and methods for the prediction and systematic manipulation of interactions are investigated.'.

ies, the need for numerical simulations drastically increased in the recent decades. Nowadays, the simulation of processes, machines, processes structure interaction and entire process chains is considered as a powerful tool to increase the efficiency of single processes and production chains.

The main optimisation goal for milling operations involved in mass production is to increase the metal removal rate, while maintaining an optimal product quality. In addition to the available spindle power, the loss of process stability imposes an upper bound to the increase of the material removal rate. In case of unstable processes, the resulting large oscillations of tool and work piece may destroy the tool, cause damages in the machine structure and lead to a poor product quality, i.e., for example, a rough work piece surface. The challenges in research are therefore on the one hand, for given machines and processes, to improve the reliability of stability prediction methods and on the other hand, for new machines, to formulate optimal design directives.

The stability prediction for metal cutting operations usually involves a process and a structure model. While the process models relate the cutting or tool engagement conditions to the cutting forces acting between tool and work piece, the structure models describe the reaction of machine and work piece to the applied external cutting forces. The structure response, i.e. tool displacement and work piece deformation at the cutting zone, usually changes the engagement conditions which leads in turn to a perturbation of the cutting forces. Depending on the predefined process parameters and on the dynamical characteristics of the structure, the cutting force perturbation either decays or increases in time. The uncritical case of decaying perturbations finally leads to the desired stationary cutting conditions. Increasing cutting force perturbations, the so–called regenerative chatter, provoke strong vibrations of machine and work piece and thus lead to the undesired unstable processes.

The research on this problem started in the early 1950s with pioneering works of Tobias [99, 100] and Tlusty [97, 98] dealing with drilling, turning and metal cutting in general. The large number of papers published on the stability prediction reveals the relevance of this research field.

Time domain simulations in combination with a heuristic stability criterion exploiting either the evolution the cutting forces [60, 91, 92] or the evolution of the uncut chip thickness [23], are a flexible and straightforward approach to characterise the stability of cutting processes. As shown by Lee et al. [59,61], they allow to employ the elaborated cutting force models proposed by Oxley [70] for stability prediction. Moreover, time domain simulations can be useful to simulate the machined surface for complex tool geometries [6] or for small radial immersion milling [23].

Another research direction is the accurate and efficient prediction of stability limits over a wide range of process parameters. For milling problems, Altintas and Budak [4] proposed an analytical method for the stability prediction where the time dependent directional factors are approximated by the zero order component of their Fourier series. In another work [17, 18] the same authors showed that the analytical approach also works for more accurate approximations of the directional factors. Insperger et al. [48] reformulated the stability problem in terms of stability conditions for delayed differential equations with time periodic coefficients and proposed a new

numerical method for the stability prediction. For further details on the mathematical theory and the numerical methods the reader is referred to Section 2.2.

The dynamical characteristics of the machine structure are usually incorporated by means of a frequency response function (FRF) measured at the tool centre point (see e.g. [3, 33]). Since the configuration of the milling machine usually does not change markedly during the cutting operations, the FRFs at the tool centre point (TCP) include all necessary information for stability prediction purposes. The gyroscopic effects caused by the spindle rotation become relevant only for high spindle speeds (see e.g. [33, 35]). Since the stability predictions methods presented in [4, 17, 18, 33] are formulated in frequency domain, the collected FRFs can be directly used to calculate the stability limits. Fitting the measured FRFs either by a sum of FRFs corresponding to single degree of freedom oscillators or by a FRF corresponding to an abstract linear multi degree of freedom system, provides an equivalent set of state equations reproducing the structure response in time domain. Such a time domain representation is an alternative approach that has been successfully employed in many stability predictions methods (see e.g. [9, 21, 48, 51]).

In case that the compliance of work piece and machine tool have the same order of magnitude, the work piece characteristics affect the process stability. This happens especially in the production of blade integrated disks (BLISKs) for aeroengines or during the machining of other thin walled projecting structures. The FRF at the cutting zone describes the work piece response to the forces arising from the cutting process. In contrast to the FRF of the machine tool, the work piece FRF changes throughout the cutting process. During the milling operation the tool position changes due to the feed and the cutting zone travels along the work piece. Depending on the cutting zone position different eigenmodes and frequencies become relevant for the corresponding FRF. In order to incorporate the work piece effects in the standard stability prediction methods, the work piece dynamics can be approximately represented by several FRFs measured along the tool path [12, 56, 72]. Another effect is related to the material removal. During the milling operation, the locally decreasing wall thickness of the work piece leads to a shift in the eigenfrequencies and probably increases the work piece compliance. As shown by Atlar et al. [8] for beam like structures and by Alan et al. [1] for three dimensional thin walled structures, the changing FRFs due to the material removal can be analytically approximated by the so called matrix inversion method proposed by Özgüven [71]. Incorporating the resulting FRFs in the standard stability prediction finally provides the stability diagrams corresponding to different stages of the machining process.

Furthermore, temperature effects may cause a poor product quality and geometric errors in the machined surface. For special geometries and adverse machining conditions, the heat generated by the cutting process locally leads to a significant rise of the work piece temperature (see e.g. [107]). The resulting thermal expansion leads to large work piece deformations and too much or too few material is removed from the work piece (see e.g. [108]). In addition to the effects related to thermal expansion, the work piece temperatures affect the process stability limits as well. In an experimental study, Uhlmann et al. [103] showed that a preheating of the work piece partly increases the stability limits.

1.3 Time domain simulations of process structure interaction phenomena

The modelling of process structure interaction phenomena in production processes usually leads to coupled systems of ordinary and partial differential equations. While different process models relating the engagement conditions to the forces acting on tool and work piece usually present a similar mathematical structure, the machine and work piece models vary in each application. As a consequence, the resulting complete systems present a particular structure and tailored numerical algorithms have to be employed to guarantee an efficient simulation of the underlying process.

In grinding, for example, the deformation of spindle and the attached grinding wheel usually dominate the structural response to process forces acting on the wheel. Correspondingly, the approach proposed in [106] for a NC shape grinding application, involves an elastic solid representation of the spindle, the spindle bearings and the grinding wheel. The model can be adapted to vibration measurements by adjusting the material parameters for each part and the discretisation with adaptive finite elements in space and a Newmark scheme in time guarantee an efficient and accurate simulation of the grinding process [10]. In tool grinding processes, large work piece deformations dominate the process structure interaction. In contrast to the shape grinding example, the spindle and the grinding wheel are assumed to be rigid while the work piece, i.e. a slender drill, is modelled as a cantilever beam with varying cross section and tailored boundary conditions representing the clamping [74]. The lathe model to simulate a facing process presented in [16] consists of rigid and flexible bodies connected by joints with nonlinear constitutive equations. A rigid body represents the work piece and in addition to the standard process models, the authors formulate a contact problem to accurately reproduce the interaction between tool and work piece.

In milling, the tool spindle system plays a crucial role. In order to study the effect of the spindle bearings and the spindle rotation on the process stability, Großmann et al. [35] proposed an elaborate spindle model. The flexible multi body system employed for the spindle representation accurately reproduces the FRF at the TCP for idle and rotating state and provides useful information about the effects related to changes in the bearing stiffness.

Abstract flexible multi body systems can be used to reconstruct the frequency response function for particular locations on machine parts. In micro milling, for example, the frequency response function cannot be measured directly at the tool centre point. In the approach proposed by Shi et al. [88], an oscillator chain reproducing the FRF measured at the tool holder is combined with a Bernoulli cantilever beam model representing the tool dynamics. Finally, the model incorporating spindle rotation effects is utilised to calculate stability charts for the underlying micro milling process.

A grinding model to simulate the work piece temperature, as well as the heat conduction in the machine tool structure is discussed in [11]. While the work piece model involves unstationary heat conduction and thermal expansion, the spindle and the attached grinding wheel are represented as a thermo–elastic system without neglecting the acceleration terms.

1.4 Motivations for the present work

Even though the structure representation by means of measured frequency response functions has been applied successfully in the stability prediction of milling problems, the approach is not suitable for the machine optimisation because it provides only few information about of the general behaviour of the milling system. A common direction to improve the performance of milling machines is to reduce the time needed for the axis travel by increasing the travelling speed. Higher travelling speeds can be achieved by reducing the weight of the structural parts. As a consequence, the stiffness of the machine structure decreases and, along with that, the maximum chatter free material removal rate usually diminishes, too.

In order to study these effects numerically, the machine structure has to be represented with realistic models providing structural information. A popular approach in production technology is to model each machine part as an elastic body and to connect the different parts by special joint elements. This strategy, however, leads to very large systems which often involve unacceptable computational costs. An alternative strategy is to employ multi body systems for the machine structure simulation. Multi body systems provide more structural information than the FRF approach and require less computational effort than the fully elastic models. The performance of multi body systems can be further improved by replacing important parts by elastic models with a few degrees of freedom. The resulting models, the so called flexible multi body systems, provide more reliable results without severely increasing the computational costs.

As outlined in Section 1.2, the standard approach to incorporate work piece effects in milling simulations is to represent the work piece characteristics by means of several measured FRFs. This approach, however, seems to be cumbersome in the daily production routine, because unlike the machine, the work piece changes frequently. Moreover, the empirical FRF based approach is not suitable for the simulation of heat conduction in the work piece. Alternatively, the work piece can be represented as a three dimensional thermo–elastic solid. This approach allows to simulate different geometries, incorporates the effects of a travelling cutting zone and is suitable for temperature simulations. If the focus is on stability analysis only, the work piece can alternatively be represented as a one or two dimensional elastic structure, that is, for example, a rod, a cantilever beam, a plate or a shell.

In view of the above considerations, the combination of a multi-body system representing the machine structure with a thermo–elastic solid model for the work piece seems to be a promising new approach for the simulation of process structure interaction in milling. Based on the well studied models describing each subsystem, i.e. a multi-body system for the machine and a thermo–elastic solid model for the work piece, the main modelling challenge is to incorporate the effect of process forces and to derive the equations describing the coupling of both structural models.

Consequently, one objective of the present work is to present a new model describing the coupling of machine and work piece, the development of tailored numerical algorithms for the underlying coupled system and the simulation of a particular production process to illustrate the features of the new model. As usual in time domain simulations, a heuristic criterion provides information to evaluate the process stability. A second objective is to determine the stability limits corresponding to

the coupled system employing a rigorous stability criterion. Since the system can be approximated by a large system of periodic delay differential equations (PDDEs), the goal is to develop a new numerically efficient stability analysis method which allows to predict the stability limits for such systems.

1.5 Contribution of the present work

The main contributions of this thesis are twofold: first, a new model for milling processes is presented that incorporates the machine dynamics and thermo–mechanical work piece effects. While the detailed representation of the machine structure by means of a multi body system provides useful information to discover structure optimisation potentials, the work piece representation as a three dimensional thermo–elastic solid guarantees high flexibility since a large class of possible work piece geometries fits in this framework. Moreover, in order to incorporate the regenerative effect, a new Dexel based material removal model is introduced that allows, in contrast to current approaches, a realistic simulation of the generated work piece surface even for (thermo–)elastic work piece models. The second novelty is related to the need for an efficient and reliable stability analysis method for large systems of periodic delay differential equations (PDDEs). Such systems arise, for example, from the above mentioned complex milling models involving a machine model and the discrete elasticity equations in 3D describing the work piece dynamics. The key concepts in order to achieve this goal are, on the one hand, a new stability analysis approach based on the solution of non linear eigenvalue problems and, on the other hand, the consequent use of recently developed model reduction techniques.

The present work is organised as follows. Chapter 2 deals with the stability analysis of milling processes. By means of time domain simulations in combination with a new chatter criterion it is shown that the predicted stability limits are almost independent of the employed empirical cutting force model. Differences can only be observed for strong variations in the feed per tooth. The main part of Chapter 2 is devoted to the development of a new stability analysis method for periodic delay differential equations. In particular, these systems describe the dynamics of milling processes. In contrast to the common solution operator discretisation approach, the new method based on the solution of nonlinear eigenvalue problems and continuation potentially allows, even for large systems, to compute the stability limits accurately. In Section 2.3, the new method is applied to study the dynamics of a coupled milling model involving the dynamics of a simple machine and a rod–like work piece. The presented results reveal the effect of the coupling and show the influence of the discretisation error. For the first time, model reduction techniques are considered in the framework of stability prediction. The new approach introduced in Section 2.3.2 drastically improves the efficiency without introducing relevant errors and thus opens new research directions in stability analysis.

Chapter 3 is devoted to the derivation of a complex milling model involving the dynamics of machine and work piece as well as thermal effects. The strategy to derive a milling model based on a multi body system characterising the machine, a work piece represented as a thermo–elastic solid and an empirical cutting force model for the coupling of both parts, requires a new modelling approach. Consequently,

the focus is on the rigorous derivation of a system of partial and ordinary differential equations describing the new milling model and on an extensive discussion of several modelling issues. As a result, the regenerative effect is not reproduced by means of a delayed term but by means of a subsequent modification of the work piece surface. In contrast to similar techniques proposed by Campomanes et al. [23], Sims [91] or Suhrmann et al. [95], the approach presented in this work allows for the first time to incorporate the tool vibrations and arbitrary deformations of the work piece surface. Since the material removal model considered here generates an approximate machined work piece surface, the results of the virtual machining can be very useful in practise. In addition, the new strategy allows to describe the effects related to a travelling cutting zone in a straightforward way.

In Chapter 4 the focus is on the development of a tailored numerical algorithm to solve the system of equations derived in Chapter 3 for the new milling model. In a first step, the finite element method is utilised to derive a space discretisation of the thermo–elastic system representing the work piece. Next, for each subsystem, different time integration schemes are introduced and extensively discussed in order to develop an optimal strategy for the coupled system. The final result is a new time integration scheme based on a fixed point iteration that guarantees a fully implicit coupling of the semi-discrete subsystems in each time step. The remainder of Chapter 4 is devoted to the implementation of the material removal model, another important issue. Special attention is paid to the incorporation of the work piece deformations and to the construction of new work piece grids based on a Dexel representation.

The objective of the simulations presented in Chapter 5 is to illustrate the main features of the new model. At first, it is shown that the machine model accurately reproduces the stability limits calculated on the basis of a measured FRF by means of the new stability prediction method presented in Chapter 2. Time domain simulations involving the full system illustrate that the structure of the employed work piece affects the process stability. While for rather stiff geometries the process stability is dominated by the characteristics of the machine, the situation changes completely in case of a supple work piece. The simulations illustrate that a process, previously identified as stable, can be destabilised due to the dynamical work piece characteristics. The simulation of temperature effects show that, in slot milling, the work piece temperature only moderately increases and that the induced thermal expansion does not lead to relevant geometric errors in the machined surface.

Chapter 6 covers the comparison of the predicted and measured stability lobe diagrams including the chatter frequencies. Moreover, it is shown that the work piece effects observed in the simulations can be detected experimentally as well. The chapter is completed by an extensive discussion of possible sources for measurement errors and further experimental issues.

The last section is devoted to some concluding remarks and to the discussion of further research directions arising from the content of the present work.

Chapter 2

Stability analysis

2.1 Dynamics of a simple milling system

2.1.1 Oscillator equations

The milling process can be represented schematically by a turning cutter removing material from the work piece, the latter translating in the direction of feed as depicted in Figure 2.1.

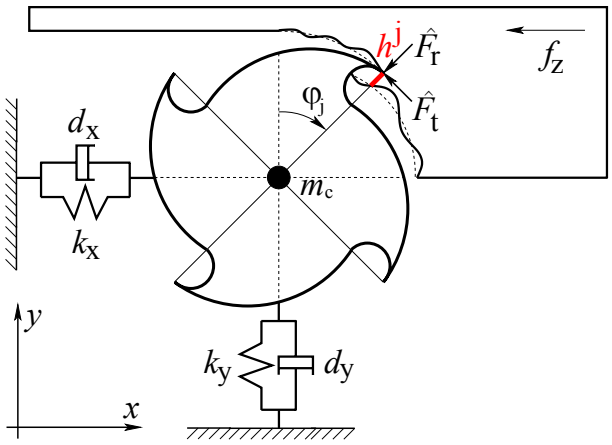

Figure 2.1: Schematic representation of the milling process.

As shown in [3, p.105], the simplest structure model for milling problems is an oscillator with two degrees of freedom. For such a model, the equations of motion describing the cutter motion are given by

$$\ddot{u} + \underbrace{\begin{bmatrix} 2\xi_1\omega_1 & 0 \\ 0 & 2\xi_2\omega_2 \end{bmatrix}}_{D} \dot{u} + \underbrace{\begin{bmatrix} \omega_1^2 & 0 \\ 0 & \omega_2^2 \end{bmatrix}}_{K} u = \frac{1}{m_c} F \,, \tag{2.1}$$

where m_c denotes the modal mass. The respective eigen–angular–frequencies in x- and y-direction are denoted by $\omega_i = 2\pi f_i = \sqrt{k_i/m_c}$ and the modal damping

m_c	ζ_i	f_i
0.06 kg	1.2 %	2241.49 Hz

Table 2.1: Oscillator parameters.

in each direction is represented by $\xi_i = d_i/2\sqrt{m_c k_i}$. Throughout the following sections, the parameters characterising the oscillator are chosen according to the values indicated by Table 2.1. As shown in Figure 2.2, the given values can be interpreted as an approximation of the dominant peak appearing in the frequency response function measured at the tool centre point of the milling machine employed for the experimental part of the present work (see Section 6.2). Since the dominant peak is related to an eigenmode of the rotationally symmetric spindle-tool system, it is fair to assume that the oscillators representing the main peak have the same mass, the same stiffness and the same damping.

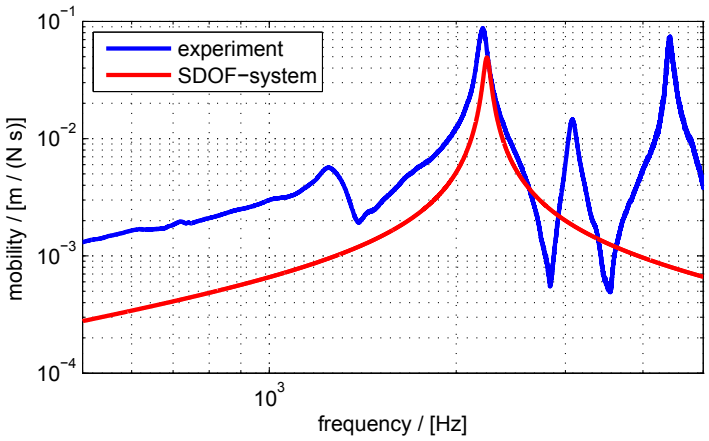

Figure 2.2: Experimental mobility frequency response function[1] (see Figure 6.2 in Section 6.2) compared to a single degree of freedom oscillator approximation of the main peak.

The cutting forces given by $F = [F_x, F_y]^T$ appear on the right hand side of (2.1) as external forces. By means of an orthogonal transformation the external force can be expressed as a sum of the forces acting $\hat{F}(h^j) = [\hat{F}_r(h^j), \hat{F}_t(h^j)]^T$ on each tooth, i.e.

$$F = -\sum_{j=1}^{N_z} a_p g(\varphi_j) \begin{bmatrix} \sin\varphi_j & \cos\varphi_j \\ \cos\varphi_j & -\sin\varphi_j \end{bmatrix} \hat{F}(h^j), \tag{2.2}$$

where

$$\varphi_j(\varphi(t)) = \varphi(t) + (j-1)\frac{2\pi}{N_z}, \quad \varphi(t) = 2\pi n\, t, \tag{2.3}$$

[1]The experiments have been carried out by P. Rasper under supervision of Prof. E. Uhlmann at IWF, TU-Berlin (for further details see e.g. [75] and Section 6.2).

represents the time dependent angle of tooth 'j' indicated in Figure 2.1. The parameter n represents the rotation speed in rps, while N_z denotes the number of tooth. Note that the considered cutter has no helix angle. Depending on the immersion, the tool enters and leaves the cut at different angles φ_{st} (entry) and φ_{ex} (exit). During the free-flight, i.e. $\varphi_j \notin (\varphi_{st}, \varphi_{ex})$, no cutting forces act on the tool, a fact that can be modelled by means of a switch function [48]

$$g(\varphi_j) = \begin{cases} 1, & \varphi_{st} \leqslant \mathrm{mod}(\varphi_j, 2\pi) \leqslant \varphi_{ex}, \\ 0 & \text{otherwise} \end{cases} \tag{2.4}$$

For the model illustrated in Figure 2.1 the starting- and exit-angles are $\varphi_{st} = 0$ and $\varphi_{ex} = \frac{\pi}{2}$. The function $\mathrm{mod}(., 2\pi)$ projects an arbitrary angle argument on the interval $[0, 2\pi]$. The forces $\hat{F}(h^j)$ acting in radial and tangential direction on the tip of each tooth (see Figure 2.1) depend on the uncut chip thickness h^j, on the axial depth of cut a_p (immersion depth perpendicular to the x-y plane) and possibly on the cutting speed v_c, i.e. the tangential velocity at the tip of the tooth. The effects related to the plastic deformation of the work material with high strain rates govern the chip formation process in metal cutting. Since the underlying model equations present a very intricated structure, the usual approach is to employ empirical cutting force models instead of solving the equations describing the plastic deformation process. A large number of empirical approaches to determine the cutting forces for given process parameters have been developed in the past.

2.1.2 Cutting force models

During a milling operation the tool tries to cut a chip with the corresponding approximate static chip thickness $h_{stat} = f_z \sin\varphi_j$. The reaction force generated by the cutting operation induces a displacement of the tool and, according to the dynamical characteristics of the milling system, a wavy surface is generated. The subsequent tooth oscillates because of the previously induced motion and cuts into a wavy surface produced by the preceding tooth. Mathematically, this mechanism can be expressed by the following formula for the uncut chip thickness, i.e.

$$h^j = [\sin\varphi_j, \cos\varphi_j] \left(\begin{bmatrix} f_z \\ 0 \end{bmatrix} + \begin{bmatrix} u_1(t) - u_1(t-\tau) \\ u_2(t) - u_2(t-\tau) \end{bmatrix} \right) \tag{2.5}$$

$$= \underbrace{f_z \sin\varphi_j}_{h^j_{stat}} + \underbrace{[u_1(t) - u_1(t-\tau)]\sin\varphi_j + [u_2(t) - u_2(t-\tau)]\cos\varphi_j}_{h^j_{dyn}}, \tag{2.6}$$

with a delay $\tau = (nN_z)^{-1}$. In order to ease the presentation of the cutting force model, the focus is on a tool with a single tooth and the index 'j' can be dropped from the expression of the uncut chip thickness. In case of tools with several teeth the total cutting force can be computed by summing up the contributions of each tooth. A simple linear cutting force model relating the uncut chip thickness, the axial depth of cut and the cutting forces has been proposed by Weck [105]. The empirical relation reads

$$\hat{F} = \hat{K} a_p h, \tag{2.7}$$

with parameters $\hat{K} = [\hat{K}_r, \hat{K}_t]^T$, the specific cutting forces. Altintas [3] extended this approach. He introduced additional parameters $\hat{K}^e = [\hat{K}_r^e, \hat{K}_t^e]^T$, the so called edge forces, to account for the contribution of friction to the cutting force for $h = 0$ mm, i.e.

$$\hat{F} = \hat{K} a_p h + \hat{K}^e a_p. \tag{2.8}$$

Another possibility is to use a non-linear relation between cutting force and chip thickness, as was proposed by Tobias [99] or Stépán [93]

$$\hat{F} = \hat{K} a_p h_+^{x_f}. \tag{2.9}$$

In this approach $x_f \in (0, 1]$ is another empirical parameter. Note that due to the fact that $x_f \in (0, 1]$, the above expression is not well defined for $h < 0$. Consequently, h has to be replaced by its positive part being defined as

$$h_+ = \max(h, 0) = \begin{cases} h & \text{if } h > 0, \\ 0 & \text{otherwise.} \end{cases} \tag{2.10}$$

Replacing h by h_+ introduces an additional non-linearity in the computation of the cutting forces. An attempt which usually allows a good representation of the experimental data was developed by Kienzle and Victor in the early 1950s. The model which is described in detail by Tönshoff & Denkena [101], reads

$$\hat{F} = \hat{K}(h_+) a_p h_+, \quad \text{with} \quad \hat{K}(h_+) = [K_r(h_+), K_t(h_+)]^T \quad \text{and} \tag{2.11}$$

$$\hat{K}_i(h_+) = \begin{cases} \hat{k}_i^3 h_+^{-m_i^3} & , 10^{-3}\text{mm} \leqslant h_+ \leqslant 10^{-2}\text{mm} \\ \hat{k}_i^2 h_+^{-m_i^2} & , 10^{-2}\text{mm} < h_+ \leqslant 10^{-1}\text{mm} \\ \hat{k}_i^1 h_+^{-m_i^1} & , 10^{-1}\text{mm} < h_+ \leqslant 1\text{mm} \end{cases}.$$

As mentioned before, the large number of free parameters, i.e. $\hat{k}_i^j$ and m_i^j with $j = 1, \ldots 3$, guarantees a precise reproduction of the experimental data. Faassen [33] presents a combination of the models shown above. He combines Stépán's model (2.9) with the edge effects introduced by Altintas (2.8), i.e.

$$\hat{F} = \hat{K} a_p h_+^{x_f} + \hat{K}_e a_p. \tag{2.12}$$

Recently new cutting force models have been proposed to incorporate process damping effects which seem to be important especially for low cutting speeds (see e.g. [5, 19]). Moreover, the effect of tool wear has been investigated and also incorporated in the cutting force models (see e.g. [55]). However, since the present work focuses on sharp tools and high cutting speeds, the process damping and tool wear effects are assumed to be negligible.

2.1.3 Experimental determination of the cutting constants

Every model presented above, contains empirical parameters which have to be determined from experimental data. A standard approach to solve the parameter identification problem is the least squares method proposed by Altintas (see [3, Sec. 2.8.1]). The cutting force measurements described in Section 6.3 provide an evolution of the cutting forces in x- ,y- and z-direction for several values of f_z. The time discrete cutting forces $F_k^{exp}(t_i, f_z)$, $k = 1, 2, 3$, can be averaged over a tooth period to get

$$\bar{F}_k^{exp}(f_z) = \frac{1}{\tau} \sum_{i=1}^{N} \left(F_k^{exp}(t_{i-1}, f_z) + F_k^{exp}(t_i, f_z)\right) \frac{\Delta t}{2}, \tag{2.13}$$

with Δt denoting the time step size corresponding to the experimental data and $N = \tau/t_N$ the number of averaged time steps. Note that the time integration in (2.13) has been carried out on the discrete level employing the trapezoidal rule. A similar expression can be derived exploiting (2.2) together with one of the empirical cutting force models. Assuming a rigid machine, i.e. $h^j(t) = h(\varphi_j(t)) = h_{stat}(\varphi_j(t)) = f_z \sin \varphi_j(t)$, leads to the average cutting force

$$\bar{F}_k(K_{CF}, f_z) = \frac{1}{\tau} \sum_{j=1}^{N_z} \int_0^{\tau} F_k\big(K_{CF}, f_z, \varphi_j(t)\big) dt \tag{2.14}$$

$$= \frac{N_z n}{2\pi n} \sum_{j=1}^{N_z} \int_0^{\tau} F_k\Big(K_{CF}, f_z, \varphi_j\big(\varphi(t)\big)\Big) (\varphi(t))' dt \tag{2.15}$$

$$= \frac{1}{\varphi_p} \sum_{j=1}^{N_z} \int_{\varphi_{st}}^{\varphi_{ex}} F_k\big(K_{CF}, f_z, \varphi_j(\psi)\big) d\psi, \tag{2.16}$$

with $\varphi_p = 2\pi/N_z$ denoting the pitch angle and K_{CF} a vector containing the empirical model parameters. The objective functional measuring the squared distance between model and experimental cutting forces reads

$$J(K_{CF}) = \sum_{k=1}^{2} \sum_{i=1}^{m} \left[\bar{F}_k^{exp}(f_z^i) - \bar{F}_k(K_{CF}, f_z^i)\right]^2. \tag{2.17}$$

where f_z^i denotes the different values for the feed per tooth. The constraint minimisation of (2.17) by means of Gauss-Newton methods (for numerical and theoretical aspects see e.g. [84]) finally provides an optimal set of parameters K_{CF}. The imposed constraints guarantee the predefined limits for the empirical parameters and in case of model (2.11) the continuous dependence on the uncut chip thickness. The results of the optimisation process are summarised in Table 2.2, where the residual J^{min} of the objective functional is given in the last row. The constants corresponding to the model (2.11) are given in Table 2.3. The residual J^{min} can be interpreted as an indicator for the accuracy of each fit. Note that, depending on the analytical form of the cutting force model, the approximation of the experimental mean cutting forces is more or less accurate. Consequently, each cutting force model provides for given chip thickness and immersion a slightly different force in x- and y-direction (see (2.2)), which may in turn affect the computed stability limit.

	Weck	Altintas	Stépán	Faassen
$\hat{K}_r$	690 N/mm^2	363 N/mm^2	448 N/mm$^{(1+x_f)}$	342 N/mm$^{(1+x_f)}$
$\hat{K}_t$	894 N/mm^2	770 N/mm^2	565 N/mm$^{(1+x_f)}$	724 N/mm$^{(1+x_f)}$
$\hat{K}_r^e$	–	90 N/mm^2	–	82 N/mm^2
$\hat{K}_t^e$	–	34 N/mm^2	–	18 N/mm^2
x_f	–	–	0.63	0.89
J^{min}	4254.18 N	816.4 N	2090.41 N	796.5 N

Table 2.2: Summary of the cutting constants corresponding to the models of Weck, Altintas, Stépán and Faassen, determined from experimental data[2] for $n = 16600$ rpm.

	$0.001 < \bar{h} < 0.01$	$0.01 \leq \bar{h} < 0.1$	$0.1 \leq \bar{h} < 1$
$\hat{k}_r^i$	325	243	343
$\hat{k}_t^i$	396	633	706
m_r^i	0.65	0.71	0.56
m_t^i	0.35	0.25	0.2

Table 2.3: Summary of the cutting constants corresponding to the model of Kienzle-Victor ($J^{min} = 383$ N), determined from experimental data[2] for $n = 16600$ rpm ($\bar{h} = h/h_0$, $h_0 = 1$ mm, k_r^i and k_t^i are given in N/mm$^{1-m_r^i}$ and N/mm$^{1-m_t^i}$).

2.1.4 Evolution of stable and unstable solutions in time

Reformulating the milling models following from Section 2.1.1 and 2.1.2 in first order form, i.e. introducing a new variable $v = \dot{u}$ and setting $y = [u, v]^T$, leads to the following general periodic delay differential equation (PDDE)

$$\dot{y}(t) = f(t, y(t), y(t-\tau)), \qquad t \in [0, t_e], \tag{2.18}$$

with $f(t, ., .) = f(t + \tau, ., .)$ and the initial condition $y(s) = \phi(s)$, $s \in [-\tau, 0]$. Delay differential equations having a structure like (2.18) can be numerically solved by means of modified Runge-Kutta type time integration algorithms (for further details see e.g. [37, 86]). The milling system (2.1) equipped with Stépán's cutting force model (2.9) for a tool with a single tooth (see Table 2.2) serves as an example for the time domain simulation. The spindle speed has been set to $n = 16600$ rpm and $f_z = 0.2$ mm. The corresponding evolution of the uncut chip thickness for $a_p = 1$ mm and $a_p = 1.5$ mm is illustrated in Figure 2.3. In the first case, after an initial perturbation, the uncut chip thickness converges to its stationary value, given by $h_{stat}^j = f_z \sin \varphi_j$. In the second case, the magnitude of h increases due to superimposed high frequency oscillations, the so called chatter vibrations. Since the superimposed oscillations lead to a poor product quality, it is, from a practical point of view, necessary to choose the process parameters so that any perturbation vanishes and the uncut chip thickness approaches the stationary evolution.

[2]The experiments have been carried out by P. Rasper and C. Mense under supervision of Prof. E. Uhlmann at IWF, TU-Berlin (for further details see e.g. [104] and Section 6.3).

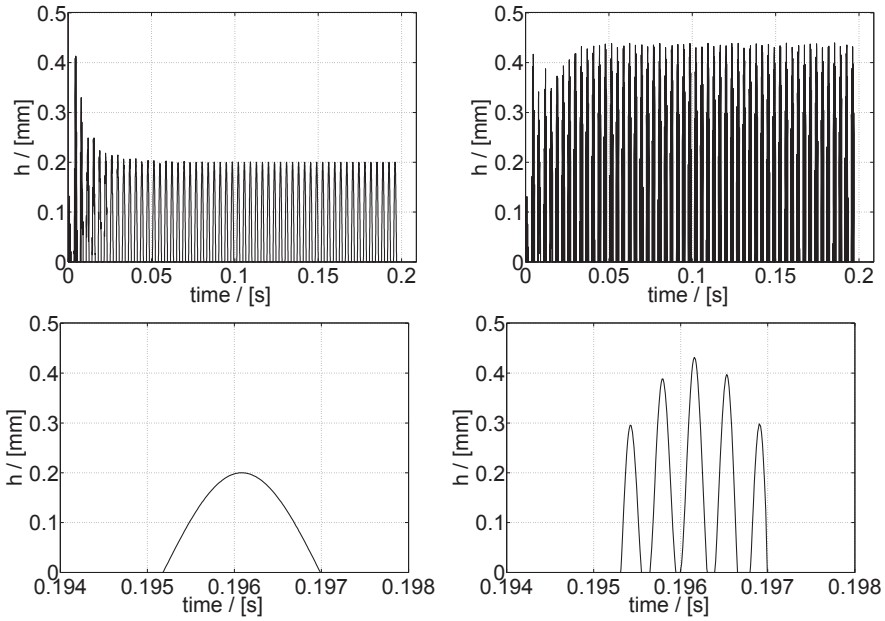

Figure 2.3: Evolution of the uncut chip thickness for a stable (left) and unstable (right) cut simulated with Stépán's cutting force model (2.9) and a feed per tooth $f_z = 0.2$ mm.

These requirements correspond to the mathematical concept of uniformly asymptotically stable solutions (for a precise definition see Appendix A). Consequently, the following heuristic chatter criterion will be constructed so that only uniformly asymptotically stable solutions are identified as stable.

2.1.5 A chatter indicator

As shown in Section 2.1.4 the solution of the milling model summarised by (2.18) may become unstable if the parameter a_p exceeds a limit value. Even though a rigorous stability analysis approach is presented in Section 2.2, it is, for the comparison of the empirical cutting force models, sufficient to work with an approximate stability criterion, the so called chatter indicator. Moreover, a possibly difficult linearisation of the system (h_+ is not differentiable) can be avoided since the numerically computed solution in time domain provides all the necessary information. For a more rigorous justification of the chatter indicator the reader is referred to pp. 25.

Sims [91] presents a criterion which uses Fourier analysis of the data to distinguish oscillations due to separate excitation from those due to self excitation. Based on this distinction it is possible to judge whether the amplitude of self exited vibrations decays or increases. In the case of an increase the state is identified as unstable. Li [60] proposes another chatter indicator, comparing the dynamic cutting force with the static one. Campomanes [23] makes use of a similar indicator, but he considers directly the dynamic and static chip thickness. However, the latter methods use a chatter threshold to identify unstable processes. The precise threshold value has to be deduced from numerical experiments and assumes values between 1.04 and 1.4. Another method to classify the results of the time domain simulation has been

introduced by Smith and Tlusty [92]. They use a peak to peak forces scheme to identify stable cutting conditions.

An alternative approach avoiding the difficulty of defining an empirical chatter threshold value, is to consider for each tooth the difference between the total uncut chip thickness $h^j = h^j_{dyn} + h^j_{stat}$ and its stationary part h^j_{stat}, i.e.

$$e_h(t) = \frac{1}{f_z} \sum_{j=1}^{N_z} |h^j(t) - h^j_{stat}(t)|. \tag{2.19}$$

For every time, the parameter $e_h(t)$ can be computed from the corresponding numerical solution of the milling system. Consequently $e_h(t)$ is the starting point for the derivation of a chatter indicator. Recall that in case of uniformly asymptotically stable solutions any small perturbation vanishes and the uncut chip thickness approaches the value h^j_{stat}. Correspondingly, the local deviation of total and stationary uncut chip thickness e_h decreases in time. Exploiting the evolution of e_h leads to the following number

$$\eta = \max_{s \in I_e} e_h(s) - \max_{s \in I_s} e_h(s), \tag{2.20}$$

with $I_s = (t_0, k\tau)$ and $I_e = ((m-k)\tau, m\tau)$, $m > k$. While for $\eta < 0$, the simulated milling process is classified as stable, positive values of η indicate unstable processes. The stability limit for a given spindle speed can computed applying Algorithm 1 which exploits the characteristics of η. While the the parameter k is rather uncritical, a wrong choice of m leads to serious errors because the computed stability limit depends on the number of simulated revolutions of the tool [91]. The value of the chatter indicator ($m = 55$ and $k = 3$) corresponding to the stable simulation shown in Figure 2.3 is $\eta = -0.225$. The value for the unstable case is $\eta = 1.129$.

Algorithm 1 Stability limit computation

1: Choose iteration parameters m, k, with $m > k \geq N_z$
2: Choose a_p^{st} so that $\eta(a_p^{st}) < 0$
3: Choose a_p so that the $\eta(a_p) > 0$
4: **while** $(a_p - a_p^{st}) > TOL$ **do**
5: $a_p := (a_p + a_p^{st})/2$
6: Solve problem (2.1) numerically on $[0, t_E = m\tau]$, with $\tau = (nN_z)^{-1}$.
7: Calculate η according to (2.20)
8: **if** $\eta < 0$ **then**
9: $a_p^{st} := a_p$, (system is stable)
10: **end if**
11: **end while**

2.1.6 Comparison of the empirical cutting force models

Combining an empirical cutting force model with the simple milling system (2.1) leads, depending on the employed model, to different linear or nonlinear periodic delay differential equations. Although the models have a similar structure, they provide for a given uncut chip thickness different cutting force values. Consequently,

the corresponding stability limits are expected to be different. Computing the stability limit for each cutting force model by means of time domain simulations and the chatter indicator reveals the differences between the cutting force models.

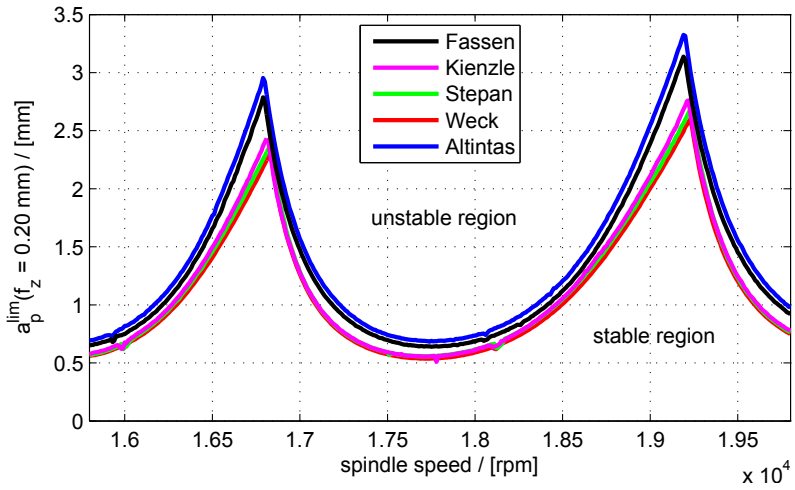

Figure 2.4: Comparison of the stability charts computed for different cutting force models and $f_z = 0.2$ mm.

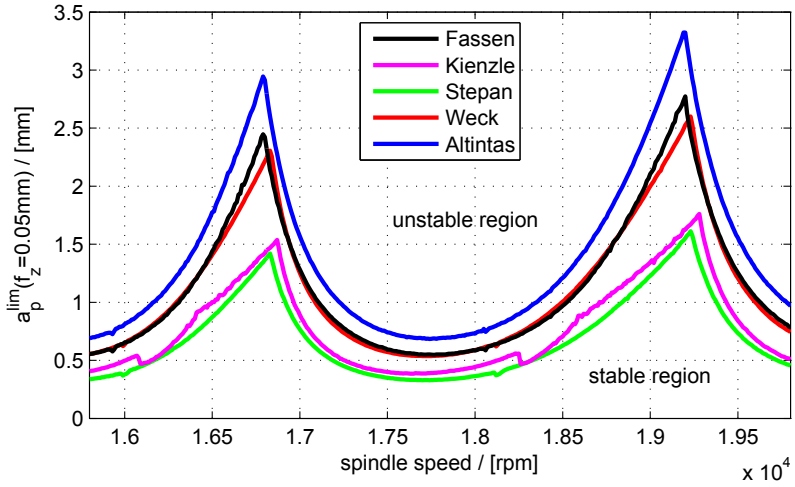

Figure 2.5: Comparison of the stability charts computed for different cutting force models and $f_z = 0.05$ mm.

While for $f_z = 0.2$ mm the variation of the predicted stability limits is rather small (see Figure 2.4), large deviations can be observed in case of $f_z = 0.05$ mm (see Figure 2.5). Analysing the difference between the stability limits for $f_z = 0.2$ mm and $f_z = 0.05$ mm illustrated in Figure 2.6 leads to the conclusion that the nonlinear cutting force models, i.e. (2.12), (2.11) and (2.9), predict, depending on the chosen feed, different stability limits. In contrast to the nonlinear models, the linear models predict the same stability limits for all values of f_z.

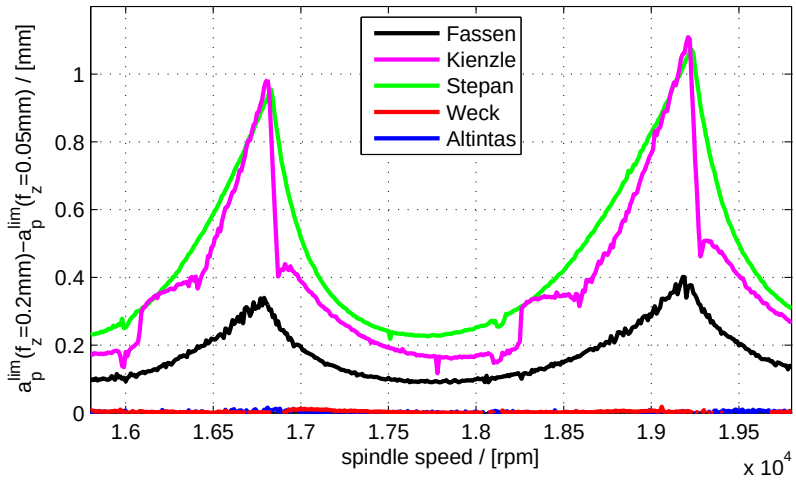

Figure 2.6: Comparison of the difference between the stability charts corresponding to $f_z = 0.2$ mm and $f_z = 0.05$ mm.

2.2 Stability analysis for large DDE systems with periodic coefficients

2.2.1 Introduction to stability analysis for milling systems

Stability condition

The main objective in stability analysis for milling systems usually is to determine the stability of periodic solutions. As outlined by Hale [38, p. 191], the approach presented in this section can be interpreted as an extension of the Floquet theory for ordinary differential equations. The motivation for the strategy of analysing periodic solutions can be illustrated by means of the uncut chip thickness (2.5) which only depends on the difference between current and delayed solution. Consequently, the general delay differential equation 2.18 simplifies for milling models to

$$\dot{y}(t) = f_{mi}(t, y(t), y(t) - y(t-\tau)), \qquad t \in [0, t_e], \tag{2.21}$$

with initial condition $y(s) = \phi(s)$, $s \in [-\tau, 0]$ and $f_{mi} : \mathbb{R} \times \mathbb{R}^n \times \mathbb{R}^n \mapsto \mathbb{R}^n$. In case of τ-periodic functions, i.e. $y_p(t) = y_p(t+\tau)$, (2.21) becomes an ordinary differential equation characterising the periodic solution, i.e.

$$\dot{y}_p = f_{mi}(t, y_p(t), 0) = \tilde{f}_{mi}(t, y_p(t)), \qquad t \in [0, t_e], \tag{2.22}$$

with the initial condition $y_p(0) = 0$. For small perturbations, the stability of a periodic solution y_p can be determined by means of linear stability analysis. Rewriting the solution of the general equation $y(t)$ as the sum of a periodic function y_p and a small perturbation x, i.e. $y(t) = y_p(t) + x(t)$, linearising the right hand side in $x(t)$, $x(t-\tau)$ and exploiting the equation for y_p leads to the following linear delay

differential equation describing the evolution of the small perturbation $x(t)$, the so called *first variational equation* (see [54]), i.e.

$$\dot{x}(t) = A(t)x(t) + B(t)x(t-\tau), \qquad t \in [0, t_e], \tag{2.23}$$

with the initial condition $x(s) = \phi(s)$, $s \in [-\tau, 0]$ and periodic and possibly non smooth matrices (with respect to time)

$$\begin{aligned} A(t) &= \partial_2 f_{mi}(t, y_p, 0) + \partial_3 f_{mi}(t, y_p, 0), \\ B(t) &= -\partial_3 f_{mi}(t, y_p, 0), \end{aligned}$$

where $\partial_i f_{mi}(t, x_p, 0)$ denotes the partial derivative of f_{mi} with respect to the 'ith' argument evaluated at $(t, y_p, 0)$. Since for small perturbations the stability properties of $y_p(t)$ are the same as those of the trivial solution $x(t) = 0$ (see [54, p.243]), the problem of determining the stability of a periodic solutions reduces to the analysis of the linear delay differential equation (2.23) for the evolution of x. In case of a linear milling system (2.23) follows immediately from the fact that the solution y can be written as a superposition of y_p and x. If the matrices $A(t)$ and $B(t)$ are measurable in t, the solution of (2.23) is continuous, i.e. $x(t) \in C([-\tau, t_e])$ (see [38, p. 55]). By defining

$$x_t(s) = x(t+s) : [-\tau, 0] \mapsto \mathbb{R}^n, \tag{2.24}$$

(2.23) can be rewritten as a linear retarded functional differential equation (RFDE), i.e.

$$\dot{x}(t) = A(t)x_t(0) + B(t)x_t(-\tau) = L(t, x_t), \qquad t \in [0, t_e], \tag{2.25}$$

with initial condition $x(s) = \phi(s)$, $s \in [-\tau, 0]$. The mapping $L : D \mapsto \mathbb{R}^n$ with $L(t, .) = L(t + \tau, .)$ is called linear periodic functional on $D \subset \mathbb{R} \times C([-\tau, 0])$. The solution operator $T(t, 0)$ corresponding to (2.23) mapping a given function $\phi \in C([-\tau, 0])$ to the solution on $[t - \tau, t]$ is defined by

$$\begin{aligned} T(t,0) : C([-\tau,0]) &\mapsto C([-\tau,0]) \\ \phi &\mapsto T(t,0)\phi = x_t. \end{aligned} \tag{2.26}$$

The special solution operator for $t = \tau$, i.e.

$$U\phi = T(\tau, 0)\phi, \qquad \phi \in C([-\tau, 0]), \tag{2.27}$$

is called monodromy operator. Following the lines of Hale ([38, p. 192]), the spectrum $\sigma(U)$ of U is at most countable, and is a compact subset of the complex plane with the only possible accumulation point being zero. If $\mu \neq 0$ is in $\sigma(U)$, then μ is in the point spectrum $P\sigma(U)$, i.e.

$$U\phi = \mu\phi, \tag{2.28}$$

with $0 \neq \phi \in C([-\tau, 0])$. Any $\mu \neq 0$ satisfying (2.28) is called *characteristic multiplier* of (2.25) and any λ for which $\mu = e^{\lambda\tau}$ is called *characteristic exponent* of (2.25). The stability condition for the zero solution of (2.25) and (2.23) respectively, can be formulated by the following theorem.

Theorem 2.1 *[38, p. 195] The solution $x = 0$ of (2.25) is uniformly asymptotically stable (for a precise definition see Appendix A) if and only if all the characteristic multipliers of (2.25) have moduli less than 1.*

The above theorem is the starting point for several numerical methods. The usual strategy is to compute a finite dimensional approximation U_a of the monodromy operator U and to calculate the approximate characteristic multipliers μ_a by solving a standard linear eigenvalue problem (2.28) for U_a.

Example for the Monodromy operator approximation

The construction of an approximate monodromy operator U_a corresponding to (2.25) can be illustrated by means of a straightforward time discretisation of (2.25) employing an implicit Euler scheme. To this end, let $I_\Delta = [0, \Delta t, \ldots, \tau - \Delta t, N\Delta t = \tau]$ be a discretisation of the time interval $[0, \tau]$ with constant step size $\Delta t = \tau/N$, $x_i^r = x(t_i - \tau)$ the retarded discrete solution of (2.25) and $x_i = x(t_i)$ the current discrete solution of (2.25) on the interval $[0, \tau]$. Approximating the time derivative appearing in (2.25) by means of finite differences leads to the following discrete version of (2.25), i.e.

$$x_i - x_{i-1} = \Delta t A_i x_i + \Delta t B_i x_i^r,$$

with $A_i = A(t_i)$ and $B_i = B(t_i)$. Evaluating the discrete equation for each $t \in I_\Delta$ gives

$$\begin{aligned} x_1 - \Delta t A_1 x_1 &= \Delta t B_1 x_1^r + x_0 = \Delta t B_1 x_1^r + x_N^r, \\ x_2 - x_1 - \Delta t A_2 x_2 &= \Delta t B_2 x_2^r, \\ &\vdots \\ x_N - x_{N-1} - \Delta t A_N x_N &= \Delta t B_N x_N^r. \end{aligned}$$

In matrix form, the set of discrete equations reads

$$\underbrace{\begin{bmatrix} 1 - \Delta t A_1 & 0 & \ldots & 0 \\ -1 & 1 - \Delta t A_2 & \ldots & 0 \\ \vdots & & \ddots & \vdots \\ 0 & \ldots & -1 & 1 - \Delta t A_N \end{bmatrix}}_{:= \mathbf{A}_\Delta} \begin{bmatrix} x_1 \\ x_2 \\ \vdots \\ x_N \end{bmatrix} = \underbrace{\begin{bmatrix} \Delta t B_1 & 0 & \ldots & 1 \\ 0 & \Delta t B_2 & \ldots & 0 \\ \vdots & & \ddots & \vdots \\ 0 & \ldots & 0 & \Delta t B_N \end{bmatrix}}_{:= \mathbf{B}_\Delta} \begin{bmatrix} x_1^r \\ x_2^r \\ \vdots \\ x_N^r \end{bmatrix}.$$

With the matrices $\mathbf{A}_\Delta$ and $\mathbf{B}_\Delta$, the approximation of the monodromy operator mapping the discrete solution from the interval $[-\tau, 0]$ to the discrete solution on the interval $[0, \tau]$ can finally be written as

$$U_a = (\mathbf{A}_\Delta)^{-1} \mathbf{B}_\Delta. \tag{2.29}$$

Note that the above derivation only illustrates the general strategy to construct the discrete monodromy operator. The numerical methods pursuing the monodromy operator discretisation approach usually involve more efficient discretisation schemes with a higher order of convergence. For a more detailed discussion of the different methods, the reader is referred to the following sections.

Zero-order approximation

An alternative strategy to calculate approximate stability limits is the so called zero order approach introduced by Altintas and Budak [4]. The basic strategy of this method is to replace the time dependent matrices $A(t)$, $B(t)$ by suitable constant approximations A_0, B_0 and to compute characteristic exponents by solving a nonlinear eigenvalue problem. The basic solution strategy can be illustrated considering the matrices $A(t)$ and $B(t)$ corresponding to milling model obtained by combining (2.1) and Weck's cutting force model (2.7). Rewriting the system in first order form and performing some rearrangements finally leads to the general form (2.23) with matrices

$$A(t) = \begin{bmatrix} 0 & 1 \\ C(t) - K & -D \end{bmatrix}, \quad B(t) = \begin{bmatrix} 0 & 0 \\ -C(t) & 0 \end{bmatrix}, \tag{2.30}$$

and the periodic matrix

$$\begin{aligned} C(t) &= -\frac{a_p}{m_c} \sum_{j=1}^{N_z} g(\varphi_j) \begin{bmatrix} \sin\varphi_j & \cos\varphi_j \\ -\cos\varphi_j & \sin\varphi_j \end{bmatrix} \begin{bmatrix} \hat{K}_n \\ \hat{K}_t \end{bmatrix} [\sin\varphi_j, \cos\varphi_j] \\ &= C(t+\tau). \end{aligned} \tag{2.31}$$

Since $C(t)$ is a τ-periodic function, it has a Fourier representation, i.e.

$$C(t) = \sum_{n=-\infty}^{\infty} C_n e^{2\pi i \frac{n}{\tau} t}, \tag{2.32}$$

with coefficients

$$C_n = \frac{1}{\tau} \int_0^{\tau} C(t) e^{-2\pi i \frac{n}{\tau} t} dt. \tag{2.33}$$

Replacing $C(t)$ by the zero order term C_0 finally leads to the constant approximations

$$A_0 = \begin{bmatrix} 0 & 1 \\ C_0 - K & -D \end{bmatrix}, \quad B_0 = \begin{bmatrix} 0 & 0 \\ -C_0 & 0 \end{bmatrix}, \tag{2.34}$$

and (2.23) transforms to the constant coefficient delay differential equation

$$\dot{x}(t) = A_0 x(t) + B_0 x(t-\tau), \qquad t \in [0, t_e], \tag{2.35}$$

with the initial condition $x(s) = \phi(s)$, $s \in [-\tau, 0]$. Inserting the general ansatz $x(t) = v e^{\lambda t}$ into (2.35) leads to the nonlinear eigenvalue problem for the determination of λ

$$\left(\lambda \mathbf{I} - A_0 - B_0 e^{-\lambda\tau}\right) v = 0, \; v \neq 0, \quad \Leftrightarrow \quad \det\left(\lambda \mathbf{I} - A_0 - B_0 e^{-\lambda\tau}\right) = 0. \tag{2.36}$$

Currently, a two-stage approach is a common and very effective way to compute the multipliers (or the characteristic roots) for the constant-coefficient delay differential equation (2.35). The two-stage approach consists of approximating all interesting characteristic roots and using the approximations as starting guess to local correction

method. The two-stage approach is implemented in the popular software package DDE-BIFTOOL (see [31, 83]) and has been employed in other contexts (see [36]). While the first step is typically the discretisation of an infinite dimensional operator, e.g. the monodromy operator appearing in (2.28), employing a linear multistep method in DDE-BIFTOOL, or spectral methods as proposed in [13], the second step is normally a Newton iteration. As discussed in [53], methods from the numerical linear algebra field, e.g. *residual inverse iteration* (see [69]), seem to be very efficient for directly solving the nonlinear eigenvalue problem (2.36) corresponding to (2.35).

Another popular method, that can be extended to the time periodic case, has been proposed by Altinas and Budak [3,4]. In order to recover the framework of this approach, the eigenvalue problem has to be rewritten in reduced form exploiting the special structure of A_0 and B_0, i.e.

$$\left(\lambda^2\mathbf{I} + \lambda D + K - (1 - e^{-\lambda\tau})\frac{a_p}{m_c}\bar{C}_0\right) w = 0, \qquad w \neq 0, \tag{2.37}$$

with $w = [v_1, v_2]^T$ and $C_0 = \frac{a_p}{m_c}\bar{C}_0$. Replacing the eigenvector by $w = m_c\Phi(\lambda)\tilde{w}$ and introducing a new parameter $\Lambda(\lambda) = -(1 - e^{-\lambda\tau})a_p$ leads to

$$\Big(\mathbf{I} + \Lambda(\lambda)\bar{C}_0\Phi(\lambda)\Big)\tilde{w} = 0, \qquad \tilde{w} \neq 0 \tag{2.38}$$

with $\Phi(\lambda) = (1/m_c)(\lambda^2\mathbf{I} + \lambda D + K)^{-1}$ denoting the so called frequency response function. Note that in practise, the frequency response function is usually directly derived from measurements at the tool centre point (see e.g. [33]). As shown in [3,4], the stability limit can be analytically computed from the rearranged eigenvalue problem (2.38) performing the following steps. Choosing $\lambda = i\omega_C$ and solving (2.38) gives a complex solution Λ^*. Exploiting the definition

$$\Lambda^* = -(1 - e^{-i\omega_C\tau})a_p = -(1 - \cos\omega_C\tau + i\sin\omega_C\tau)a_p,$$

yields two equations to determine $a_p(\Lambda^*)$ and $\tau(\omega_C, \Lambda^*)$, i.e.

$$a_p(\Lambda^*) = -\frac{\text{Re }\Lambda^*}{2}\left(1 + \left[\frac{\text{Im }\Lambda^*}{\text{Re }\Lambda^*}\right]^2\right), \tag{2.39}$$

$$0 = \text{Re }\Lambda^*\sin\omega_C\tau + \text{Im }\Lambda^*(\cos\omega_C\tau - 1). \tag{2.40}$$

where the second equation can be rearranged to compute delay and spindle speed, i.e.

$$n(\omega_C, \Lambda^*) = \frac{1}{N_z\tau(\omega_C, \Lambda^*)} = \frac{\omega_C}{N_z\big[(2k+1)\pi - 2\arctan\left(\text{Im }\Lambda^*/\text{Re }\Lambda^*\right)\big]}. \tag{2.41}$$

The integer number $k = 0, 1, \ldots$ is an additional parameter to switch between the different lobes. The system of equations (2.39), (2.41) and (2.38) therefore determines, for a given frequency ω_C, the stability limit in terms of a_p and n. The final stability lobe diagram illustrated in Figure 2.7 can be constructed varying the values of ω_C and k and computing the corresponding solution given by Λ^*, $n(\omega_C, \Lambda^*)$ and $a_p(\Lambda^*)$. The chatter frequency diagram shows how the frequency ω_C changes with the spindle speed.

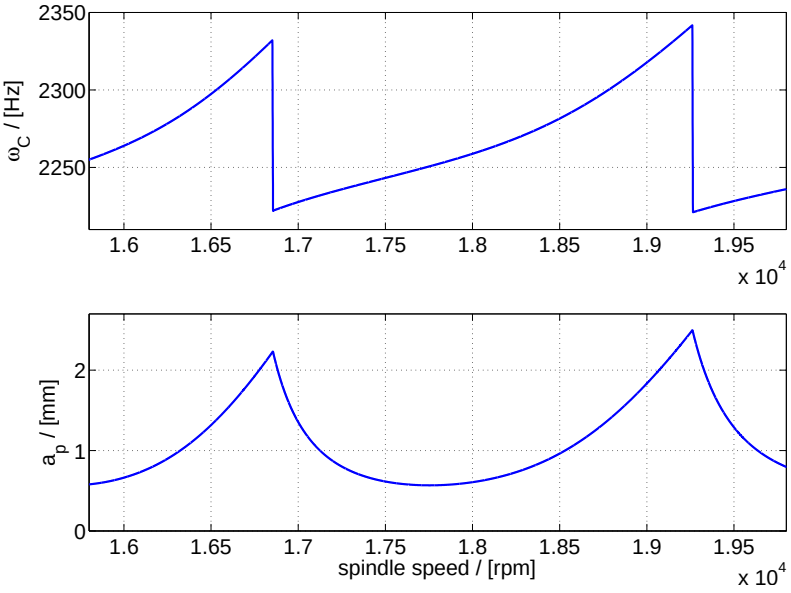

Figure 2.7: Stability chart and chatter frequency ω_C computed with Alintas' method.

Time-periodic case

Similar to the constant coefficient case arising from the zero order approximation discussed above, a two step approach seems to be an effective way to compute the characteristic multipliers corresponding to (2.28). Although there are several methods which could be used as a first step of the two-stage approach, there are up to the authors knowledge only a few works focusing on the second step (see e.g. [80]).

The methods dealing with the first step of the two-step approach, are based on an approximation of the monodromy-operator (2.28). Spectral discretisation has been employed by several groups to develop efficient techniques (see e.g. [14, 20, 21]). A partition of the period τ is used in the semi-discretisation approach to approximate the solution of the periodic delay differential equation by a sequence of inhomogeneous ordinary differential equations with constant coefficients. The corresponding sequence of fundamental solutions can be used to construct an approximation of the monodromy operator ([46, 49–51]). A collocation discretisation combined with a Newton correction is presented in [96].

Models related to milling have been widely studied using time periodic delay differential equations. Typical issues are the analysis of different instabilities, i.e. quasi periodic and periodic 2 chatter (see e.g. [22, 46, 48, 49, 51, 63, 64, 96]), and the effect of tool properties and tool asymmetries (see [47, 113]), which cannot be reproduced by the zero order approach. Although these effects do not occur in the simple milling system, the model with periodic coefficients predicts more realistic chatter frequencies than the zero order approach (see Figure 2.7 and 2.8). For additional considerations related to the presence of multiple chatter frequencies, the reader is referred to pp. 25. The oscillators involved in the time periodic models are similar to the simple milling model introduced in Section 2.1 and have thus at most 2 degrees of freedom. Larger systems modelling a more complex structure have been analysed by means of an improved semi-discretisation algorithm [41]. However,

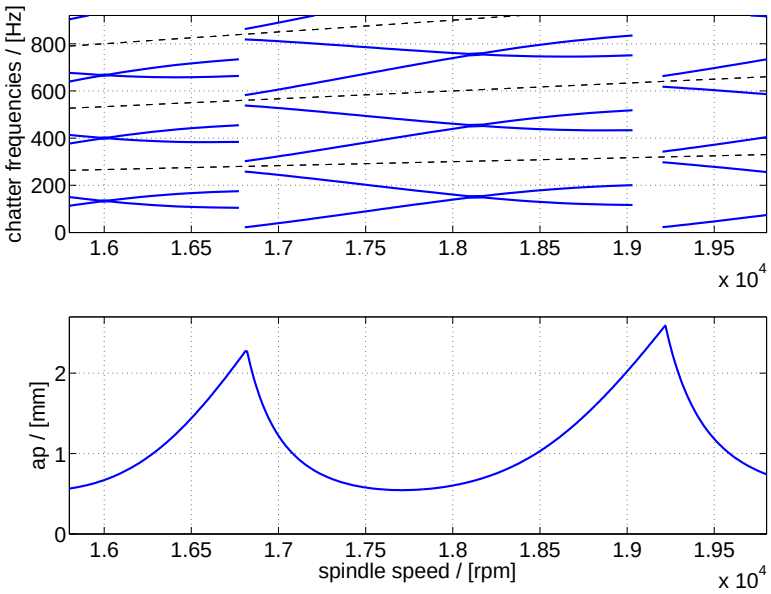

Figure 2.8: Stability chart and chatter frequencies for the time periodic example (for further considerations related to the occurrence of multiple chatter frequencies see pp. 25).

coupled systems involving partial differential equations to represent the work piece and large systems of ordinary differential equations to model the milling machine, have not been investigated comprehensively (see [80]).

The experience with the constant-coefficient case shows, that a good two-stage approach and in particular an efficient correction scheme is necessary if larger systems shall be treated accurately and reliably. As shown in [80], the strategy being presented in [53] of directly solving the nonlinear eigenvalue problem (2.36) associated to (2.35), can be transferred to the periodic coefficient case. Since the corresponding nonlinear eigenvalue problem involves the unknown fundamental matrix of a periodic ordinary equation, the main challenge is to develop an efficient solution algorithm for this problem. While the *residual inverse iteration* (see [69]) has been used in [80], the focus in this work will be on Newton type methods. These methods and their applications are extensively discussed in [53, 65].

2.2.2 The nonlinear eigenvalue problem for the TPDDE

A nonlinear eigenvalue problem for TPDDEs

As outlined by Hale [38], the characteristic exponents for the time periodic delay differential equation (2.23) can be computed from a characteristic equation similar to (2.36). The starting point for the derivation of such an equation is the following

Theorem 2.2 *[38, p. 193]* $\mu = e^{\lambda\tau}$ *is a characteristic multiplier of* (2.23) *if and only if there is a nonzero solution of* (2.23) *of the form* $x(t) = p(t)e^{\lambda t}$ *where* $p(t) = p(t+\tau)$.

In order to verify the condition for the characteristic multiplier, $x(t) = p(t)e^{\lambda t}$ can be inserted into (2.23) to obtain

$$\dot{y} = \dot{p}e^{\lambda t} + \lambda p e^{\lambda t} = Ape^{\lambda t} + Be^{-\lambda\tau}pe^{\lambda t}. \tag{2.42}$$

Since $e^{\lambda t} \neq 0$, $p(t)$ satisfies the following linear periodic ordinary differential equation

$$\dot{p}(t) = \left(A(t) + B(t)e^{-\lambda\tau} - \lambda I\right) p(t) = C(t,\lambda)p(t). \tag{2.43}$$

Now let $\Phi(t,s,\lambda)$ with $\Phi(0,s,\lambda) = \mathbf{I}$ be a fundamental solution of (2.43) (which usually cannot be computed analytically). By definition, the solution of (2.43) is given by

$$p(t) = \Phi(t,0,\lambda)p(0) = \Phi(t,0,\lambda)p_0, \tag{2.44}$$

with p_0 denoting the initial condition for $p(t)$. Exploiting the above relation, the periodicity condition for $p(t)$ becomes

$$p_0 = p(\tau) = \Phi(\tau,0,\lambda)p_0. \tag{2.45}$$

Since (2.45) has nontrivial solutions if and only if

$$\det\left(\Phi(\tau,0,\lambda) - \mathbf{I}\right) = 0 \quad \Leftrightarrow \quad \underbrace{\left(\Phi(\tau,0,\lambda) - \mathbf{I}\right)}_{T(\lambda)} p_0 = 0, \tag{2.46}$$

with $p_0 \neq 0$, the periodicity condition for $p(t)$ provides an equation to determine the characteristic exponent λ.

Remark 2.3 The characteristic equation (2.36) corresponding to the constant constant coefficient case can be recovered from the time periodic case. For constant A, B the fundamental solution of (2.23) reads

$$\Phi(t,0,\lambda) = \exp\left(\left[A + Be^{-\lambda\tau} - \lambda\mathbf{I}\right] t\right). \tag{2.47}$$

Accordingly, the periodicity condition becomes

$$p_0 = \exp\left(\left[A + Be^{-\lambda\tau} - \lambda\mathbf{I}\right] \tau\right)p_0. \tag{2.48}$$

The fact that $\lambda\mathbf{I}$ commutes with A, B allows to rewrite (2.48) as

$$p_0 = e^{-\lambda\tau}\exp\Big(\left[A + Be^{-\lambda\tau}\right] \tau\Big)p_0, \tag{2.49}$$

which implies with $\mu = e^{\lambda\tau}$ that

$$\left(\exp\Big(\left[A + Be^{-\lambda\tau}\right] \tau\Big) - \mu\mathbf{I}\right)p_0 = 0. \tag{2.50}$$

Consequently, μ is in the spectrum of $\exp\left(\left[A + Be^{-\lambda\tau}\right] \tau\right)$. The spectral mapping principle (see e.g. [29, Appendix II, Theorem 4.17]) states that

$$\sigma_P\Big(\exp\left(\left[A + Be^{-\lambda\tau}\right] \tau\right)\Big) = \exp\left(\tau\sigma_P(A + Be^{-\lambda\tau})\right), \tag{2.51}$$

with $\sigma_P(.)$ denoting the point spectrum. Thus, there is a $\nu \in \sigma_P(A + Be^{-\lambda\tau})$ so that $e^{\nu\tau} = \mu \equiv e^{\lambda\tau}$. Since $\tau \neq 0$, $\nu = \lambda$, i.e. λ is in $\sigma_P\left(A + Be^{-\lambda\tau}\right)$ and therefore satisfies the characteristic equation

$$(A + Be^{-\lambda\tau} - \lambda\mathbf{I})x = 0, \quad x \neq 0. \tag{2.52}$$

Justification of the chatter indicator and chatter frequencies

As shown above and indicated by the Floquet theory for periodic delay differential equations, the particular solution of (2.23) corresponding to a characteristic exponent λ can be written as (see e.g. [47])

$$x(t) = p(t)e^{\lambda t} + \bar{p}(t)e^{\bar{\lambda} t}, \tag{2.53}$$

where $p(t) = p(t+\tau)$ denotes a periodic coefficient and $\bar{p}$ the corresponding conjugated value. In terms of $x(t)$, the uncut chip thickness (2.6) reads

$$h^j = h^j_{stat} + [x(t) - x(t-\tau)]e_j, \tag{2.54}$$

with $e_j = (\sin\varphi_j, \cos\varphi_j)^T$. Since the chatter indicator involves the difference $h^j - h^j_{stat}$, the focus is on the evolution of the second term, i.e.

$$\begin{aligned} |[x(t) - x(t-\tau)]\, e_j(t)| &= \Big|(p(t)e^{\lambda t} + \bar{p}(t)e^{\bar{\lambda} t})e_j - \\ &\qquad \Big(p(t)e^{\lambda(t-\tau)} + \bar{p}(t)e^{\bar{\lambda}(t-\tau)}\Big)e_j\Big| \qquad (2.55) \\ &= \Big|p(t)e_j e^{\lambda t}(1 - e^{-\lambda\tau}) + \bar{p}(t)e_j e^{\bar{\lambda} t}(1 - e^{-\bar{\lambda}\tau})\Big| \qquad (2.56) \end{aligned}$$

Choosing $\lambda = \alpha + i\beta$ with $\alpha > 0$ ($\Leftrightarrow$ solution is unstable) and $0 < \beta < \pi$ gives

$$\begin{aligned} |\,[x(t) - x(t-\tau)]\, e_j(t)| &= \Big|\Big(p(t)e^{i\beta t}(1 - e^{-\lambda\tau}) + \bar{p}(t)e^{-i\beta t}(1 - e^{-\bar{\lambda}\tau})\Big)\, e_j\Big|\, |e^{\alpha t}| \\ &= c(t)\left|e^{\alpha t}\right|, \end{aligned}$$

with a τ-periodic and real coefficient $c(t) = c(t+\tau)$. Replacing the time by $t = (k+\varepsilon)\tau$ with $0 \le \varepsilon \le 1$ so that $0 < c_\varepsilon = c((k+\varepsilon)\tau)$ leads to the limit

$$\lim_{k\to\infty} |[x_\varepsilon(k) - x_\varepsilon(k-1)]\, e_j((k+\varepsilon)\tau)| = c_\varepsilon \lim_{k\to\infty} \left|e^{\alpha(k+\varepsilon)\tau}\right| = \infty, \tag{2.57}$$

where $x_\varepsilon(j) = x((j+\varepsilon)\tau)$. Consequently, there is an $\varepsilon \in [0,1]$ so that the uncut chip thickness tends to infinity for characteristic exponents λ with $\mathrm{Re}\,\lambda = \alpha > 0$. Due to this property the evolution of the uncut chip thickness indicates unstable processes.

In addition to the analysis of the uncut chip thickness evolution, (2.53) provides information about the chatter frequencies (see Insperger et al. [47]). For the calculation of the chatter frequencies occurring in a process on the stability limit, i.e. $\lambda = i\omega$, (2.53) reads

$$x(t) = p(t)e^{i\omega t} + \bar{p}(t)e^{-i\omega t}. \tag{2.58}$$

Following the arguments of Insperger, the periodic coefficient can be represented by its Fourier series, i.e.

$$p(t) = \sum_{k=-\infty}^{\infty} C_k e^{2\pi i k t/\tau}, \tag{2.59}$$

and thus the particular solution becomes

$$x(t) = \sum_{k=-\infty}^{\infty} C_k e^{i(2\pi k/\tau+\omega)t} + \bar{C}_k e^{-i(2\pi k/\tau+\omega)t}, \tag{2.60}$$

$$= \sum_{k=-\infty}^{\infty} C_k e^{2\pi i(k/\tau+\omega/(2\pi))t} + \bar{C}_k e^{-i2\pi(k/\tau+\omega/(2\pi))t}, \tag{2.61}$$

with amplitudes C_k, $\bar{C}_k$ and chatter frequencies

$$f_C = \pm\frac{\omega}{2\pi} + \frac{k}{\tau} = \pm\frac{\omega}{2\pi} + knN_z, \tag{2.62}$$

with $k = 0, \pm1, \pm2, \ldots$. Note that only positive frequencies are physically meaningful. The chatter frequencies occurring in Figure 2.8 have been calculated with the above formula (2.62). The parameter ω denoting the imaginary part of λ can be either directly derived from the computed characteristic exponent or calculated from the characteristic multiplier μ (see [47]), i.e.

$$\omega = \frac{1}{\tau}\arctan\left(\frac{\text{Im }\mu}{\text{Re }\mu}\right). \tag{2.63}$$

2.2.3 Residual inverse vs. augmented Newton

In some contexts, the following class of problems is known as nonlinear eigenvalue problems: find $\lambda \in \mathbb{C}$ and $v \in \mathbb{C}^n\backslash\{0\}$ such that

$$T(\lambda)v = 0. \tag{2.64}$$

There are numerous methods for nonlinear eigenvalue problems; see, e.g. [65, 82]. Clearly, (2.46) is a nonlinear eigenvalue problem of the form (2.64). This is a key observation in this work and will finally lead to an efficient algorithm for the computation of stability limits of the zero solution of (2.23). In [80] the *residual inverse iteration* (RESINV, see e.g. [69]) has been employed to solve the nonlinear eigenvalue problem (2.64). One version of RESINV is the repeated solution of a scalar nonlinear equation, solving a linear system and updating a vector,

$$v_k^T T(\lambda_{k+1})v_k = 0, \tag{2.65}$$

$$T(\mu)\Delta v_{k+1} = T(\lambda_{k+1})v_k \tag{2.66}$$

$$v_{k+1} = v_k - \Delta v_{k+1}. \tag{2.67}$$

Although the RESINV method works satisfactorily for some problems, it seems advantageous to use the so called augmented Newton method (see e.g. [52, 65]) instead. The algorithm for the augmented Newton method basically consists of the repeated solution of a linear system, updating the eigenvalue and computing the eigenvector, i.e.

$$u_{k+1} = T(\lambda_k)^{-1}T'(\lambda_k)v_k \tag{2.68}$$

$$\alpha_{k+1} = \frac{1}{d^H u_{k+1}} \tag{2.69}$$

$$\lambda_{k+1} = \lambda_k - \alpha_{k+1} \tag{2.70}$$

$$v_{k+1} = \alpha_{k+1}u_{k+1}, \tag{2.71}$$

where d^H represents an arbitrary left vector, e.g. $d^H = (1, \ldots, 1)^T$. An important difference between RESINV and Newton's method is that in case of residual inverse the matrix in the linear system $T(\mu)$ does not change throughout the iteration. This might be advantageous if this is the computationally dominating part of the iteration. The trade-off is that, unlike Newton, residual inverse iteration only has linear convergence (to simple eigenvalues). The quadratic convergence and the fact that the method works also for non simple eigenvalues (see [52]) compensate the difficulties arising due to the repeated evaluation of the operator $T(\lambda)$.

Evaluating the matrix operator

Since the matrix-operator $T(\lambda) = \Phi(\tau, 0, \lambda) - \mathbf{I}$ cannot be computed analytically, the main challenge in the presented approach is the efficient evaluation of $T(\lambda)$ and its derivative $T'(\lambda)$. In order to develop an effective approach, consider the result of $T(\lambda)$ applied to an arbitrary vector y, i.e.

$$T(\lambda)y = \Phi(\tau, 0, \lambda)y - y = p(\tau, 0, \lambda, y) - y, \tag{2.72}$$

with $p(t, 0, \lambda, y)$ representing the solution of (2.43) at time τ for a parameter λ and initial value y. Similarly, the result of the operation $T'(\lambda)y$ can be written as

$$T'(\lambda)y = \partial_\lambda \Phi(\tau, 0, \lambda)y = \partial_\lambda p(\tau, 0, \lambda, y). \tag{2.73}$$

While $p(\tau, 0, \lambda, y)$ in (2.72) can be directly computed solving (2.43), the value of the derivative $\partial_\lambda p(\tau, 0, \lambda, y)$ remains unknown. In order to derive an equation to compute $\partial_\lambda p(\tau, 0, \lambda, y)$, assume that p is sufficiently smooth and compute the derivative of (2.43) with respect to λ, i.e.

$$\partial_\lambda \partial_t p = \partial_t \partial_\lambda p = \partial_t g = \partial_\lambda C(t, \lambda)p + C(t, \lambda)g, \tag{2.74}$$

with $g = \partial_\lambda p$. Combining (2.74) with (2.43) leads to the following system of linear periodic ordinary differential equations

$$\frac{\partial}{\partial t} \begin{bmatrix} p \\ g \end{bmatrix} = \begin{bmatrix} C(t, \lambda) & 0 \\ \partial_\lambda C(t, \lambda) & C(t, \lambda) \end{bmatrix} \begin{bmatrix} p \\ g \end{bmatrix}. \tag{2.75}$$

The appropriate initial value for g can be motivated by the following argument. First, integrate (2.43) in time and rearrange the expression to get an explicit formula for the corresponding initial condition

$$y = p(t, \lambda) - \int_0^t C(s, \lambda)p(s, \lambda)ds. \tag{2.76}$$

Since the initial condition $p(0) = y$ does not depend on λ, the derivative of (2.76) with respect to λ reads

$$\begin{aligned} 0 &= \partial_\lambda p(t, \lambda) - \int_0^t \partial_\lambda \left(C(s, \lambda)p(s, \lambda) \right) ds \\ &= g(t, \lambda) - \int_0^t \partial_\lambda C(s, \lambda)p(s, \lambda) + C(s, \lambda)g(s, \lambda)ds \\ &= g(0), \end{aligned} \tag{2.77}$$

which can be interpreted as the integral formulation of the second equation in (2.75). Consequently, (2.77) provides an expression for the initial condition for the second equation in (2.75), i.e. $g(0) = 0$. Thus, the solution of (2.75) for initial condition $(y, 0)^T$ finally yields $p(\tau, 0, \lambda, y)$ and the corresponding derivative $g(\tau, 0, \lambda, y) = \partial_\lambda p(\tau, 0, \lambda, y)$. However, instead of the vectors p and g, the augmented Newton method needs the corresponding fundamental matrices $\Phi(\tau, 0, \lambda)$ and $\partial_\lambda \Phi(\tau, 0, \lambda)$. Rewriting (2.75) as a matrix differential equation, i.e.

$$\frac{\partial}{\partial t}\Psi = \begin{bmatrix} C(t,\lambda) & 0 \\ \partial_\lambda C(t,\lambda) & C(t,\lambda) \end{bmatrix} \Psi, \tag{2.78}$$

leads with initial value

$$\Psi(0, 0, \lambda) = \mathbf{I}, \tag{2.79}$$

to the fundamental solution matrix of (2.75) denoted by

$$\Psi(t, 0, \lambda) = \begin{bmatrix} \Phi(t,0,\lambda) & \mathbf{0} \\ \psi_\lambda(t,0,\lambda) & \psi(t,0,\lambda) \end{bmatrix}. \tag{2.80}$$

Since (2.78) is linear, the fundamental solution can be directly approximated employing a standard ODE solver, i.e. ode113 (see e.g. [85]). Now, all the necessary evaluations occurring in the augmented Newton method, can be expressed by means of the approximated fundamental matrix $\Psi^A(\tau, 0, \lambda)$, i.e.

$$T(\lambda_k) = R_p^T \Psi^A(\tau, 0, \lambda_k) R_p - \mathbf{I} \tag{2.81}$$

$$T'(\lambda_k) v_k = R_g \Psi^A(\tau, 0, \lambda_k) \begin{bmatrix} v_k \\ 0 \end{bmatrix}, \tag{2.82}$$

with rectangular matrices

$$R_p = \begin{bmatrix} \mathbf{I} \\ \mathbf{0} \end{bmatrix} \qquad \text{and} \qquad R_g = \begin{bmatrix} \mathbf{0} & \mathbf{I} \end{bmatrix}. \tag{2.83}$$

Note that, the expressions (2.81) and (2.82) can also be used to compute the evaluations occurring in the residual inverse iteration, i.e.

$$T(\mu) = R_p^T \Psi^A(\tau, 0, \mu) R_p - \mathbf{I} \tag{2.84}$$

$$T(\lambda_{k+1}) v_k = R_p^T \Psi^A(\tau, 0, \lambda_{k+1}) \begin{bmatrix} v_k \\ 0 \end{bmatrix} - v_k \tag{2.85}$$

$$T'(\lambda_{k+1}) v_k = R_g \Psi^A(\tau, 0, \lambda_{k+1}) \begin{bmatrix} v_k \\ 0 \end{bmatrix}, \tag{2.86}$$

where the last expression is needed to employ Newton's method for the scalar equation (c.f. [80]).

Algorithmic details

The augmented Newton algorithm can be described through the following scheme. Let λ_0 denote the starting guess for the eigenvalue and let v_0 represent the corresponding eigenvector. The first guess for the eigenvalue typically follows from the first step of the two step approach or from the preceding step of a continuation procedure.

Algorithm 2 AUGMENTED NEWTON

Set RESTOL, stopIter = false, $\lambda = \lambda_0$ and $v = v_0$.
while NOT(stopIter) **do**
  Compute $T(\lambda)$ and $T'(\lambda)v$ according to (2.81) and (2.82).
  Compute residual $r = T(\lambda)v$.
  if $|r| < RESTOL$ **then**
    stopIter = true
  else
    Solve linear system (2.68) to compute u.
    Calculate α, λ and v according to (2.69), (2.70) and (2.71).
  end if
end while

Similarly, the following scheme summarises the residual inverse iteration being used in [80], i.e.

Algorithm 3 RESINV

Set RESTOL, $\mu = \lambda_0$, $\lambda = \lambda_0$ and $v = v_0$.
Compute $T(\mu)$ according to (2.84).
while NOT(stopIter) **do**
  Solve nonlinear equation (2.65) to update λ.
  Compute residual $r = T(\lambda)v$.
  if $|r| < RESTOL$ **then**
    stopIter = true
  else
    Solve linear system (2.66) to get Δv.
    Update $v = v - \Delta v$.
  end if
end while

Two step approach and continuation

Recall that the main goal in stability analysis in milling is to predict the stability limit curve in the a_p-n-plane defined by $|\mu| = 1$ or $\mathrm{Re}\,\lambda = 0$ respectively. An example for such a limit curve is given in Figure 2.8. For general problems involving delay differential equations, the first step in a two step approach is the approximation of the spectrum by means of a solution operator discretisation approach followed by a Newton iteration (see e.g. [83]). Similarly, the first step in the analysis of milling problems is choosing a point (a_p^0, n^0) in the parameter plane,

computing the corresponding monodromy operator approximation U_a (see p. 19) by means of time-domain finite elements [64], semi-discretisation [51] or spectral methods [21] and solving the arising linear eigenvalue problem (2.28) to determine the characteristic multipliers. Instead of computing the whole spectrum and selecting the value with largest magnitude, it is more efficient to compute a small part of the spectrum by means of Arnoldi-type methods being implemented in the popular package ARPACK (see e.g. [58]). These methods are designed to compute a small ordered subset $\sigma_{LM}(U_a) \subset \sigma(U_a)$ of the spectrum containing for example the eigenvalues with largest magnitude. Among them, the member with largest magnitude $\mu_{max} \in \sigma_{LM}(U_a)$ serves as starting guess for the continuation method. Note that the corresponding characteristic exponent reads

$$\text{Re } \lambda_{max} = \frac{1}{\tau} \ln\left(\sqrt{\mu_{max}\bar{\mu}_{max}}\right), \quad \text{Im } \lambda_{max} = \frac{1}{\tau} \arctan\left(\frac{\text{Im } \mu_{max}}{\text{Re } \mu_{max}}\right) \tag{2.87}$$

After having found a suitable characteristic exponent, the second step is the computation of the implicitly defined stability limit curve, i.e.

$$\text{Re } \lambda(n, a_p) = 0,$$

employing a suitable continuation method (see e.g. Allgower et al. [2]). The Euler-Newton continuation method, which shall be used in the present work, is usually formulated as a predictor-corrector scheme. In order to explain the predictor step, reformulate the above stability limit condition as

$$H(u) = 0, \tag{2.88}$$

with $H : \mathbb{R}^N \mapsto \mathbb{R}^{N-1}$ and $u = (n, a_p)^T$. Next, assume that u is a parametrised curve with curve parameter s, i.e. $u : \mathbb{R} \mapsto \mathbb{R}^N$. Consequently, differentiating (2.88) with respect to s gives

$$H'(u)\frac{du}{ds} = 0, \tag{2.89}$$

with an $(N-1) \times N$ matrix $A := H'(u)$ and the corresponding tangent vector

$$t(A) := \frac{du}{ds}, \tag{2.90}$$

with $t(A) \in \mathbb{R}^N$. Note that due to (2.89), $t(A)$ is in the kernel of A. Approximating the derivative of u with respect to s in (2.90) by finite differences leads to the predictor step

$$v = u(s) + ht(A) = u + ht(H'(u(s))).$$

Since the predictor $v = u^P(s+h)$ represents only an approximate solution of (2.88), the corresponding point $u^C(s+h)$ on the implicitly defined curve has to be found solving the minimisation problem

$$\begin{aligned} &\min_w \frac{1}{2}\|v - w\|^2 \\ &\text{s.t. } H(w) = 0, \end{aligned}$$

with the necessary condition (see [2, p. 20])

$$H(w) = 0,$$
$$t(H'(w))^T(w - v) = 0.$$

As outlined in [2, pp. 22-27], the system being defined by the necessary condition can be solved performing a Newton iteration involving the Moore-Penrose inverse of $H'(v)$. The corresponding Newton update reads

$$\Delta v = -\left[H'(v)\right]^+ H(v), \tag{2.91}$$

with $[H'(v)]^+ = (H'(v))^T[(H'(v))(H'(v))^T]^{-1}$ denoting the Moore-Penrose inverse. Finally, the above considerations can be summarised by the following continuation algorithm.

Algorithm 4 NEWTON-EULER-CONTINUATION

```
1: Set TOL and choose h > 0.
2: Set lower and upper bounds u^L, u^U.
3: Initialise u, with H(u) = 0.
4: stopIter1 = false.
5: while NOT(stopIter1) do
6:    Perform Euler step: v = u + ht(H'(u)).
7:    stopIter2=false.
8:    while NOT(stopIter2) do
9:       Compute update: Δv = −[H'(v)]^+ H(v)
10:      Update v = v + Δv.
11:      Compute residual r = H(v).
12:      if |r| < TOL then
13:         stopIter2=true
14:      end if
15:   end while
16:   u = v
17:   if u > u^L and u < u^U then
18:      Choose a new step length h > 0
19:   else
20:      stopIter1=true
21:   end if
22: end while
```

2.3 Applications

2.3.1 Validation of the method

The first example is a well studied one-dimensional milling system. The experimentally validated stability boundaries have been independently predicted by different

methods (see e.g. [64] or [22]) . The model equation can be derived in a similar way as presented in Section 2.1 and read

$$\ddot{y}(t) + 2\zeta\omega_0\dot{y}(t) + \omega_0^2 y(t) = -\frac{a_p b(t)}{m}\left(y(t) - y(t-\tau)\right), \tag{2.92}$$

$$b(t) = \sum_{j=1}^{N_z} g(\varphi_j(t))\left[\hat{K}_n \sin(\varphi_j(t)) + \hat{K}_t \cos(\varphi_j(t))\right]\sin(\varphi_j(t)), \tag{2.93}$$

$$\varphi_j(t) = 2\pi\left(nt + (j-1)/N_z\right), \tag{2.94}$$

where $g(.)$ represents the switch function (2.4). The material and cutting parameters have been taken form [22] with entry and exit angles $\varphi_s = 0$ and $\varphi_e = \pi$, corresponding to an immersion ration $a/D = 1$.

Equation (2.92) models the dynamics of a milling process where a rigid cutter machines a rigid work piece that was mounted on a flexible device. Since this setting exhibits a frequency response function similar to a 1D harmonic oscillator, the stability limits, predicted from the analysis of the one-dimensional system (2.92), are in perfect agreement with the experimental results (c.f. [64]). In [22], the system has been analysed for up- and down milling and different immersion ratios $a_e/D = 0.25,\ 0.5,\ 0.75,\ 1$. Figure 2.9 shows the result of the recalculation of the

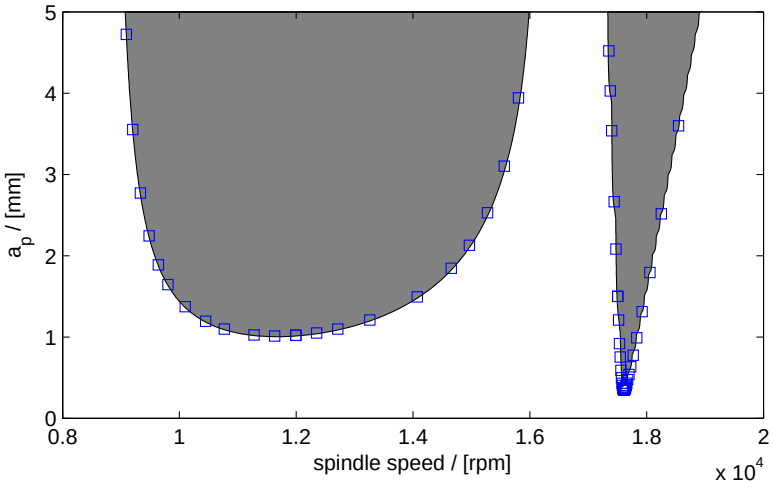

Figure 2.9: Recalculation of the down milling example (grey shaded region: unstable region computed with the Chebychev-Collocation-Method [22], blue squares: stability limit calculated with the new approach based on nonlinear eigenvalue problems).

down milling example given in [22] for a radial immersion ratio of $a/D = 1$. As illustrated in Figure 2.9, the results obtained by the augmented Newton method in combination with the continuation algorithm are in perfect agreement with the stability limits obtained with Butcher's Chebychev-Collocation-Method. In contrast to the RESINV approach discussed in [80], the unstable region corresponding to a Flip-bifurcation, i.e. $|\mu| > 1$, Im $\mu = 0$, can be reproduced utilising the augmented Newton method.

2.3.2 Stability of a PDE-DDE-milling model

Modelling

Generally, the stability limits for a milling process depend on the cutting forces and on the dynamical characteristics of milling machine and work piece. ODE-systems derived from modal analysis data provide reliable models for the milling machine and the attached cutter. The work piece is often assumed to be rigid. However, when machining thin walled pieces the latter assumption eventually leads to large errors in the stability limit prediction. In order to overcome this difficulty, the ODE-system for machine and cutter can be extended by additional equations accounting for the work piece characteristics that are usually assumed to be constant (see [3]). Because of the material removal and since the cutting zone translates along the work piece boundary, the work piece characteristics, i.e. the impulse response function, change during the cutting operation. In order to account for these effects, the work piece has to be considered as series of continuous damped elastic bodies each being represented by a partial differential equation (c.f. [42]). The coupling of machine and work piece representation via the cutting forces, finally leads to a coupled DDE-PDE-system with delay.

Fig 2.10 shows an example of a simple coupled DDE-PDE-system with delay. While the oscillator on the right represents the rigid milling cutter mounted on a flexible device, the rod on the left is a model for a damped elastic work piece. In particular this example illustrates the usefulness of the numerical method by analysing the effect of the coupling. The evolution of the characteristic exponents corresponding to the coupled system is compared to the evolution of the characteristic exponents corresponding decoupled systems. The two decoupled systems can be derived from the equations of the coupled system by the assumptions that either the work piece is perfectly rigid, or that the rigid cutter is mounted on a perfectly rigid device. Setting the coupling vector c^h appearing in (2.109) or in (2.110) to $c^h = 0$, leads to the independent equations for work piece and cutter. Moreover, the assumption that the work piece is perfectly rigid gives a system presenting the same structure as (2.92). The equations of motion for the rod and the rigid cutter

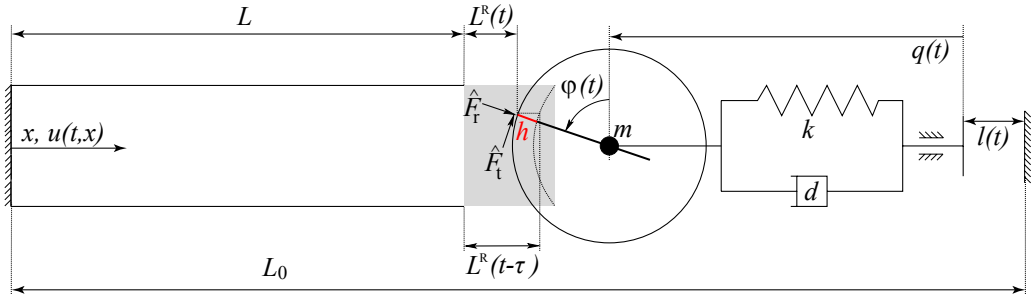

Figure 2.10: Scheme of the coupled DDE-PDE milling model (the grey shaded area represents the massless perfectly rigid part).

mounted on a flexible device read

$$\varrho_0 \; u_{tt}(t,x) - \partial_x \sigma(u(t,x)) = 0, \tag{2.95}$$

$$u(t,0) = 0, \; \sigma(t,L) = -F/A, \tag{2.96}$$

$$\ddot{q}(t) + 2\zeta\omega_0 \dot{q}(t) + {\omega_0}^2 q(t) = -F/m, \tag{2.97}$$

with $\zeta = \frac{d}{2\sqrt{km}}$ and $\omega_0^2 = \frac{k}{m}$. Since the focus is on engineering materials, the stress is described by the following relation

$$\sigma(u(t,x)) = E\partial_x u(t,x) + \eta \partial_x u_t(t,x), \tag{2.98}$$

with E denoting the elastic modulus and η a damping constant corresponding to the Voigt model. The variational form of (2.95) reads

$$\begin{aligned} &\int_0^L \varrho_0 u_{tt}(t,x)v(x)dx + \int_0^L \sigma(u(t,x))\partial_x v(x)dx \\ &\quad = \sigma(u(t,L))v(L) = -\frac{F}{A}v(L), \quad \forall v \in V, \end{aligned} \tag{2.99}$$

where $V = \{v \in H^1([0,L]), v|_0 = 0\}$. The cutting forces F occurring during the metal cutting process act on the work piece boundary and on the cutter. In the present example Weck's empirical cutting force model (2.7) relates the uncut chip thickness to the forces acting perpendicularly ($\hat{F}_t$) and normally ($\hat{F}_r$) to the cutting edge, i.e. the tip of the cutter in Figure 2.10. The above mentioned force F follows from the projection of the cutting force vector in x-direction, i.e.

$$F(t,h) = g(\varphi(t)) \left[\sin\varphi, \cos\varphi\right] \begin{bmatrix} \hat{F}_r(h) \\ \hat{F}_t(h) \end{bmatrix} \tag{2.100}$$

where $g(.)$ denotes the switch function introduced in (2.4). Note that, for the sake of simplicity, the focus is on milling cutters with only one tooth and zero helix angle. Since the uncut chip thickness entering in the cutting force model depends on the deformations of work piece and cutter, the formula for the simple model, i.e. (2.6), has to be refined. To this end, let the rod in Figure 2.10 be composed of two parts. The first damped elastic part, of length L, is followed by a small rigid and massless part with varying length $L^R(t)$ that is removed during the cutting operation. Explicit formulae for the quantity L^R at time t and time $t-\tau$ can be derived from Figure 2.10, i.e.

$$L^R(t) + u(t,L) + L = L_0 - l(t) - \frac{D}{2}\sin\varphi - q(t), \tag{2.101}$$

$$\begin{aligned} L^R(t-\tau) + u(t-\tau,L) + L &= L_0 - l(t-\tau) \\ &\quad - \frac{D}{2}\sin\varphi - q(t-\tau). \end{aligned} \tag{2.102}$$

The uncut chip thickness is defined as the difference of $L_R(t-\tau)$ and $L_R(t)$, projected

on the vector pointing from the centre to the tip of the cutter, i.e.

$$\begin{aligned} h &= \left[(L^R(t-\tau) - L^R(t)\right] \sin\varphi \\ &= [l(t) - l(t-\tau)] \sin\varphi \\ &\quad + [u(t,L) - u(t-\tau,L) + q(t) - q(t-\tau)] \sin\varphi \\ &= f_z \sin\varphi \\ &\quad + [u(t,L) - u(t-\tau,L) + q(t) - q(t-\tau)] \sin\varphi, \end{aligned} \tag{2.103}$$

with $f_z = l(t) - l(t-\tau)$ denoting the feed per tooth. Exploiting the above-mentioned expression for the uncut chip thickness, the formula for the cutting forces reads

$$\begin{aligned} F &= g(t) \left(\sin\varphi \hat{K}_r + \cos\varphi \hat{K}_t\right) a_p \{[q(t) - q(t-\tau)] \\ &\quad + [u(t,L) - u(t-\tau,L)] + f_z\} \sin\varphi \\ &= a_p g(t) \left(\sin^2\varphi \; K_R + \cos\varphi \sin\varphi \; K_T\right) \times \\ &\quad \{f_z + [q(t) - q(t-\tau)] + [u(t,L) - u(t-\tau,L)]\} \\ &= a_p w(t) \left[q(t) - q(t-\tau)\right] \\ &\quad + a_p w(t) \left[u(t,L) - u(t-\tau,L)\right] \\ &\quad + \; a_p w(t) f_z \end{aligned} \tag{2.104}$$

where the function $w(t) := g(t) \left(\sin^2\varphi \; \hat{K}_r + \cos\varphi \sin\varphi \; \hat{K}_t\right)$ denotes a τ-periodic coefficient.

Discretisation

The next step is the space discretisation of the PDE-part in variational from (2.99) utilising the Garlerkin method. To this end, let $\text{span}(\psi^1 \dots \psi^{N_n}) = V_h \subset V$ be a finite set of piecewise linear basis functions $\psi_k(x)$. By means of the finite representation, the displacement field can be approximated by

$$u(t,x) \approx \sum_{i=1}^{N_n} u_i^h(t) \psi_i(x), \tag{2.105}$$

with N_n denoting the number of basis elements. Choosing $v(x) = \psi_j(x)$ in (2.99) leads to the corresponding finite dimensional approximation,i.e.

$$M^h \ddot{u}^h + D^h \dot{u}^h + K u^h = r^h, \tag{2.106}$$

with mass, damping and stiffness matrices

$$M_{ij}^h = \varrho_0 \int_0^L \psi_i \psi_j dx, \qquad D_{ij}^h = \eta \int_0^L \partial_x \psi_i \partial_x \psi_j dx, \tag{2.107}$$

$$K_{ij}^h = E \int_0^L \partial_x \psi_i \partial_x \psi_j dx, \tag{2.108}$$

and the right hand side

$$r_j^h = -\frac{F}{A} \psi_j(L) \approx -\frac{F^h}{A} \psi_j(L).$$

Inserting the approximation (2.105) in the cutting force formula leads to the discrete cutting force F^h, i.e.

$$\begin{aligned} F^h = F^h_{ODE} + F^h_{PDE} + F^h_p \\ a_p w(t) \left(q(t) - q(t-\tau)\right) \\ + a_p w(t) \sum_{k=1}^{N_n} \psi_k(L) \left(u^h_k(t) - u^h_k(t-\tau)\right) \\ + a_p w(t) f_z. \end{aligned}$$

Finally, the semi discrete approximation of (2.95), (2.97) and (2.104) reads

$$\begin{bmatrix} \ddot{u}^h(t) \\ \ddot{q}(t) \end{bmatrix} + \begin{bmatrix} (M^h)^{-1}D^h & 0 \\ 0 & 2\zeta\omega_0 \end{bmatrix} \begin{bmatrix} \dot{u}^h(t) \\ \dot{q}(t) \end{bmatrix} + \begin{bmatrix} (M^h)^{-1}K^h & 0 \\ 0 & \omega_0^2 \end{bmatrix} \begin{bmatrix} u^h(t) \\ q(t) \end{bmatrix} = R^h = \\ -\frac{a_p w(t)}{A} \begin{bmatrix} (M^h)^{-1}C^h & (M^h)^{-1}c^h \\ (A/m)(c^h)^T & A/m \end{bmatrix} \left(\begin{bmatrix} u^h(t) \\ q(t) \end{bmatrix} - \begin{bmatrix} u^h(t-\tau) \\ q(t-\tau) \end{bmatrix} + \begin{bmatrix} 0 \\ f_z \end{bmatrix} \right), \quad (2.109)$$

with coupling vector $c^h = (\psi_1(L) \dots \psi_{N_n}(L))^T$ and coupling matrix $C^h_{jk} = \psi_j(L)\psi_k(L)$. Now, the general form (2.35) can be recovered from (2.109) by rewriting the equations in first order form and performing some additional rearrangements.

Stability of the coupled system

The right hand side R^h of (2.109) can be divided into a term involving the state $(u^h(t),\, u^h(t-\tau),\, q(t),\, q(t-\tau))$ and a periodic term only depending on f_z. Due to the linearity of the system, the solution is therefore composed of two independent contributions: a periodic part corresponding to the periodic right hand side involving f_z and a homogeneous part corresponding to the state dependent term in R^h. Since the stability of the zero solution is the main objective of the analysis considered here, the focus is on the homogeneous equation, i.e.

$$\begin{bmatrix} \ddot{u}^h(t) \\ \ddot{q}(t) \end{bmatrix} + \begin{bmatrix} (M^h)^{-1}D^h & 0 \\ 0 & 2\zeta\omega_0 \end{bmatrix} \begin{bmatrix} \dot{u}^h(t) \\ \dot{q}(t) \end{bmatrix} + \begin{bmatrix} (M^h)^{-1}K^h & 0 \\ 0 & \omega_0^2 \end{bmatrix} \begin{bmatrix} u^h(t) \\ q(t) \end{bmatrix} \\ + \frac{a_p w(t)}{A} \begin{bmatrix} (M^h)^{-1}C^h & (M^h)^{-1}c^h \\ (A/m)(c^h)^T & A/m \end{bmatrix} \left(\begin{bmatrix} u^h(t) \\ q(t) \end{bmatrix} - \begin{bmatrix} u^h(t-\tau) \\ q(t-\tau) \end{bmatrix} \right) = 0, \quad (2.110)$$

The stability limits of the coupled system (2.110) can be determined employing the augmented Newton method in combination with the continuation algorithm. The material and cutting parameters are $m = 0.06$ kg, $\zeta = 1.2$ %, $\omega_0 = 2\pi \times 2241.49$ Hz, $N_z = 1$, $\hat{K}_r = 690.0$ N/(mm^2) and $\hat{K}_t = 894.0$ N/(mm^2). The entry and exit angles have been chosen as $\varphi_s = 0$ and $\varphi_e = \pi$. The material parameters for the rod equation have been set to $\rho = 0.27$ kg/mm^3, $E = 70 \times 10^4$ kg / (s^2 mm), $\eta = 0.0378$ kg / (mm s), $L = 0.1$ mm and $A = 10$ mm^2. The rod was discretised with 5 elements. Note that the rod parameters are artificial values that have been chosen for presentation purposes. Figure 2.11 shows the result of the stability analysis. As in Section 2.3.1 the white region characterises the combinations of a_p and n where the solution of the coupled system is asymptotically stable. The blue lines show the evolution of the paths defined by Re $(\lambda(n, a_p)) = 0$.

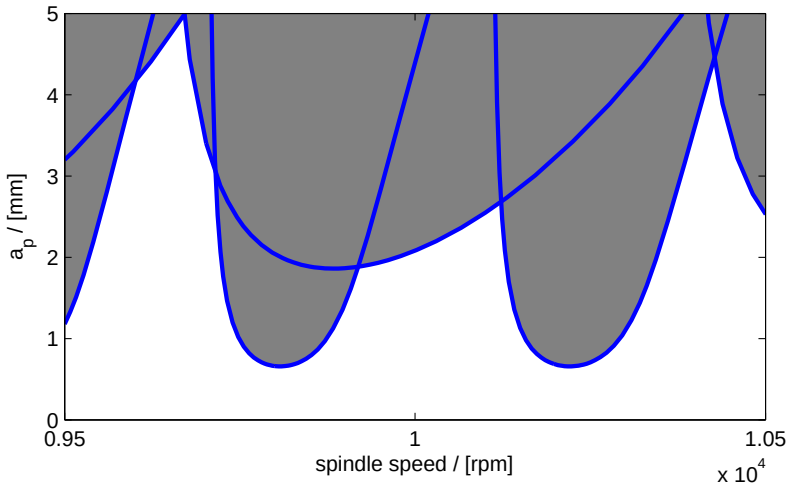

Figure 2.11: Stability chart for the coupled system (grey shaded area represents the unstable regions).

Effect of the coupling

For the investigation of the difference between the coupled system and the decoupled subsystems, equation (2.110) has to be simplified. Setting $c^h = 0$ yields two independent systems. While the first part reads

$$\ddot{u}^h(t) + (M^h)^{-1} D^h \dot{u}^h(t) + (M^h)^{-1} K^h u^h(t) = -\frac{a_p w(t)}{A} (M^h)^{-1} C^h \left(u^h(t) - u^h(t-\tau) \right), \tag{2.111}$$

the second equation reduces to an expression presenting the same form as (2.92), i.e.

$$\ddot{q}(t) + 2\zeta\omega_0 \dot{q}(t) + \omega_0^2 q(t) = -\frac{a_p w(t)}{m} \left(q(t) - q(t-\tau) \right). \tag{2.112}$$

After having decoupled the system, the path following can be carried out for each equation separately. The comparison of the corresponding stability lobes reveals the effect of the coupling. In Figure 2.12 the red lines represent the stability lobes corresponding to the coupled system. The result of the computations for the decoupled system has been plotted with blue lines. The main differences between the blue and the red lines occur in the right part of each stability lobe. While the lobe corresponding to an eigenvalue of the oscillator equation (2.112) lies below the lobe of the coupled system, the stability limit corresponding to an eigenvalue of the rod equation(2.111) is higher than the respective curve for the coupled system.

Discretisation error

The finite element discretisation of the continuous rod equation introduces a discretisation error. In order to display this effect of the discretisation consider the stability lobe that has a minimum at $n = 9800$ rpm (see Figure 2.11). Refining the discretisation, i.e. $N_n = 10,\ 20,\ 35$ points, and recalculating the stability lobe

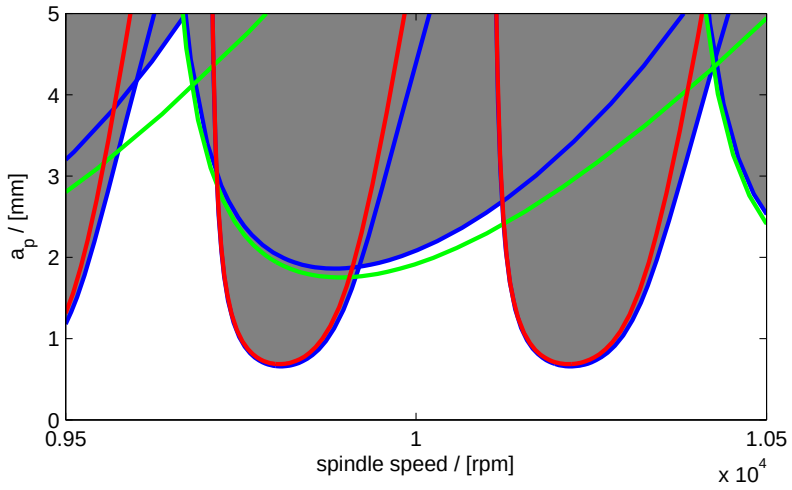

Figure 2.12: Comparison of the coupled (blue lines) system and decoupled systems (green lines: ODE, red lines: PDE).

for each grid size reveals the effect of the approximation. Figure 2.13 shows that the stability lobe moves to the left for smaller grid sizes. This observation can be explained with the fact that the finite element approximation leads to an overestimation of the first eigenfrequency of the continuous rod equation. The refinement of the grid reduces the approximation error and the lowest eigenfrequency converges to the value of the continuous system. Since the position of the stability lobe is determined by one of the eigenfrequencies of the oscillation system, the lobe translates because of the better approximation of the first eigenfrequency of the rod equation.

Model reduction

As the previous section shows, the discretisation error occurring in the rod equation leads to a shift in the predicted stability lobe. Even though grid refinement is a possible remedy, the resulting increase in computation time due larger systems is often not acceptable. One way to overcome this problem is to employ model reduction techniques. In order to introduce the model reduction framework, revisit the discrete rod equation (2.106) with an arbitrary stress *input* s^a acting on the boundary $x = L$, i.e.

$$M^h \ddot{u}^h + D^h \dot{u}^h + K u^h = b^h s^a, \tag{2.113}$$

with the $N_n \times 1$-coupling vector $b^h = (\psi_1(L), \ldots, \psi_{N_n}(L))^T$. Moreover, let the rod displacement at $x = L$ be the quantity of interest, i.e. the *output*, which is defined as

$$y = \sum_{k=1}^{N_n} \psi_k(L) u_k^h = (b^h)^T u_h. \tag{2.114}$$

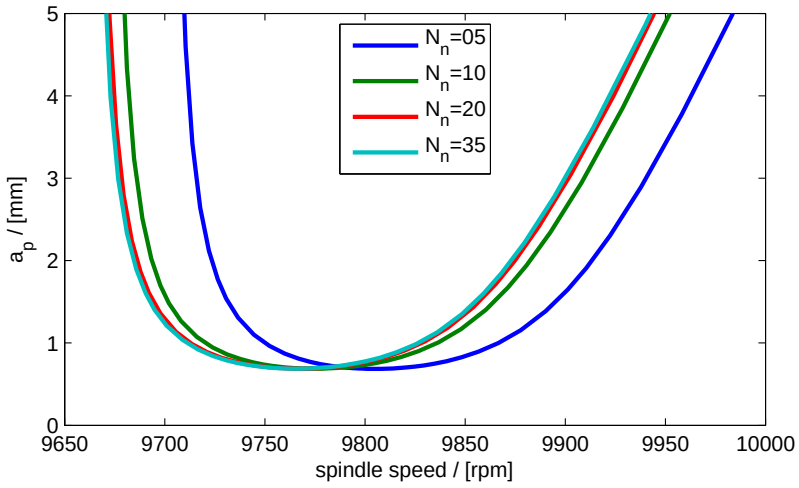

Figure 2.13: Convergence of the stability lobe.

tol	$10^0 - 10^{-4}$	10^{-5}	10^{-6}	10^{-7}	10^{-8}	10^{-9}	10^{-10}	10^{-11}	10^{-12}	10^{-12}
r	1	2	3	6	13	21	26	30	32	33

Table 2.4: Dimension r of the reduced system for different tolerances (original system: $N_n = 35$).

Introducing a new variable $v = Tu^h$ and multiplying the rod equation from the left by W^T leads to the system

$$W^T M^h T\ddot{v} + W^T D^h T\dot{v} + W^T K T v = W^T b^h s^a \tag{2.115}$$

$$\Leftrightarrow \tilde{M}\ddot{v} + \tilde{D}\dot{v} + \tilde{K}v = \tilde{B}s^a, \tag{2.116}$$

with new matrices $\tilde{M}$, $\tilde{D}$, $\tilde{D}$ and $\tilde{B}$. Similarly, the output can be reformulated as

$$y = (b^h)^T T v = \tilde{C}v, \tag{2.117}$$

with another matrix $\tilde{C}$. The objective of model reduction techniques is to determine $N_n \times r$ - matrices W and T with $r < N_n$, as small as possible so that the error in the observation y is smaller than a predefined tolerance tol. Among the available model reduction techniques, the balanced truncation method is an efficient and flexible tool that has been successfully applied to second order problems [77] and coupled systems [76,78]. For the present example, i.e. a discrete rod equation with $N_n = 35$, the matrices W and T have been computed employing the second-order balanced truncation model reduction method with position balancing (see [77]). As shown in Table 2.4, the dimension of the reduced system depends on the predefined tolerance. A milling system presenting a structure similar to (2.111) can be recovered from the reduced system defining the output as

$$y = \tilde{C}\left(v(t) - v(t-\tau)\right), \tag{2.118}$$

and feeding y back into the input, i.e.

$$s^a = -\frac{a_p w(t)}{A} y. \tag{2.119}$$

Correspondingly, the reduced discrete periodic rod equation with delay reads

$$\tilde{M}\ddot{v} + \tilde{D}\dot{v} + \tilde{K}v = -\frac{a_p w(t)}{A}\tilde{B}\tilde{C}\left(v(t) - v(t-\tau)\right). \tag{2.120}$$

Moreover, the rod equation occurring in the coupled system (2.110) can be replaced by the reduced system. Defining a modified cutting force as

$$\tilde{F} = a_p w(t)\left(q(t) - q(t-\tau)\right) + a_p w(t) y + a_p w(t) f_z, \tag{2.121}$$

with y being given by (2.118), leads to the system

$$\tilde{M}\ddot{v} + \tilde{D}\dot{v} + \tilde{K}v = -\tilde{B}\frac{\tilde{F}}{A}, \tag{2.122}$$

$$\ddot{q} + 2\zeta\omega_0\dot{q} + \omega_0^2 q = -\frac{\tilde{F}}{m}. \tag{2.123}$$

The equation describing the evolution of the corresponding homogeneous solution reads

$$\begin{bmatrix}\ddot{v}(t)\\ \ddot{q}(t)\end{bmatrix} + \begin{bmatrix}\tilde{M}^{-1}\tilde{D} & 0\\ 0 & 2\zeta\omega_0\end{bmatrix}\begin{bmatrix}\dot{v}(t)\\ \dot{q}(t)\end{bmatrix} + \begin{bmatrix}\tilde{M}^{-1}\tilde{K} & 0\\ 0 & \omega_0^2\end{bmatrix}\begin{bmatrix}v(t)\\ q(t)\end{bmatrix}$$
$$+\frac{a_p w(t)}{A}\begin{bmatrix}\tilde{M}^{-1}\tilde{B}\tilde{C} & \tilde{M}^{-1}\tilde{B}\\ (A/m)\tilde{C} & A/m\end{bmatrix}\left(\begin{bmatrix}v(t)\\ q(t)\end{bmatrix} - \begin{bmatrix}v(t-\tau)\\ q(t-\tau)\end{bmatrix}\right) = 0 \tag{2.124}$$

and presents the same structure as (2.110). The effect of the model reduction can be analysed numerically by comparing the stability lobe illustrated in Fig. 2.13 for a discretisation with $N_n = 35$ and the lobes predicted by the reduced system (2.120) for different model reduction levels.

The stability lobes illustrated in Fig. 2.14 reveal that the model reduction is a promising approach to reduce the computation time without introducing large errors in the predicted stability limits. Even for the largest tolerance ($tol = 10^{-4}$), the maximal relative error is lower than 2.5%. Higher accuracy can easily be achieved by choosing smaller tolerances, e.g. $tol = 10^{-8}$. Another issue is the usage of reduced systems in coupled problems such as (2.124).

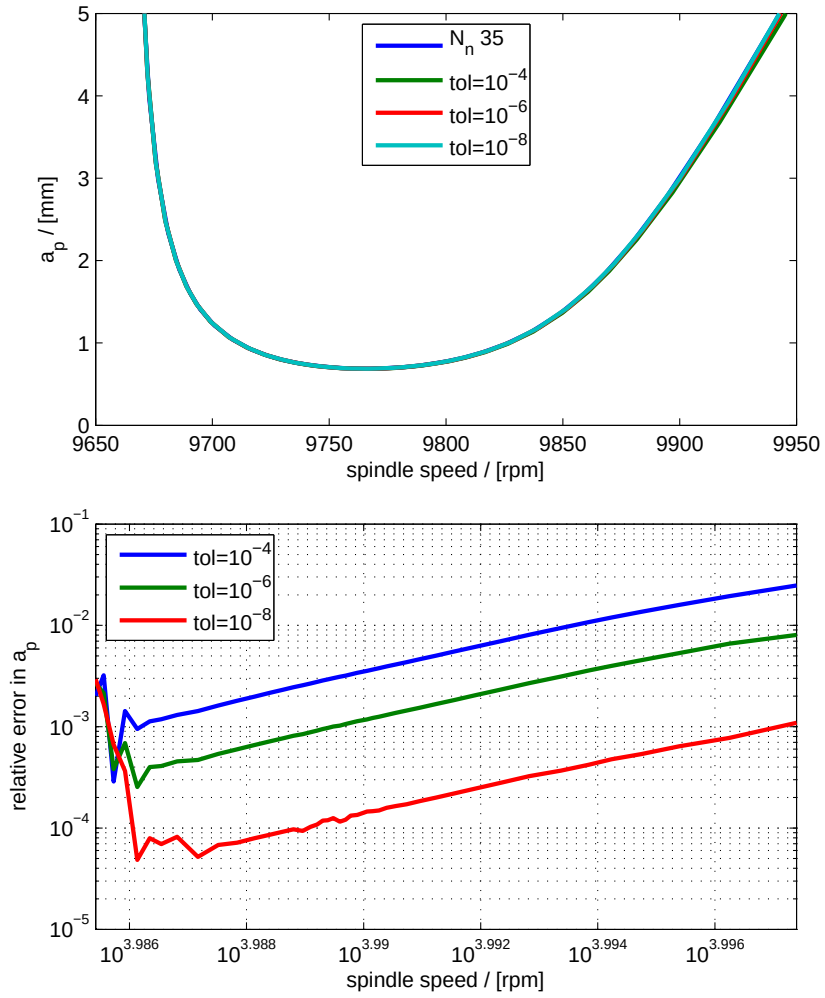

Figure 2.14: Comparison of stability lobes corresponding to different reduction levels and the relative error for each approximation.

A comparison of the stability lobes of the coupled system involving the reduced rod equation and the corresponding decoupled problems illustrated in Fig. 2.15 reveals that the coupled system with the reduced PDE perfectly reproduces the coupling phenomena shown in Fig. 2.12. Consequently, the model reduction approach allows to reduce the system size without loosing the accuracy in terms of the predicted stability limits.

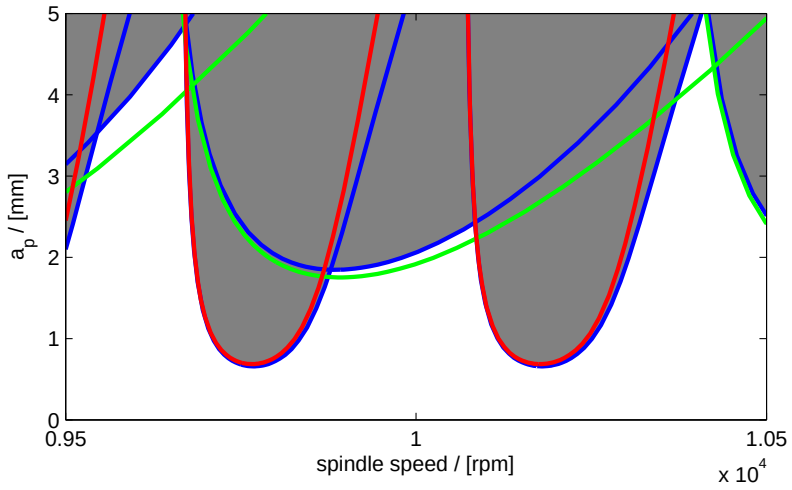

Figure 2.15: Comparison of the coupled (blue lines) system with reduced rod equation and the corresponding decoupled systems (green lines: ODE, red lines: reduced PDE).

Concluding remarks

The new stability analysis method based on the augmented Newton scheme in combination with Newton-Euler continuation can be used to analyse the stability of coupled DDE-PDE-systems. It has been shown that stability limits of the coupled system differ from the stability limits of the corresponding decoupled systems. The most significant discrepancy can be noticed on the right part of each lobe. Thus, the disregard of structural components during the modelling of a milling system may lead to errors in the prediction of the stability limits. The finite element approximation of the PDE-part causes further errors in the prediction of the stability limits. The stability lobes translate with decreasing grid size in the direction of lower values of n. It has been shown that the model reduction approach is a powerful tool to cope with stability problems for coupled systems. The presented examples reveal that employing model reduction techniques lead to important reduction of computation time while maintaining a high level of accuracy.

2.3.3 Stability of multi degree of freedom systems

Measured machine dynamics and abstract representation

The starting point for the prediction of stability limits corresponding to the milling machine employed for the cutting tests in the present work (see Chapter 6) is the (mobility) frequency response function (FRF) measured at the tool centre point (TCP) which describes the response of the machine to a force acting at the TCP in

frequency domain. The corresponding experimental FRF[3] is given by the blue line shown in Fig. 2.16. Since the main interaction between structure and process occurs at the tool, the FRF contains all the relevant information for the stability prediction. In contrast to the approach proposed by Altintas [3], the iterative method presented in the previous sections needs a time domain formulation of the dynamical system, i.e. the frequency response function. Such a formulation can be derived considering the equations of motion for the oscillator chain depicted in Fig. (2.17), i.e.

$$M\ddot{x} + D\dot{x} + Kx = BF(t), \tag{2.125}$$

where

$$M = \mathrm{diag}(m_1, \ldots, m_N), \quad D = \begin{bmatrix} d_1 + d_2 & -d_2 & \ldots & 0 \\ -d_2 & \ddots & & \vdots \\ \vdots & & d_{N-1} + d_N & -d_{N-1} \\ 0 & \ldots & -d_{N-1} & d_N \end{bmatrix}$$

$$K = \begin{bmatrix} k_1 + d_2 & -k_2 & \ldots & 0 \\ -k_2 & \ddots & & \vdots \\ \vdots & & k_{N-1} + k_N & -k_{N-1} \\ 0 & \ldots & -k_{N-1} & k_N \end{bmatrix}, \qquad B = \begin{bmatrix} 0 \\ \vdots \\ 0 \\ 1 \end{bmatrix}.$$

In the stationary regime, $x = \hat{x}(\omega)e^{i\omega t}$ is the response of the oscillator chain subjected to a force $F(t) = \hat{F}e^{i\omega t}$. Inserting force and response into (2.125) and performing some rearrangements leads to

$$\hat{x}(\omega) = \left(-\omega^2 M + i\omega D + K\right)^{-1} B\hat{F}. \tag{2.126}$$

Since the position x_N of the mass N is given by $x_N = B^T x$, the frequency response function of the oscillator chain at the last element reads

$$\hat{Y}(\omega) = \frac{\hat{x}_N(\omega)}{\hat{F}} = B^T \left(-\omega^2 M + i\omega D + K\right)^{-1} B \tag{2.127}$$

The function $\hat{Y}$ involves the masses $m_1, \ldots, m_N$, the damping constants $d_1, \ldots, d_N$ and stiffness parameters $k_1, \ldots, k_N$. Consequently, the FRF corresponding to the oscillator chain can be fitted to a measured FRF by varying the chain parameters in a minimisation of the functional

$$J(m_i, d_i, k_i) = \sum_{k=1}^{N_{meas}} \left(|Y(\omega_k)| - |Y_k^{exp}|\right)^2, \tag{2.128}$$

where $\{Y_k^{exp}\}$ denotes the set of discrete experimental data. The result of this approach is illustrated in Fig 2.16 and the corresponding fit parameters are summarised in Table 2.5.

[3]The experiments have been carried out by P. Rasper under supervision of Prof. E. Uhlmann at IWF, TU-Berlin (for further details see e.g. [75] and Section 6.2).

	el. 1	el. 2	el. 3	el. 5
m / [kg]	0.920	0.329	0.034	0.011
d / [kg s^{-1}]	1637.649	0.058	0.000065	6.3199
k / [10^7 kg s^{-2}]	9.851	7.451	1.013	0.549

Table 2.5: Oscillator chain parameters corresponding to the FRF-fit.

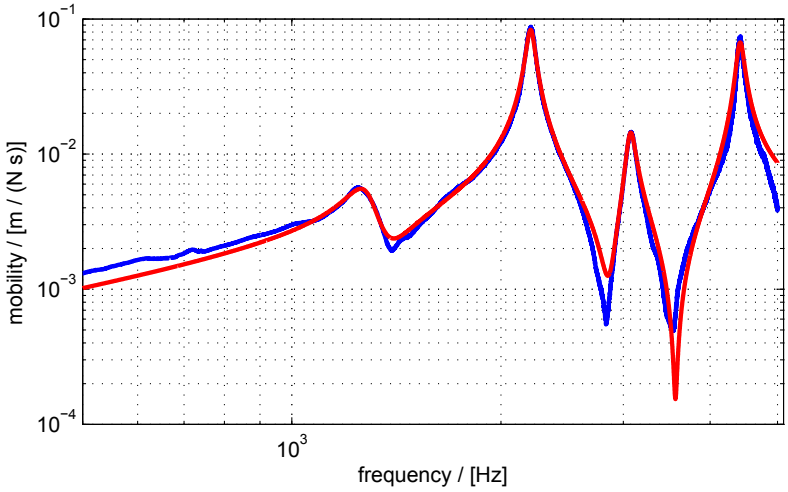

Figure 2.16: Mobility frequency response function measured at the tool centre point[4] (blue) and fitted by multi degree of freedom oscillator chain (red).

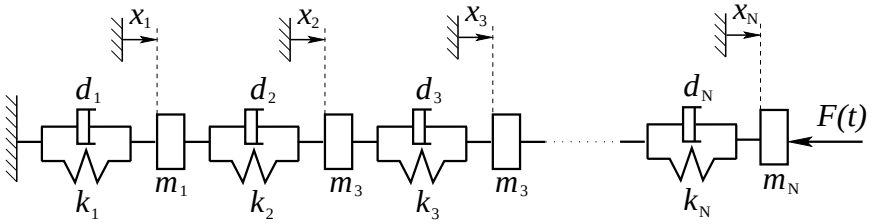

Figure 2.17: Oscillator chain as an example for a multi degree of freedom system.

Although in the present example an oscillator chain has been employed to construct a time domain representation of the experimental FRF, other configurations are conceivable too, as long as they accurately reproduce the measurements. In case that the experimental data comprises a sufficiently large set of FRFs, the time domain representation can be reconstructed from the multi degree of freedom fit approach being presented in [32].

[4]The experiments have been carried out by P. Rasper under supervision of Prof. E. Uhlmann at IWF, TU-Berlin (for further details see e.g. [75] and Section 6.2).

A multi degree of freedom milling model

The milling model involving the previously derived oscillator chains has a similar structure as the system illustrated in Fig. 2.1. The oscillator chains replacing the simple spring-damper element share their final mass, i.e. the end element representing the tool. Since the spindle-tool system is symmetric, the dynamical characteristics of the tool can be approximated by two perpendicular oscillator chains. The equations of motion corresponding to this multi degree of freedom model can be summarised as follows

$$\begin{bmatrix} M_1^c & 0 \\ 0 & M_2^c \end{bmatrix} \begin{bmatrix} \ddot{u}_1^c \\ \ddot{u}_2^c \end{bmatrix} + \begin{bmatrix} D_1^c & 0 \\ 0 & D_2^c \end{bmatrix} \begin{bmatrix} \dot{u}_1^c \\ \dot{u}_1^c \end{bmatrix} + \begin{bmatrix} K_1^c & 0 \\ 0 & K_2^c \end{bmatrix} \begin{bmatrix} u_1^c \\ u_2^c \end{bmatrix} = B^c \begin{bmatrix} F_x \\ F_y \end{bmatrix}, \tag{2.129}$$

where M_i^c denotes the mass, D_i^c the damping and K_i^c stiffness matrix corresponding to the oscillator chain 'i'. The vector components u_i^c represent the coordinates describing the chain 'i'. The matrix projecting the cutting forces F_x and F_y on the chain coordinates reads

$$B^c = \begin{bmatrix} 0 & \dots & 0 & 1 & 0 & \dots & 0 & 0 \\ 0 & \dots & 0 & 0 & 0 & \dots & 0 & 1 \end{bmatrix}^T. \tag{2.130}$$

The cutting forces are given by (2.2) in combination with an empirical cutting force model. The uncut chip thickness entering in the empirical model can be computed from the chain coordinates $u_1^c = [x_1, \dots, x_N]^T$ and $u_2^c = [y_1, \dots, y_N]^T$ employing the projection matrix B^c, i.e.

$$h = [\sin\varphi_j, \cos\varphi_j](B^c)^T \left[B^c \begin{bmatrix} f_z \\ 0 \end{bmatrix} + \begin{bmatrix} u_1^c(t) - u_1^c(t-\tau) \\ u_2^c(t) - u_2^c(t-\tau) \end{bmatrix} \right]. \tag{2.131}$$

Employing Weck's cutting force model (2.7), the right hand side of (2.129) can be written as

$$B^c \begin{bmatrix} F_x \\ F_y \end{bmatrix} = -a_p B^c D(t) (B^c)^T \left(B^c \begin{bmatrix} f_z \\ 0 \end{bmatrix} + \begin{bmatrix} u_1^c(t) \\ u_1^c(t) \end{bmatrix} - \begin{bmatrix} u_1^c(t-\tau) \\ u_1^c(t-\tau) \end{bmatrix} \right), \tag{2.132}$$

with periodic matrix

$$D(t) = \sum_{j=1}^{N_z} g(\varphi_j) \begin{bmatrix} \sin\varphi_j & \cos\varphi_j \\ \cos\varphi_j & -\sin\varphi_j \end{bmatrix} \begin{bmatrix} \hat{K}_r \\ \hat{K}_t \end{bmatrix} [\sin\varphi_j, \cos\varphi_j].$$

Finally, the matrices $A(t)$ and $B(t)$ appearing in the general linear periodic delay equation (2.35) can be derived from above expressions by rewriting the equation for the homogeneous solution of (2.129) in first order form and collecting the coefficients of the current and delayed state vector.

Stability prediction

The stability limits of the abstract multi degree of freedom milling system derived above can be computed employing the iterative method. The result of the continuation procedure is illustrated in Fig. 2.18. The stability plot is similar to the

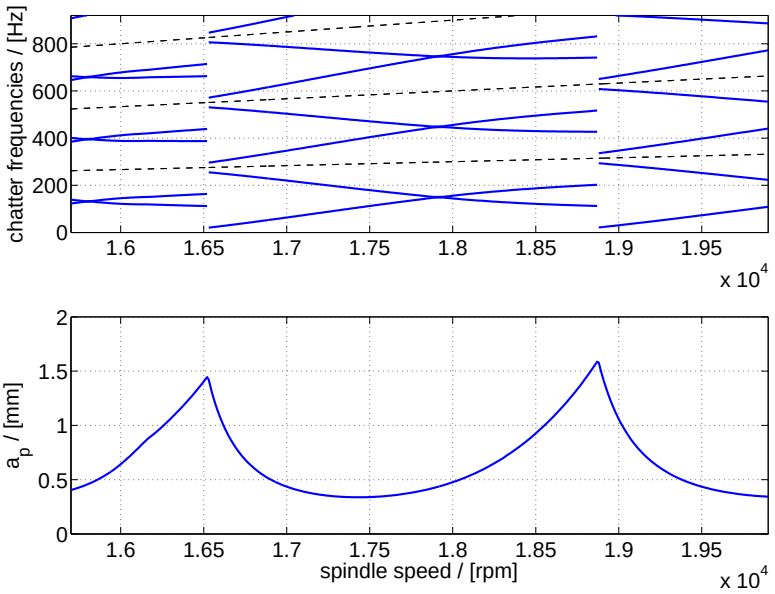

Figure 2.18: Chatter frequencies and stability chart for the multi degree of freedom milling system.

diagram computed for the 2 degree of freedom model. Since the underlying FRF (see Fig. 2.16) is dominated by the peak located at 2200 Hz, the MDOF system has similar stability limits than a 2 degree of freedom model reproducing the main peak. As outlined in [75], the measured FRF play a crucial role in the stability prediction. The example discussed in [75] reveals that the excitation method, i.e. hammer or shaker, and the angular position of the spindle importantly affect the measured FRFs which leads, in turn, to completely different stability diagrams.

Moreover, the stability lobe diagram illustrated in Figure 2.18 illustrates the stability limit corresponding to the milling system employed for the cutting tests in the present work (see Chapter 6). Throughout the rest of this work, the Diagram 2.18 serves as a reference solution for the complex milling model involving a machine model based on the multi body approach. Since the oscillator chain and the more realistic multi body model reproduce the same experimental FRF, it is expected that both models predict similar stability limits.

Chapter 3

Modelling

3.1 Modelling concept

As outlined in Chapter 2, the stability of milling processes depends on the dynamical characteristics of the structure, i.e. typically machine and work piece, and on the coupling effects arising from the interaction with the process. Unstable processes can be identified analysing either the evolution of the uncut chip thickness (cf. Section 2.1.5) or the simulated cutting force spectrum. In both cases the precision of the predicted stability limit increases with the length of the simulated time interval. However, due to the presence of high characteristic frequencies, the time step size is strictly limited, which finally leads to unacceptable computation times especially for models with many degrees of freedom. In view of these problems, modelling the machine structure as a multi body system, the work piece as either rigid, visco-elastic or thermo–elastic body and employing an empirical cutting force model as presented in Section 2.1.2 seems to be the best trade-off between accuracy and efficiency. Consequently, the nonlinear thermo–plastic effects dominating the chip formation cannot be simulated with present approach. From a macroscopic point of view, the largest part of the work piece behaves like a (thermo–) elastic body. Plastic deformations usually occur only in regions close to the cutting edges and can therefore be incorporated employing an empirical cutting force model. Due to these simplifications, the material removal cannot be simulated directly and has to be approximated by an heuristic approach.

For milling processes where the difference between exit and entry angle is smaller than the pitch angle of the cutter such an approach can be constructed applying a method of steps. In each step the work piece reference domain is considered to be constant and the system equations are solved until the cutting edge leaves the work piece. Before the next cutting edge starts cutting, the previously computed solution is used to construct a new work piece reference domain before pursuing the simulation. Consequently, the modelling and the simulation process consists of two parts. While the first part deals with the phenomena occurring during one tooth period, the second part focuses on the construction of a series of work piece reference domains and thus on an implementation of the method of steps.

Note that in the present work the focus is on a single tooth cutter. Due to this restriction the above condition that the difference between entry and exit angle has

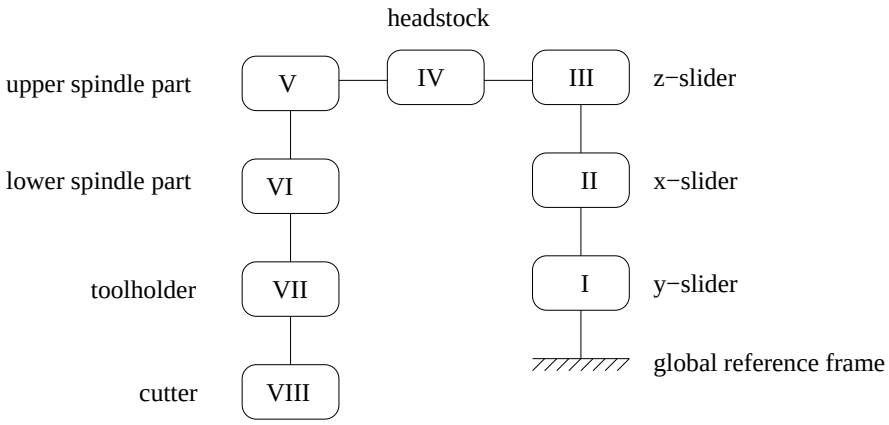

Figure 3.1: Schematic representation of the multi body system.

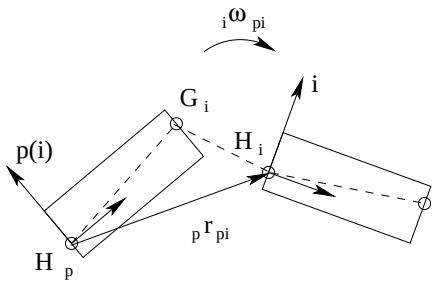

Figure 3.2: Body i and the corresponding predecessor $p(i)$.

to be always smaller than the pitch angle of the tool is satisfied for all possible immersion ratios.

3.2 Multi body systems

3.2.1 General structure

Orthogonal transformations, angular velocity

The machine structure can be considered as a system of rigid bodies which are connected to each other by spring-damper coupling elements. However, the rigid bodies do not exactly represent the machine parts. Since the most important measured mode shapes shall be properly reproduced, the machine parts usually have to be divided in several bodies. The additional assumption that each body has a unique predecessor leads to the tree-like structure illustrated in Figure 3.1. As outlined by Bremer et al. [15], such an arrangement can be exploited for the construction of efficient algorithms to assemble the equations of motion. The tree-like structure allows to define a field $p(.)$ that associates to each body i the corresponding predecessor $p(i)$. The orthogonal transformations between the reference frames q and $p(q)$ are a

product of elementary transformations, i.e. $A_{qp} = A_\alpha A_\beta A_\gamma$, with $\det(A_{qp}) = 1$ and

$$A_\alpha = \begin{bmatrix} 1 & 0 & 0 \\ 0 & \cos\alpha & \sin\alpha \\ 0 & -\sin\alpha & \cos\alpha \end{bmatrix}, A_\beta = \begin{bmatrix} \cos\beta & 0 & -\sin\beta \\ 0 & 1 & 0 \\ \sin\beta & 0 & \cos\beta \end{bmatrix},$$
$$A_\gamma = \begin{bmatrix} \cos\gamma & \sin\gamma & 0 \\ -\sin\gamma & \cos\gamma & 0 \\ 0 & 0 & 1 \end{bmatrix}.$$

The relative angular velocity matrix between frame q and p is defined as

$$ {}_q\Omega_{pq} = A_{qp}\dot{A}_{pq}, \tag{3.1}$$

while the corresponding relative angular velocity vector reads

$$ {}_q\omega_{pq} = \begin{bmatrix} \dot{\alpha} \\ 0 \\ 0 \end{bmatrix} + A_\alpha \begin{bmatrix} 0 \\ \dot{\beta} \\ 0 \end{bmatrix} + A_\alpha A_\beta \begin{bmatrix} 0 \\ 0 \\ \dot{\gamma} \end{bmatrix}. \tag{3.2}$$

Accelerations, velocities and motion for tree-like structures

The vector with components given in system i pointing from the global reference frame (index $i = 0$) to the origin of body i reads

$$ {}_ir_{0i} = \sum_{j=1}^{i} A_{ipp} r_{pj}, \quad \text{with} \quad p = p(j), \tag{3.3}$$

where the orthogonal matrix A_{ip} transforms the components of a vector given in frame p to frame i. The total velocity of the origin of body i with components given in frame i reads

$$ {}_iv_{0i} = \sum_{j=1}^{i} A_{ip} \left({}_p\dot{r}_{pj} + {}_p\Omega_{0pp} r_{pj} \right), \quad \text{with} \quad p = p(j). \tag{3.4}$$

The angular velocity ${}_i\omega_{0i}$ and the corresponding skew symmetric total angular velocity matrix ${}_i\Omega_{0i} = -{}_i\Omega_{0i}^T$ can be constructed as follows

$$ {}_i\omega_{0i} = \sum_{j=1}^{i} A_{ij}\ {}_j\omega_{pj}, \quad {}_i\Omega_{0i} = \sum_{j=1}^{i} A_{ij}\ {}_j\Omega_{pj}, \quad \text{with} \quad p = p(j). \tag{3.5}$$

Correspondingly, the total angular acceleration vector and the corresponding matrix are given by

$$ {}_i\alpha_{0i} = \sum_{j=1}^{i} A_{ij} \left({}_j\dot{\omega}_{pj} + {}_j\Omega_{0jj}\omega_{pj} \right), \tag{3.6}$$

$$ {}_i\Upsilon_{0i} = \sum_{j=1}^{i} A_{ij} \left({}_j\dot{\Omega}_{pj} + {}_j\Omega_{0jj}\Omega_{pj} \right), \quad \text{with} \quad p = p(j). \tag{3.7}$$

With the above definitions, the total acceleration of the origin of body i with components given in frame i reads

$$ {}_i a_{0i} = \sum_{j=1}^{i} A_{ip} \left[{}_p\ddot{r}_{pj} + \left({}_p\Upsilon_{0p} + {}_p\Omega_{0p}\, {}_p\Omega_{0p} \right) {}_p r_{pj} + 2 {}_p\Omega_{0p}\, {}_p\dot{r}_{pj} \right], \tag{3.8} $$

with $p = p(j)$.

Local Jacobians, minimal coordinates

The position and orientation of a rigid body q can be uniquely defined with respect to a reference frame $p(q)$ with a 3 component vector ${}_p r_{pq}$ and 3 angles α, β, γ determining an orthogonal transformation matrix A_{qp}. However, in a specific application, some of the coordinates may be fixed or given by known functions. The remaining degrees of freedom can be summarised by the so called minimal coordinates z_q. As outlined in [15, p. 49], the motion vectors and the angular velocities can therefore be written as a function of time and the set of minimal coordinates, i.e.

$$ {}_p r_{pq} = {}_p\hat{r}_{pq}(z_q, t), \tag{3.9} $$

$$ {}_q\omega_{pq} = {}_q\hat{\omega}_{pq}(z_q, \dot{z}_q, t). \tag{3.10} $$

Moreover, the minimal coordinates can be employed to express the relative accelerations introduced above (cf. [15, p. 49]), i.e.

$$ A_{jp}\, {}_p\ddot{r}_{pj} = J_{Tj}\ddot{z}_j + A_{jp} \left[\left(\frac{\partial\, {}_p\dot{r}_{pj}}{\partial z_j} \right) \dot{z}_j + \left(\frac{\partial\, {}_p\dot{r}_{pj}}{\partial t} \right) \right], \tag{3.11} $$

$$ {}_j\dot{\omega}_{pj} = J_{Rj}\ddot{z}_j + \left[\left(\frac{\partial\, {}_j\dot{\omega}_{pj}}{\partial z_j} \right) \dot{z}_j + \left(\frac{\partial\, {}_j\dot{\omega}_{pj}}{\partial t} \right) \right], \tag{3.12} $$

with possibly rectangular Jacobian matrices

$$ J_{Tj} = \left(\frac{\partial \left[A_{jp}\, {}_p\dot{r}_{pj} \right]}{\partial \dot{z}_j} \right) \quad \text{and} \quad J_{Rj} = \left(\frac{\partial\, {}_j\omega_{pj}}{\partial \dot{z}_j} \right). \tag{3.13} $$

Jourdain's principle

The equations of motion can be assembled exploiting Jourdain's principle. As outlined in [15, p. 54], the Newton-Euler equations for a M degree of freedom system being composed of N rigid bodies read

$$ \sum_{i=1}^{N} \left[\left(\bar{\bar{J}}_{Ri} \right)^T, \left(\bar{\bar{J}}_{Ti} \right)^T \right] \left\{ \bar{M}_i b_i + \bar{\xi}_i - \bar{q}_i^e \right\} = 0, \tag{3.14} $$

where

$$ \left(\bar{\bar{J}}_{Ri} \right) = \left(\frac{\partial_i \omega_{0i}}{\partial \dot{z}} \right), \quad \left(\bar{\bar{J}}_{Ti} \right) = \left(\frac{\partial_i v_{0i}}{\partial \dot{z}} \right), $$

denote the global Jacobian matrices with dimension $3 \times M$ for rotation and translation, respectively. $\bar{M}_i$ represents the generalised 6×6 mass matrix incorporating mass and inertia tensor, i.e.

$$\bar{M}_i = \begin{pmatrix} \mathbf{T}_i^H & m_{ii}\tilde{r}_{ic} \\ m_{ii}\tilde{r}_{ic}^T & m_i\mathbf{I} \end{pmatrix},$$

where $\mathbf{I}$ denotes the 3×3 identity matrix and m_i the mass of body i. The 3×3 skew symmetric matrices ${}_i\tilde{r}_{ic}$ correspond to the cross product of the vector ${}_ir_{ic}$ pointing from the origin to the centre of mass with another vector, i.e.

$${}_i\tilde{r}_{ic} = -{}_i\tilde{r}_{ic}^T = \begin{pmatrix} 0 & -({}_ir_{ic})_3 & ({}_ir_{ic})_2 \\ ({}_ir_{ic})_3 & 0 & -({}_ir_{ic})_1 \\ -({}_ir_{ic})_2 & ({}_ir_{ic})_1 & 0 \end{pmatrix}.$$

The 3×3 matrix $\mathbf{T}_i^H$ denotes the inertia tensor being defined as

$$\mathbf{T}_i^H = -\int_{Bi} ({}_i\tilde{r}_{cp})({}_i\tilde{r}_{cp})dV + m_i\ {}_i\tilde{r}_{ic}\ {}_i\tilde{r}_{ic}^T,$$

with

$$({}_i\tilde{r}_{cp}) = \begin{pmatrix} 0 & ({}_ir_{ic})_3 - x_3 & x_2 - ({}_ir_{ic})_2 \\ x_3 - ({}_ir_{ic})_3 & 0 & ({}_ir_{ic})_1 - x_1 \\ ({}_ir_{ic})_2 - x_2 & x_1 - ({}_ir_{ic})_1 & 0 \end{pmatrix}.$$

The vector b_i represents the vector of total acceleration (3.8) and total angular acceleration (3.7), i.e.

$$b_i = \begin{pmatrix} {}_i\alpha_{0i} \\ {}_ia_{0i} \end{pmatrix}.$$

While $\bar{\xi}_i$ incorporates additional inertia terms, i.e.

$$\bar{\xi}_i = \begin{pmatrix} {}_i\Omega_{0i}\left[I_i^H\right]{}_i\omega_{0i} \\ {}_i\Omega_{0i}\left[m_i\ {}_i\tilde{r}_{ic}^T\right]\omega_{0i} \end{pmatrix},$$

the vector $\bar{q}_i^e$ being defined as

$$\bar{q}_i^e = \begin{pmatrix} {}_i\tilde{r}_{ic}f_i^e + l_i^e \\ f_i^e \end{pmatrix} \tag{3.15}$$

represents the generalised external forces acting on body i. Reordering expression (3.14), exploiting (3.11), (3.12) and collecting all terms involving $\ddot{z}$ leads to the following nonlinear system of ordinary differential equations (cf. [15, p. 55])

$$M(t,z)\ddot{z} + \zeta(t,z,\dot{z}) = \bar{\bar{J}}^T\left((\bar{q}_1^e)^T,\ldots,(\bar{q}_N^e)^T\right)^T = q^e, \tag{3.16}$$

where $\bar{\bar{J}}$ denotes the global Jacobian matrix with dimension $6N \times M$. Due to the supposed tree-like structure of the multi body system, the above equation of motion can be assembled efficiently by means of an iteration over all bodies starting at the

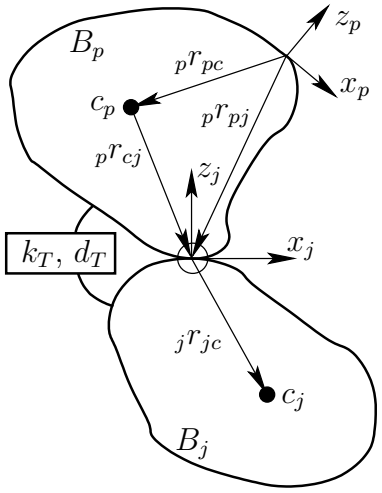

Figure 3.3: Torque acting between two attached bodies.

body with index 'o', i.e. the global reference frame. A tailored algorithm provides the mass matrix $M(t, z)$, the vector $\zeta(t, z, \dot{z})$ and the right hand side q^e for each set of values of z, $\dot{z}$ and t. In contrast to approaches based on computer algebra software, the iterative method provides the equations of motion implicitly which leads to an efficient simulation code that can be applied for very large systems.

The outlined procedure to construct the equations of motions for a multi body system needs an expression for the generalised external force q^e. In case of milling machines such an expression can be found from the forces and torques provided by coupling elements representing the interaction between the rigid bodies. The different contributions usually involve model parameters that have to be determined from experimental data.

3.2.2 External forces and torques

Example of a reaction torque for two attached bodies

The configuration illustrated in Figure 3.3 serves as a first example for the coupling of two rigid bodies. The two bodies are attached to each other at a coupling point which coincides with the origin of the reference frame corresponding to body B_j. Although Figure 3.3 only shows the y=const plane, the body B_j may rotate around the x_j- and y_j-axis with respect to body B_p. The angle corresponding to a rotation around the z_j-axis is fixed, and the vector ${}_pr_{pj}$ pointing from the origin of body B_p to the origin of body B_j is assumed to be independent of the minimal coordinates. In present example, the two rotations around the x_i and y_i axis shall evoke reaction torques ${}_pl_p^r$ and ${}_jl_j^r$ between both bodies if the vectors ${}_pr_{cj}$ and $A_{pj}{}_jr_{jc}$ are not parallel to each other. The orthogonal matrix A_{pj} transforms vector components given in frame j into the corresponding components in frame p. Exploiting the definitions of the scalar and cross product provides two expressions for the angle φ between the

considered vectors, i.e.

$$\cos\varphi = \frac{({}_p r_{cj}, A_{pjj} r_{jc})}{\|{}_p r_{cj}\| \|A_{pjj} r_{jc}\|}, \qquad \sin\varphi = \frac{\|{}_p r_{cj} \times A_{pjj} r_{jc}\|}{\|{}_p r_{cj}\| \|A_{pjj} r_{jc}\|}, \tag{3.17}$$

which leads to

$$\varphi = \arctan\left(\frac{\|{}_p r_{cj} \times A_{pjj} r_{jc}\|}{({}_p r_{cj}, A_{pjj} r_{jc})}\right). \tag{3.18}$$

The torque vector acting on body p follows immediately from the rotation spring equation and a viscose damping model, i.e.

$${}_p l_p^r = k_T \varphi \; {}_p n + d_T A_{pj} \; {}_j\omega_{pj}, \tag{3.19}$$

with the normal vector

$${}_p n = \begin{cases} \frac{{}_p r_{cj} \times A_{pjj} r_{jc}}{\|{}_p r_{cj} \times A_{pjj} r_{jc}\|} & \text{if} \quad \|{}_p r_{cj} \times A_{pjj} r_{jc}\| \neq 0, \\ 0 & \text{otherwise,} \end{cases} \tag{3.20}$$

and ${}_j\omega_{pj}$ denoting the relative angular velocity between the two bodies. The coefficients k_T and d_T represent the stiffness of the torsional spring and the damping coefficient of the torsional damper. Both are empirical parameters that have to be determined from experiments. Following Newton's third law (*action-reaction law*) and transforming the result into reference frame j, leads to the following expression for the torque vector acting on body B_j, i.e.

$${}_j l_j^r = A_{jp}(- \; {}_p l_p^r) = -k_T \varphi \; A_{jp} \; {}_p n - d_T \; {}_j\omega_{pj}. \tag{3.21}$$

Both torques partly modify the generalised force vector (3.15). While ${}_p l_p^r$ has to be added to l_p^e the torque ${}_j l_j^r$ contributes to l_j^e. Note that the outlined procedure can be pursued for any arbitrary pair of vectors defined on body B_p and B_j. The vectors ${}_p r_{cj}$ and $A_{pjj} r_{jc}$ have only been used as an illustrative example to describe the necessary modelling steps.

Example of a reaction force between two bodies

The strategy to calculate the coupling forces between two interacting bodies is similar to the method for the torque computation. As shown in Figure 3.4, the two bodies B_p and B_j are assumed to be connected by means of a generalised spring. Although Figure 3.4 only shows the y=const plane, both bodies can move in all space directions. If the motion leads to a change in the prescribed distance ${}_\alpha r_{ab}$ between the points a and b, reaction forces ${}_p f_p^r$ and ${}_j f_j^r$ act on body B_p and B_j, respectively. In order to compute the distance and the relative velocity between the points a and b, the position and velocity of both points have to be expressed utilising the position and orientation of the involved bodies. Exploiting (3.3) for each body gives

$${}_p r_{0a} = \; {}_p r_{pa} + {}_p r_{0p} = \; {}_p r_{pa} + \sum_{k=1}^{p} A_{pq} \; {}_q r_{qk}, \quad \text{with} \quad q = q(k), \tag{3.22}$$

$${}_j r_{0b} = \; {}_j r_{jb} + {}_j r_{0j} = \; {}_j r_{jb} + \sum_{k=1}^{j} A_{jq} \; {}_q r_{qk}, \quad \text{with} \quad q = q(k). \tag{3.23}$$

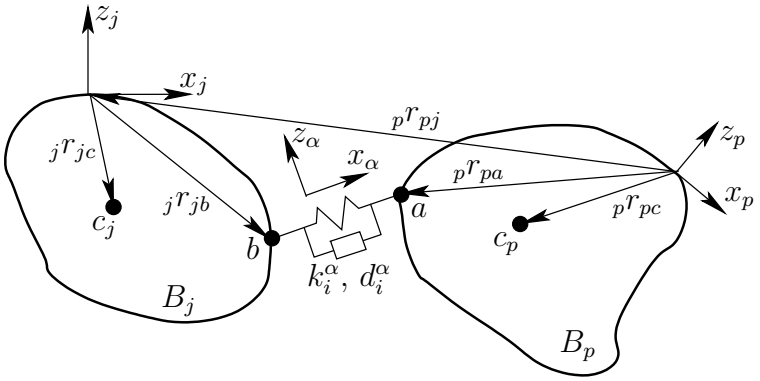

Figure 3.4: Coupling forces acting between two bodies.

By means of (3.4) the total velocities of point a and b read

$$\begin{aligned} {}_pv_{0a} &= {}_p\dot{r}_{pa} + {}_p\Omega_{0pp}r_{pa} + {}_pv_{0p} \\ &= {}_p\dot{r}_{pa} + {}_p\Omega_{0pp}r_{pa} + \sum_{k=1}^{p} A_{pq}\left({}_q\dot{r}_{qk} + {}_q\Omega_{0qq}r_{qk}\right), \end{aligned} \tag{3.24}$$

$$\begin{aligned} {}_jv_{0b} &= {}_j\dot{r}_{jb} + {}_j\Omega_{0jj}r_{jb} + {}_jv_{0j} \\ &= {}_j\dot{r}_{jb} + {}_j\Omega_{0jj}r_{jb} + \sum_{k=1}^{j} A_{jq}\left({}_q\dot{r}_{qk} + {}_q\Omega_{0qq}r_{qk}\right), \end{aligned} \tag{3.25}$$

and again with $q = q(k)$. Since the constitutive equation for the coupling element is assumed to be given in reference frame α, distance vector and relative velocity have to be expressed in the coupling element frame, i.e.

$${}_\alpha\Delta_{ab} = A_{\alpha jj}r_{0b} - A_{\alpha pp}r_{0a}, \qquad {}_\alpha v^r_{ab} = A_{\alpha jj}v_{0b} - A_{\alpha pp}v_{0a}. \tag{3.26}$$

The constitutive law for the coupling element finally provides the reaction force in the corresponding reference frame α

$${}_\alpha f^R = \mathrm{diag}\{k_x^\alpha, k_y^\alpha, k_z^\alpha\}\left({}_\alpha\Delta_{ab} - {}_\alpha r^0_{ab}\right) + \mathrm{diag}\{d_x^\alpha, d_y^\alpha, d_z^\alpha\}{}_\alpha v^r_{ab}, \tag{3.27}$$

with k_x^α, k_y^α, k_z^α, d_x^α, d_y^α, d_z^α and ${}_\alpha r^0_{ab}$ representing the empirical parameters of the coupling element. As mentioned in the previous section the empirical parameters have to be determined from experimental data. The reaction forces act according to Newton's third law (*action-reaction law*) on both bodies with opposite sign. Consequently the contributions to the generalised force for body B_p and body B_j read

$${}_pf^R_p = A_{p\alpha\alpha}f^R, \qquad {}_jf^R_j = -A_{j\alpha\alpha}f^R. \tag{3.28}$$

As already discussed in the previous section, the coupling elements contain empirical parameters that have to be determined from experimental data. In the following the right hand side of (3.16) is therefore considered as a function of the minimal coordinates and a parameter vector p^c representing the empirical parameters, i.e.

$$q^e = \hat{q}^e(t, z, \dot{z}, p^c). \tag{3.29}$$

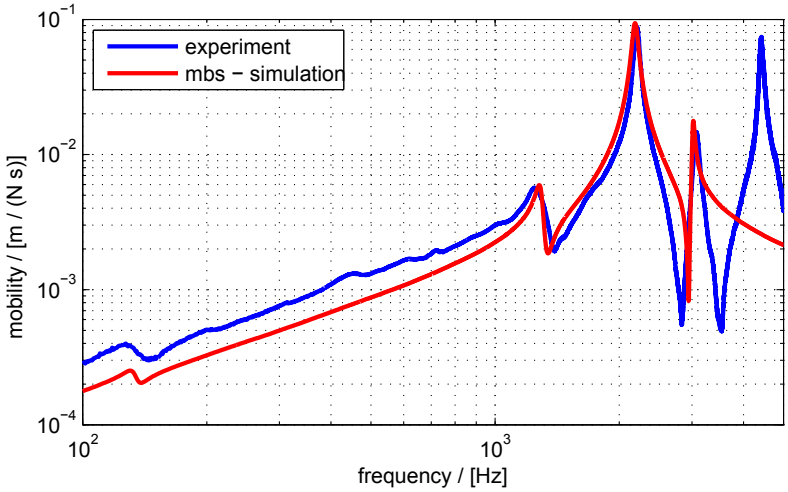

Figure 3.5: Experimental[1] and simulated mobility frequency response function.

3.3 Construction of a multi body system based on experimental data

3.3.1 General strategy

The development procedure of a multi body system representing a machine structure can be summarised as follows. The first step, an experimental modal analysis, provides the eigenfrequencies and the corresponding mode shapes. Next, considering the measured mode shapes, the rigid bodies for the model can be defined. Finally, after having implemented the mathematical model, the remaining free coupling parameters have to be found comparing the experimentally and numerically determined frequency response functions for several points on the machine structure. Mathematically, this problem corresponds to the minimisation of a cost functional that measures the differences between the measured and the simulated frequency response functions.

3.3.2 Semi empirical approach

Determination of the rigid bodies

The blue line depicted in Figure 3.5 shows the mobility frequency response functions (FRF) measured at the tool centre point (TCP) of the milling machine employed for the cutting tests in the framework of this work.[1] As already discussed in Section 2.3.3, the measured mobility FRF clearly displays four dominant eigenfrequencies located at about 1243 Hz, 2208 Hz, 3075 Hz and 4423 Hz. Another small peak can be observed at about 128 Hz. Due to the high frequencies, it can be as-

[1]The mobility FRF measurements have been carried out by P. Rasper under supervision of Prof. E. Uhlmann at IWF, TU-Berlin (for further details see e.g. [75] and Section 6.2).

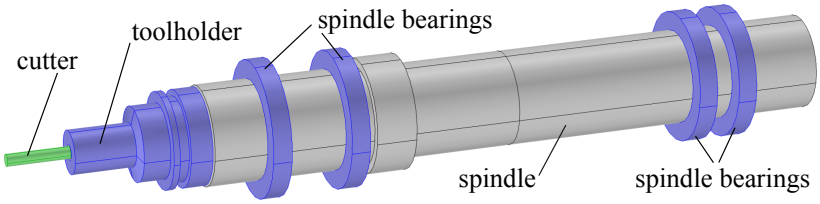

Figure 3.6: Complex model of the machine spindle.

sumed that the four dominating peaks are related to eigenmodes of the tool–spindle system. Only the peak at 128 Hz corresponds to an eigenmode of the machine structure, i.e. the assembly being composed of machine base, side plates, crossbar, x-slider and headstock. Consequently, the focus is on a detailed modelling of the tool–spindle system, while remaining parts can be represented by simple elements only reproducing the feed along x–, y– and z–axis.

In contrast to the general strategy, in the present application, the eigenmodes corresponding to the tool–spindle system are not available because the main part of the spindle is covered by the headstock. An alternative strategy to find the mode shapes of the spindle shaft is to perform an eigenfrequency analysis based on the finite element model shown in Figure 3.6 consisting of cutter, toolholder and spindle. The coupling between the different parts and the representation of the bearings are modelled by connecting domains with special material properties. These parameters, i.e. elastic modulus, Poisson's ratio and mass density, can be adjusted so that the eigenfrequencies of the whole assembly match those observed in the experiments. The corresponding set of eigenvectors provides information that can be exploited to construct a rigid body assembly approximating the mode shapes of the continuous model. The result of the modelling process is shown in Figure 3.7. The approximate model of the spindle system consists of the rigid bodies corresponding to the tool, the toolholder and two spindle segments. The different parts are connected by the elastic rotational joints described in Section 3.2.2. The different joints impose the following conditions

- due to the joint IV, the spindle part 1 rotates around two axes with respect to the preceding reference frame,
- the attachment point on top of spindle part 1 is fixed in the preceding reference frame,
- the rotation angle $\varphi_3(t)$ describing the rotation around the z–axis of the spindle part 1 with respect to the preceding reference frame has been set to $\varphi_3(t) = 2\pi nt$, where n denotes the fixed spindle speed,
- due to the joint III , the spindle part 2 rotates around two axes with respect to spindle part 1 and joint III blocks the rotation around the z–axis of spindle part 2 with respect to spindle part 1,
- the attachment point on top of spindle part 2 is fixed in the reference frame corresponding to spindle part 1,

- due to the joint II , the toolholder rotates around two axes with respect to spindle part 2 and joint II blocks the rotation around the z–axis of the toolholder with respect to spindle part 2,
- the attachment point on top of the toolholder is fixed in the reference frame corresponding to spindle part 2,
- due to the joint I , the tool rotates around two axes with respect to the toolholder and joint I blocks the rotation around the z–axis of the tool with respect to the toolholder,
- the attachment point on top of the tool is fixed in the reference frame corresponding to the toolholder,

By means of the rotational joint IV and the transverse joints, the complete assembly can be connected to the next part, i.e. the headstock. While the rigid joint blocks the translations in x,y- and z-direction, the transverse joints produce a reaction force if the z-axis of spindle part 2 is shifted away from the centre. Moreover, recall that each elastic coupling element, i.e. the rotational and the transverse joints, involves an empirical stiffness and damping parameter.

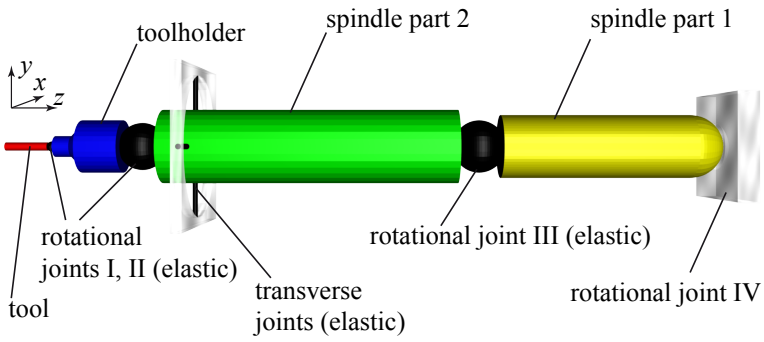

Figure 3.7: Multi body model of the machine spindle.

The final machine model illustrated in Figure 3.8 can be constructed combining the spindle system with three additional bodies representing the headstock, the x-slider and the crossbeam attached to the side columns, i.e. the y–slider. While the x-slider translates with respect to the crossbar in x-direction, the headstock moves with respect to the x-slider in z-direction. The crossbar can rotate around the z-axis and travel in y-direction. As before, the rigid bodies are connected to each other by means of transverse joints with additional stiffness and damping parameters.

Identification of the joint parameters

Following the arguments presented in Section 3.2.1, the equation of motion describing the dynamics of the system can be summarised by (3.16), i.e.

$$M(t,z)\ddot{z} + \zeta(t,z,\dot{z}) = q^e(t,z,\dot{z},p^c,g^e), \tag{3.30}$$

body	translational DOF	rotational DOF
y-slider	1	1
x-slider	1	0
headstock	1	0
spindle part 1	0	2
spindle part 2	0	2
toolholder	0	2
tool	0	2

Table 3.1: Summary of the translational and rotational degrees of freedom (DOF) corresponding to each body.

with q^e representing the external forces and torques applied via joints on each body. The parameter g^e represents the external forces arising in the cutting process or in frequency response measurements. The vector p^c contains the free coupling parameters like joint stiffness or joint damping. Due to the presence of predefined parameters like feed of spindle rotation speed the time appears explicitly in the expressions for M, ζ and q^e. While the unknown parameters like mass and inertia tensor can be computed exploiting the given CAD data, the joint stiffness and joint damping parameters have to be found solving a parameter identification problem. The basic strategy is to excite the model with an approximated impulse, i.e.

$$g^e(t) = {}_oD_j(t) = {}_o\mathbf{e}_j \frac{1}{\varepsilon\sqrt{\pi}} \exp\left(-\frac{(t-t_s)^2}{\varepsilon^2}\right), \quad t_s = 10^{-5},\ \varepsilon = 10^{-4},$$

at the TCP and to compute numerically the time domain velocity response of the system evaluating (3.4) in the global reference frame, i.e.

$$\begin{aligned} {}_ov_{oa} &= {}_o\hat{v}_{oa}(t, p^c) \\ &= A_{oi}\left[{}_i\Omega_{oii} r_{ia} + {}_iv_{0i}\right] \\ &= A_{oi}\left[{}_i\Omega_{oii} r_{ia} + \sum_{j=1}^{i} A_{ip}\left({}_p\dot{r}_{pj} + {}_p\Omega_{0pp} r_{pj}\right)\right], \quad \text{with} \quad p = p(j). \end{aligned} \tag{3.31}$$

where ${}_ir_{ia}$ represents the vector from the origin of body 'i' to the excitation point 'a' on body 'i'. The vector ${}_o\mathbf{e}_j$ denotes the unit vector pointing in j-direction of reference frame 'o'. Transforming both signals in frequency domain by means fast Fourier transform (FFT) and taking the ratio of the transformed signals provides a discrete, complex valued function $H_{ij}(f, p^c)$, the so called mobility frequency response function, i.e.

$$H_{ij}(f, p^c) = \frac{\mathcal{F}[({}_ov_{oa})_i](f)}{\mathcal{F}[{}_oD_j](f)},$$

where $\mathcal{F}[.]$ denotes the Fourier transform operator. The experimental mobility frequency response function $H_{ij}^E(f)$ can be derived from the auto and cross spectral densities corresponding to the measured force and response data (see e.g. [32, pp.

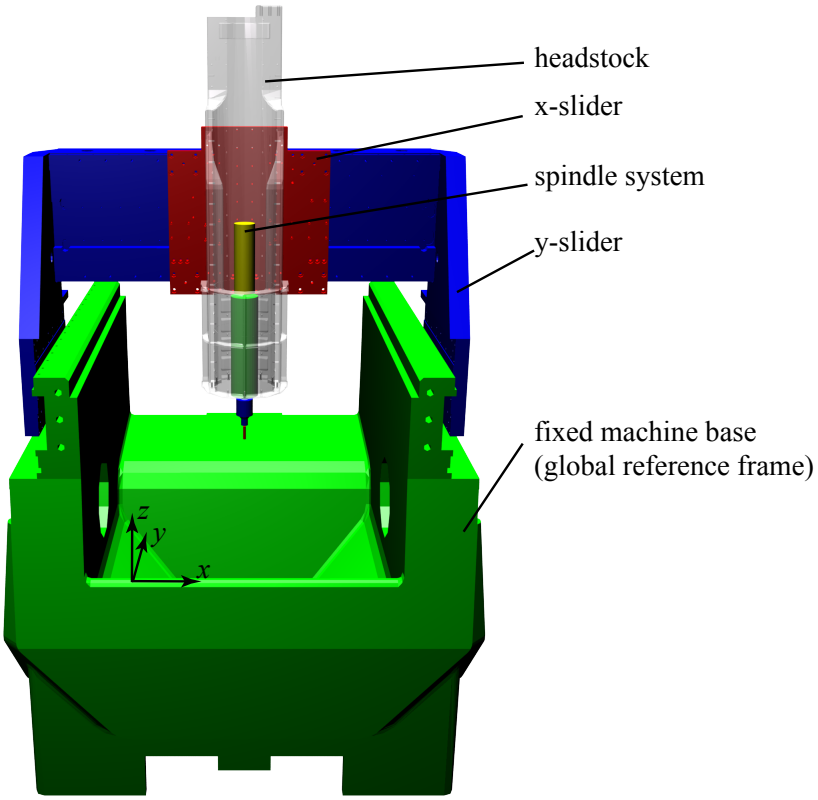

Figure 3.8: Multi body system representing the milling machine.

79]). Minimising the cost functional measuring the distance between experimental and simulated values, i.e.

$$J(p^c) = \sum_{k=1}^{N^{sp}} w_k \frac{1}{2} \left(|H_{yy}(f_k, p^c)| - |H_{yy}^E(f_k)| \right)^2, \tag{3.32}$$

provides a set of parameters p^c_{opt} that guarantees for the underlying multi body system an optimal fit of the experimental data. The discrete weight function w_k suppresses the influence of critical experimental data. Figure 3.5 illustrates the result of the parameter identification procedure. The deviations between experiments and simulation are due to the approximations made in the modelling step. In particular, the peak located at approximately 4500 Hz cannot be reproduced with the current model. In order to improve the results, the model could be further refined by splitting up the spindle in four elements and by introducing an additional body on top of the spindle part 1. The current model, however, reproduces the main peaks observed in the experiments and is therefore expected to predict the stability limits accurately.

3.4 Representation of the work piece

3.4.1 Preliminaries and assumptions

In many milling applications the work piece has a block-like geometry which is clamped on the machine table. This leads to a very stiff assembly presenting a compliance with small magnitude at the cutting zone. Consequently, the oscillations of the tool dominate the process and the work piece can be represented as a rigid body. However, in case of thinwalled parts with a more flexible structure, the situation is completely different. The compliance at cutting zone and tool have a similar order of magnitude and work piece effects have to be taken into account. Usually, thinwalled parts can be described employing (cantilever) beam or plate models. These models arising from a 1D or 2D formulation of the momentum balance, accurately reproduce the dynamical characteristics of the work piece and guarantee efficient numerical simulations because the corresponding discrete systems are rather small. However, the most flexible approach is a full 3D representation of the work piece. Many effects occurring in practise including complex geometries and undesired material removal due to thermal expansion can be simulated with this model. Consequently, in the present work the focus is on a full 3D description of the work piece. The derivation of the model equations and the modelling of thermal effects are the main objective of the following sections. Damping effects occurring in the work piece are related to material and structural (clamping, stick-slip effects etc.) damping (see e.g. [57]). A detailed discussion concerning the relevance of each mechanism is beyond the scope of this work. In the present chapter, the focus is therefore on the (thermo–) elastic behaviour of the work material. In the simulations (cf. Chapter 5), the main damping effects are incorporated by means of a semi–empirical approach.

3.4.2 The general equations of thermo–elasticity with internal variables

In order to derive the equations describing the work piece, recall the local balance equations for momentum (B.18) and internal energy (B.28) in material coordinates derived in appendix B

$$\hat{\varrho}_0 \hat{v}_t - \mathrm{Div}(F \cdot S) = \hat{\varrho}_0 \hat{f}, \tag{3.33}$$

$$\hat{\varrho}_0 \hat{e}_t + \mathrm{Div}(\hat{Q}) = \frac{1}{2} S : C_t + \hat{\varrho}_0 \hat{r}. \tag{3.34}$$

In symbolic notation Div(.) and Grad(.) denote the differential operators with respect to the material coordinates.

Material laws, Clausius-Duhem inequality

As shown in Section B, the balance of entropy reads in material coordinates

$$\hat{\eta}_t + \frac{1}{\hat{\varrho}_0} \mathrm{Div}\big(\Phi\big) = \hat{\sigma} + \hat{s} \geq 0. \tag{3.35}$$

Since for ordinary thermo–elastic bodies the material entropy flux can be written as $\Phi = Q/T$ (cf. [67, p. 261]), the above inequality leads to

$$\hat{\varrho}_0\hat{\eta}_t + \frac{1}{T}\mathrm{Div}(Q) - \frac{1}{T^2}Q \cdot \mathrm{Grad}(T) \geq 0. \tag{3.36}$$

Next, replace $\mathrm{Div}(Q)$ by the rearranged energy-balance, i.e.

$$\hat{\varrho}_0\hat{\eta}_t + \frac{1}{T}\left(\frac{1}{2}S : C_t - \varrho_0\hat{e}_t\right) - \frac{1}{T^2}Q \cdot \mathrm{Grad}(T) \geq 0. \tag{3.37}$$

The multiplication with the absolute temperature $T > 0$, and the fact that $(\hat{\eta}T)_t = \hat{\eta}_t T + \hat{\eta}T_t$, yields

$$-\hat{\varrho}_0\left[\hat{e}_t - (T\hat{\eta})_t\right] - \hat{\varrho}_0\hat{\eta}T_t + \frac{1}{2}S : C_t - \frac{1}{T}Q \cdot \mathrm{Grad}(T) \geq 0. \tag{3.38}$$

Identifying $\hat{e}_t - (T\hat{\eta})_t = \hat{\psi}_t$ as the time derivative of the free energy leads to the Clausius-Duhem inequality, i.e.

$$-\hat{\varrho}_0(\hat{\psi}_t + \hat{\eta}T_t) + \frac{1}{2}S : C_t - \frac{1}{T}Q \cdot \mathrm{Grad}(T) \geq 0. \tag{3.39}$$

In the present application, the temperature $T = \tilde{T}(t, \mathbf{X})$, the Cauchy-Green Deformation tensor $C = \hat{C}(t, \mathbf{X})$ and the internal variables $\hat{\xi} = \tilde{\xi}(t, \mathbf{X})$ represent the unknown fields. Consequently, the free energy is considered to be a function of these variables, i.e. $\hat{\psi} = \tilde{\psi}(C, T, \hat{\xi})$, which implies the time derivative

$$\hat{\psi}_t = \frac{\partial\hat{\psi}}{\partial C} : C_t + \frac{\partial\hat{\psi}}{\partial T}T_t + \frac{\partial\hat{\psi}}{\partial\hat{\xi}}(\hat{\xi})_t. \tag{3.40}$$

Combining the above time derivative with (3.39) leads to the *dissipation* inequality

$$-\hat{\varrho}_0(\frac{\partial\hat{\psi}}{\partial T} + \hat{\eta})T_t - (\hat{\varrho}_0\frac{\partial\hat{\psi}}{\partial C} - \frac{1}{2}S) : C_t - \frac{1}{T}Q \cdot \mathrm{Grad}(T) - \frac{\partial\hat{\psi}}{\partial\hat{\xi}}(\hat{\xi})_t \geq 0. \tag{3.41}$$

Since the inequality holds for all values of T_t, and C_t, the corresponding coefficients have to vanish. This leads to the following relations

$$\begin{aligned} \hat{\eta} &= \hat{\tilde{\eta}}(C, T, \hat{\xi}) = -\frac{\partial\hat{\psi}}{\partial T}, \\ S &= \hat{S}(C, T, \hat{\xi}) = 2\hat{\varrho}_0\frac{\partial\hat{\psi}}{\partial C}. \\ 0 &\leq -\frac{1}{T}Q \cdot \mathrm{Grad}(T) - \frac{\partial\hat{\psi}}{\partial\hat{\xi}}(\hat{\xi})_t. \end{aligned} \tag{3.42}$$

The remaining inequality (3.42) requires the following constitutive law for the heat flux

$$Q = -K(C, T, \hat{\xi}) \cdot \mathrm{Grad}(T), \tag{3.43}$$

with $K(C,T,\hat{\xi})$ denoting the heat conductivity tensor. Note that $K(C,T,\hat{\xi})$ has to be positive semi definite to ascertain that (3.41) is satisfied for all values of $C,T,\hat{\xi}$. A similar condition holds for the time derivative of the internal variables, that can be written in the following form of evolution equations (see [40, p. 513])

$$(\hat{\xi})_t = -\Xi \frac{\partial \hat{\psi}}{\partial \hat{\xi}}, \tag{3.44}$$

with a symmetric and positive definite matrix Ξ possibly depending on combinations of the unknown fields C, T, and $\hat{\xi}$.

Material laws, internal energy

In order to find the constitutive relation for the internal energy $\hat{e}$, consider the time derivative of the entropy density together with(3.40) and (3.41), i.e.

$$\begin{aligned}
\hat{\eta}_t &= -\frac{\partial}{\partial t}\left(\frac{\partial \hat{\psi}}{\partial T}\right) = -\frac{\partial \hat{\psi}_t}{\partial T} \\
&= -\frac{\partial}{\partial T}\left(\frac{\partial \hat{\psi}}{\partial C} : C_t + \frac{\partial \hat{\psi}}{\partial T} T_t + \frac{\partial \hat{\psi}}{\partial \hat{\xi}} (\hat{\xi})_t\right) \\
&= -\frac{1}{2\hat{\varrho}_0}\frac{\partial S}{\partial T} : C_t + \frac{\partial s}{\partial T} T_t - \frac{\partial^2 \hat{\psi}}{\partial T \partial \hat{\xi}} (\hat{\xi})_t.
\end{aligned} \tag{3.45}$$

Next, recall the relation $\hat{e} = \hat{\psi} + T\hat{\eta}$ and its time derivative $e_t = \hat{\psi}_t + T_t\hat{\eta} + T\hat{\eta}_t$. Combining the time derivative of the internal energy $\hat{e}_t$ with (3.45) and exploiting (3.41) yields

$$\begin{aligned}
\hat{e}_t &= \frac{\partial \hat{\psi}}{\partial C} : C_t + \frac{\partial \hat{\psi}}{\partial T} T_t + \frac{\partial \hat{\psi}}{\partial \hat{\xi}} (\hat{\xi})_t + T_t\hat{\eta} + T\hat{\eta}_t \\
&= \frac{1}{2\hat{\varrho}_0} S : C_t - \hat{\eta} T_t + \frac{\partial \hat{\psi}}{\partial \hat{\xi}} (\hat{\xi})_t + \hat{\eta} T_t + T\hat{\eta}_t \\
&= \frac{1}{2\hat{\varrho}_0} S : C_t + \frac{\partial \hat{\psi}}{\partial \hat{\xi}} (\hat{\xi})_t + T\left[-\frac{1}{2\hat{\varrho}_0}\frac{\partial S}{\partial T} : C_t + \frac{\partial \hat{\eta}}{\partial T} T_t - \frac{\partial^2 \hat{\psi}}{\partial T \partial \hat{\xi}} (\hat{\xi})_t\right] \\
&= \frac{1}{2\hat{\varrho}_0} S : C_t - \frac{T}{2\hat{\varrho}_0}\frac{\partial S}{\partial T} : C_t + T\frac{\partial \hat{\eta}}{\partial T} T_t + \frac{\partial}{\partial \hat{\xi}}\left(\hat{\psi} + T\hat{\eta}\right)(\hat{\xi})_t.
\end{aligned}$$

Inserting the above expression for $\hat{e}_t$ into balance of internal energy (3.34) finally leads to

$$\hat{\varrho}_0 T \frac{\partial \hat{\eta}}{\partial T} T_t + \mathrm{Div}(\hat{Q}) = \frac{T}{2}\frac{\partial S}{\partial T} : C_t + \hat{\varrho}_0 \hat{r} - \hat{\varrho}_0 \frac{\partial}{\partial \hat{\xi}}\left(\hat{\psi} + T\hat{\eta}\right)(\hat{\xi})_t. \tag{3.46}$$

With the definition of the specific heat at constant deformation (cf. [40, p. 513]), i.e.

$$c_D := T\frac{\partial \hat{\eta}}{\partial T} = -T\frac{\partial^2 \hat{\psi}}{\partial T^2}, \tag{3.47}$$

and the constitutive law for the heat flux (3.43), the balance of internal energy for thermo–elasticity with internal variable can be written as

$$\begin{aligned} c_D T_t - \frac{1}{\hat{\varrho}_0} \mathrm{Div}\left[K(C,T,\hat{\xi}) \cdot \mathrm{Grad}(T)\right] = \\ = \frac{T}{2\hat{\varrho}_0}\frac{\partial S}{\partial T} : C_t + \hat{r} - \frac{\partial(\hat{\psi} + T\hat{\eta})}{\partial \hat{\xi}}\hat{\xi}_t. \end{aligned} \tag{3.48}$$

Material laws, heat flux

In order to relate the material heat flux given by (3.43) to the the heat flux in Euler coordinates consider the following identities ($i = 1, \ldots, 3$)

$$\begin{aligned} q_i &= -\kappa \frac{\partial T}{\partial x_i}, \\ &= -\kappa \frac{\partial X_j}{\partial x_i}\frac{\partial T}{\partial X_j}, \\ &= -\kappa (F^{-1})_{ji}\frac{\partial T}{\partial X_j}. \end{aligned} \tag{3.49}$$

As shown in Section B.3, the material heat flux can be expressed by means of the heat flux in Euler coordinates, i.e.

$$Q_j = J(F^{-1})_{ji} q_i. \tag{3.50}$$

Combning the above expression with (3.49) yields

$$Q_j = -\kappa J (F^{-1})_{ji}(F^{-1})_{ki}\frac{\partial T}{\partial X_k}. \tag{3.51}$$

Comparing (3.51) and (3.43) finally provides an expression for the material heat flux, i.e.

$$K_{jk}(C,T,\hat{\xi}) = -\kappa J (F^{-1})_{ji}(F^{-1})_{ki} = -\kappa J (C^{-1})_{jk}. \tag{3.52}$$

Hookes law can be used as constitutive equation for stress

$$S = C^{el}(E - E^*), \tag{3.53}$$

where $E = \frac{1}{2}(C - \mathbf{I})$ represents the total strain tensor and $E^* = \alpha(T - T_0)\mathbf{I}$ the inelastic deformations, i.e. the thermal expansion. The forth order elasticity tensor

$$\left(C^{el}\right)_{ijkl} = \lambda \delta_{ij}\delta_{kl} + \mu(\delta_{ik}\delta_{jl} + \delta_{il}\delta_{jk}),$$

which has been introduced in (D.26), contains the elastic constants λ and μ. Note that in case of thermo–elasticity no additional variables are required and the additional terms involving $\hat{\xi}$ can be dropped from (3.48).

Linearised balance equations

The equations of linear thermo–elasticity can be derived form (3.33) with (3.53) and (3.48) assuming that the deformation $u(t, \mathbf{X})$ and the deviation from a constant reference temperature T_0, i.e. $\Theta = T - T_0$, are small quantities. In order to exploit the latter assumption, rewrite the balance of internal energy in terms of Θ, i.e.

$$\begin{aligned} c_D\Theta_t - \frac{1}{\hat{\varrho}_0}\mathrm{Div}\left[K(C,T)\cdot\mathrm{Grad}(\Theta)\right] = \\ = \frac{T}{2\hat{\varrho}_0}\frac{\partial S}{\partial\Theta} : C_t + \hat{r}. \end{aligned}$$

Next, recall the definition of the deformation gradient, i.e. $F = \mathbf{I} + \mathrm{Grad}(u)$ and introduce, for small u and Θ, the following approximations

$$\begin{aligned} E \approx \varepsilon &= \frac{1}{2}\left(\mathrm{Grad}(u) + (\mathrm{Grad}(u))^T\right), \\ C_t = (2E + \mathbf{I})_t &= 2E_t \approx 2\varepsilon_t, \\ F\cdot S &\approx C^{el}(\varepsilon - \alpha\Theta), \\ C^{-1} &\approx 1 - 2\varepsilon, \\ J &\approx 1 + \mathrm{Div}(u), \\ Q &= -\kappa J(C^{-1})\mathrm{Grad}(\Theta) \approx -\kappa\mathrm{Grad}(\Theta). \end{aligned}$$

Inserting the approximations into the equations of thermo–elasticity and linearising the resulting system, finally gives

$$u_{tt} = \frac{1}{\hat{\varrho}_0}\mathrm{div}(\sigma) + s_m^e, \tag{3.54}$$

$$\begin{aligned} \sigma &= \lambda tr(\varepsilon)\mathbf{I} + 2\mu\varepsilon - 3K\alpha\Theta\mathbf{I} \quad \text{with} \quad K = \frac{1}{3}(3\lambda + 2\mu), \\ \varepsilon &= \frac{1}{2}\left(\mathrm{Grad}(u) + (\mathrm{Grad}(u))^T\right), \\ \hat{\varrho}_0 c_D\Theta_t &= \kappa\Delta\Theta - 3K\alpha T\mathrm{Div}(u_t) + \hat{\varrho}_0 s_e^e \\ &\approx \kappa\Delta\Theta - 3K\alpha T_0\mathrm{Div}(u_t) + \hat{\varrho}_0 s_e^e, \end{aligned} \tag{3.55}$$

where λ and μ are the Lamé constants, T_0 denotes the reference temperature, κ the heat conductivity and α is the thermal expansion coefficient. The additional terms appearing on the right hand side of momentum (s_m^e) and energy ($\hat{r} := s_e^e$) balance represent source terms. They shall be used to model the effect of the cutting process.

3.5 Coupling of machine and work piece

3.5.1 Adaption of an empirical cutting force model

The cutting forces acting on cutter and work piece can be described by one of the empirical models being discussed in Section 2.1.2. Weck's approach (2.7), i.e.

$$\hat{F} = a_p\ \hat{K}(T_{ce})\ h, \tag{3.56}$$

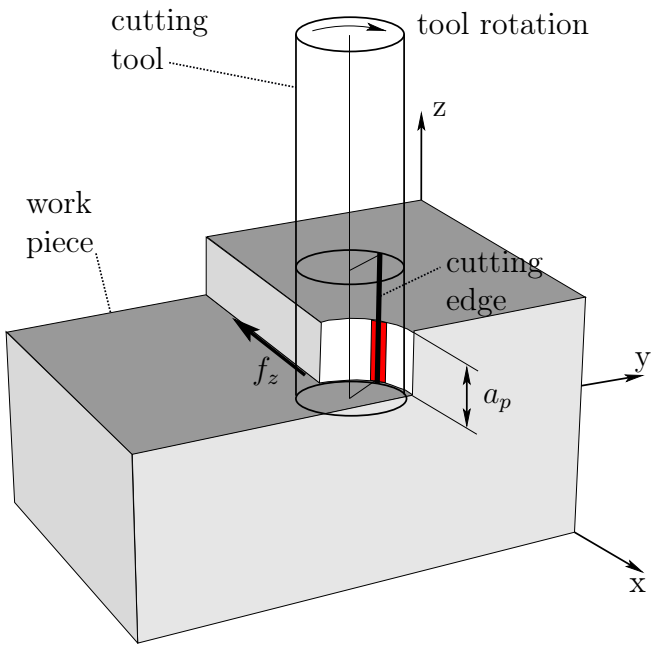

Figure 3.9: Scheme illustrating cutter, work piece, feed per tooth f_z and the axial depth of cut a_p.

with axial depth of cut a_p and the uncut chip thickness h, relates, for a cutting edge without helix angle, the parameters a_p and h to the forces acting on the tool in the opposite direction of feed, i.e. $\hat{F}_t$, in the direction normal to the cutting edge, i.e. $\hat{F}_r$ and in negative z^*–direction, i.e. $\hat{F}_p$. The vector $\hat{K}$ represents an empirical parameter, the so called specific cutting force, which is usually assumed to be constant or depending on the cutting speed. However, as shown in [43], the cutting forces decrease due to higher work piece temperatures. This effect can be incorporated in the cutting force model by multiplying the constant specific cutting force vector $\hat{K}^{std} = [\hat{K}_r, \hat{K}_t, \hat{K}_p]^T$ by an empirical function involving the work piece temperature T_e at the cutting edge, i.e.

$$\hat{K}(T_e) = \hat{K}^{std} \left(cT_e\right)^{-b}, \tag{3.57}$$

with further fit parameters b and c.

3.5.2 Uncut chip thickness

Standard approach and limitations

As discussed in Chapter 2, the uncut chip thickness describes the thickness of the chip to be removed from the work piece. In case of perfectly rigid machine and work piece, the value of the uncut chip thickness can be calculated from the preset value of the feed per tooth, i.e. f_z, and the current angular position of the tool and the associated cutting edge (see e.g. Section 2.1.2). The dashed lines depicted in Figure 3.11 show the ideal path of the cutting edge and the corresponding ideal work piece surface.

In case of a flexible system, the additional oscillations lead to a perturbation of the ideal value of the uncut chip thickness. As discussed for example in Section 2.3.2, additional terms appear in the expression for the uncut chip thickness. These terms incorporate the current deformations of the system and, by means of delayed terms, the deformations of the system one tooth period before. While the current deformations define the position of tool and work piece, the delayed terms incorporate the effects of the surface created during the previous tooth path. In Section 2.3.2, the restriction to consider a 1D rod only, allowed to derive an explicit formula for the uncut chip thickness. The incorporation of a more complex work piece representation, i.e., for example, a 3D elastic solid, requires another strategy since no explicit formula can be derived for this approach.

Derivation of a new expression for the uncut chip thickness

In order to establish a new expression for the uncut chip thickness incorporating tool displacement and work piece deformations, the effect of the delayed terms has to be replaced by a more general concept. As outlined in Section 3.1, the new concept is inspired by the method of steps. While the material removal model provides, after each tooth period, a new work piece reference domain Ω_R, the focus in the present section is on the derivation of a formula for the uncut chip thickness for a single tooth period, i.e. for a constant work piece reference domain. Even though the approaches presented in [23] and in [109], respectively, do not incorporate complex work piece deformations, a similar strategy is pursued for the present problem. In order to calculate the uncut chip thickness assume that

- the tool and the associated cutting edge can penetrate the work piece without removing any material material from the work piece (the material to be removed remains on the work piece until the end of the tooth period),
- the reference configuration of the work piece Ω_R incorporating the history of the tool displacement and the history of the work piece deformations, is constant throughout the considered tooth period.

Next, consider an admissible solution of (3.16) and admissible solution of (3.54). By means of the displacement field $u(t, \mathbf{X})$, $\mathbf{X} \in \Omega_R$, i.e. the admissible solution of (3.54), the each point of the current work piece domain $\Omega(t)$ can be formulated as the sum of a point in the reference configuration and the corresponding deformation, i.e.

$$\mathbf{x} = \mathbf{X} + u_i(t, \mathbf{X}),$$

with $\mathbf{x} \in \Omega(t)$ and $\mathbf{X} \in \Omega_R$ (see appendix B). The set of points determining the current work piece configuration at time t therefore reads

$$\Omega(t) = \Omega_R + u(t, \Omega_R).$$

Since the boundary $\partial\Omega(t)$ of $\Omega(t)$ describes the current shape of the work piece, the main task for the calculation of the uncut chip thickness is to compute the distance between each immersed point on the cutting edge and the corresponding point on the current work piece surface $\partial\Omega(t)$. To this end, recall that the tool is a part of the

multi body system, and that the position of the tool is defined by the kinematics of the multi body system and the previously mentioned solution of (3.16). The location of each point on the associated cutting edge can therefore be expressed as a function of the tool position, the orientation of the reference frame attached on the tool, i.e. the frame in Figure 3.10 indicated by x^*, y^* and z^*, and and a variable $\zeta^* = (z^* - z_0^*)$ parameterising the cutting edge as a vector valued function in the tool reference frame.

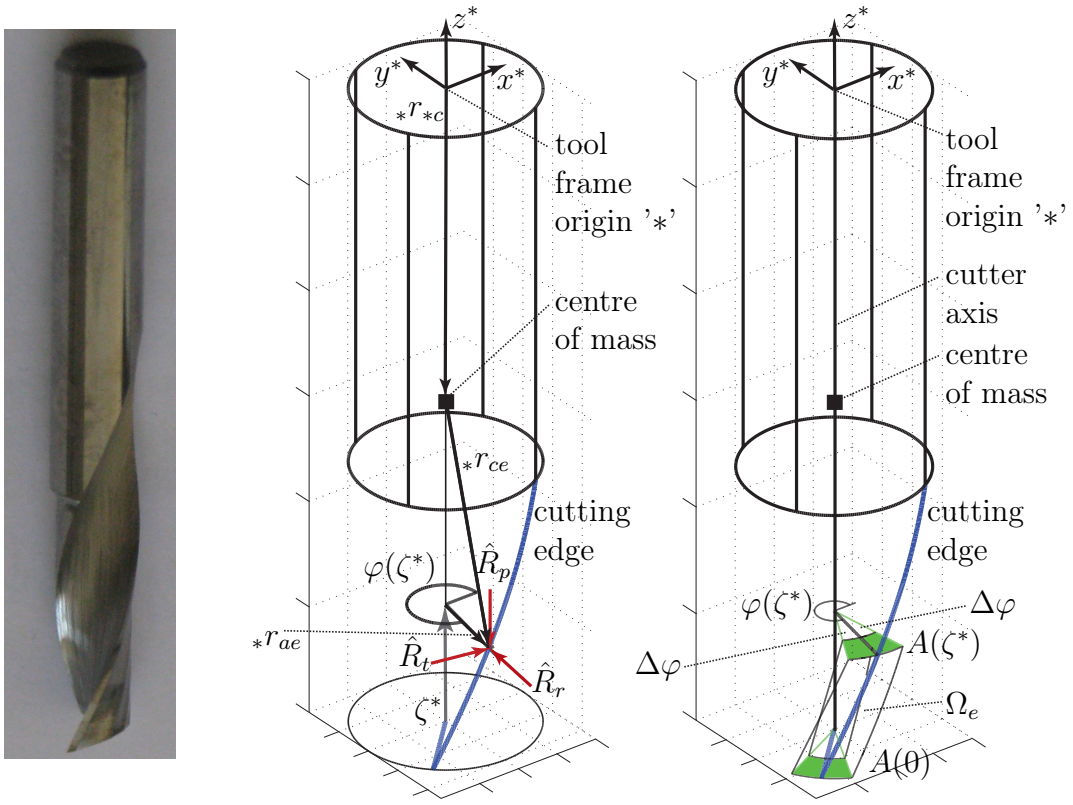

Figure 3.10: Image of a real end mill[2] and a scheme indicating the vectors which describe the cutting edge.

Using the following notations (see Fig. 3.10), i.e.

- ${}_o r_{o*}$ vector from the global origin to the origin of the tool,
- A_{o*} orthogonal transformation relating the global, i.e. the work piece reference frame 'o', to the frame attached to the tool '$*$',
- $\varphi(\zeta^*) = \varphi_0 + \zeta^* \frac{D}{2} \tan\beta$ angle of cutting edge for the parameter ζ^*,
- $O(\varphi(\zeta^*))$ orthogonal transformation relating the frame corresponding to the cutting edge to the tool frame,

[2]The image has been kindly provided by P. Rasper from IWF (head: Prof. E. Uhlmann), TU-Berlin (see e.g. [104]).

- ${}_*r_{*c}$ vector from the origin of the tool to its centre of mass,
- ${}_*r_{ae} = {}_*\tilde{r}_{ae}(\varphi(\zeta^*))$ vector perpendicular to the cutter axis pointing from the cutter axis to the cutting edge,
- ${}_*r_{ce} = {}_*\tilde{r}_{ae}(\varphi(\zeta^*)) + (\zeta - z_0^*){}_*e_{z^*} - {}_*r_{*c}$ vector from the centre of mass to the cutting edge point identified by ζ^*, with ${}_*e_{z^*}$ denoting the unit vector pointing in the direction of the tool axis,

the vector from the origin of the global reference frame (that coincides with the work piece reference frame) to the cutting edge can be written as

$$\begin{aligned} {}_o r_{ae}(\zeta^*) &= {}_o r_{o*} + A_{o*}({}_* r_{*c} + {}_* r_{ce}) \\ &= {}_o r_{o*} + A_{o*}({}_* \tilde{r}_{ae}(\varphi(\zeta^*)) + (\zeta^* - z_0^*){}_* e_{z^*}) \\ &= {}_o r_{o*} + (\zeta^* - z_0^*) A_{o**} e_{z^*} + A_{o**} \tilde{r}_{ae}(\varphi(\zeta^*)) \\ &= {}_o r_{oa}(\zeta^*) + {}_o r_{ae}(\zeta^*). \end{aligned} \tag{3.58}$$

For presentation purposes, consider, without loss of generality, a particular solution of the multi body system (3.16), so that the cutter axis is parallel to the z-axis of the work piece reference frame.

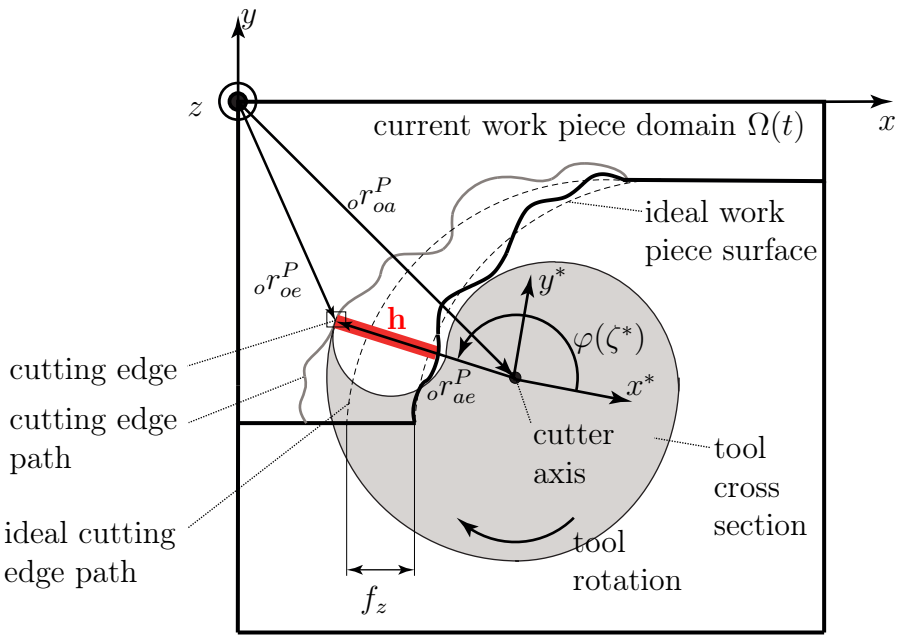

Figure 3.11: On the definition of the uncut chip thickness (the dashed lines represent the ideal tooth path and the ideal work piece shape without machine and work piece deformations).

In this case, work piece shape and the cutter position can be illustrated on a x, y-plane as shown in Fig. 3.11, where ${}_o r^P_{ae}$ and ${}_o r^P_{oa}$ represent the projections of ${}_o r_{ae}$ and ${}_o r_{oa}$ on the considered x, y-plane.

The thick black line in Figure 3.11 represents the current shape of the work piece given by $\partial\Omega(t)$ while the thick grey line illustrates the cutting edge path. As shown

in [24], [81] and indicated by the red bar in Figure 3.11, the uncut chip thickness is defined as the distance between a point on the cutting edge identified by ζ^* and the current work piece surface $\partial\Omega(t)$ measured in the direction of ${}_o r_{ae}$. Mathematically, this can be formulated as follows

$$h = \begin{cases} 0 & \text{if } {}_o r_{oe} \notin \Omega(t), \\ \max\limits_{\bar{h}\in\mathbb{H}} \bar{h} & \text{otherwise,} \end{cases} \tag{3.59}$$

with the set $\mathbb{H}$ being defined as

$$\mathbb{H} = \left\{ x \in \mathbb{R}_+ | \left({}_o r_{oe} - x \frac{{}_o r_{ae}}{\|{}_o r_{ae}\|} \right) \in \Omega(t) \right\}. \tag{3.60}$$

Consequently, the value of h possibly changes for each point on the cutting edge since it depends on the parameter ζ^*, the minimal coordinates (due to ${}_o r_{oe}$, ${}_o r_{ae}$) and, via the current shape of the work piece defined by $\partial\Omega(t)$, on the displacement field $u(t, \mathbf{X})$.

3.5.3 Cutting forces acting on the tool

Combining the expression for the uncut chip thickness with the empirical cutting force model (3.56) divided by a_p gives a force per unit length possibly assuming different values for each value of the parameter ζ^*, i.e.

$$\hat{R} = [\hat{R}_r, \hat{R}_t, \hat{R}_p]^T = \hat{K}\ h. \tag{3.61}$$

Since the components of the vector $\hat{R}$ (see e.g. Fig. 3.10 or Fig. 3.14) are given with respect to the reference frame corresponding to the cutting edge, (3.61) has to be transformed by means of the previously mentioned orthogonal transformation $O(\varphi(\zeta^*))$ in the reference frame of the tool to compute the cutting force per unit length acting on the cutter, i.e.

$$\tilde{R} = O(\varphi(\zeta^*))\hat{R} = O(\varphi(\zeta^*))\hat{K}\ h, \tag{3.62}$$

Similarly, the torque per unit length, acting on the cutter with respect to the centre of mass is given by

$$\tilde{T} = {}_* r_{ce} \times O(\varphi(\zeta^*))\hat{R} = {}_* r_{ce} \times O(\varphi(\zeta^*))\hat{K}\ h, \tag{3.63}$$

where ${}_* r_{ce}$ denotes the vector (with components given with respect to the reference frame attached on the tool) from the centre of mass to the point on the cutting edge identified by ζ^*. Integrating (3.62) and(3.63) along the cutter axis, i.e. with respect to ζ^*, finally provides the resultant (or net) force and torque acting on the cutter.

3.5.4 Heat source

General strategy to estimate the heat flux into the work piece

In the previous sections the cutting forces have been computed for a single tooth tool with nonzero helix angle. The basic strategy was to consider a x^*–, y^*–plane in the

tool frame identified by the parameter ζ^* and to calculate the uncut chip thickness and the corresponding cutting forces per unit length (see (3.62)) for each plane. Integrating the different contributions along the cutter axis, i.e. with respect to ζ^*, finally provided the resultant cutting force acting on the tool. In order to estimate the heat flux into the work piece it is assumed that, on each ζ^*–level, the oblique cutting process can be approximated by an orthogonal process. As a consequence, the third component of the cutting forces per unit length, i.e. $\hat{R}_p$, can be neglected and the generated heat will be estimated only considering the normal and tangential force per unit length, i.e. $\hat{R}_r$ and $\hat{R}_t$.

In order to derive the basic quantities for the heat flux estimation, consider the cross section through an orthogonal process with width of cut a_p illustrated in Figure 3.12. Plastic deformations dissipating the energy usually occur in the primary, secondary (or friction) and tertiary shear zone. The power consumed in the most important shear zones, i.e. the primary shear and the friction zone, can be calculated from the cutting forces, given by $\hat{F}_r$ and $\hat{F}_t$, the chip velocity v_{ch} and the velocity in the direction of the shear zone v_S. Following the arguments of Altintas, [3, pp. 4], the corresponding expressions can be derived performing the following steps. At first, note that the cutting forces $\hat{F}_r$ and $\hat{F}_t$ can be transformed in a pair of forces F_S and $F_{S\perp}$. While F_S represents the component acting in the direction of the shear zone, $F_{S\perp}$ denotes the component perpendicular to the shear zone, i.e.

$$F_{S\perp} = \hat{F}_r \cos\phi + \hat{F}_t \sin\phi$$
$$F_S = \hat{F}_t \cos\phi - \hat{F}_r \sin\phi.$$

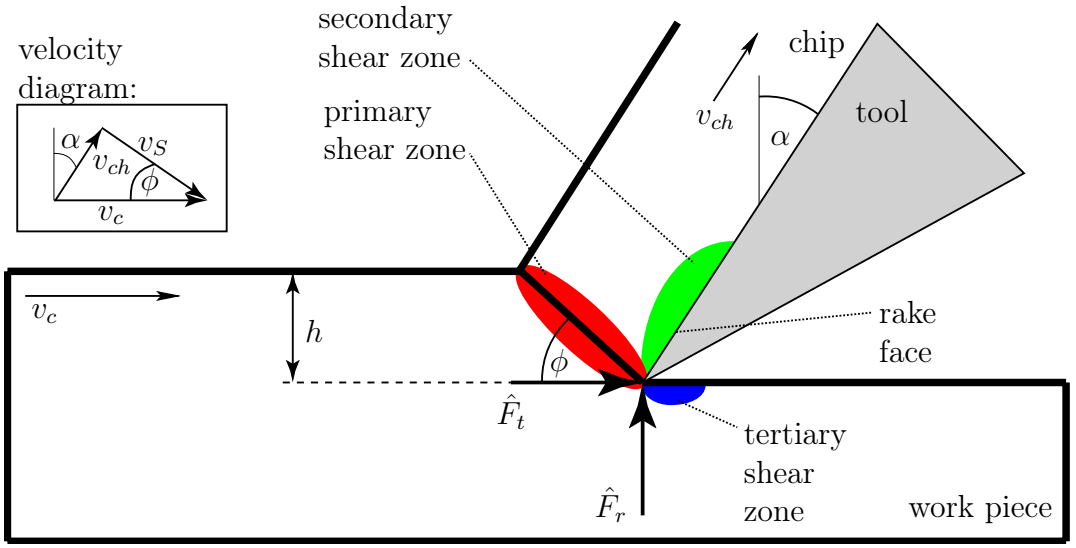

Figure 3.12: Shear zones and cutting forces for an orthogonal process with width a_p and the corresponding velocity diagram.

Next, note that the cutting forces $\hat{F}_r$ and $\hat{F}_t$ can also be transformed in a pair of

forces F_U and $F_{U\perp}$, i.e.

$$F_U = \hat{F}_r \cos\alpha + \hat{F}_t \sin\alpha$$
$$F_{U\perp} = \hat{F}_t \cos\alpha - \hat{F}_r \sin\alpha.$$

F_U acts in the direction of the rake face (see Figure 3.12) while $F_{U\perp}$ represents the force in the direction normal to the rake face. As outlined by Altintas [3, p.11], 'the total power consumed in cutting is the sum of energy spent in the shear and friction zones', i.e.

$$\begin{aligned} P &= F_S v_S + F_U v_{ch}, \\ &= \left(\hat{F}_r \cos\phi + \hat{F}_t \sin\phi\right) v_S + \left(\hat{F}_r \cos\alpha + \hat{F}_t \sin\alpha\right) v_{ch} \\ &= \left[\left(\hat{F}_r \cos\phi + \hat{F}_t \sin\phi\right) \frac{\cos\alpha}{\cos(\phi-\alpha)} + \left(\hat{F}_r \cos\alpha + \hat{F}_t \sin\alpha\right) \frac{\sin\phi}{\cos(\phi-\alpha)}\right] v_c \\ &= \hat{F}_t v_c \end{aligned}$$

where $\hat{F}_t v_c$ represents the total power drawn from the spindle motor. The chip velocity (see Figure 3.12) can be computed from the cutting speed and the shear angle, i.e.

$$v_{ch} = v_c \frac{\sin\phi}{\cos(\phi-\alpha)}, \tag{3.64}$$

while the velocity v_S in the direction of the shear plane is given by

$$v_S = v_c \frac{\cos\alpha}{\cos(\phi-\alpha)}. \tag{3.65}$$

Due to shear and friction, the cutting power is almost completely transformed into heat during the chip formation process. Since the primary shear zone is closer to the work piece, it is assumed in the present application that the total heat flux into the work piece can be estimated by means of the power dissipated in the primary shear zone only, i.e. $F_S v_S$, neglecting the heat generated in the secondary and tertiary zone.

Estimation of the heat flux into the work piece

The heat generated in the shear plane, is, to a large extent, carried away with the chip. The portion of heat flowing into the work piece depends on the cutter geometry, the work piece material and on the cutting conditions. The starting point for the derivation of a relation determining the heat flux into the work piece is an estimate of the shear plane temperature for orthogonal cutting presented by Shaw [87, pp. 219]. Based on the power dissipated in the primary shear zone, i.e. $F_S v_S$, Shaw proposes the following expression for the heat per unit time per unit area flowing into the work piece, i.e.

$$q = (1-R_1)\frac{F_S v_S}{A_S} = \frac{\left(\hat{F}_r \cos\phi + \hat{F}_t \sin\phi\right)}{A_S} \frac{\cos\alpha}{\cos(\phi-\alpha)} v_c, \tag{3.66}$$

where $A_S = a_p l_S = a_p h / \sin\phi$ denotes the shear plane area (see Figure 3.13). Since Shaw assumes that the generated heat per unit time and per unit area, i.e. $F_S v_S / A_S$, is exclusively either carried away with the chip or flows into the work piece, he introduced a new function R_1 to quantify both portions, i.e.

- $(1 - R_1) F_S v_S / A_S$: heat flux into the work piece,
- $R_1 F_S v_S / A_S$: heat carried away with the chip.

In particular, the function R_1 reads (cf. [87, p. 222])

$$R_1 = \frac{1}{1 + C_R (Ar)^{\zeta}}, \tag{3.67}$$

with a dimensionless parameter $A_r = \lambda\gamma / (v_c h)$ being a function of thermal diffusivity λ, cutting speed v_c, uncut chip thickness h and shear strain γ. In [87] the parameters C_R, ζ are given as $C_R = 1.328$ and $\zeta = 0.5$. Unfortunately, the parameters ϕ and γ remain unknown, while the other parameters can be determined from the cutting conditions, i.e. v_c, h, a_p, the tool geometry, i.e. α, and from the work piece material, i.e. λ. A possible remedy is to exploit the relations between the cutting forces $\hat{F}_r$ and $\hat{F}_t$, the shear angle and the shear strain presented in [3, pp. 10]. The shear strain, for example, can be calculated from the shear angle ϕ and the rake angle α (see Fig. 3.13), i.e.

$$\gamma = \frac{\cos\alpha}{\cos(\phi - \alpha)\sin\phi}. \tag{3.68}$$

Moreover, Merchant [66] proposes an approximation of the shear angle, i.e.

$$\phi = \frac{\pi - 2(\beta_a - \alpha)}{4}, \tag{3.69}$$

where β_a, the average friction angle, can be calculated from the cutting forces (see [3, p. 11]), i.e.

$$\beta_a = \alpha + \arctan\frac{\hat{F}_r}{\hat{F}_t}. \tag{3.70}$$

Combining both expressions leads to the following relation between the cutting forces and the shear angle, i.e.

$$\phi = \frac{1}{2}\left[\frac{\pi}{2} - \arctan\left(\frac{\hat{F}_r}{\hat{F}_t}\right)\right]. \tag{3.71}$$

Consequently, the heat flux into the work piece can be estimated from the cutting forces $\hat{F}_r$ and $\hat{F}_t$, the process parameters v_c, h, a_p, the abstract parameters $C_R = 1.328$ and $\zeta = 0.5$, the tool geometry parameter α, and the thermal diffusity of the work piece material λ.

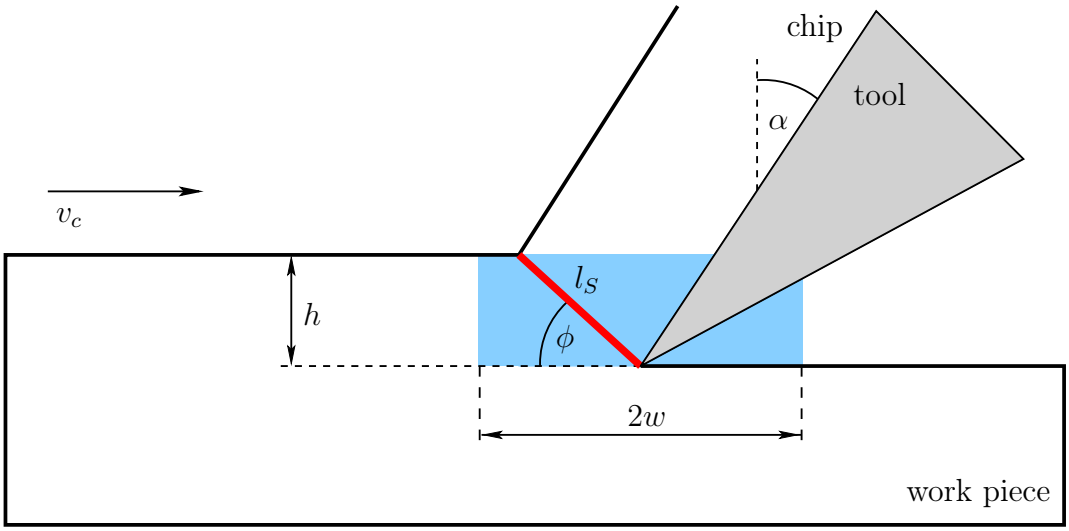

Figure 3.13: Section of an orthogonal cut (width a_p).

Reformulation of the heat flux as source term

The quantity q is a heat flux per unit time and per unit area distributed along the primary shear zone. As mentioned before, the length l_S of the primary shear zone (cf. Fig. 3.13) can be related to the uncut chip thickness h since the vertical component reads

$$l_S \sin\phi = h \Leftrightarrow l_S = \frac{h}{\sin\phi}. \tag{3.72}$$

Correspondingly, the total heat P_q flowing in to the work piece per unit time can be computed multiplying q with the shear zone area, i.e. $A_S = l_S a_p$,

$$P_q = qA_S = q\, l_S a_p = (1 - R_1) F_S v_S. \tag{3.73}$$

In the framework of the milling model involving the effects of machine and work piece, the heat flux into to the work piece is incorporated by means of a source term. This quantity corresponds to a the heat flux per unit volume and per unit time. Consequently, in order to construct an appropriate source term, the total heat given by (3.73) has to be divided by an approximate volume corresponding to the cutting zone. Relating P_q to the volume defined by $V_q = 2wha_p$ (see Figure 3.13), finally leads to the source term r describing the amount of heat r flowing into the work piece per unit volume and unit time, i.e.

$$r = \frac{P_q}{V_q} = (1 - R_1) \frac{\left(\hat{F}_t \cos\phi - \hat{F}_r \sin\phi\right)}{2wha_p} \frac{\cos\alpha}{\cos(\phi - \alpha)} v_c, \tag{3.74}$$

where $2w$ represents an arbitrary distribution parameter (see Figure 3.13).

Heat flux modification due to the material removal

The above formula (3.74) for the source term describing the heat flux into the work piece, has been derived assuming stationary cutting conditions. Due to the

permanent chip flow, the amount of heat determined by the parameter R_1 is carried away from the cutting zone. The remaining portion, i.e. $(1 - R_1)$ flows into the work piece. The presented approach can therefore be used to directly estimate the heat flux into the work piece without simulating the material removal.

However, the milling model being developed in the present work involves a material removal simulation. After the simulation of a single tooth period, the chip is indeed removed from the work piece by means of a tailored algorithm. Because of this approach, the amount of heat carried away with the chip is implicitly incorporated in the present model. Consequently, the function R_1 can be dropped from the equations and the source term representing the heat flux into the work piece is given for the present model by the expression

$$r = \frac{P_q}{V_q} = \frac{\left(\hat{F}_t \cos\phi - \hat{F}_r \sin\phi\right)}{2whha_p} \frac{\cos\alpha}{\cos(\phi - \alpha)} v_c. \tag{3.75}$$

Exploiting additionally the structure of the cutting force model (3.56), finally leads to the following approximate heat source

$$r = \frac{\left(\hat{R}_t \cos\phi - \hat{R}_r \sin\phi\right)}{2wh} \frac{v_c \cos\alpha}{\cos(\phi - \alpha)}, \quad \phi = \frac{1}{2}\left[\frac{\pi}{2} - \arctan\left(\frac{\hat{R}_r}{\hat{R}_t}\right)\right], \tag{3.76}$$

where $2w$ represents the width of an arbitrary area located around the cutting edge (for further details the reader is referred to the next section).

3.5.5 Boundary conditions and source terms

Similar to the resulting force on the cutter, the volume forces s_m^e acting on the right hand side of (3.54) and the corresponding source term s_e^e appearing in (3.55) have to be calculated from the relative cutting force given in (3.61) and the heat source (3.76). Applying the orthogonal transformation between global reference and tool frame A_{o*} to (3.62) provides the components of the relative cutting force in the work piece reference frame, i.e.

$$R = A_{o*}\tilde{R} = A_{o*}O(\varphi(\zeta^*))\hat{K}\ h. \tag{3.77}$$

Since the presented model is a macroscopic approach that cannot reproduce the chip formation, the relative cutting forces have to be distributed over an area $A(\zeta^*)$ being located between cutting edge and work piece surface (see Fig. 3.10) employing model parameter $\Delta\varphi$. For a set of minimal coordinates so that the cutter axis is parallel to the $z-$axis of the work piece frame, the area $A(\zeta^*)$ is illustrated in Figure 3.14. For all points of the work piece domain not being in the domain Ω_e (see Figure 3.10) around the cutting edge, the source terms are equal to zero. In order to verify this condition, at first the coordinates of a point ${}_o r$ given in the work piece reference frame have to be transformed in the reference frame of the tool (denoted by '$*$'), i.e.

$${}_* r({}_o r) = A_{to}\left({}_o r - {}_o r_{o*}\right), \tag{3.78}$$

with ${}_{o}r_{o*}$ denoting the vector from the origin of the work piece frame 'o' to the origin of the tool frame '$*$'. By means of the cylindrical coordinates corresponding to ${}_{*}r = \left(({}_{*}r)_{x^*}, ({}_{*}r)_{y^*}, ({}_{*}r)_{z^*}\right)^T$, i.e.

$$\begin{aligned}
\rho({}_{*}r) &= \sqrt{[({}_{*}r)_{x*}]^2 + [({}_{*}r)_{y*}]^2}, \\
\psi({}_{*}r) &= \arctan\left(\frac{({}_{*}r)_{y*}}{({}_{*}r)_{x*}}\right), \\
\zeta^*({}_{*}r) &= ({}_{*}r)_{z^*} - z_0^*,
\end{aligned}$$

the condition for ${}_{*}r$ being in Ω_e (see Figure 3.10) can be formulated as follows

$${}_{*}r \in \Omega_e \quad \Leftrightarrow \quad \begin{cases} |\psi({}_{*}r) - \varphi(\zeta^*({}_{*}r))| \leq \Delta\varphi \\ -h(\zeta^*({}_{*}r)) \leq \rho({}_{*}r) - \frac{D}{2} \leq 0 \end{cases} \tag{3.79}$$

with $\varphi(.)$ denoting the angle of the cutting edge. The angle $\Delta\varphi$ is illustrated in Figure 3.10 and Fig. 3.14, respectively. For a given point on the cutting edge ${}_{*}r_{ae}$ and a given level ζ^*, the area $A(\zeta^*)$ is defined as the set of all points that are enclosed by the green disc ring segment. The segment is defined by the arcs through ${}_{*}r_{ae}$ with radius $D/2$ and length $\Delta\varphi D$ and through $(1 - h/\|{}_{*}r_{ae}\|){}_{*}r_{ae}$ with radius $D/2 - h$ and length $2\Delta\varphi(D/2 - h)$. Thus, the volume force reads

$$\hat{\varrho}_0 s_e^m({}_{o}r) = \begin{cases} 0 & \text{if}_{*}r({}_{o}r) \notin \Omega_e, \\ -\frac{R}{A(\zeta^*({}_{*}r))} & \text{otherwise}, \end{cases} \tag{3.80}$$

with R given by (3.77). The corresponding heat source appearing on the right hand side of (3.55) reads

$$\hat{\varrho}_0 s_e^e({}_{o}r) = \begin{cases} 0 & \text{if}_{*}r({}_{o}r) \notin \Omega_e, \\ \frac{H}{A(\zeta^*({}_{*}r))} & \text{otherwise}, \end{cases} \tag{3.81}$$

with H being related to (3.76) by

$$H = rA = \left(\hat{R}_t \cos\phi - \hat{R}_r \sin\phi\right) \frac{v_c \cos\alpha}{\cos(\phi - \alpha)}, \tag{3.82}$$

with the shear angle

$$\phi = \frac{1}{2}\left[\frac{\pi}{2} - \arctan\left(\frac{\hat{R}_r}{\hat{R}_t}\right)\right].$$

Note that the source terms depend on the displacement field (due to the involved uncut chip thickness h), possibly on the work piece temperature (due to temperature dependent cutting coefficient) and on the set of minimal coordinates (due to the transformation A_{o*} and due to the vector ${}_{o}r_{o*}$).

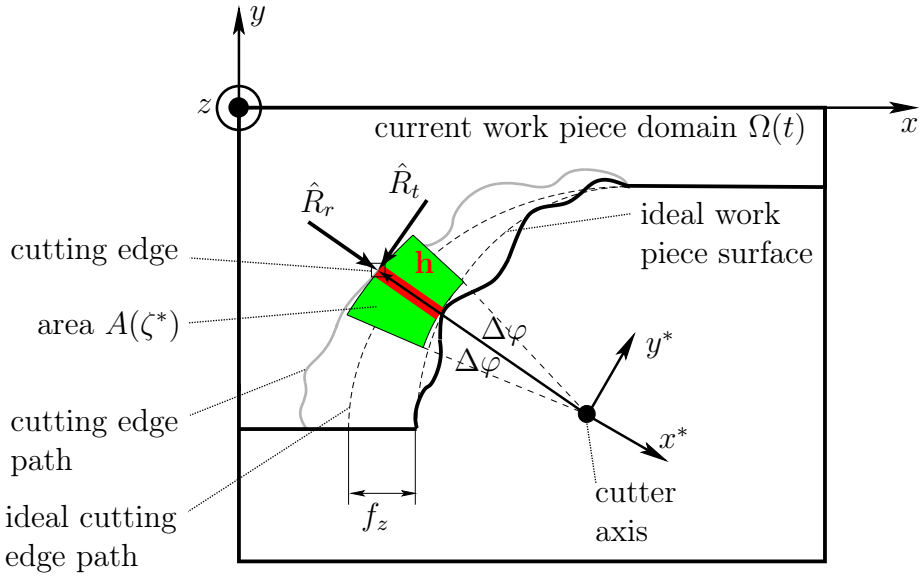

Figure 3.14: On the definition of the volume force.

3.5.6 Summary of the equations describing the milling system for a single tooth period

The milling model describing the the work piece oscillations, the heat conduction in the work piece and the machine oscillations induced by the milling process can be summarised by the following system of equations, i.e.

$$\hat{\varrho}_0 u_{tt} = \mathrm{Div}(\sigma) + \hat{\varrho}_0 s_m^e(t, z, \dot{z}, u, \Theta) \quad \text{on } \Omega_R, \tag{3.83a}$$

$$\sigma = \lambda tr(\varepsilon)\mathbf{I} + 2\mu\varepsilon - 3K\alpha\Theta\mathbf{I}, \quad \text{on } \Omega_R, \tag{3.83b}$$

$$\hat{\varrho}_0 c_D \Theta_t + \mathrm{Grad}(Q) = -3K\alpha T_0 \mathrm{Div}(u_t) + \hat{\varrho}_0 s_e^e(t, z, \dot{z}, u, \Theta), \quad \text{on } \Omega_R, \tag{3.83c}$$

$$Q = -\kappa \mathrm{Grad}(\Theta) \tag{3.83d}$$

$$M(t, z)\ddot{z} + \zeta(t, z, \dot{z}) = q^e(t, z, \dot{z}, u, \Theta), \tag{3.83e}$$

Equation (3.83a) represents the balance of momentum for the work piece. The quantity $\hat{\varrho}_0$ represents the mass density of the work piece in the reference configuration Ω_R. Equation (3.83b) is the linearised stress tensor relating the deformations, i.e.

$$\varepsilon = \frac{1}{2}\left(\mathrm{Grad}(u) + (\mathrm{Grad}(u))^T\right),$$

and the temperature difference $\Theta = T - T_0$ to the stresses in the work piece. The parameters λ and μ denote the elastic constants while α represents the thermal expansion coefficient. The parameter $K = \lambda + (2/3)\mu$ is the bulk modulus. Equation (3.83c) is the balance of energy describing the heat conduction in the work piece. The parameter c_D represents the specific heat for constant deformations while Q denotes the heat flux which is, due Fouriers law, related to the temperature gradient. The parameter κ appearing in (3.83d), i.e. Fouriers law, is the thermal (or heat) conductivity. The first term on the right hand side of (3.83c) is necessary to

model the temperature change due to compression or expansion of the work piece. Equation (3.83e) describes the multi body system in terms of the corresponding minimal coordinates z. The coefficient $M(t,z)$ is the state dependent mass matrix while the function $\zeta(t,z,\dot{z})$ incorporates additional inertial effects. The function $q^e(t,z,\dot{z},u,\Theta)$, i.e. the vector of external forces, appearing on the right hand side of (3.83e) incorporates the joint reactions between the rigid bodies and depends, due to the cutting forces, on the solution of (3.83a) and (3.83c), respectively. Similarly, the source terms s_m^e, s_e^e depend, due to the cutting forces and the heat generated by the process, on the solution of (3.83a), (3.83c) and (3.83e).

3.5.7 Geometry update

As mentioned before, the work piece surface can be constructed employing a material removal model. The main idea is to construct a volume based on cutting edge path and work piece deformations that can be subtracted from a given work piece domain by means of Boolean operations.

To this end recall that during one tooth period, each point on the cutting edge follows a certain path depending on the motion of the cutter. In a sub interval some points of the cutting edge penetrate the deformed work piece surface and the cutter is cutting. Thus, a work piece deformation can be associated to each point ${}_o r_{ce}(\zeta^*)$, of the cutting edge (see (3.58)) being in the work piece domain $\Omega(t)$, i.e.

$$ {}_o r_{oe}(\zeta^*) = X_{oe} + u(t, X_{oe}), \quad X_{oe} \in \Omega_R,\ \zeta^* \in [0, a_p^e], \tag{3.84} $$

where a_p^e denotes the axial depth of cut corresponding to the cutting edge. With solution $X_{oe}^*(t, {}_o r_{oe}(\zeta^*))$ of the above equation and the cutting edge points a new point y can be defined that corresponds either to the cutting edge or to the new shape of the reference domain, i.e.

$$ y = \begin{cases} {}_o r_{oe}(\zeta^*) & \text{if } {}_o r_{oe}(\zeta^*) \notin \Omega(t), \\ X_{oe}^*(t,\ {}_o r_{oe},(\zeta^*)) & \text{otherwise.} \end{cases} \tag{3.85} $$

Monitoring these points $y \subset \mathbb{R}^3$ during a time interval enclosing the actual cutting period gives a set of points that describe an open surface in the three dimensional space. From such a surface a set $\Omega_c \subset \mathbb{R}^3$ can be constructed that represents the points travelled by the cutting edge and incorporating the work piece deformations. The new work piece reference domain Ω_R^{new} can be found subtracting the domain Ω_c from the given work piece reference domain Ω_R, i.e.

$$ \Omega_R^{new} = \Omega_R \setminus \Omega_c. \tag{3.86} $$

The presented strategy leads to a series of work piece domains each incorporating the motion of the cutting edge and the corresponding work piece deformations during the preceding tooth path. Together with the expression for the uncut chip thickness the model leads to a nonlinear system of coupled ordinary and partial differential equations. The history of work piece and cutter motion is stored in the work piece surface.

Chapter 4

Discretisation and numerical algorithms

4.1 Variational formulation and space discretisation

4.1.1 Existence of a unique weak solution

The milling model derived in Chapter 3 can be summarised by the following system of equations (see Section 3.5.6), i.e.

$$\begin{aligned}
\hat{\varrho}_0 u_{tt} &= \mathrm{Div}(\sigma) + \hat{\varrho}_0 s_m^e(t,z,\dot{z},u,\Theta) && \text{on } \Omega_R, && (4.1a)\\
\sigma &= \lambda tr(\varepsilon)\mathbf{I} + 2\mu\varepsilon - 3K\alpha\Theta\mathbf{I}, && \text{on } \Omega_R,\\
\varepsilon &= \frac{1}{2}\left(\mathrm{Grad}(u) + (\mathrm{Grad}(u))^T\right), && \text{on } \Omega_R,\\
\hat{\varrho}_0 c_D \Theta_t + \mathrm{Grad}(Q) &= -3K\alpha T_0 \mathrm{Div}(u_t) + \hat{\varrho}_0 s_e^e(t,z,\dot{z},u,\Theta), && \text{on } \Omega_R, && (4.1b)\\
Q &= -\kappa \mathrm{Grad}(\Theta), && \text{on } \Omega_R,\\
M(t,z)\ddot{z} + \zeta(t,z,\dot{z}) &= q^e(t,z,\dot{z},u,\Theta), && && (4.1c)
\end{aligned}$$

where the source terms s_m^e, s_e^e (see Sections 3.5.4 and 3.5.5) and the generalised external forces q^e (see Section 3.5.3) incorporate the coupling effects. The corresponding initial conditions are

$$\begin{gathered}
u(0,\mathbf{X}) = u_0(\mathbf{X}) = 0,\ u_t(0,\mathbf{X}) = v_0(\mathbf{X}) = 0,\\
\Theta(0,\mathbf{X}) = \Theta_0(\mathbf{X}) = 0,\\
z(0) = z_0 = 0,\ \dot{z}(0) = z_0^v = 0,
\end{gathered}$$

with $\mathbf{X} \in \Omega_R$. Moreover, the following boundary conditions are imposed to the system

$$\begin{aligned}
\sigma \cdot n &= 0 \quad && \text{on} \quad && \Gamma_N \subset \partial\Omega_R,\\
-\kappa \mathrm{Grad}(\Theta)\cdot n &= 0 \quad && \text{on} \quad && \Gamma_N \subset \partial\Omega_R,\\
u &= 0 \quad && \text{on} \quad && \Gamma_D \subset \partial\Omega_R,\\
\Theta &= 0 \quad && \text{on} \quad && \Gamma_D \subset \partial\Omega_R,
\end{aligned}$$

where n denotes the corresponding normal vector. The Dirichlet type conditions take into account that the work piece is fixed on the machine table. Since all coupling effects are included in the source terms, no stresses act on the boundary, therefore homogeneous Neumann type conditions can be imposed for the normal stress on $\Gamma_N = \partial\Omega_R \setminus \Gamma_D$. The homogeneous Neumann type condition for the heat flux on $\Gamma_N = \partial\Omega_R \setminus \Gamma_D$ can be motivated by the assumption that effects like heat transfer or radiation are small compared to the heat source s_e^e.

The weak form of (4.1a) and (4.1b) can be constructed by multiplying both equations with test functions $v \in V = \{v \in H^1(\Omega_R, \mathbb{R}^3) : v|_{\Gamma_D} = 0\}$, $w \in W = \{v \in H^1(\Omega_R, \mathbb{R}) : v|_{\Gamma_D} = 0\}$ and integrating over Ω_R. Integration by parts and exploiting the boundary conditions, leads with the identity $\sigma(u,\Theta) : \mathrm{Grad}(v) = \sigma(u,\Theta) : \varepsilon(v)$ to the weak formulation of the coupled system, i.e.

$$\int_{\Omega_R} \hat{\varrho}_0 u_{tt} v d\mathbf{X} + \int_{\Omega_R} \sigma(u,\Theta) : \varepsilon(v) d\mathbf{X} = \int_{\Omega_R} \hat{\varrho}_0 s_m^e(t,z,\dot{z},u,\Theta) v d\mathbf{X} \quad \forall v, \tag{4.2a}$$

$$\begin{aligned} \int_{\Omega_R} \hat{\varrho}_0 c_D \Theta_t w d\mathbf{X} + \int_{\Omega_R} \kappa \mathrm{Grad}(\Theta) \cdot \mathrm{Grad}(w) d\mathbf{X} + \int_{\Omega_R} 3K\alpha T_0 \mathrm{div}(u_t) w dx \\ = \int_{\Omega_R} \hat{\varrho}_0 s_e^e(t,z,\dot{z},u,\Theta) w d\mathbf{X} \quad \forall w, \end{aligned} \tag{4.2b}$$

$$M(t,z)\ddot{z} + \zeta(t,z,\dot{z}) = q^e(t,z,\dot{z},u,\Theta). \tag{4.2c}$$

In [24] the authors show for a similar problem involving, instead of $\sigma(u,\Theta)$, the regularised stress $\sigma_r(u,\dot{u},\Theta) = \sigma(u,\Theta) + \delta_r \varepsilon(\dot{u})$ the existence of a unique solution with the regularity $u \in L^\infty(0,\tau;V)$, $\dot{u} \in L^\infty(0,\tau;L^2(\Omega_R,\mathbb{R}^3)) \cap L^2(0,\tau;V)$ and $\ddot{u} \in L^\infty(0,\tau;V^*)$. For the temperature field they show that $\Theta \in L^\infty(0,\tau;L^2(\Omega_R))$, $\mathrm{Grad}(\Theta) \in L^2(0,\tau;L^2(\Omega_R;\mathbb{R}^3))$ and $\dot{\Theta} \in L^2(0,\tau;(H^1(\Omega_R))^*)$. Even though the authors analyse the solution on an interval $[0,\tau)$, the results hold for arbitrary time intervals as well, because the solution can be continued employing the method of steps. The time τ represents the delay which is equal to the length of a single tooth period.

Although the system being in the focus of the present work involves a more elaborated machine model and another coupling model than the system discussed in [24], the mathematical structure of both systems is quite similar and it is fair to assume that the regularity results also hold for the present system. Consequently, the above results are the starting point for the space discretisation because the spaces V and W can be approximated with finite elements.

4.1.2 Space discretisation with finite elements

The semi-discrete equations corresponding to the coupled system of the two variational equalities (4.2a), (4.2b) and the ordinary differential equation (4.2c) can be derived employing the Galerkin method described, for example, in [24]. To this end,

let $\{\psi_1, \psi_2, \ldots\}$ be a basis of W and let

$$\left\{ \begin{pmatrix} \psi_1 \\ 0 \\ 0 \end{pmatrix}, \begin{pmatrix} 0 \\ \psi_1 \\ 0 \end{pmatrix}, \begin{pmatrix} 0 \\ 0 \\ \psi_1 \end{pmatrix}, \begin{pmatrix} \psi_2 \\ 0 \\ 0 \end{pmatrix}, \begin{pmatrix} 0 \\ \psi_2 \\ 0 \end{pmatrix}, \begin{pmatrix} 0 \\ 0 \\ \psi_2 \end{pmatrix}, \ldots \right\} = \{v_1, v_2, v_3, v_4, v_5, v_6, \ldots\} \tag{4.3}$$

be a basis of V with $v_1 = (\psi_1, 0, 0)^T, \ldots, v_4 = (\psi_2, 0, 0)^T, \ldots, v_{3n} = (0, 0, \psi_n)^T$. The Galerkin approximation of a weak solution can be constructed by choosing a finite set of basis functions, i.e. $W_n = \operatorname{span}\{\psi_1, \psi_2, \ldots, \psi_n\}$ and $V_n = \operatorname{span}\{v_1, v_2, \ldots, v_{3n}\}$. The corresponding approximations read

$$u^n(\mathbf{X}, t) = \sum_{j=1}^{3n} d^j(t) v_j(\mathbf{X}) \,, \;\; \Theta^n(\mathbf{X}, t) = \sum_{k=1}^{n} \gamma^k(t) \psi_k(\mathbf{X}) \,. \tag{4.4}$$

With the additional requirement that the functions u^n and Θ^n satisfy (4.2a) and (4.2b) on the spaces V_n, W_n respectively, the weak formulation reduces to the following system of ordinary differential equations for the unknown functions $d^j(t)$ with $j = 1, \ldots, 3n$ and $\gamma^k(t)$ with $k = 1, \ldots, n$, i.e.

$$\mathbf{M} \left[\ddot{d^j}(t)\right] + \mathbf{K} \left[d^j(t)\right] = \mathbf{C} \left[\gamma^k(t)\right] + \mathbf{R}(t, z, \dot{z}, \left[d^j(t)\right], \left[\gamma^k(t)\right]), \tag{4.5a}$$

$$\mathbf{m} \left[\dot{\gamma}^k(t)\right] + \mathbf{k}[\gamma^k(t)] + \mathbf{c} \left[\dot{d^j}(t)\right] = \mathbf{r}(t, z, \dot{z}, , \left[d^j(t)\right], \left[\gamma^k(t)\right]). \tag{4.5b}$$

where z, $\dot{z}$ are a solution of the system

$$M(t, z)\ddot{z} + \zeta(t, z, \dot{z}) = \tilde{q}^e(t, z, \dot{z}, , \left[d^j(t)\right], \left[\gamma^k(t)\right]). \tag{4.5c}$$

The square brackets represent the vectors corresponding to the unknown functions, i.e.

$$\left[d^j(t)\right] = \left(d^1(t), d^2(t), \ldots, d^{3n}(t)\right)^T,$$
$$\left[\gamma^k(t)\right] = \left(\gamma^1(t), \gamma^2(t), \ldots, \gamma^n(t)\right)^T.$$

Note that the construction of the finite dimensional system is outlined in Appendix C. The corresponding initial conditions can be calculated solving the linear systems derived in the Appendix C.3. The finite dimensional representations for the initial conditions $u_0, v_0 \in V$ read with (C.21)

$$\left[d^j(0)\right] = \mathbf{M}^{-1} \left(\mathbf{R}^0(u_0)\right), \qquad \left[\dot{d^j}(0)\right] = \mathbf{M}^{-1} \left(\mathbf{R}^0(v_0)\right). \tag{4.6}$$

The finite dimensional representations for the initial condition $\Theta_0 \in W$ reads with (C.23)

$$\left[\gamma^k(0)\right] = \mathbf{m}^{-1} \left(\mathbf{r}^0(\Theta_0)\right). \tag{4.7}$$

4.1.3 Computation of the uncut chip thickness for linear finite elements

As outlined in Section 3.5.2, the uncut chip thickness h corresponding to a point on the cutting edge given by ${}_o r_{oe}$, can be computed solving the following problem

$$h = \begin{cases} 0 & \text{if } {}_o r_{oe} \notin \Omega(t), \\ \max\limits_{h^* \in \mathbb{H}} h^* & \text{otherwise,} \end{cases} \tag{4.8}$$

with the set $\mathbb{H}$ being defined as

$$\mathbb{H} = \left\{ y \in \mathbb{R}_+ | \left({}_o r_{oe} - y \frac{{}_o r_{ae}}{\| {}_o r_{ae} \|} \right) \in \Omega(t) \right\}, \tag{4.9}$$

where the vector ${}_o r_{ae}$ points from the tool axis to the point on the cutting edge defined by ${}_o r_{oe}$ (see Figure 3.10 or Figure 3.11). $\Omega(t) = \Omega_R + u(t, \Omega_R)$ denotes the deformed work piece domain. Solving the maximisation problem in (4.8) under the restriction imposed by the set $\mathbb{H}$ is equivalent to the task of finding the point on the line

$$\mathcal{L}(y) = {}_o r_{oe} - y \frac{{}_o r_{ae}}{\| {}_o r_{ae} \|}, \quad \text{with} \quad y \in \mathbb{R}_+,$$

intersecting with the deformed boundary of the work piece given by $\partial\Omega(t)$. By definition, the parameter y^* solving this problem corresponds to the uncut chip thickness $h = y^*$.

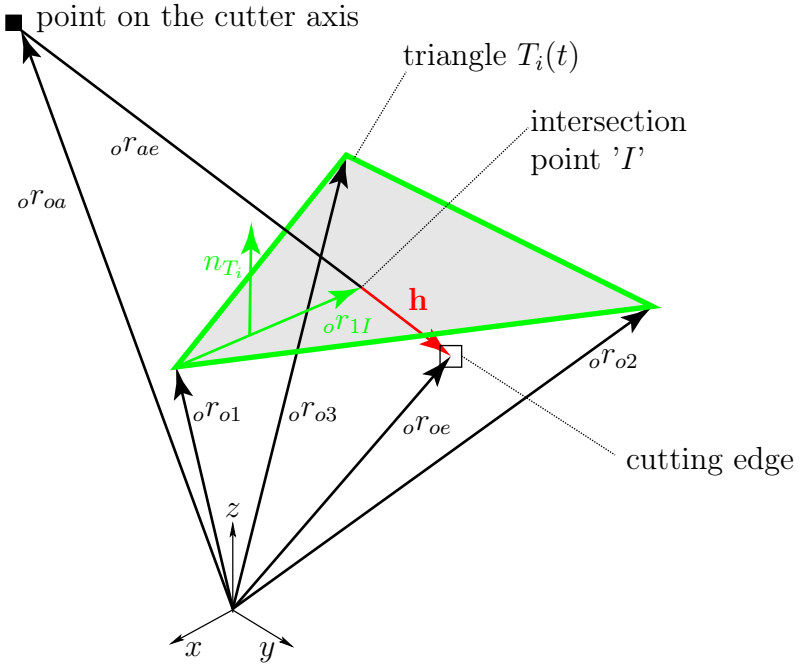

Figure 4.1: Example of an intersection between vector and triangle.

In the discrete case, the union of triangles $T_i(t)$ describes the current work piece

surface , i.e.

$$\partial\Omega(t) \approx \partial\Omega_h(t) = \bigcup_{i=1}^{N_T} T_i(t). \tag{4.10}$$

Figure 4.1 illustrates a configuration where the vector between the cutter axis and the cutting edge, i.e. ${}_o r_{ae}$, intersects a part of the discrete work piece boundary, i.e. the triangle T_i, at the intersection point 'I'. In case of a configuration where the vector ${}_o r_{ae}$ does not intersect the triangle T_i, the intersection point is located in the interior of another triangle, say $T_k(t) \in \partial\Omega_h(t)$, $k \neq i$. The edge points of the triangle T_i, i.e. ${}_o r_{o1}$, ${}_o r_{o2}$ and ${}_o r_{o3}$, are given by the edge points ${}_o R_{o1}$, ${}_o R_{o2}$ and ${}_o R_{o3}$ of the triangle in the reference configuration and the corresponding displacements, i.e.

$${}_o r_{ok} = {}_o R_{ok} + u(t, {}_o R_{ok}), \text{ with } {}_o R_{ok} \in \partial\Omega_R, \ k = 1, \ldots, 3. \tag{4.11}$$

Since the triangle illustrated in Figure 4.1 represents the boundary of the deformed work piece, the 'point on the cutter axis' is located outside of the current work piece domain $\Omega(t)$ while the point named 'cutting edge' is in the interior of $\Omega(t)$. As discussed in Section 3.5.2 and shown in Figure 3.10 and 3.11, respectively, the quantity ${}_o r_{oa}$ represents the vector from the origin of the global reference frame to a point on the cutter axis. Similarly, ${}_o r_{oe}$ denotes the vector from the origin of the global reference frame to a point on the cutting edge. ${}_o r_{ae}$ is the vector connecting ${}_o r_{oa}$ and ${}_o r_{oe}$. The parameter n_{T_i} denotes the outer-pointing normal vector corresponding to the part of the current discrete work piece surface given by the triangle T_i. The vector ${}_o r_{1I}$ lying in the plane defined by the triangle T_i connects the triangle edge '1' with the intersection point 'I'. As discussed before, the uncut chip thickness h is the distance from the cutting edge to the current work piece surface measured in the opposite direction of ${}_o r_{ae}$. In Figure 4.1, the uncut chip thickness 'h' is therefore the distance between the cutting edge and the intersection point 'I'.

Since the intersection point and the corresponding triangle are unknown, the uncut chip thickness has to be computed by finding the intersection between a triangle $T_i(t)$ and the set of points given by the definition $\mathbb{H}$. To this end, recall that each point ${}_o r_1 + {}_o r_{1I}$ on a triangle T_i can be written as a convex linear combination of the edge points ${}_o r_{o1}$, ${}_o r_{o2}$, ${}_o r_{o3}$ i.e.

$$\begin{aligned} T_i \ni {}_o r_{o1} + {}_o r_{1I} &= {}_o r_{o1} + b_2({}_o r_{o2} - {}_o r_{o1}) + b_3({}_o r_{o3} - {}_o r_{o1}) \\ &= b_1 \, {}_o r_{o1} + b_2 {}_o r_{o2} + b_3 {}_o r_{o3}, \end{aligned} \tag{4.12}$$

with the non negative (barycentric) coordinates $b_1 = 1 - b_2 - b_3$, b_2, b_3. The point ${}_o r_{o1} + {}_o r_{1I} \notin T_i$ if at least one of the barycentric coordinates is negative. As shown in Figure 4.1, the vector ${}_o r_1 + {}_o r_{1I}$ can also be expressed exploiting the definition of the set $\mathbb{H}$ given by (4.9), i.e.

$${}_o r_1 + {}_o r_{1I} = {}_o r_{oe} - b_4 \frac{{}_o r_{ae}}{\| {}_o r_{ae} \|}, \tag{4.13}$$

where b_4 denotes another positive number. Equating (4.12) and (4.13) leads together with the definition of b_1 to a linear set of equations to determine the parameters $b_1, \ldots, b_4$, i.e.

$$b_1\ {}_o r_1 + b_2\ {}_o r_2 + b_3\ {}_o r_3 + b_4 \frac{{}_o r_{ae}}{\|{}_o r_{ae}\|} = {}_o r_{oe}$$
$$b_1 + b_2 + b_3 = 1.$$

Rewriting the equations as linear system gives

$$\sum_{j=1}^{4} L_{ij} b_j = f_i. \tag{4.14}$$

Solving the linear system (4.14) for each triangle $T_i \subset \partial\Omega_h(t)$ and checking the condition $b_j(T_i) \geq 0$, $j = 1, \ldots, 4$, finally provides the triangle T_k being intersected by the line ${}_o r_{oe} - b_4(T_k)\ {}_o r_{ae}(\|{}_o r_{ae}\|)^{-1}$, with $b_4(T_k) \in \mathbb{R}_+$, and thus the corresponding uncut chip thickness $h = b_4(T_k)$.

4.2 Time discretisation

4.2.1 Momentum balance

In the present work, the Newmark scheme presented in [45, pp. 490] is used for the time discretisation of the semi-discrete balance of momentum (4.5a). In order to further clarify the time integration scheme, drop the term involving the temperature and rewrite (4.5a) as follows

$$\mathbf{M}\mathbf{a} + \mathbf{D}\mathbf{v} + \mathbf{K}\mathbf{d} = \mathbf{R}, \tag{4.15}$$

where $\mathbf{D}$ denotes an additional damping matrix. Since $\mathbf{D}$ represents an additional term, the (thermo-) elastic system can always be recovered from (4.15) setting $\mathbf{D} = 0$. For presentation purposes the state vector has been replaced by $\mathbf{d} = [d^j(t)]$, the velocity vector by $\mathbf{v} = \left[\dot{d}^j(t)\right]$ and the acceleration vector by $\mathbf{a} = \left[\ddot{d}^j(t)\right]$. Moreover, let $\mathbf{R}$ be a vector only depending on time. The initial conditions computed from (4.6) are denoted by $\mathbf{d}_0$ and $\mathbf{v}_0$. The corresponding initial acceleration $\mathbf{a}_0$ can be computed solving the problem

$$\mathbf{M}\mathbf{a}_0 = -\mathbf{D}\mathbf{v}_0 - \mathbf{K}\mathbf{d}_0 + \mathbf{R}(0). \tag{4.16}$$

Next, assume that the solution of (4.15) is given in terms of the state vectors $\mathbf{a}_k = \mathbf{a}(t_k)$, $\mathbf{v}_k = \mathbf{v}(t_k)$ and $\mathbf{d}_k = \mathbf{d}(t_k)$ for time $t_k = k\Delta t$. As outlined in [45], the new state vectors for t_{k+1} are related to the given vectors at time t_k and to the new accelerations $\mathbf{a}_{k+1}$ by the following expressions

$$\mathbf{d}_{k+1} = \tilde{\mathbf{d}}_{k+1} + \beta(\Delta t)^2 \mathbf{a}_{k+1}, \tag{4.17}$$
$$\mathbf{v}_{k+1} = \tilde{\mathbf{v}}_{k+1} + \gamma(\Delta t)\mathbf{a}_{k+1}, \tag{4.18}$$

method	type	β	γ	stability condition	order of accuracy
average acceleration	implicit	1/4	1/2	unconditional	2
linear acceleration	implicit	1/6	1/2	$f_c \approx 0.5513$ Hz	2
Fox-Goodwin	implicit	1/12	1/2	$f_c \approx 0.3898$ Hz	2
Central difference	explicit[1]	0	1/2	$f_c \approx 0.3183$ Hz	2
damped Newmark	implicit	0.3025	0.6	unconditional	1

Table 4.1: Properties of Newmark's scheme depending on the parameters β and γ given by Hughes [45, p. 493] ([1]$\mathbf{M}$ and $\mathbf{D}$ need to be diagonal for the central difference method to be explicit).

with predictors

$$\tilde{\mathbf{d}}_{k+1} = \mathbf{d}_k + (\Delta t)\mathbf{v}_k + \frac{(\Delta t)^2}{2}(1-2\beta)\mathbf{a}_k, \tag{4.19}$$

$$\tilde{\mathbf{v}}_{k+1} = \mathbf{v}_k + (1-\gamma)(\Delta t)\mathbf{a}_k, \tag{4.20}$$

and parameters β and γ. Inserting the formulae (4.17) and (4.18) into (4.15) leads, after some rearrangements, to a linear system determining $\mathbf{a}_{k+1}$, i.e.

$$\left(\mathbf{M} + \gamma(\Delta t)\mathbf{D} + \beta(\Delta t)^2\mathbf{K}\right)\mathbf{a}_{k+1} = \mathbf{R}(t_{k+1}) - \mathbf{D}\tilde{\mathbf{v}}_{k+1} - \mathbf{K}\tilde{\mathbf{d}}_{k+1}. \tag{4.21}$$

Solving the linear system for $\mathbf{a}_{k+1}$ and computing the new vectors $\mathbf{d}_{k+1}$, $\mathbf{v}_{k+1}$ from (4.17) and (4.18) finally provides a new set of state vectors for the next iteration.

The choice of the parameters β and γ determine the numerical characteristics of the Newmark scheme. Depending on the values of β and γ the numerical scheme may be conditionally or unconditionally stable and may introduce additional numerical damping, see [45]. The results given in [45] are summarised in Table 4.1 The critical frequency is related to the time step size by

$$\Delta t \leq \frac{f_c}{f^h_{max}}, \tag{4.22}$$

with f^h_{max} denoting the maximal eigenfrequency of the discrete undamped system, i.e. for $D = 0$. For the present application the scheme called average acceleration seems to be the best choice. Since the scheme produces no additional numerical damping, it allows to study destabilising work piece effects in milling. Moreover, the frequency response of the work piece is usually dominated by the low frequency behaviour. For the accurate and efficient simulation of these effects the time step size can be chosen relatively large. However, in case of conditionally stable schemes, the upper bound for time step size imposed by (4.22) is much smaller than the admissible step size for the accurate simulation of the low frequency effects. Moreover, for the present problem, the advantages of the explicit scheme cannot be exploited because the matrices $\mathbf{M}$ and $\mathbf{D}$ are not diagonal. In contrast to conditionally stable schemes the unconditionally stable scheme does not impose an upper bound on the time step size and therefore seems to be the better choice.

4.2.2 Heat equation

A generalised trapezoidal rule is used for the time discretisation of the energy balance equation (4.5b). In order to further clarify the integration scheme drop the coupling term from the equations and rewrite (4.5b) as follows

$$\mathbf{m}\boldsymbol{\zeta} + \mathbf{k}\boldsymbol{\gamma} = \mathbf{r}. \tag{4.23}$$

Note that for presentation purposes, the coefficients have been replaced by $\boldsymbol{\zeta} = \left[\dot{\gamma}^k\right]$ and $\boldsymbol{\gamma} = \left[\gamma^k\right]$. As before, let $\mathbf{r}$ be a vector only depending on time. The initial condition computed from (4.7) is denoted by $\boldsymbol{\gamma}_0$. The initial value for $\boldsymbol{\zeta}$, i.e. $\boldsymbol{\zeta}(0) = \boldsymbol{\zeta}_0$, can be computed solving the linear system

$$\mathbf{m}\boldsymbol{\zeta} = \mathbf{r}(0) - \mathbf{k}\boldsymbol{\gamma}_0. \tag{4.24}$$

Next, assume that the solution of (4.23) is given for time $t_k = k\Delta t$ in terms of the vectors $\boldsymbol{\zeta}_k = \boldsymbol{\zeta}(t_k)$ and $\boldsymbol{\gamma}_k = \boldsymbol{\gamma}(t_k)$. As outlined in [45, pp. 490], the new vector $\boldsymbol{\gamma}(t_{k+1})$ for time t_{k+1} is related to the given vectors at time t_k and to $\boldsymbol{\zeta}_{k+1}$ by the following expression

$$\boldsymbol{\gamma}_{k+1} = \tilde{\boldsymbol{\gamma}}_{k+1} + \delta(\Delta t)\boldsymbol{\zeta}_{k+1}, \tag{4.25}$$

with predictor

$$\tilde{\boldsymbol{\gamma}}_{k+1} = \boldsymbol{\gamma}_k + (\Delta t)(1-\delta)\boldsymbol{\zeta}_k, \tag{4.26}$$

and parameter δ. Inserting the formula (4.25) into (4.23) leads, after some rearrangements, to a linear system determining $\boldsymbol{\zeta}_{k+1}$, i.e.

$$\left(\mathbf{m} + \delta(\Delta t)\mathbf{k}\right)\boldsymbol{\zeta}_{k+1} = \mathbf{r}(t_{k+1}) - \mathbf{k}\tilde{\boldsymbol{\gamma}}_{k+1}. \tag{4.27}$$

Solving the linear system for $\boldsymbol{\zeta}_{k+1}$ and computing the new vectors $\boldsymbol{\gamma}_{k+1}$ from (4.25) provides a new set of vectors for the next iteration.

Similar to the Newmark's method, the choice of the parameter δ leads to different numerical schemes. The methods summarised in Table 4.2 are either implicit or explicit and have different orders of accuracy (see [45, pp. 465]). Note that, the parameter λ^h_{max} is the maximal eigenvalue corresponding to the problem

$$(\mathbf{k} - \lambda^h\mathbf{m})\mathbf{x} = 0 \qquad \mathbf{x} \neq 0. \tag{4.28}$$

Since the matrices $\mathbf{m}$ and $\mathbf{k}$ are symmetric, the eigenvalue problem has only real solutions λ^h_i. In order to choose an optimal method among the possibilities given in Table 4.2, recall that refining the grid leads to higher maximal eigenvalues λ^h_{max}. This may in turn impose a step size restriction for the forward Euler scheme because the stability condition $\Delta t \leq 2/\lambda^h_{max}$ has to be satisfied for each grid. Since unconditionally stable methods do not impose such a restriction, they are usually the better choice. Moreover, note that, for the present problem, the advantages of the explicit Euler scheme cannot be exploited because the matrix $\mathbf{m}$ is not diagonal. Among the unconditionally stable schemes, the method derived from the trapezoidal rule presents the highest order of accuracy and is therefore chosen for the present application.

method	type	δ	stability condition	order of accuracy
forward Euler	explicit[1]	0	$\Delta t \leq 2/\lambda^h_{max}$	1
trapezoidal rule	implicit	1/2	unconditional	2
backward Euler	implicit	1	unconditional	1

Table 4.2: Properties of the generalised trapezoidal rule depending on the parameter δ ([1] $\mathbf{m}$ needs to be diagonal for the forward Euler method to be explicit).

Remark 4.1 Note that the mass matrix $\mathbf{m}$ usually does not have the M-matrix property (see Definition 4.3). Moreover, for the presented standard finite element approach in 3D, the matrix $\mathbf{k}$ does not have the M-matrix property as well. Consequently the iteration matrix $\mathbf{m} + \delta\Delta t\mathbf{k}$ is no M-matrix and the present method does not satisfy a discrete maximum principle [39]. Possible remedies are the use of Finite-Volume schemes on Delauny meshes (see e.g. [44]) or tailored discretisation techniques like orthogonal subdomain collocation (OSC) (see [27]) or prismatic meshes (see e.g. [39])

Definition 4.2 *[34, p. 114] The class Z_n ($n \geq 0$) is the set of all real square matrices of order n whose off-diagonal entries are nonpositive, i.e.*

$$Z_n = \{A = (a_{ik}), i, k = 1, \ldots, n; a_{ik} \leq 0, i \neq k\}.$$

A matrix belonging to the class Z_n is called Z–matrix.

Definition 4.3 *A Z-matrix (see Definition 4.2) A is called a (nonsingular) M-matrix if There exists a diagonal matrix D having positive diagonal entries such that the entries of the matrix $AD = (w_{ik})$ satisfy the condition $w_{ii} > \sum_{k\neq i} |w_{ik}|$ for each i. For further equivalent properties see [34, p. 114], or [110].*

4.2.3 Multi-body system

In order to discuss the time discretisation methods for (4.2c) consider a generalised force vector q^e that depends only on the solution of (4.2c), i.e.

$$\tilde{q}^e(t, z, \dot{z}, \mathbf{d}, \boldsymbol{\gamma}) = \bar{q}^e(t, z, \dot{z}).$$

Next, reformulate (4.2c) in first order form, i.e.

$$\begin{bmatrix} \dot{z} \\ \dot{y} \end{bmatrix} = \begin{bmatrix} y \\ M^{-1}(t, z)\left(\bar{q}^e(t, z, y) - \zeta(t, z, y)\right) \end{bmatrix}, \tag{4.29}$$

which can be written in compact form, i.e.

$$\dot{x} = \bar{f}(t, x). \tag{4.30}$$

A general strategy to solve ordinary differential equations like (4.30) are Runge-Kutta methods. As outlined in [37], these methods can be summarised by the following scheme. Let s be an integer (the "number of stages") and a_{21}, a_{31}, a_{32}, ...,

a_{s1}, a_{s2}, ..., $a_{s,s-1}$, b_1, ..., b_s, c_2, ..., c_s be real coefficients. Then the method to compute $x_{i+1} = x(t_{i+1})$ for given $x_i = x(t_i)$,

$$\begin{aligned} k_1 &= \bar{f}(t_i, x_i) \\ k_2 &= \bar{f}(t_i + c_2\Delta t, x_i + \Delta t a_{21} k_1) \\ k_3 &= \bar{f}(t_i + c_3\Delta t, x_i + \Delta t(a_{31}k_1 + a_{32}k_2)) \\ &\vdots \\ k_s &= \bar{f}(t_i + c_s\Delta t, x_i + \Delta t(a_{s1}k_1 + \ldots + a_{s,s-1}k_{s-1})) \\ x_{i+1} &= x_i + \Delta t(b_1 k_1 + \ldots + b_s k_s) \end{aligned} \tag{4.31}$$

is called an s-stage explicit Runge-Kutta method for (4.30). Usually, the c_i satisfy the conditions

$$c_i = \sum_{j=1}^{i-1} a_{ij}, \qquad i = 2, \ldots, s. \tag{4.32}$$

Now, a particular Runge-Kutta method can be constructed defining a so called Butcher tableau shown in Table 4.3.

0					
c_2	a_{21}				
c_3	a_{31}	a_{32}			
$\vdots$	$\vdots$	$\vdots$	$\ddots$		
c_s	a_{s1}	a_{s2}	$\ldots$	$a_{s,s-1}$	
	b_1	b_2	$\ldots$	b_{s-1}	b_s

Table 4.3: Butcher tableau for an arbitrary s-stage Runge-Kutta method.

Efficient adaptive Runge-Kutta type methods are usually constructed from two different sets of coefficients (see e.g. [37]). The sets of coefficients satisfy the requirements that

- corresponding methods have different orders of accuracy (typically ≥ 5),
- the tableau of the lower order method is embedded in the tableau of the higher order method.

This strategy works well provided that the underlying equation (4.30) is non stiff and that its right hand side is sufficiently smooth. In the present application, however, the right hand side involves the solution of the discrete thermo–elastic system. In contrast to the problem (4.30), the equation for the multi body system reads

$$\dot{x} = f(t, x, \mathbf{d}(t), \boldsymbol{\gamma}(t)) = \bar{f}(t, x), \tag{4.33}$$

with time dependent vectors $\mathbf{d}(t)$ and $\boldsymbol{\gamma}(t)$. Both vectors have to be computed solving a system of coupled partial differential equations. As outlined in sections 4.2.1 and 4.2.2 the time discretisation of the partial differential equations has been carried

out employing one step methods. Due to this restriction, the right hand side cannot be provided at arbitrary times and (4.33) has to be discretised with the simple one step scheme (von Heun's method) shown in Table 4.4.

0		
1	1	
	1/2	1/2

Table 4.4: Butcher tableau for von Heun's method.

The corresponding second order Runge-Kutta method involving the vectors $\mathbf{d}(t_i)$, $\boldsymbol{\gamma}(t_i)$, $\mathbf{d}(t_{i+1})$ and $\boldsymbol{\gamma}(t_{i+1})$ reads

$$\begin{aligned} k_1 &= \bar{f}(t_i, x_i) = f(t_i, x_i, \mathbf{d}_i, \boldsymbol{\gamma}_i) \\ k_2 &= \bar{f}(t_i + \Delta t, x_i + \Delta t k_1) \\ &= f(t_{i+1}, x_i + \Delta t k_1, \mathbf{d}_{i+1}, \boldsymbol{\gamma}_{i+1}) \\ x_{i+1} &= x_i + \frac{\Delta t}{2}(k_1 + k_2). \end{aligned}$$

4.3 Time integration algorithm for the coupled system

After the discussion of time discretisation schemes for the decoupled problems, the strategies can be combined to obtain a time integration method for the coupled system. With the considerations of Section 4.2.1-4.2.3, the coupled system (4.5a)-(4.5c) can be summarised as follows

$$\mathbf{M}\mathbf{a} + \mathbf{D}\mathbf{v} + \mathbf{K}\mathbf{d} = \mathbf{C}\boldsymbol{\gamma} + \mathbf{R}(t, x, \mathbf{d}, \boldsymbol{\gamma}) \tag{4.34a}$$

$$\mathbf{m}\boldsymbol{\zeta} + \mathbf{k}\boldsymbol{\gamma} + \mathbf{c}\mathbf{v} = \mathbf{r}(t, x, \mathbf{d}, \boldsymbol{\gamma}). \tag{4.34b}$$

$$\dot{x} = f(t, x, \mathbf{d}, \boldsymbol{\gamma}), \tag{4.34c}$$

where (4.34c) represents the first order formulation of (4.5c) with $x = (z, \dot{z})^T$. The initial values for $\mathbf{a}$, i.e. $\mathbf{a}_0 = \mathbf{a}(0)$, and $\boldsymbol{\zeta}$, i.e. $\boldsymbol{\zeta}_0 = \boldsymbol{\zeta}(0)$, can be computed from $\mathbf{d}_0$, $\mathbf{v}_0$, $\boldsymbol{\gamma}_0$ and x_0 solving the linear systems

$$\mathbf{M}\mathbf{a}_0 = \mathbf{C}\boldsymbol{\gamma}_0 + \mathbf{R}(0, x_0, \mathbf{d}_0, \boldsymbol{\gamma}_0) - \mathbf{D}\mathbf{v}_0 - \mathbf{K}\mathbf{d}_0, \tag{4.35a}$$

$$\mathbf{m}\boldsymbol{\zeta}_0 = \mathbf{r}(0, x_0, \mathbf{d}_0, \boldsymbol{\gamma}_0) - \mathbf{k}\boldsymbol{\gamma}_0 - \mathbf{c}\mathbf{v}_0. \tag{4.35b}$$

Next, assume that a solution of the system (4.34a) – (4.34c) denoted by $\mathbf{a}_k$, $\mathbf{v}_k$, $\mathbf{d}_k$, $\boldsymbol{\zeta}_k$, $\boldsymbol{\gamma}_k$ and x_k is given at time t_k. By virtue of the given solution and the relations (4.17), (4.18) and (4.25), the system (4.34a) – (4.34c) can be rewritten, as

a set of non linear equations determining the solution at time t_{k+1}, i.e.

$$\begin{bmatrix} \mathbf{L} & -\delta\Delta t\mathbf{C} \\ \gamma\Delta t\mathbf{c} & \mathbf{l} \end{bmatrix} \begin{bmatrix} \mathbf{a}_{k+1} \\ \boldsymbol{\zeta}_{k+1} \end{bmatrix} = \begin{bmatrix} \mathbf{R}(t_{k+1}, x_{k+1}, \mathbf{a}_{k+1}, \boldsymbol{\zeta}_{k+1}) \\ \mathbf{r}(t_{k+1}, x_{k+1}, \mathbf{a}_{k+1}, \boldsymbol{\zeta}_{k+1}) \end{bmatrix} - \begin{bmatrix} \mathbf{D} & -\mathbf{C} \\ \mathbf{c} & \mathbf{k} \end{bmatrix} \begin{bmatrix} \tilde{\mathbf{v}}_{k+1} \\ \tilde{\boldsymbol{\gamma}}_{k+1} \end{bmatrix} - \begin{bmatrix} \mathbf{K}\tilde{\mathbf{d}}_{k+1} \\ \mathbf{0} \end{bmatrix}, \tag{4.36a}$$

$$\begin{aligned} k_1 &= f(t_k, x_k, \mathbf{a}_k, \boldsymbol{\gamma}_k) \\ k_2 &= f(t_{k+1}, x_k + \Delta t\, k_1, \mathbf{a}_{k+1}, \boldsymbol{\zeta}_{k+1}) \\ x_{k+1} &= x_k + \frac{\Delta t}{2}(k_1 + k_2) \end{aligned} \tag{4.36b}$$

with predictors $\tilde{\mathbf{v}}_{k+1}$, $\tilde{\mathbf{d}}_{k+1}$, $\tilde{\boldsymbol{\gamma}}_{k+1}$ only depending on the solution at time t_k and matrices $\mathbf{L} = \mathbf{M} + \gamma(\Delta t)\mathbf{D} + \beta(\Delta t)^2\mathbf{K}$ and $\mathbf{l} = \mathbf{m} + \delta(\Delta t)\mathbf{k}$. With the new variable $\mathbf{Y} = (\mathbf{a}_{k+1}, \boldsymbol{\zeta}_{k+1}, x_{k+1})$, the system determining the solution of the coupled system at time t_{k+1} can be reformulated as a nonlinear equation, i.e.

$$0 = F(\mathbf{Y}). \tag{4.37}$$

A standard algorithm to solve a system of non linear equations like (4.37) is Newton's method. The corresponding iteration to find a solution starting from the initial guess $\mathbf{Y} = (\mathbf{a}_k, \boldsymbol{\zeta}_k, x_k)$ consists of the repeated execution of the following steps

1. compute the residual $\mathbf{Z} = F(\mathbf{Y})$
2. solve linear system $\mathbf{A}\Delta\mathbf{Y} = -\mathbf{Z}$
3. update the solution $\mathbf{Y} = \mathbf{Y} + \Delta\mathbf{Y}$,

where the matrix $\mathbf{A}$ usually is the gradient of F, i.e. $\mathbf{A} = \nabla F(\mathbf{Y})$. For the present application it is, however, very difficult to evaluate the gradient ∇F. Due to the complicated structure and the dimension of the underlying equations, the gradient can neither be provided analytically nor be computed by means of finite differences. A possible remedy is, accepting slower convergence, to use the approximation $\mathbf{A} \approx \mathbf{I}$. Since the quality of the initial guess increases with decreasing step size Δt, the resulting fixed point iteration is expected to work satisfactorily at least for small time steps.

4.4 Simulation of the material removal

4.4.1 Dexel-model to simulate the material removal

Material removal simulation and Dexel models

The second part of the algorithm deals with the generation of a new work piece reference domain after each tooth period. In case of milling models involving a rigid work piece, material removal models have been developed based on a constructive solid geometry (CSG) approach (see e.g. [109]) or by considering 'arc surfaces' (see e.g. [23]). An alternative approach is to employ so called Dexel models as discussed

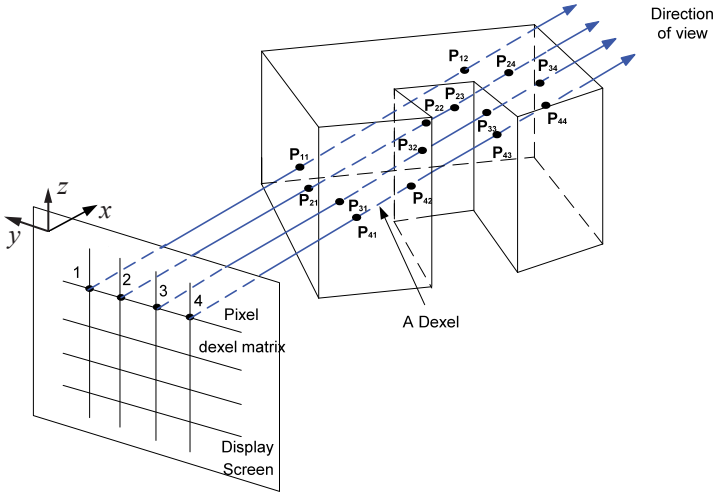

Figure 4.2: Rays and Dexels for the description of the work piece geometry as shown in [112, 114].

for example in [94]. Dexel models are a particular discrete representation of a 3-dimensional object which has been designed to simulate the material removal in virtual sculpting or virtual machining operations [73, 94]. The basic idea of the Dexel representation is illustrated in Figure 4.2. From an observation plane (display screen) rays are casted in the normal direction of the plane. Depending on the shape of the object, each ray enters and leaves the object several times. The section of a ray being inside of the object is called Dexel. The set of points corresponding to the head and tail coordinates of each Dexel can be used to reconstruct a polyhedral domain from the Dexel representation [114]. Recently, new techniques, the so called tri–Dexel models, have been proposed to improve the quality of the reconstructed surface by employing, instead of one, three sets of orthogonal rays to represent the 3-dimensional object [73, 112].

Construction of the tooth-path-volume incorporating work piece deformations

As described in Section 3.5.7, the simulated work piece deformations and cutter motions provide data to construct a tooth-path-volume. The starting point for the considerations is the description of the cutting edge points in the work piece reference frame (3.58), i.e.

$$ {}_{o}r_{oe} = {}_{o}\tilde{r}_{oe}(t, z, \zeta^*), \tag{4.38} $$

where $z = \tilde{z}(t)$ denotes the solution of the multi body system (3.16) at time t and $\zeta^* \in [0, a_p^e]$ the parameter corresponding to the parametrisation of the cutting edge. By virtue of a discrete parametrisation of the cutting edge, i.e.

$$ \Pi = \{\zeta_1^* = 0, \zeta_2^* = \zeta_1^* + \Delta\zeta^*, \ldots, \zeta_{N_{oe}} = a_p^e\}, $$

the set of points $\mathbb{E}(t)$ characterising the discrete cutting edge at time t can be written as

$$ \mathbb{E}(t) = \left\{ {}_{o}\tilde{r}_{oe}(t, z, \zeta_j^*) | \zeta_j^* \in \Pi \right\}. \tag{4.39} $$

In order to incorporate the work piece deformations (3.84) has to be solved for each element in $\mathbb{E}(t)$. Since each point on the immersed cutting edge, i.e. each ${}_o r_{oe}$, corresponds to a point of the current work piece domain, i.e. $X_e + u(t, X_e)$, the solution of (3.84), i.e. $X_e({}_o r_{oe})$, corresponds to the point in the reference domain being actually machined. For the solution of (3.84) in the discrete case, consider the current discrete work piece domain at time t given by

$$\Omega^h(t) = \Omega_R^h + u^n(t, \Omega_R^h),$$

where Ω_R^h represents the discrete reference domain and u^n the approximate displacement field (4.4). Since the current discrete work piece domain is described by a grid consisting of simplexes S_i, i.e.

$$\Omega^h(t) = \bigcup_{i=1}^{N_S} S_i,$$

solving (3.84) for a $y \in \mathbb{E}(t)$ reduces in case of linear finite elements to the problem of finding the simplex $S(y) \subset \Omega^h(t)$ with

$$y = \sum_{j=1}^{N_n} b_j(S)\mathbf{x}_j(S) \qquad \text{and} \qquad b_j \geq 0, \tag{4.40}$$

where $\mathbf{x}_j(S)$ represents the coordinates of node 'j' of the simplex $S(y)$. The parameter N_n denotes the number of nodes. After having found a simplex $S(y)$, (3.84) can be written as

$$\mathbf{X}(y) = y - \sum_{j=1}^{N_n} b_j(S) u(t, \mathbf{X}_j(S)), \tag{4.41}$$

where $\mathbf{X}_j(S)$ represents the nodes of simplex $S(y)$ in the reference configuration. Extending the above formula to elements $y \in \mathbb{E}(t)$ not being in $\Omega^h(t)$ finally leads to

$$\mathbf{X}(y) = \begin{cases} y & \text{if } y \notin \Omega^h(t_i), \\ y - \sum_{j=1}^{N_n} b_j\left(S(y)\right) u^n\left(t, \mathbf{X}_j(S(y))\right) & \text{otherwise.} \end{cases} \tag{4.42}$$

The set of cutting edge points incorporating the work piece deformations at time t can now be written as

$$\mathbb{T}(t) = \{\mathbf{X}(y) | y \in \mathbb{E}(t)\}. \tag{4.43}$$

With a discretisation of the tooth period k, i.e.

$$I^k = \left(t_1^k = (k-1)\tau, t_2^k = t_1^k + \Delta t, \ldots, t_{N_\tau}^k = k\tau\right),$$

the set of points describing the entire tooth path incorporating the work piece deformations reads

$$\mathbb{T} = \bigcup_{t \in I^k} \mathbb{T}(t). \tag{4.44}$$

In a last step the points contained in $\mathbb{T}$ can be connected by a suitable triangulation to obtain the approximation of Ω_c, i.e. Ω_c^h. An example for Ω_c^h is illustrated in Figure 4.3.

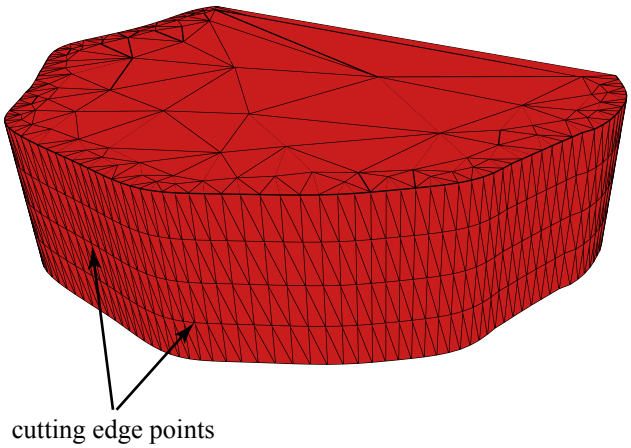

Figure 4.3: Tooth path volume constructed from $\mathbb{T}$.

Constructing the polyhedral work piece domain

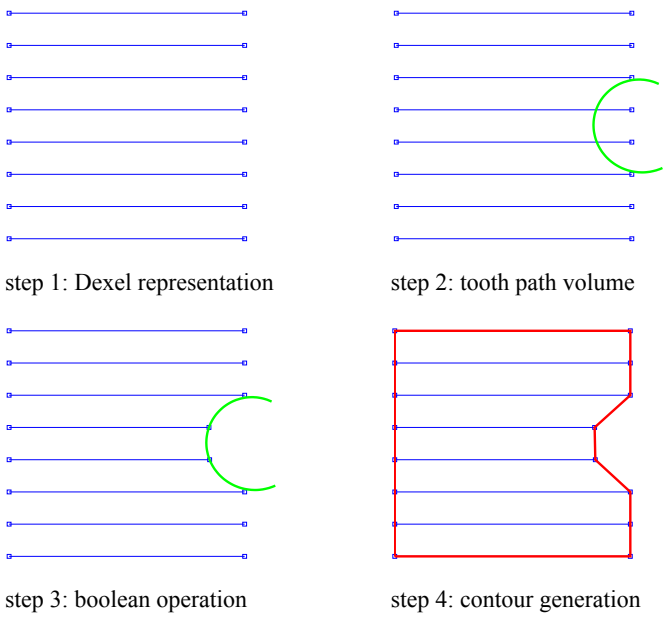

Figure 4.4: Scheme of boolean operation.

After the construction of the approximate tooth path domain Ω_c^h, the new polyhedral work piece domain $\Omega_R^{h,new}$ can be calculated implementing (3.86) on a discrete level, i.e.

$$\Omega_R^{h,new} = \Omega_R^h \setminus \Omega_c^h, \tag{4.45}$$

where Ω_R^h denotes a given polyhedral domain. Among the available methods discussed above, the uni directional Dexel representation described in [114] has been chosen in the present work to carry out the material removal simulation. Starting

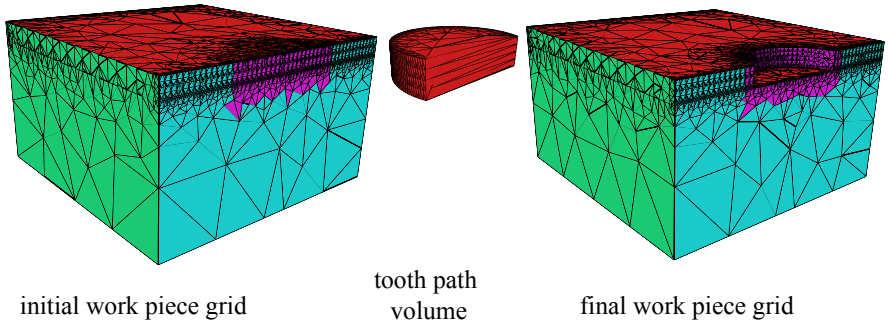

Figure 4.5: Illustration of the actual Boolean operation (left: initial grid, middle: tooth-path volume, right: new grid).

from the given domain Ω_R^h, i.e. the work piece grid on the left in Figure 4.5, the corresponding Dexel representation can be computed tracing rays in x-direction as shown in 4.2. The result is a set of Dexels organised on rays on a y-z-grid. Figure 4.4 (step 1) shows such a set of Dexels on the x-y-plane. The next step is the Boolean operation. Computing for each Dexel the section intersecting with Ω_c^h and subtracting this section from the original Dexel gives a new set of set of Dexels representing the work piece after the Boolean operation (see Figure 4.4, step 3). Note that the intersection of each Dexel and Ω_c^h can be computed efficiently because Ω_c^h is given as a polyhedral domain. After the Boolean operation, the new polyhedral work piece domain has to be constructed from the modified set of Dexels. To this end, contours are generated from the Dexels on each x-y-plane performing the operations described in [114], i.e.

- grouping of the Dexels on two adjacent rays,
- connecting adjacent Dexel points inside each group,
- creating a connection table to record the connections,
- traversing the connection table to construct the contours.

For the present example the result of the contour generation process is shown in Figure 4.4, step 4. Finally, the polyhedral domain representing the new work piece $\Omega_R^{h,new}$ can be constructed by tiling the contours on each x-y-plane using the algorithm proposed in [25] and employing the mesh generator *tetgen* (see e.g. [89, 90]). The result of the material removal operation is illustrated in Figure 4.5.

Discretisation error and uncut chip thickness

The number of rays employed for the work piece representation affects the accuracy of the computed uncut chip thickness. In order to illustrate this effect, consider a rigid block like work piece ($20 \times 20 \times 10$ mm^3) being machined by a rigid tool with diameter D=8 mm. The results of the corresponding milling simulations is illustrated in Figure 4.6. Especially for the coarse ray grid, i.e. 40×5 rays, large errors occur in the computed uncut chip thickness when the tool enters and leaves the

cut. Moreover, small oscillations can be observed during the entire cutting period. As shown in the diagrams corresponding to finer grids, i.e. 160×5 and 640×5, increasing the number of rays in y-direction reduces the error to an acceptable level. A possible remedy is to employ Tri-Dexel models as discussed in [112]. Since these models involve rays in all spatial directions, they provide more detailed information about the new surface constructed by performing the Boolean operation.

4.4.2 Transferring the solution to the new work piece grid

After the simulation of a single tooth period and the construction of a new discrete work piece domain $\Omega_R^{h,new}$, the solution, i.e. the velocity field $u_t^n(t, \mathbf{X})$, the displacement field $u^n(t, \mathbf{X})$ and the discrete temperature field $\Theta^n(t, \mathbf{X})$, given with respect to the old discrete domain Ω_R^h has to be transferred to the new grid $\Omega_R^{h,new}$. As outlined in Section 4.3, the new values of $u_{tt}^n(t, \mathbf{X})$ and $\Theta_t^n(t, \mathbf{X})$, can be calculated from the transferred fields solving the linear system (4.35a) – (4.35b). Since the new domain is a subset of the old one, i.e. $\Omega_R^{h,new} \subset \Omega_R^h$, the solution transfer can be accomplished by means of grid to grid interpolation (for algorithmic details, see e.g. [62, pp.245]).

Alternatively, the solution can be projected from the old to the new grid solving for each field a minimisation problem. For the displacement field u^n the minimisation problem reads

$$u^{n,new} = \underset{u \in V_n(\Omega_R^{new})}{\operatorname{argmin}} \frac{1}{2} \|u - u^n\|^2_{Y(\Omega_R^{new})}, \tag{4.46}$$

where u^n denotes the solution on the old grid. The general space $Y(\Omega_R^{new})$ can be chosen as $Y(\Omega_R^{new}) = L^2(\Omega_R^{new})$, $Y(\Omega_R^{new}) = H^1(\Omega_R^{new})$ or $Y(\Omega_R^{new}) = A(\Omega_R^{new})$, where $\|.\|_{A(\Omega_R^{new})}$ denotes the norm induced by the bilinear form

$$a[u, v] = \int_{\Omega_R^{new}} \sigma(u) : \varepsilon(v) d\mathbf{X}. \tag{4.47}$$

In the discrete case, the necessary condition corresponding to (4.46) can be written as a linear system where the given solution u^n appears in an integral on the right hand side. In order to evaluate this integral, the solution given on the old grid has to be interpolated to the Gauss points of the new grid. This requires, in contrast to the grid to grid interpolation, a more sophisticated interpolation algorithm that is currently not implemented in the employed simulation framework.

Due to the lack of an efficient interpolation algorithm for the projection approach, the grid to grid interpolation has been chosen for the present application. The projection approach, however, is, due to free choice of norm induced by $Y(\Omega_R^{new})$, more flexible and seems to be the better choice for future problems, provided that an efficient implementation is available. Instead of optimally projecting the displacement by choosing $Y(\Omega_R^{new}) = L^2(\Omega_R^{new})$, it might be desirable to conserve the energy of the system employing an energy norm for the projection.

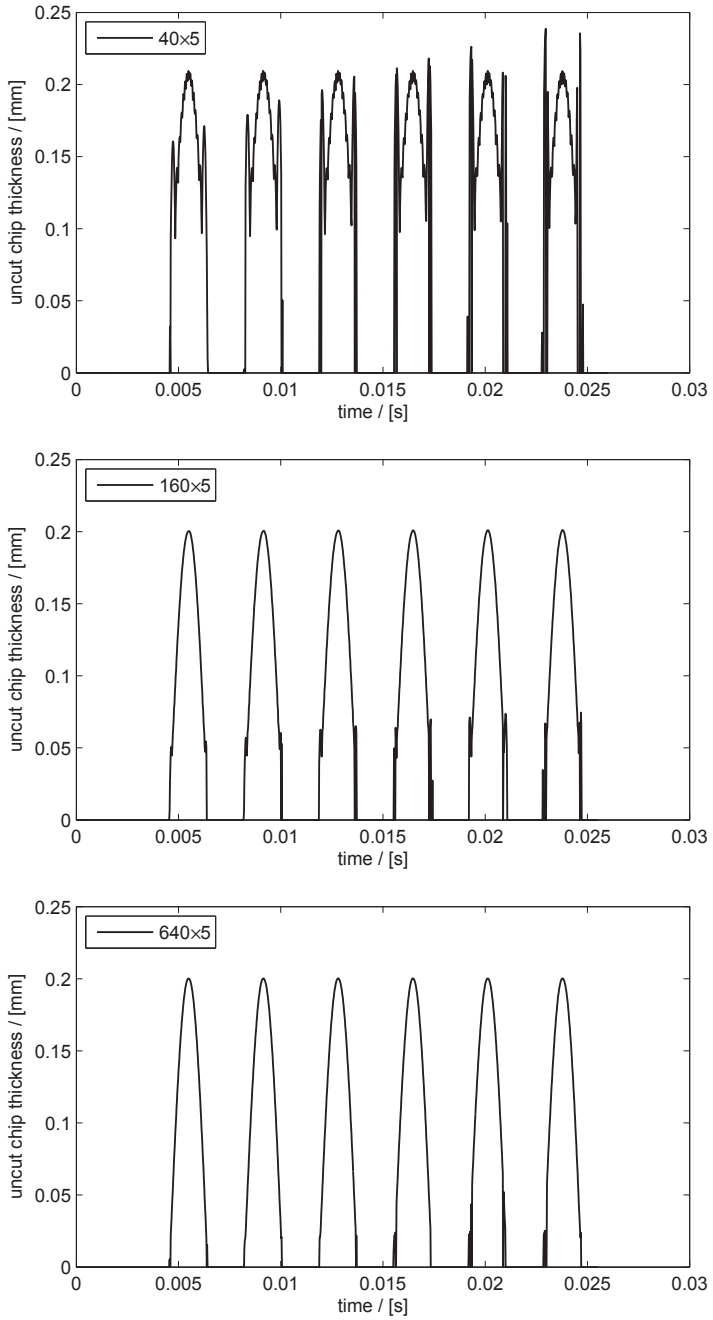

Figure 4.6: Evolution of the uncut chip thickness for different ray grids.

Chapter 5

Numerical simulations in time domain

5.1 Model hierarchy

The different aspects of the milling model (3.83a)–(3.83e) developed in Chapter 3 shall be discussed by analysing the following hierarchy of models, i.e.

1. flexible machine and rigid work piece (Section 5.2),
2. flexible machine and damped elastic work piece (Section 5.3),
3. flexible machine and damped thermo–elastic work piece (Section 5.4).

The first approach illustrates the instabilities caused by the machine system. The corresponding system can be derived from general model setting the work piece deformations to zero and the temperature to the reference value T_0. The temperature effects in the cutting force model can be suppressed choosing the fit parameters in (3.57) as $b = 1$ and $c = 1/T_0$.

If a flexible work piece is involved in the milling process, work piece oscillations may cause instabilities. Such effects can be simulated employing the second approach involving a flexible machine and a damped elastic work piece. As before, the temperature is set to the reference temperature T_0 and the parameters in (3.57) are chosen as $b = 1$ and $c = 1/T_0$.

Undesired temperature effects, like thermal expansion, high work piece temperatures as well as the temperature induced variations of the stability limits, can be analysed considering the third approach involving the flexible machine and a thermo–elastic work piece.

5.2 Rigid work piece

5.2.1 Choosing the process parameters

As discussed in Section 5.1, the rigid work piece approach allows to analyse the effects arising from the machine system. The abstract oscillator chain MDOF milling

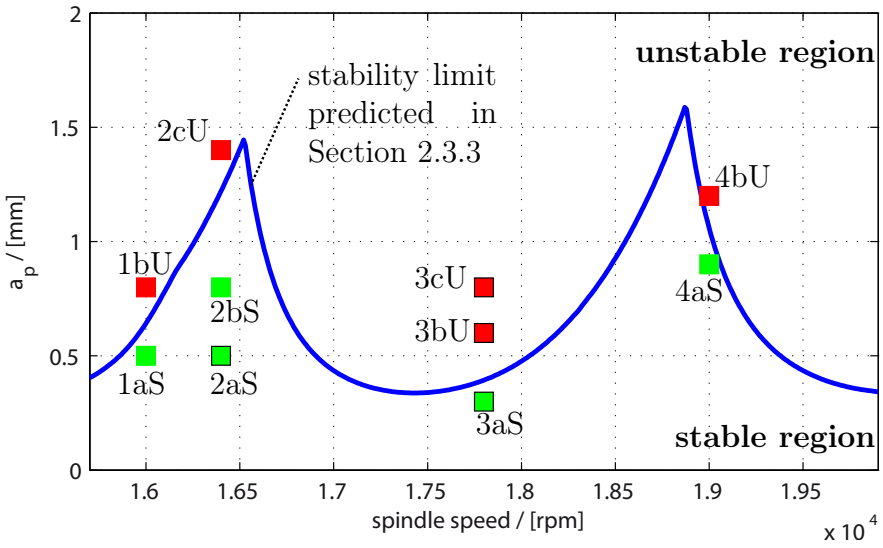

Figure 5.1: Stability lobe diagram indicating the process parameters corresponding to the simulations with rigid work piece.

model employed for the stability analysis in Section 2.3.3 has been developed based on an experimental mobility FRF measured at the TCP of the milling machine employed for the cutting tests in the present work (see Chapter 6). Since the complex multi body system has been developed based on the same experimental data, i.e. the measured mobility FRF, both models present similar dynamical characteristics at the TCP (recall that the oscillator chain model reproduces the dynamical characteristics corresponding to the TCP only). Consequently, the stability limits corresponding to the approach involving a flexible machine and a rigid work piece are expected to be similar to those predicted with the oscillator chain MDOF system discussed in Section 2.3.3.

The objective of the present section is therefore to verify this presumption. To this end, consider the stability boundary computed with the rigorous stability analysis method for the oscillator chain model and select particular process parameters close this boundary corresponding to the points 1aS, 1bU, 2aS, 2bS, 2cU, 3aS, 3bU, 4aS, 4bU shown in Figure 5.1. Preforming time domain simulations with the multi body machine model for each set of process parameters reveals, together with an heuristic stability criterion (see Section 5.2.2), the stability characteristics of milling model involving the complex multi body system. If the processes corresponding to the parameter sets 1bU, 2cU, 3bU, 3cU, 4bU are unstable and if the processes corresponding to the parameter sets 1aS, 2aS, 2bS, 3aS, 4aS are stable, it can be concluded that the milling model involving the complex multi body system properly reproduces the expected the stability characteristics.

5.2.2 Identifying unstable processes

The characteristics of a milling process can be analysed considering the uncut chip thickness and the resulting cutting force acting on the work piece. As discussed in

Section 2.1.5, the evolution of the uncut chip thickness provides information about the process stability. In case of unstable processes, the uncut chip thickness does not approach a stationary evolution. Additional oscillations superimposed on the stationary evolution become perceivable and do not vanish until the end of the simulation. In case of stable processes the chatter vibrations decay and the uncut thickness converges to the stationary evolution.

The cutting forces acting on the work piece can be either determined by integrating in each time step (3.80) over the approximate work piece domain Ω_R^h, i.e.

$$\mathbf{F}(t) = \int_{\Omega_R^h} \hat{\varrho}_0 s_m^e(t) dX, \tag{5.1}$$

or by integrating in each time step (3.62) along the cutter axis and transforming the result into the global reference frame, i.e.

$$\mathbf{F}(t) = -A_{ot}(t) \int_0^{a_p} \tilde{R}(t, \zeta^*) d\zeta^*. \tag{5.2}$$

Dividing the x-component of the computed cutting force $\mathbf{F}$ by the corresponding axial depth of cut and transforming the obtained value in frequency domain by means of a fast Fourier transform (FFT) leads to the relative force spectrum illustrated, for example, in Figure 5.3. The peaks are located at multiples of the tooth passing frequency. In order to distinguish the peaks appearing at multiples of the tooth passing frequency and the peaks appearing in between, red squares indicate multiples of the tooth passing frequency. Moreover, note that, due to the interrupted cutting, the cutting force can be interpreted as a multi frequency excitation, even in the stable case. Consequently, the relative cutting force spectrum usually involves a peak located at the tooth passing frequency and additional peaks appearing at multiples of the tooth passing frequency. Moreover, the relative cutting force spectrum indicates unstable processes as well. If additional peaks occur between the peaks corresponding to multiples of the tooth passing frequency, the process is considered as unstable (see e.g. [91]).

5.2.3 Example 1aS

The process parameters corresponding to example 1aS are $a_p = 0.5$ mm and $n = 16000$ rpm. As indicated in Figure 5.1, the process corresponding to this set of parameters is located below the limit and has therefore been predicted as stable. The evolution of the uncut chip thickness illustrated in Figure 5.2 confirms the presumption. The facts that the initial perturbations vanish after the first few tooth periods and that the uncut chip thickness approaches a stationary evolution clearly indicate a the the simulated process is stable. In addition, the squares indicating multiples of the tooth passing frequency in relative cutting force spectrum (see Figure 5.3) are located on top of each peak and no additional chatter peaks appear in between. From these facts it can be concluded the process corresponding to the set of parameters 1aS is stable.

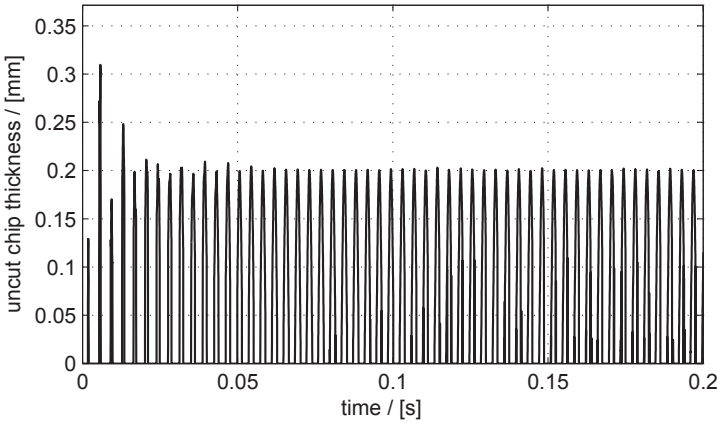

Figure 5.2: Evolution of the uncut chip thickness for example 1aS.

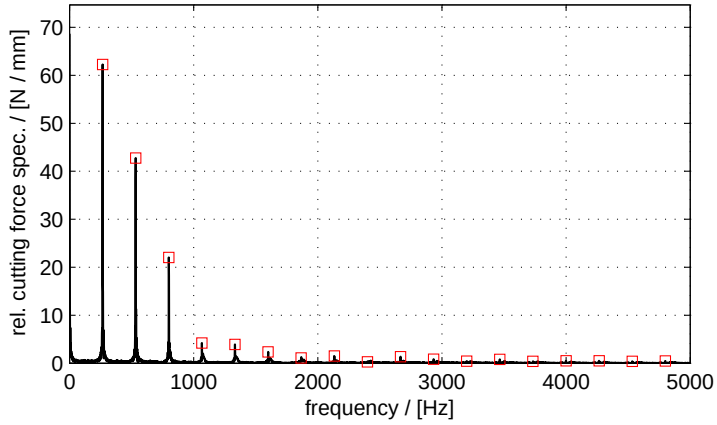

Figure 5.3: Relative cutting force spectrum for example 1aS.

5.2.4 Example 1bU

The process parameters corresponding to example 1bU are $a_p = 0.8$ mm and $n = 16000$ rpm. As indicated in Figure 5.1, the process corresponding to this set of parameters is located above the limit and and should therefore lead to unstable cutting conditions. The evolution of the uncut chip thickness illustrated in Figure 5.4 confirms the presumption. Even though the initial perturbations converge at the beginning, the magnitude of the of the uncut chip thickness increases after the tool has been fully immersed and remains on a high level for the rest of the simulation. In contrast to example 1aS, additional chatter peaks appear in relative cutting force spectrum (see Figure 5.5) between the tooth passing peaks marked with squares. The chatter peaks at 2005 Hz, 2274 Hz, 2539 Hz, 2805 Hz and 3070 Hz and the evolution of the uncut chip thickness reveal that the corresponding process is unstable.

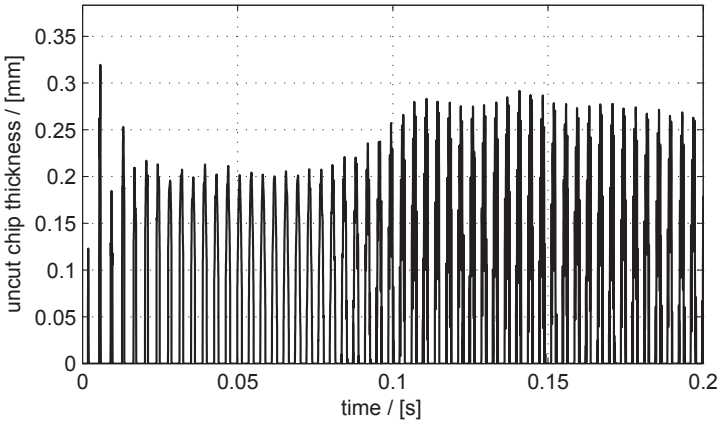

Figure 5.4: Evolution of the uncut chip thickness for example 1bU.

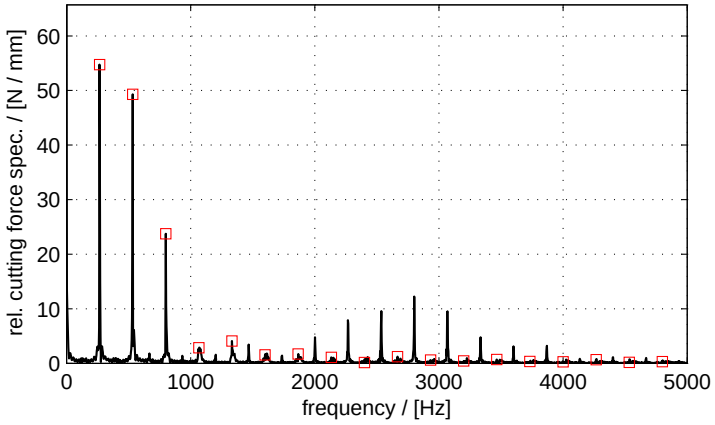

Figure 5.5: Relative cutting force spectrum for example 1bU.

5.2.5 Example 2aS and 2bS

The process parameters corresponding to examples 2aS and 2bS are $n = 16400$ rpm, $a_p = 0.5$ mm and $a_p = 0.8$, respectively. As indicated in Figure 5.1, the processes corresponding to these sets of parameters are located below the stability boundary and have therefore been predicted as stable. The evolutions of the uncut chip thickness illustrated in Figure 5.6 and Figure 5.7 confirm the presumptions. The facts that for both examples the initial perturbations vanish after the first few tooth periods and that the uncut chip thickness approaches the stationary evolution, clearly indicate that the simulated processes are stable. Since the squares indicating multiples of the tooth passing frequency in relative cutting force spectrae (see Figure 5.8 and Figure 5.9) are located on top of each peak and no additional chatter peaks appear in between, it can be concluded the processes corresponding to the sets of parameters 2aS and 2bS are stable.

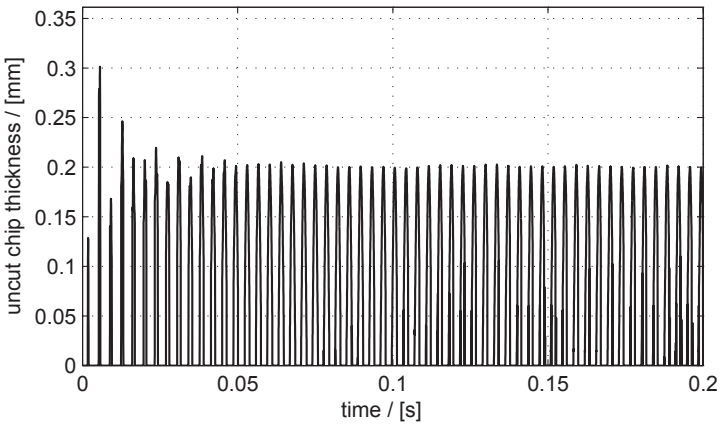

Figure 5.6: Evolution of the uncut chip thickness for example 2aS.

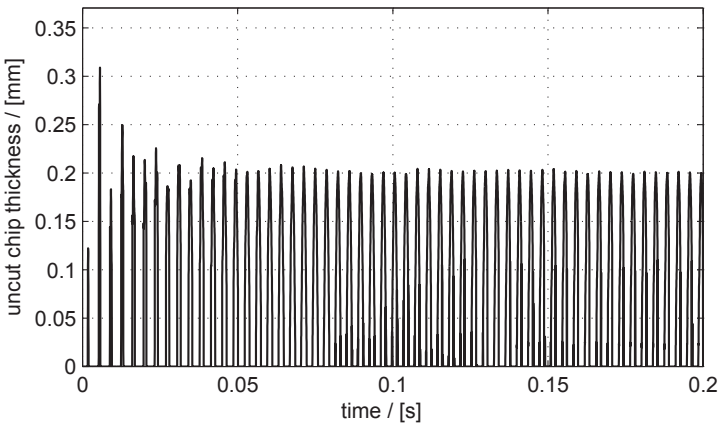

Figure 5.7: Evolution of the uncut chip thickness for example 2bS.

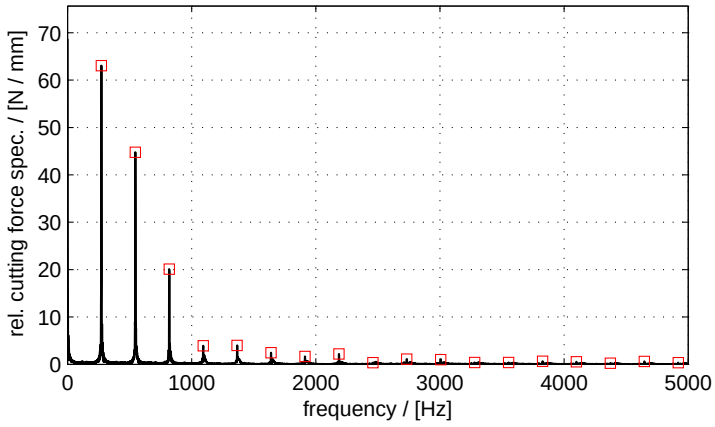

Figure 5.8: Relative cutting force spectrum for example 2aS.

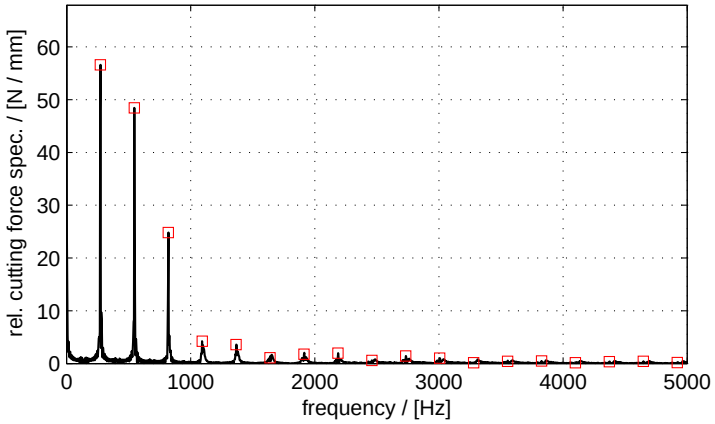

Figure 5.9: Relative cutting force spectrum for example 2bS.

5.2.6 Example 2cU

The process parameters corresponding to example 2cU are a_p=1.3 mm and n = 16400 rpm. As indicated in Figure 5.1, the process corresponding to this set of parameters is located above the limit and has therefore been predicted as unstable. The evolution of the uncut chip thickness illustrated in Figure 5.10 confirms the presumption. Even though the initial perturbations decay at the beginning, the magnitude of the of the uncut chip thickness increases after the tool has been fully immersed and remains on a high level for the rest of the simulation.

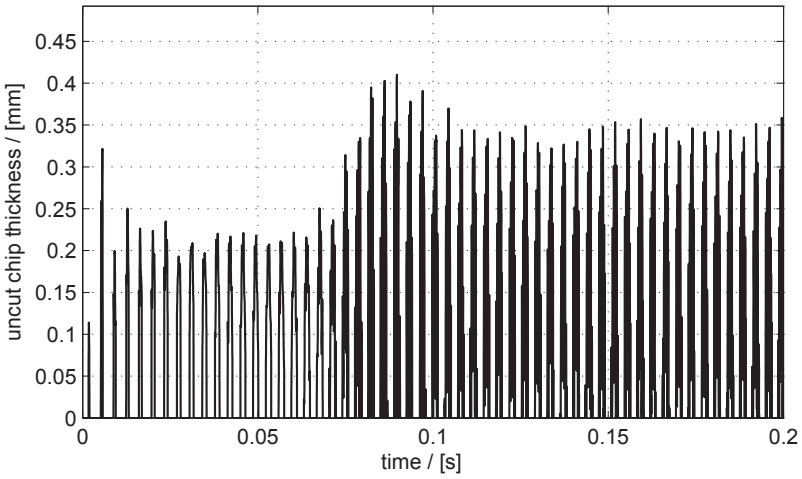

Figure 5.10: Evolution of the uncut chip thickness for example 2cU.

In contrast to examples 2aS and 2bS, additional chatter peaks appear in relative cutting force spectrum (see Figure 5.11) between the tooth passing peaks marked with squares. The chatter peaks at 2014 Hz, 2289 Hz, 2563 Hz, 2832 Hz, 3107 Hz and 3381 Hz and the evolution of the uncut chip thickness reveal that the corresponding process is unstable.

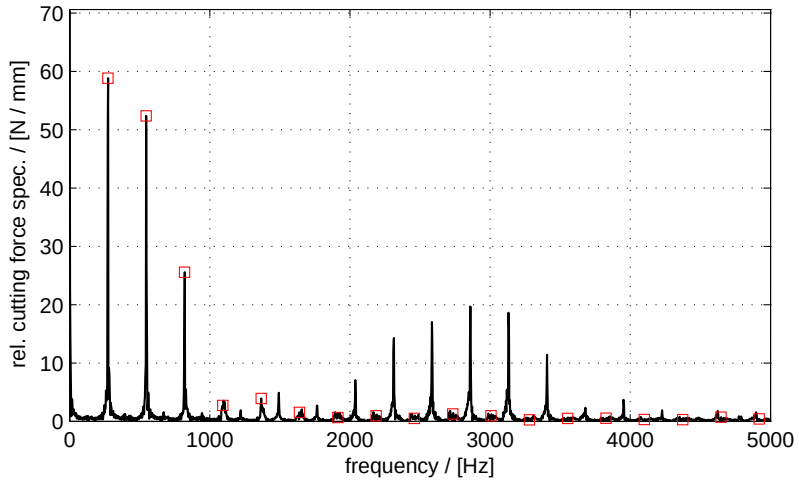

Figure 5.11: Relative cutting force spectrum for example 2cU.

5.2.7 Example 3aS

The process parameters corresponding to example 3aS are $a_p = 0.3$ mm and $n = 17800$ rpm. As indicated in Figure 5.1, the process corresponding to this set of parameters is located below the stability limit and has therefore been predicted as stable. The evolution of the uncut chip thickness illustrated in Figure 5.12 confirms the presumption. The facts that the initial perturbations vanish after the first few tooth periods and that the uncut chip thickness approaches the stationary evolution clearly indicate that the simulated process is stable.

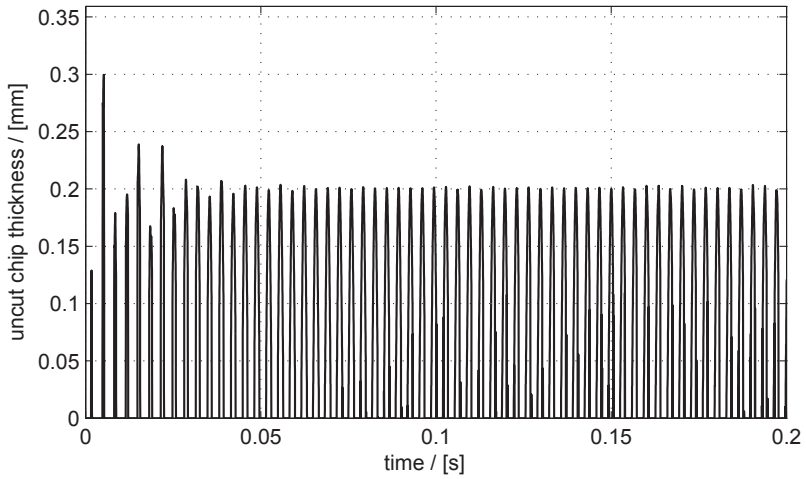

Figure 5.12: Evolution of the uncut chip thickness for example 3aS.

In addition, the squares indicating multiples of the tooth passing frequency in relative cutting force spectrum (see Figure 5.13) are located on top of each peak and no

additional chatter peaks appear in between. From these facts it may be concluded the process corresponding to the set of parameters 3a is stable.

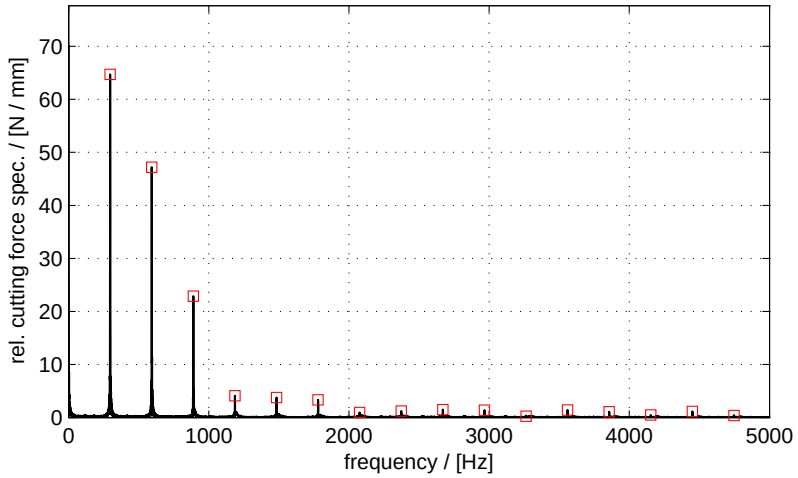

Figure 5.13: Relative cutting force spectrum for example 3aS.

5.2.8 Example 3bU and 3cU

The process parameters corresponding to example 3bU and 3cU are $n = 17800$ rpm, $a_p = 0.6$ mm and $a_p = 0.8$ mm, respectively. As indicated in Figure 5.1, the processes corresponding to these sets of parameters are located above the limit and have therefore been predicted as unstable. The evolution of the uncut chip thicknesses illustrated in Figure 5.14 and Figure 5.15 confirm the presumption.

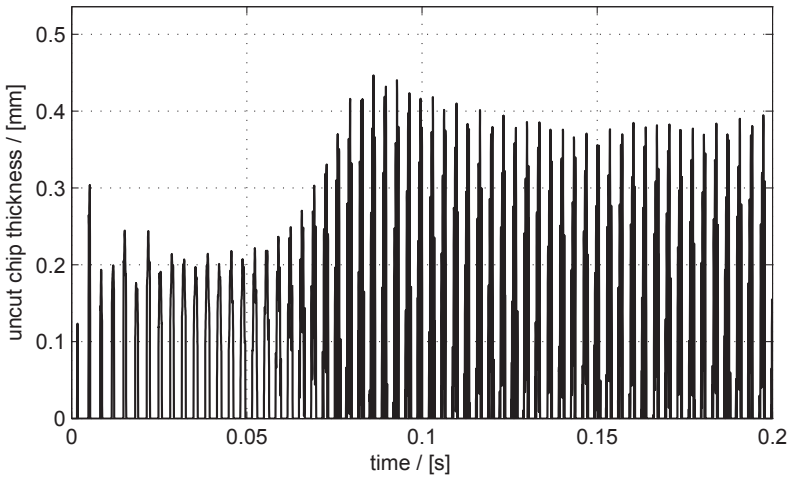

Figure 5.14: Evolution of the uncut chip thickness for example 3bU.

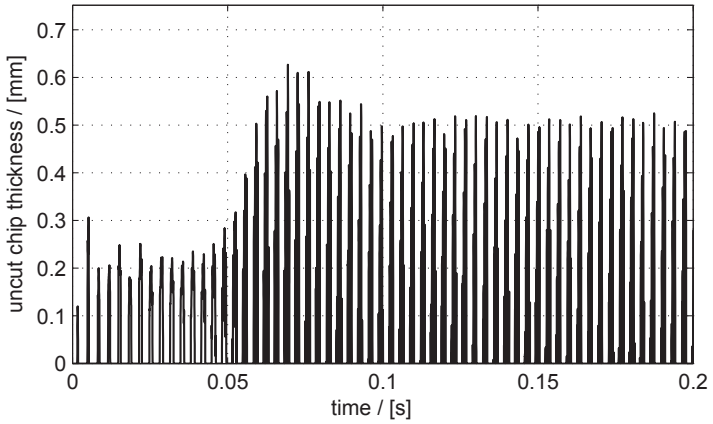

Figure 5.15: Evolution of the uncut chip thickness for example 3cU.

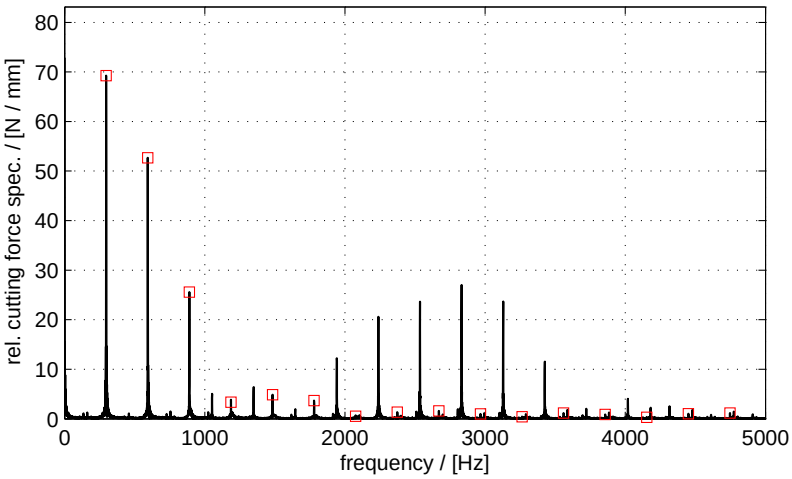

Figure 5.16: Relative cutting force spectrum for example 3bU.

Even though the initial perturbations decay at the beginning, the magnitude of the uncut chip thicknesses increase after the tool has been fully immersed and remain on a high level for the rest of the simulation in both cases. The only difference is that the chatter oscillations corresponding to case 3cU present a larger amplitude as in case 3bU. In contrast to example 3aS, additional chatter peaks appear in relative cutting force spectrae (see Figure 5.16 and Figure 5.17) between the tooth passing peaks marked with squares. The chatter peaks at 1950 Hz, 2246 Hz, 2542 Hz, 2838 Hz, 3137 Hz and 3433 Hz and the evolution of the uncut chip thickness reveal that the corresponding processes are unstable.

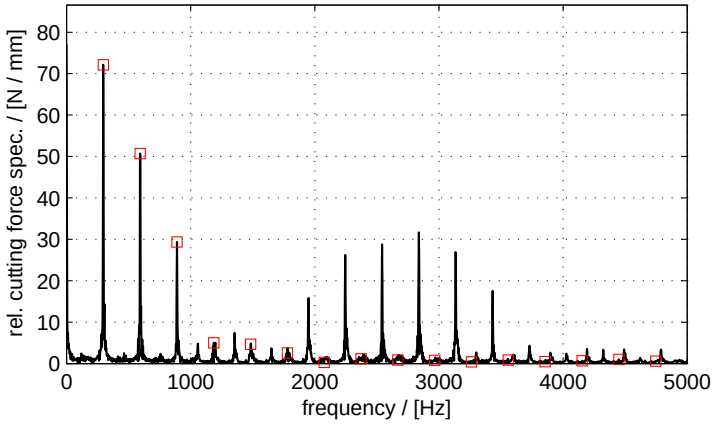

Figure 5.17: Relative cutting force spectrum for example 3cU.

5.2.9 Example 4aS

The process parameters corresponding to example 4aS are $a_p = 0.8$ mm and $n = 19000$ rpm. As indicated in Figure 5.1, the process corresponding to this set of parameters is located below the line indicating the stability boundary and has therefore been predicted as stable. The evolution of the uncut chip thickness illustrated in Figure 5.18 confirms the presumption. The facts that the initial perturbations vanish after the first few tooth periods and that the uncut chip thickness approach the stationary evolution, clearly indicate that the simulated process is stable.

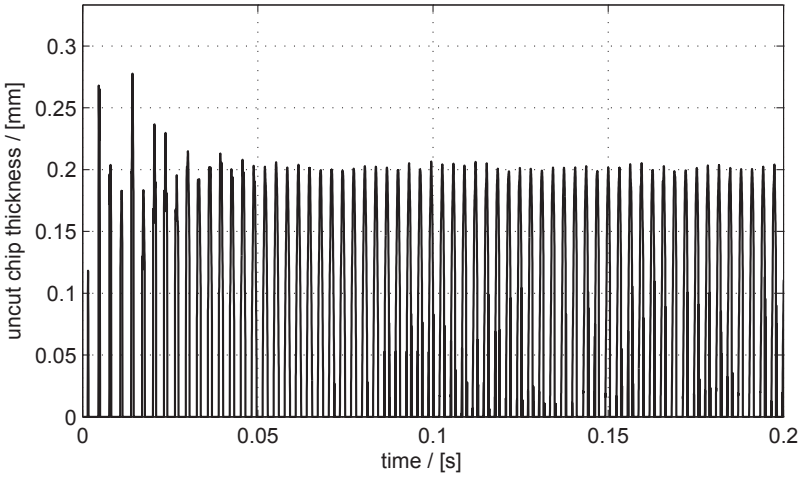

Figure 5.18: Evolution of the uncut chip thickness for example 4aS.

In addition, the squares indicating multiples of the tooth passing frequency in relative cutting force spectrum (see Figure 5.19) are located on top of each peak and no additional chatter peaks appear in between. From these facts it can be concluded the process corresponding to the set of parameters 4aS is stable.

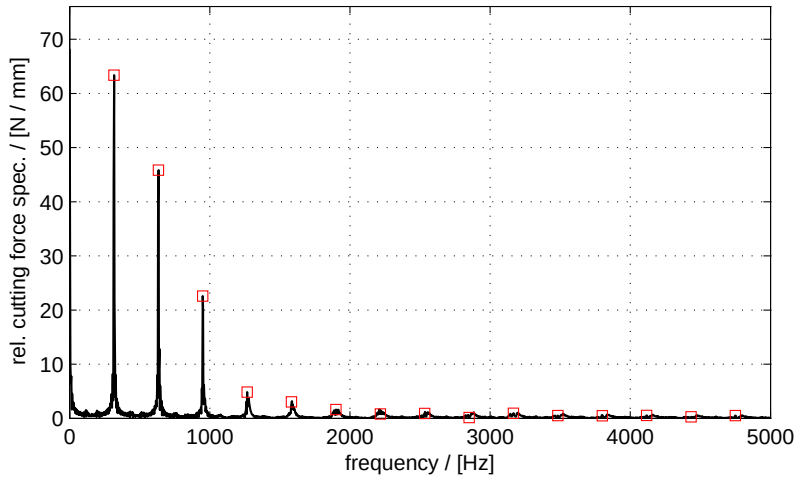

Figure 5.19: Relative cutting force spectrum for example 4aS.

5.2.10 Example 4bU

The process parameters corresponding to example 4bU are $a_p = 1.2$ mm and $n = 19000$ rpm. As indicated in Figure 5.1, the process corresponding to this set of parameters is located above the limit and has therefore been predicted as unstable. The evolution of the uncut chip thickness illustrated in Figure 5.20 confirms the presumption. Even though the initial perturbations decay at the beginning, the magnitude of the of the uncut chip thickness increases after the tool has been fully immersed and remains on a high level for the rest of the simulation.

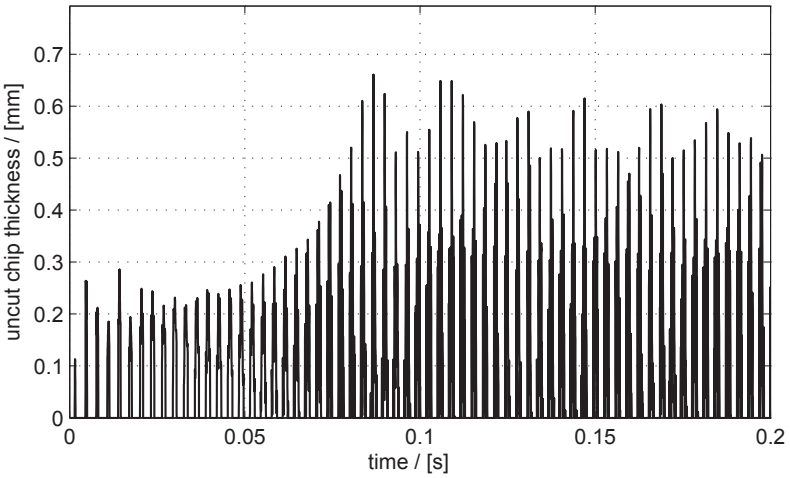

Figure 5.20: Evolution of the uncut chip thickness for example 4bU.

In contrast to example 4aS, additional chatter peaks appear in relative cutting force spectrum (see Figure 5.21) between the tooth passing peaks marked with squares. The chatter peaks at 1950 Hz, 2246 Hz, 2542 Hz, 2838 Hz, 3137 Hz and 3433 Hz

and the evolution of the uncut chip thickness reveals that the corresponding process is unstable.

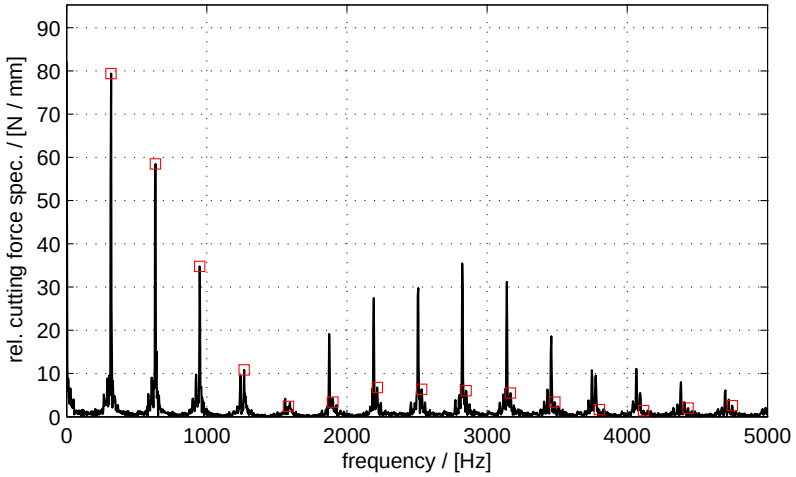

Figure 5.21: Relative cutting force spectrum for example 4bU.

Due to the material removal model, the machined work piece surface is another result of the simulation. In case of exmple 4bU, i.e. an unstable processes, the simulated work piece surface exhibits chatter marks.

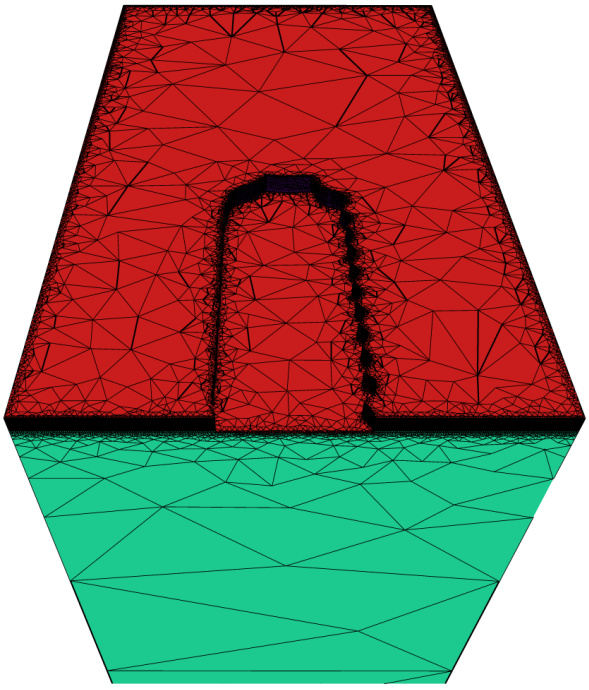

Figure 5.22: A part of the simulated work piece for the slot milling process corresponding example 4bU.

The corresponding work piece grid is illustrated in Figure 5.22 where the wavy

surface on the right part of the milled slot clearly demonstrates the bad surface quality.

5.2.11 Results of the time domain simulations with the multi body machine model and rigid work piece

The results of the time domain milling simulations with the flexible machine and rigid work piece are summarised in Table 5.1.

point No.	n / [rpm]	a_p / [mm]	process behaviour
1aS	16000	0.5	stable
1bU	16000	0.8	unstable
2aS	16400	0.5	stable
2bS	16400	0.8	stable
2cU	16400	1.3	unstable
3aS	17800	0.3	stable
3bU	17800	0.6	unstable
3cU	17800	0.8	unstable
4aS	19000	0.8	stable
4bU	19000	1.2	unstable

Table 5.1: Simulated processes and stability.

The results confirm the presumption that the milling system involving a multi body machine model and a rigid work piece presents approximately the same stability limits as the milling system involving an abstract oscillator chain machine model presented in Section 2.3.3. Note that an experimental validation of the stability limits independently predicted with each model will be presented in Chapter 6.

5.3 Damped elastic work piece

5.3.1 Modelling of work piece damping effects in milling simulations

The work piece in the machining examples considered in the present work, is either directly fixed on the machine table or attached via bolted joints to a rigid support plate which is clamped on the machine table (see Figure 5.23). The work piece is subjected to alternating stresses arising from the material removal during the cutting process. However, in large parts of the work piece the stress intensity is rather small. For the given examples, high stresses only occur in vicinity of the clamping and close to the cutting region. Thermo–elastic effects (transverse thermal currents) being discussed in the appendix D.1.1 and elasto–slip effects occurring in the joints (cf. appendix D.1.2) are therefore the most important damping mechanisms in the work piece. While the first effect can be reproduced by a visco–elastic material model with a tailored relaxation function (cf. appendix D.2), the second and possibly

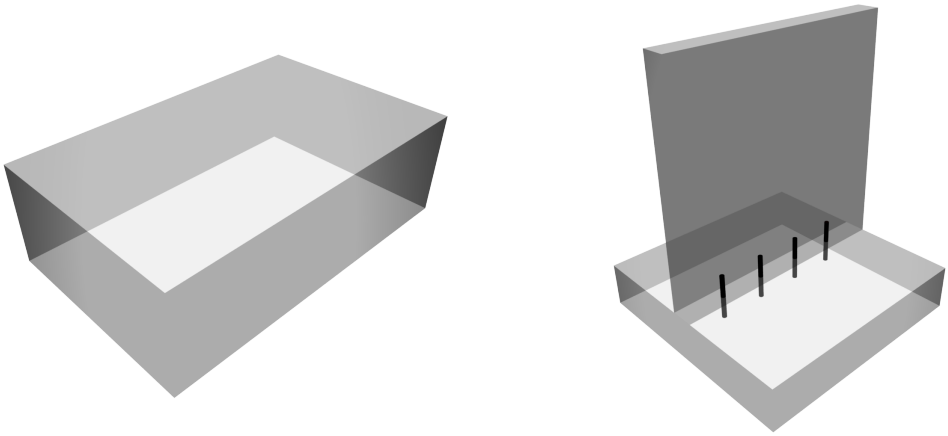

Figure 5.23: Block work piece and supple work piece attached via bolted joints on the support plate.

more important contribution does not fit into the general visco–elastic framework presented in appendix D.

An alternative approach to model the work piece damping is inspired by modal testing problems being discussed, for example, in [32]. Following the arguments presented in [45], the damping matrix $\mathbf{D}$ can be computed on the space discrete level as a linear combination of mass- and stiffness matrix, i.e. with the matrices introduced in (4.5a),

$$\mathbf{D} = a\mathbf{M} + b\mathbf{K}, \tag{5.3}$$

where a and b denote two unknown parameters, that have to be identified from modal testing data. Since the parameters may change for each configuration, the modal damping is not a constitutive law as the models discussed above.

5.3.2 Identification of damping parameters

Modelling of the clamping

The strategy to determine the damping parameters a and b appearing in (5.3) is similar to the approach employed in the identification of the joint parameters in Section 3.3. The effect of the bolted joints shown in Figure 5.23 can be modelled imposing a homogeneous Dirichlet boundary condition on a strip with width w_D on the bottom face of the work piece. Since the parameter w_D and the grid size affect the eigenfrequencies of the undamped, discrete work piece model, i.e. solutions of the eigenvalue problem

$$\mathbf{K}\mathbf{e} = \omega^2\mathbf{M}\mathbf{e}, \qquad \mathbf{e} \neq 0, \tag{5.4}$$

w_D has to be chosen so that the computed eigenfrequencies match those observed in the experiments.

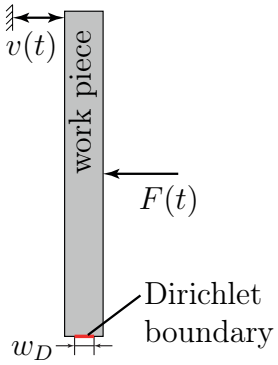

Figure 5.24: Scheme of the setup to determine the mobility FRF of the work piece.

Strategy to identify the damping parameters

The damping parameters can be determined fitting the computed mobility frequency response function of the work piece to the experimental curve. To this end, consider the setup shown in Figure 5.24 and note that for an external force

$$F(t) = \frac{1}{\varepsilon\sqrt{\pi}} \exp\left(-\frac{(t-t_s)^2}{\varepsilon^2}\right) \tag{5.5}$$

applied to a small area on the work piece boundary, the time domain velocity response reads

$$v_y^h(t) = \mathbf{C}_v \dot{\mathbf{d}}_F(t), \tag{5.6}$$

where $\mathbf{d}_F(t)$ is the solution of the discrete work piece equation, i.e.

$$\mathbf{M}\ddot{\mathbf{d}} + (a\mathbf{M} + b\mathbf{K})\,\dot{\mathbf{d}} + \mathbf{K}\mathbf{d} = \mathbf{B}_F F(t). \tag{5.7}$$

The matrix $\mathbf{C}_v$ arises from the discretisation of the integral

$$v_y(t) = \frac{1}{|\Gamma_v|} \int_{\Gamma_v} u_t(t, \mathbf{X}) \cdot \mathbf{n}\, do, \tag{5.8}$$

while the matrix $\mathbf{B}_F$ represents the discrete counterpart of the Neumann boundary condition

$$\int_{\Gamma_F} v \cdot \sigma \cdot \mathbf{n}\, do = \frac{1}{|\Gamma_F|} \int_{\Gamma_F} F(t) v \cdot \mathbf{e}_y\, do, \qquad \forall v \in V, \tag{5.9}$$

where $\mathbf{e}_y$ denotes the unit vector in y-direction. Transforming $v_y^h(t)$ and $F(t)$ in frequency domain gives the mobility FRF depending on the parameters a and b, i.e.

$$H_{wpc}(f, a, b) = \frac{\mathcal{F}[v_y^h](f)}{\mathcal{F}[F](f)}, \tag{5.10}$$

with $\mathcal{F}[.](f)$ denoting the Fourier transform operator. The cost functional measuring the difference between simulation and experiment can be written as

$$J(a, b) = \sum_{k=1}^{N_E} w^k \frac{1}{2} \left(|H_{wpc}(a, b, f_k)| - |H_{wpc}^E(f_k)|\right)^2, \tag{5.11}$$

where $H_{wpc}^E(f)$ represents the experimental mobility FRF. As before, the discrete weight function w^k suppresses critical experimental data. Minimising the cost functional with the restrictions $a \geq 0$ and $b \geq 0$, finally gives an optimal set of parameters a, b determining the damping of the discrete system.

Results

Work piece effects become important especially in the machining of thin walled structures. Since the Rayleigh damping only fits to a particular work piece configuration, it seems to be appropriate to consider the thin walled structure shown in Figure 5.23 for the damping parameter identification and to transfer the results, accepting possible errors, to work pieces with a more rigid structure. The final material and damping parameters for the thin walled work piece with dimensions $100 \times 10 \times 140$ mm^3 are summarised in Table 5.2. The width of the strip corresponding to the homogeneous Dirichlet boundary condition is w_D=2.03 mm.

parameter	value in unit 1	unit 1	value in unit 2	unit 2
$\hat{\varrho}_0$	2.7×10^{-6}	kg/mm^3	2700	kg/m^3
λ	5.108359×10^7	kg/(mm s^2)	51.08359×10^9	N/m^2
μ	2.631579×10^7	kg/(mm s^2)	26.31579×10^9	N/m^2
a	60	1/s	60	1/s
b	3×10^{-6}	s	3×10^{-6}	s

Table 5.2: Material and damping parameters for the thin walled work piece with dimensions $100 \times 10 \times 140$ mm^3 shown in Figure 5.23 and Figure 5.24, respectively.

The corresponding mobility FRF illustrated in Figure 5.25 reveals that the result of the semi-empiric approach is in good agreement with the experimental data[1]. The decay of the peaks and the locations of the antiresonances can be accurately reproduced in the simulation.

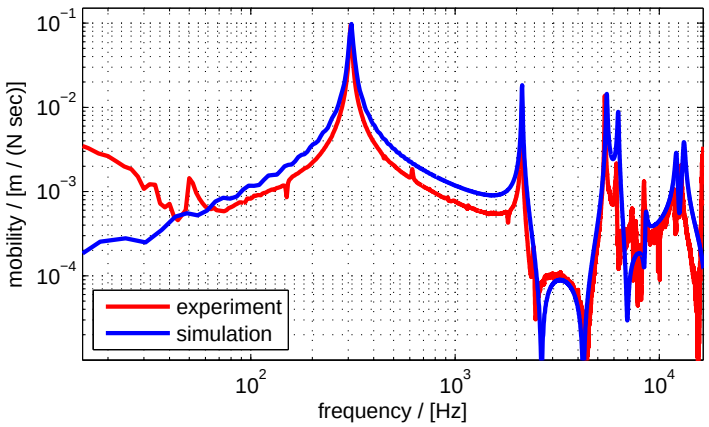

Figure 5.25: Experimental[1] and simulated mobility FRF of the work piece.

[1]The measurements of the work piece mobility FRF have been carried out by P. Rasper under supervision of Prof. E. Uhlmann at IWF, TU-Berlin [104].

5.3.3 Stiff work piece geometry

Effect of a damped elastic work piece with stiff geometry

In many milling applications, the machined work piece presents a stiff structure. Since the compliance of the machine at the TCP is bigger than the compliance of the work piece at the cutting zone, it is expected that the process stability is not affected by the incorporation of work piece vibrations. In order to analyse the presumed effects in detail, the objective of this section is to present the results obtained in the resimulation of the example processes 2aS, 3aS, 3bU and 3cU considered in Section 5.2 employing now a milling system involving the multi body machine model and a block like damped elastic work piece with dimensions $50 \times 30 \times 70$ mm^3 and material parameters as given in Table 5.2.

Example 2aS with damped elastic work piece

The evolution of the uncut chip thickness depicted in Figure 5.26 confirms the presumption from above. As in the rigid work piece example, the uncut chip thickness approaches after the initial perturbations the stationary evolution, a fact, that indicates a stable process.

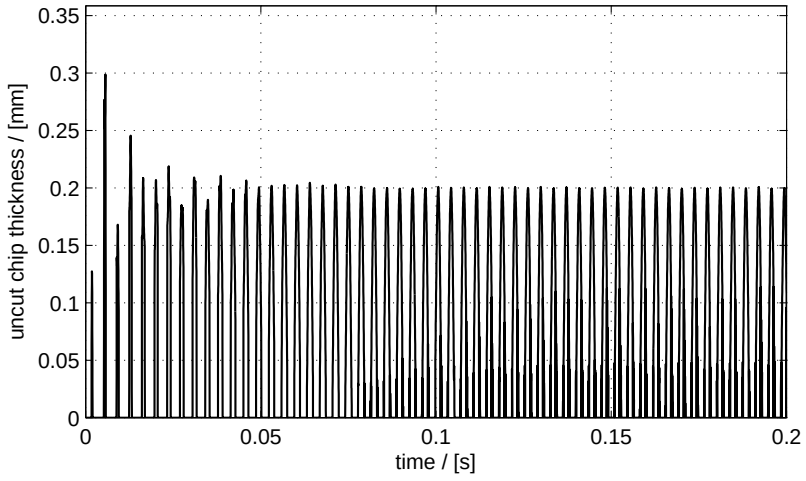

Figure 5.26: Evolution of the uncut chip thickness corresponding to example 2aS with stiff elastic work piece structure.

The analysis of the relative cutting force spectrum illustrated in Figure 5.27 reveals that the simulated process is stable. Similar to the rigid work piece example, no chatter peaks arise between the peaks located at multiples of the tooth passing frequency.

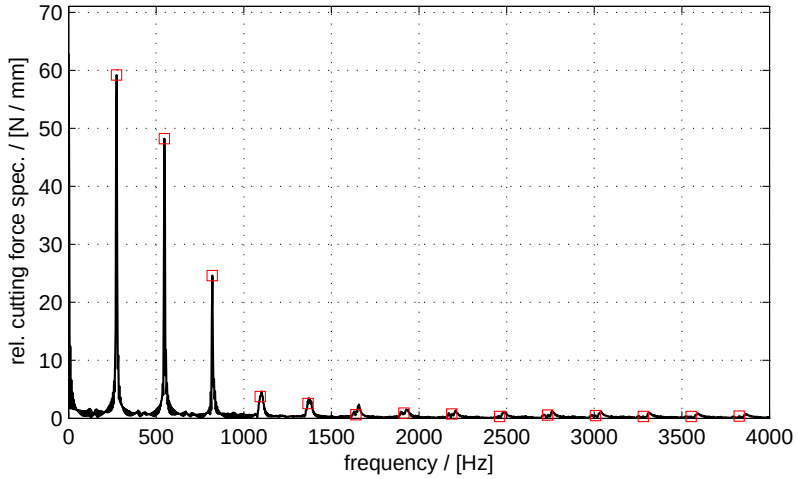

Figure 5.27: Relative cutting force spectrum corresponding to example 2aS with a stiff elastic work piece structure.

Example 3aS with damped elastic work piece

The evolution of the uncut chip thickness depicted in Figure 5.28 shows the same evolution as the uncut chip thickness computed for example 3aS with a rigid work piece. As before, the uncut chip thickness approaches after the decay of the initial perturbations the stationary evolution, a fact, that indicates a stable process.

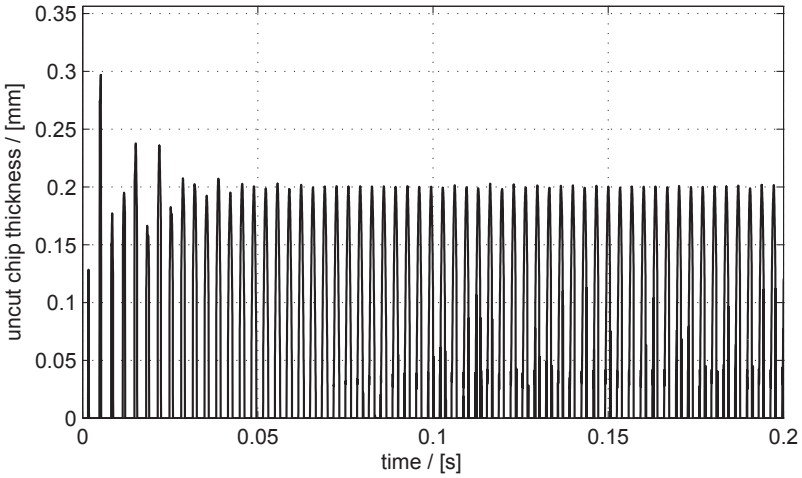

Figure 5.28: Evolution of the uncut chip thickness corresponding to example 3aS with stiff elastic work piece structure.

The analysis of the relative cutting force spectrum illustrated in Figure 5.29 confirms the conclusion drawn from the evolution of the uncut chip thickness. As in the rigid work piece example, no chatter peaks arise between the peaks located at multiples of the tooth passing frequency.

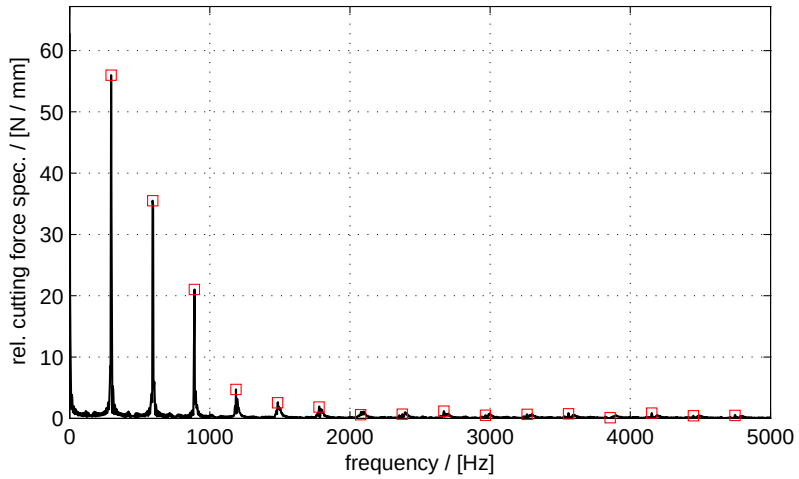

Figure 5.29: Relative cutting force spectrum corresponding to example 3aS with a stiff elastic work piece structure.

Example 3bU and 3cU with damped elastic work piece

The sets of process parameters 3bU and 3cU (see 5.1) correspond to unstable cutting conditions. The uncut chip thicknesses illustrated in Figure 5.30 and Figure 5.31 shows a similar evolution as in the rigid work piece example (see Figure 5.14). The uncut chip thickness does not converge to the stationary evolution but increases noticeably after a short decay at the beginning and remains on a high level until the end of the simulation. As mentioned before, this is a clear indicator for unstable processes and chatter.

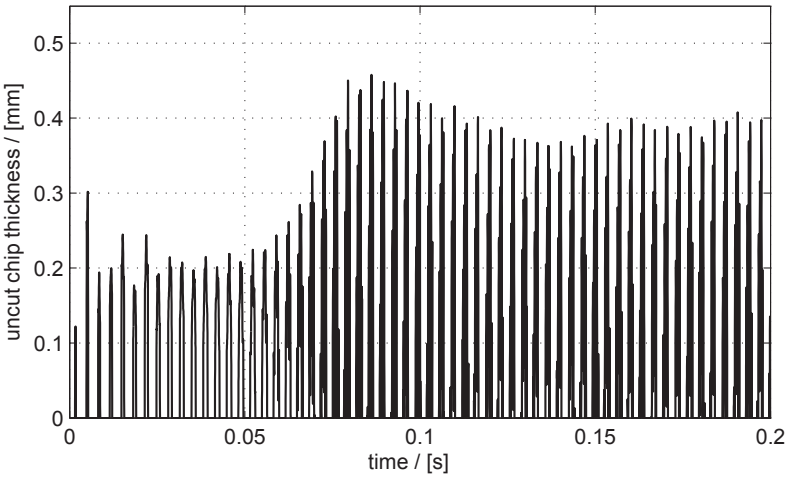

Figure 5.30: Evolution of the uncut chip thickness corresponding to example 3bU with stiff elastic work piece structure.

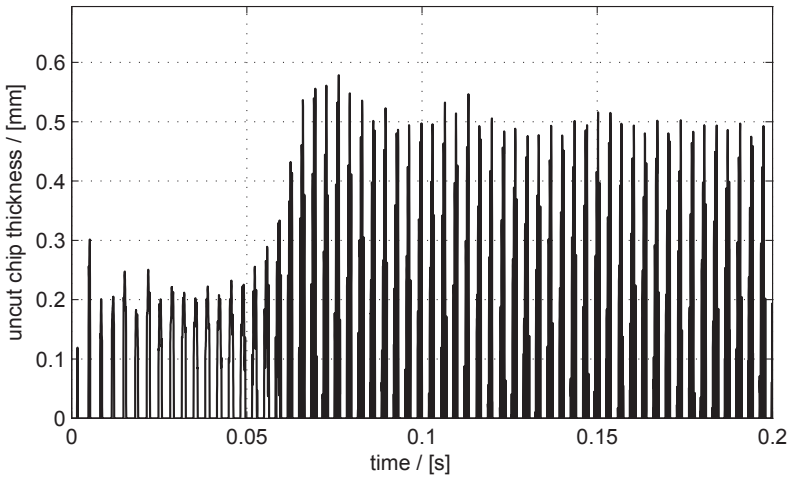

Figure 5.31: Evolution of the uncut chip thicknesses corresponding to example 3cU with stiff elastic work piece structure.

As expected from the rigid work piece example, additional chatter peaks appear in the relative cutting force spectrae depicted in Figure 5.32 and Figure 5.33, a phenomenon finally confirming that the corresponding processes are unstable.

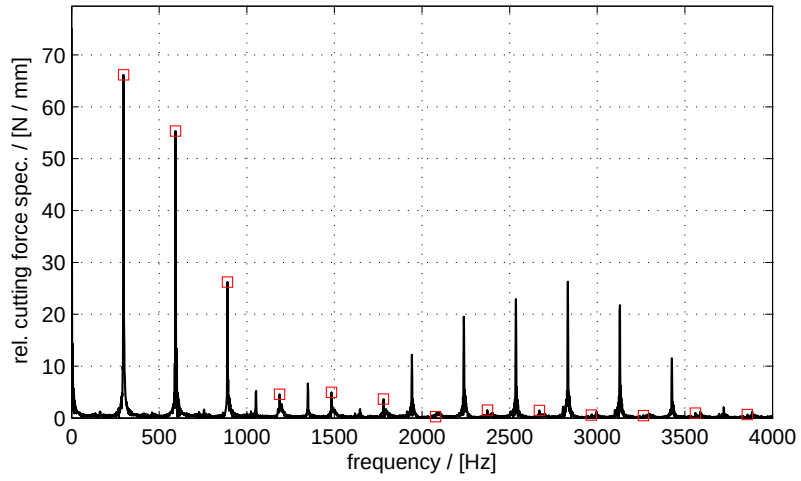

Figure 5.32: Relative cutting force spectrum corresponding to example 3bU with a stiff elastic work piece structure.

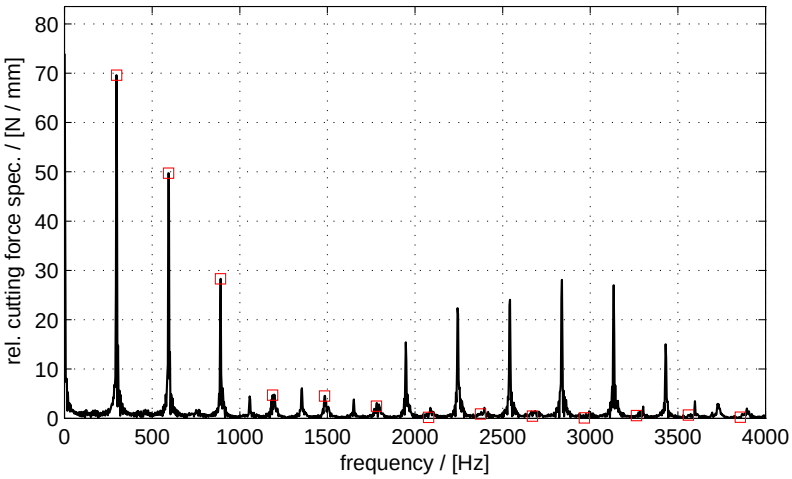

Figure 5.33: Relative cutting force spectrum corresponding to example 3cU with a stiff elastic work piece structure.

Remarks on the simulation results employing a stiff damped elastic work piece

The simulation results presented in this section confirm the presumption that employing, instead of a rigid work piece, a stiff damped elastic work piece does not affect the stability characteristics of the milling system. No appreciable differences can be discovered comparing the evolutions of the uncut chip thickness and the corresponding relative cutting force spectrae for both work piece models. Since the stiff damped elastic work piece presents a small compliance at the cutting zone the work piece reactions related to the cutting forces are very small compared to the reactions of the tool. Consequently, the machine-tool system dominates the dynamical characteristics of the whole system and the work piece effects can be neglected in case of a stiff work piece structure.

5.3.4 Supple work piece structure

In the preceding section it has been shown that a stiff work piece structure does not noticeably affect the process stability. The evolution of the uncut chip thickness and the relative cutting force spectrum are similar to the results from the rigid work piece examples. However, a supple work piece geometry may lead to instabilities. In order to illustrate this effect, choose process parameters as in example 2aS, i.e. $a_p = 0.5$ mm and $n = 16400$ rpm, previously identified as stable, and simulate the process utilising the supple work piece with dimensions $100 \times 10 \times 140$ mm^3 introduced in Section 5.3.2. Especially on top, the supple work piece exhibits a high compliance that can destabilise the previously stable milling process. Analysing the evolution of the uncut chip thickness illustrated in Figure 5.34 reveals that the process does not converge to a stationary regime. Large work piece oscillations lead to an increasing uncut chip thickness and thus to increasing cutting forces.

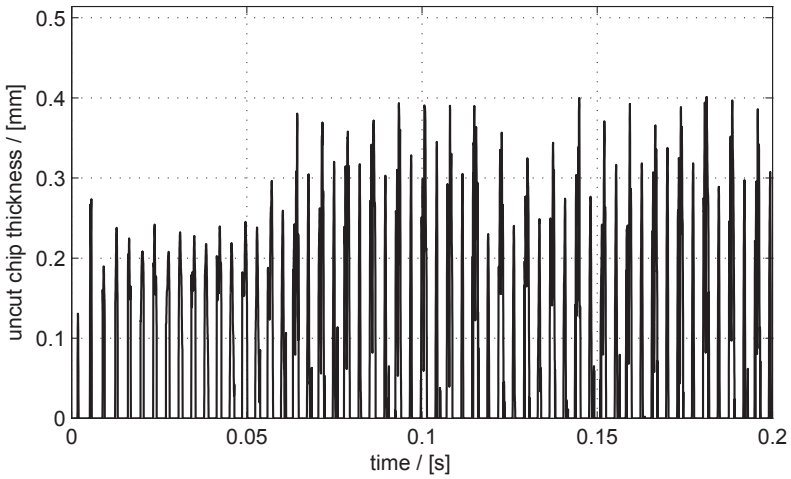

Figure 5.34: Evolution of the uncut chip thickness corresponding to example 2aS with a supple elastic work piece structure.

The additional chatter peaks appearing in the relative force spectrum shown in Figure 5.35 clearly indicate that the corresponding process is unstable. In contrast to example 3bU with stiff elastic work piece, the highest chatter peak is not located 2834 Hz at but at 136 Hz. Thus, the weak spot in the machine and work piece assembly leading to chatter vibrations is not the machine as in example 3bU and 3cU, but the supple work piece structure.

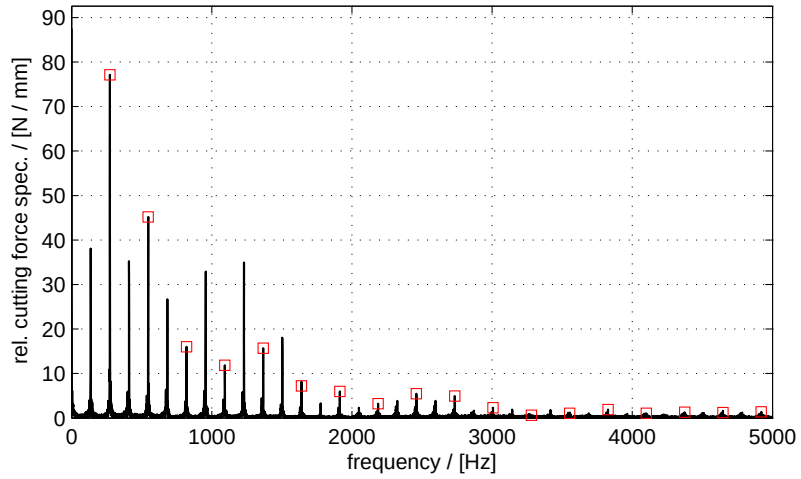

Figure 5.35: Relative cutting force spectrum corresponding to example 2aS with a supple elastic work piece structure.

5.4 Damped thermo–elastic work piece

5.4.1 Identification of the additional empirical parameters in the cutting force model

The modified cutting force model presented in Section 3.5 involves two additional parameters to incorporate the work piece temperature. Similar to cutting force coefficients, the parameters b and c appearing in (3.57) can be determined solving a least squares problem.

Experiments

The cutting force measurements have been performed at the Department of Production Technology and Factory Management (IWF) of Technische Universität Berlin by P. Rasper under the supervision of Prof. E. Uhlmann. A short summary, the main results and further references concerning the experimental studies can be found, for example, in [43]. The cutting forces measured during three different stable processes represent the experimental data for the identification procedure. For the measurements of first data set, the work piece temperature was equal to the ambient temperature, i.e. 25°C. Before the second and the third cutting test, the work piece was heated up by means of a heating plate to 50°C and to 100°C, respectively. The main observation in the cutting tests was that the cutting forces decrease with the preheating of the work piece. Further tests revealed that the experimental stability limit slightly increased in case of a preheating of the work piece as well [43].

Identification procedure

Similar to the strategy pursued for the determination of the cutting constants described in Section 2.1.3, focusing on stable processes justifies the assumption that the work piece deformation and the tool oscillations can be neglected in the simulations related to the identification procedure for the additional empirical parameters b and c. In view of these assumptions the coupled thermo–elastic system, i.e. (3.83a)–(3.83e), can be reduced to the heat equation describing the temperature distribution in the work piece. Since the enhanced cutting force model (3.57) just involves the cutting edge temperature T_e as additional parameter, the temperature distribution in the work piece provides the necessary data to evaluate the cutting forces. Reproducing the experimental procedure in the simulation requires three simulation runs. While the first run has to be performed setting the work piece reference temperature (as discussed on p. 64, the work piece temperature is given by $T = \Theta + T_0$, with reference temperature T_0) to $T_0^1 = 298.15$ K, i.e. 25° C, the second and the third run have to be carried out choosing a reference temperature of $T_0^2 = 323.15$ K, i.e. 50° C, and $T_0^3 = 317.15$ K, i.e. 100° C, respectively. The resulting cutting force evolutions for can be compared considering the following cost functional, i.e.

$$J(c,b) = \sum_{i=1}^{3} \sum_{j=1}^{2} \sum_{k=k_0}^{k_E} \left(F_j^{exp}(t_k, T_0^i) - F_j(t_i, T_{ce}(t_k), c, b, T_0^i) \right)^2, \tag{5.12}$$

where F_k^{exp} denotes the experimental and F_j the simulated cutting forces components. Finally, the minimisation of the cost functional $J(c, b)$ subjected to the constraints $c > 0$, $0 \leq b \leq 1$ provides with $b^* = 0.9998$ and $c^* = 254.33\ \mathrm{K}^{-1}$ a set of constants guaranteeing an optimal fit of the experimental data[2]. Note that the starting index k_0 and the ending index k_E have been introduced to select an appropriate subinterval with approximately stationary cutting conditions. Moreover, due to the values of the empirical parameters, i.e. $b^* = 0.9998$ and $c^* = 254.33\ \mathrm{K}^{-1}$, the cutting force model reproduces the experimental observation that the cutting forces decrease with increasing work piece temperatures.

5.4.2 Example 3cU with stiff thermo–elastic work piece

In order to illustrate the additional effects occurring due the incorporation of the work piece temperature, example 3cU is reconsidered in combination with a damped thermo–elastic work piece model. Since the temperature dependent cutting force model has been adjusted (see pp. 119) so that the high work piece temperatures lead to decreasing cutting forces, it is expected that, in the simulations, a preheating of the work piece, i.e. setting the initial temperature to $T_0 = 317.15$ K, leads to a stabilisation of the previously unstable process. However, the new cutting force model provides modified cutting forces in the non preheated case, too. This effect can be illustrated by the simulation of the example process 3cU involving a damped thermo–elastic work piece with an initial temperature equal to the ambient temperature, i.e. $T_0 = 298.15$ K.

No preheating

A stabilisation of cutting process corresponding to the parameter set 3cU can be observed in the simulations involving the damped thermo–elastic work piece with initial temperature $T_0 = 298.15$ K. Even though the evolution of the uncut chip thickness depicted in Figure 5.36 does not converge to the stationary evolution, the maximum value for $t > 0.08$ s is clearly smaller than the corresponding value of the evolution shown in Figure 5.30. Similarly, the relative cutting force spectrum illustrated in Figure 5.37 indicates that the considered process is unstable. However, the chatter peaks appearing in Figure 5.37 are much smaller than the corresponding peaks depicted in Figure 5.33. In conclusion, the modified cutting force model involving the work piece temperature evaluated at the cutting edge and the additional parameters with values $b = 0.9998$ and $c = 254.33\ \mathrm{K}^{-1}$ probably leads to an underestimation of the cutting forces.

[2] As mentioned before, the cutting force measurements have been carried out by P. Rasper under supervision of Prof. E. Uhlmann at IWF, TU-Berlin (for further details see e.g. [43], [102–104] and Section 6.3).

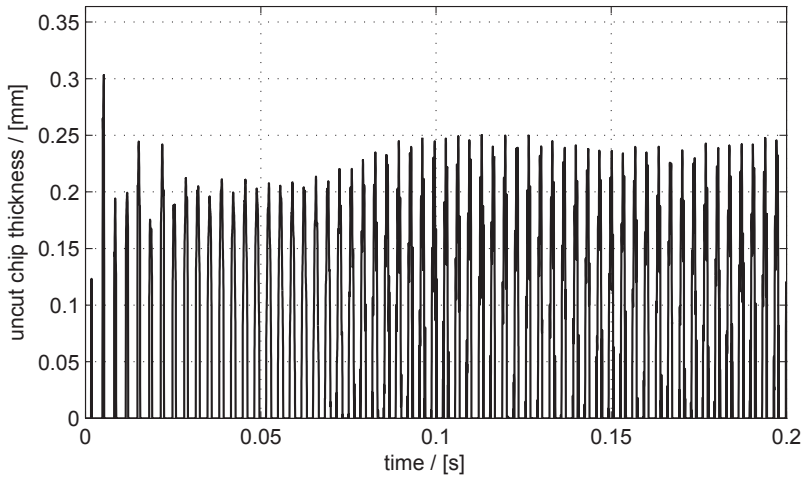

Figure 5.36: Evolution of the uncut chip thickness corresponding to example 3cU with a stiff thermo–elastic work piece structure with initial temperature of $T_0 = 298.15$ K.

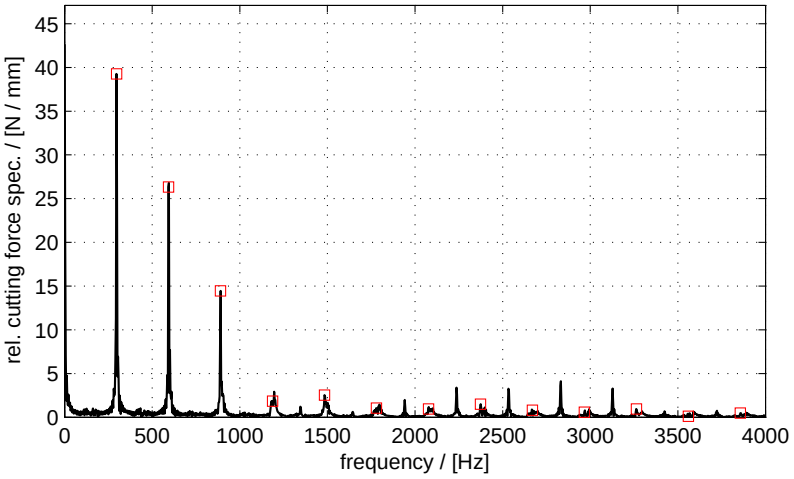

Figure 5.37: Relative cutting force spectrum corresponding to example 3cU with a stiff thermo–elastic work piece structure and initial temperature $T_0 = 298.15$ K.

Preheating to 317.15 K (100°C)

A preheating of the work piece finally stabilises the process 3cU with damped thermo–elastic work piece. As illustrated in Figure 5.38, the evolution of the uncut chip thickness approaches the stationary evolution and therefore confirms that the simulated process is stable. Similarly, the relative cutting force spectrum depicted in Figure 5.39 indicates that the process 3cU with preheated damped thermo–elastic work piece is stable. The chatter peaks that occurred in the previous examples (see Figure 5.17 and 5.33) disappeared and the relative cutting force spectrum only shows the peaks corresponding to multiples of the tooth passing frequency.

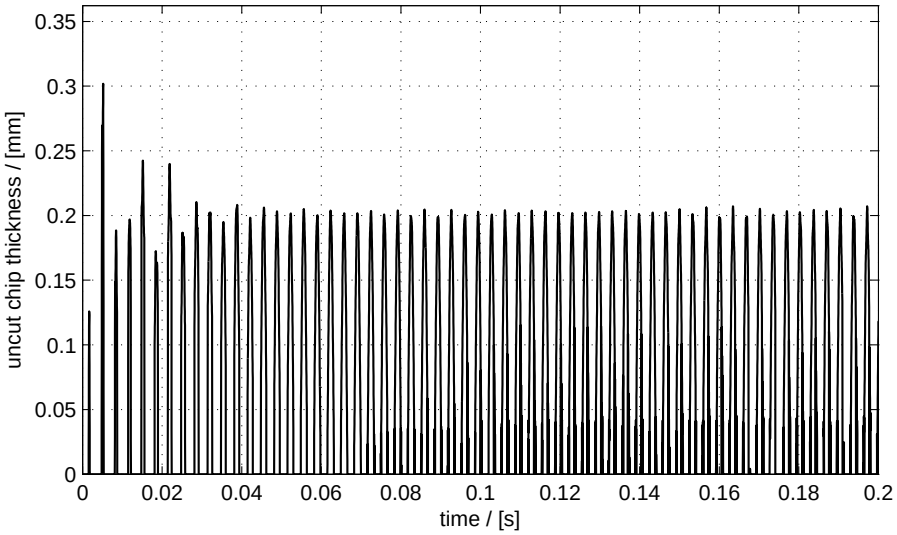

Figure 5.38: Evolution of the uncut chip thickness corresponding to example 3cU with a stiff thermo–elastic work piece structure preheated to 317.15 K.

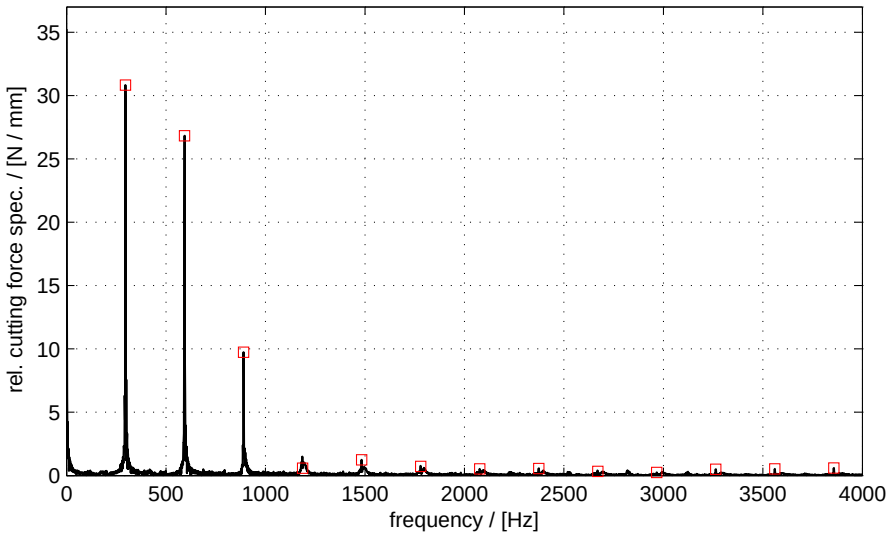

Figure 5.39: Relative cutting force spectrum corresponding to example 3cU with a stiff thermo–elastic work piece structure preheated to 317.15 K.

Preheating to 317.15 K (100°C) and increased axial depth of cut

Increasing the axial depth of cut from $a_p = 0.8$ mm to $a_p = 1.1$ mm leads to a destabilisation of the stable process considered before. The uncut chip thickness corresponding to the process with parameters $n = 17800$ rpm and $a_p = 1.1$ mm involving a damped thermo–elastic work piece is illustrated in Figure 5.40.

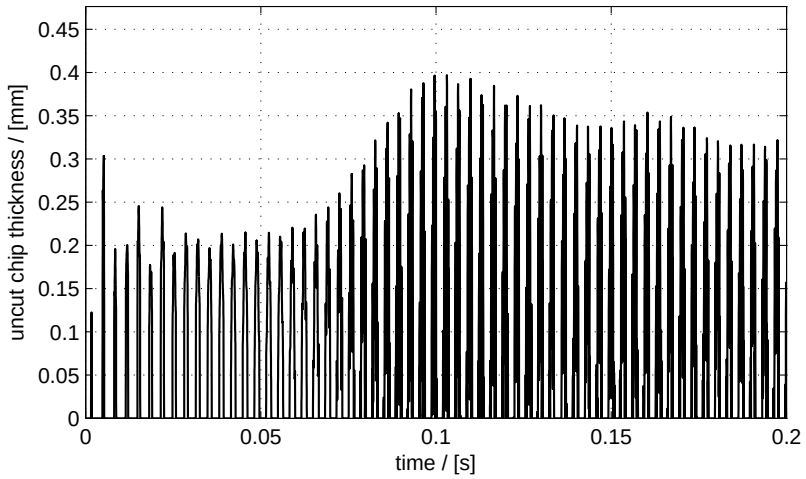

Figure 5.40: Evolution of the uncut chip thickness corresponding to a process with parameters $n = 17800$ rpm, $a_p = 1.1$ mm and a stiff thermo–elastic work piece structure preheated to 317.15 K.

The chatter oscillations and the related maximal value of the uncut chip thickness increase after the tool is fully immersed, i.e. for $t > 0.08$ s.

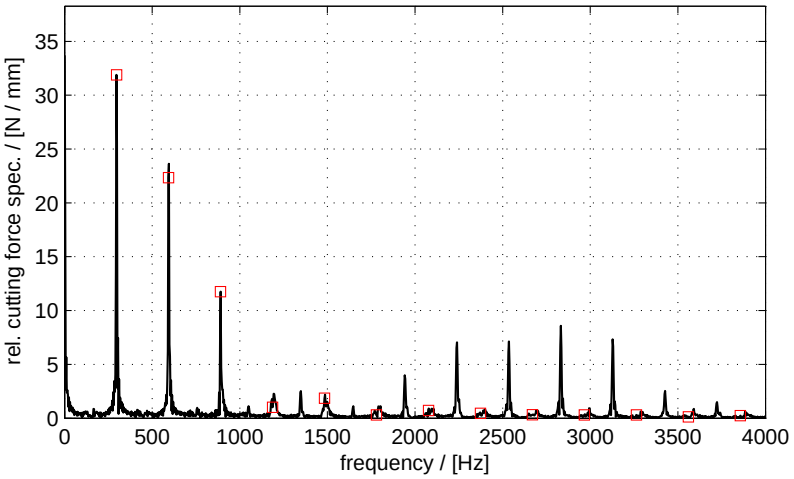

Figure 5.41: Relative cutting force spectrum corresponding to a process with parameters $n = 17800$ rpm, $a_p = 1.1$ mm and a stiff thermo–elastic work piece structure preheated to 317.15 K.

Following the arguments outlined before, the corresponding process has to be classified as unstable. The corresponding relative cutting force spectrum illustrated in Figure 5.41 confirms the conclusions drawn from the evolution of the uncut chip thickness. The chatter peaks appearing between the peak corresponding to multiples of the tooth passing frequency clearly indicate that the increase in the axial

depth of cut destabilised the process 3cU involving a damped thermo–elastic work piece preheated to 317.15 K.

Remarks concerning stability and work piece temperature

The purpose of the present section was to illustrate the implications of the temperature effects. Based on the parameters identified from the cutting tests with a preheated work piece (see Section 5.4.1), the new cutting force model generates, even for a work piece without any preheating, smaller cutting forces than the model without temperature effects. Consequently, the stability limits observed in the simulations with temperature effects are higher than the limits obtained in the simulations involving a damped elastic work piece. Since the general characteristic of the modified cutting force model strongly depends on the values of the parameters b and c, the identification procedure should be refined by incorporating more experimental data. Nevertheless, it has been shown that with the proposed model, a preheating of the work piece leads the an increase of the stability limits. Since the same effect has been observed experimentally as well (see e.g. [43, 102, 103]), the proposed cutting force model incorporating the cutting edge temperature can be interpreted as a first step to reproduce these effects in the simulations.

5.4.3 Machining of a small thin walled work piece

Geometrical errors related to thermal expansion effects and stability

Another example to analyse the temperature effects can be constructed by considering the work piece with dimensions $50 \times 7 \times 3$ mm^3 illustrated in Figure 5.42. Due to the imposed Dirichlet boundary conditions, i.e. $u = 0$ mm, $\Theta = 0$ K on $\Gamma_D \subset \partial\Omega_R$, and the heat generated by the cutting process, it is expected that the thermal expansion leads to a perceivable deformation of the work piece. Since the tool follows a predefined path, too much material might be removed from the work piece in the present configuration which finally leads to geometrical errors in the machined part. On the other hand, the particular choice of the boundary conditions gives a quite stiff work piece structure. As a consequence, it is expected that instabilities related to work piece oscillations do not occur in the framework of the considered cutting process. In this section, stability issues are not the prior motivation for the choice of the boundary conditions since the focus is primarily on the documentation of possible geometrical errors induced by the thermal deformation.

In order to study the evolution of the work piece temperature, for each time, the temperature field can be evaluated at the so called watch (or observation) points illustrated in Figure 5.43. The precise locations of these points are given in Table 5.3. For the simulations, the spindle speed has been set to 18800 rpm while the axial depth of cut has been chosen as $a_p = 1.5$ mm. In contrast to the full immersion processes considered before, a three quarter radial immersion cut is in the focus of the present example. As a consequence of the lower radial immersion the stability limit increases and the considered process is stable. The evolution of the uncut chip thickness illustrated in Figure 5.44 and the corresponding relative cutting force spectrum shown in Figure 5.45 confirm this result.

point index	x / [mm]	y / [mm]	z / [mm]
1	48.0	0.5	2.25
2	48.0	6.5	2.25
3	48.0	3.5	0.75
4	25	0.5	2.25
5	25	6.5	2.25
6	25	3.5	0.75

Table 5.3: Watch point coordinates in the work piece reference frame (see Figure 5.43).

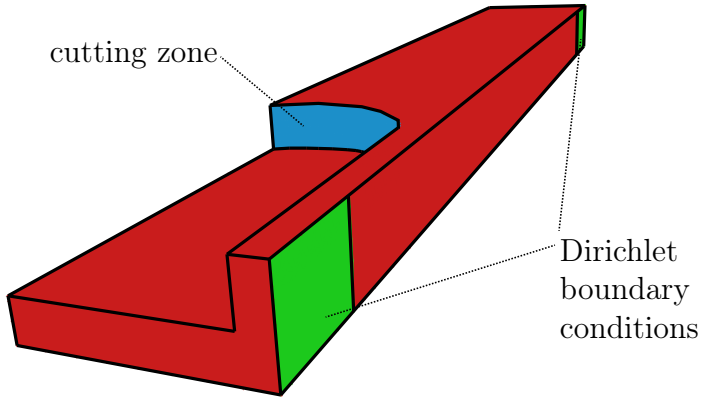

Figure 5.42: Scheme of a thin walled work piece to illustrate the temperature effects.

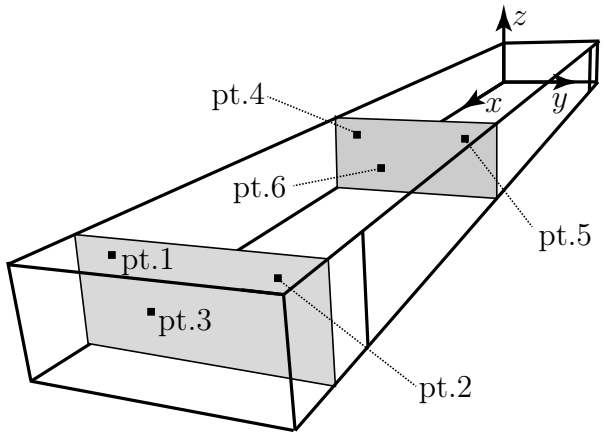

Figure 5.43: Position of the watch points to evaluate the work piece temperature and deformation.

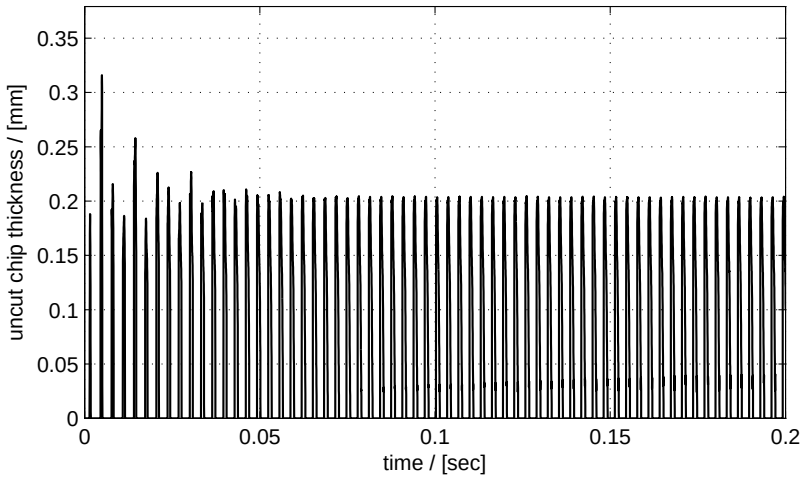

Figure 5.44: Uncut chip thickness corresponding the example with thin walled work piece.

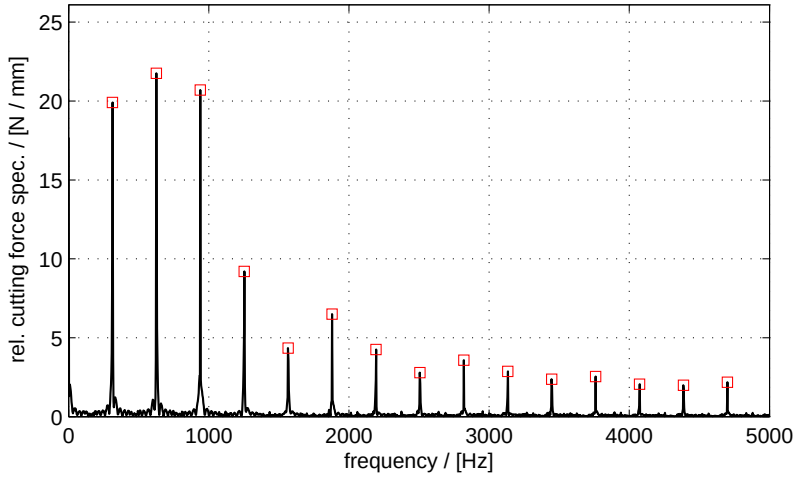

Figure 5.45: Relative cutting force spectrum corresponding the example with thin walled work piece.

Evolution of the work piece temperature

The temperature rise in the work piece is, depending on the watch (or observation) point, in a range between 20 K and 270 K. Since the points 1 and 3 are located in the tool path, the temperature measured at these points corresponds to the maximal work piece temperature during the simulation. After the material has been removed by the tool, the temperature at point 1 and 3 is set to zero. The peaks appearing in the temperature evolution illustrated in Figure 5.46 can be explained by the repeated heating due to the tooth passing. During a tooth period, when the distance between cutting edge and watch point becomes minimal, the temperature at the watch point

assumes a local maximum and decreases again. The points 2 and 5 are located in the small region that remains on the right of the tool path. The temperature rise at watch point 2 is relatively small due to the Dirichlet boundary condition. At watch point 5 the temperature rise is about with 65 K more important because the homogeneous Neummann boundary condition prevents a heat flux through the boundary. A similar phenomenon can be observed for the temperature evolution corresponding to watch point 3 and 6. Both points are located under the slot created by the tool. The temperature rise at watch point 3 remains small because of the heat flux through the Dirichlet boundary. At point 6 the temperature rises up to 50 K and remains, in contrast to the temperature at point 5, on a high level.

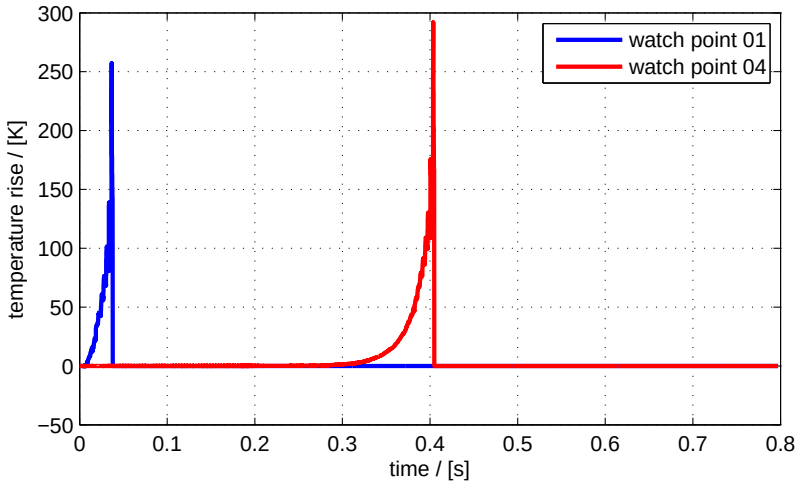

Figure 5.46: Evolution of the work piece temperature rise at watch point 1 and 4.

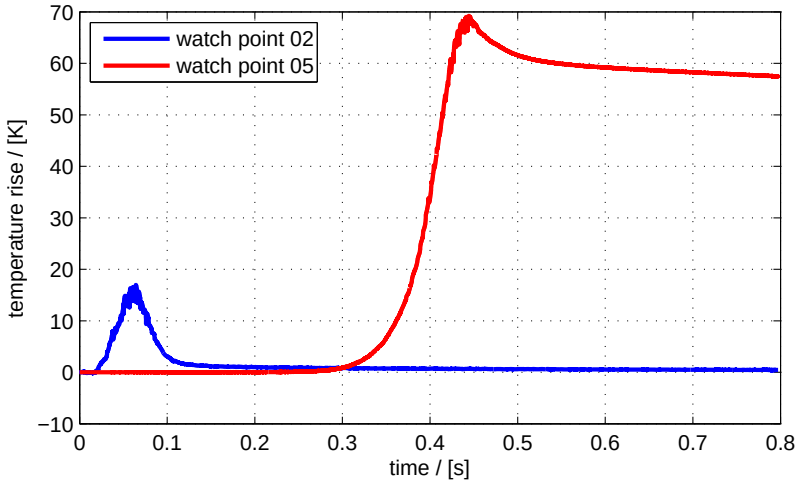

Figure 5.47: Evolution of the work piece temperature rise at watch point 2 and 5.

Even though an important increase of the work piece temperature can be observed

at the watch points 5 and 6, the resulting thermal expansion is still on a very low level.

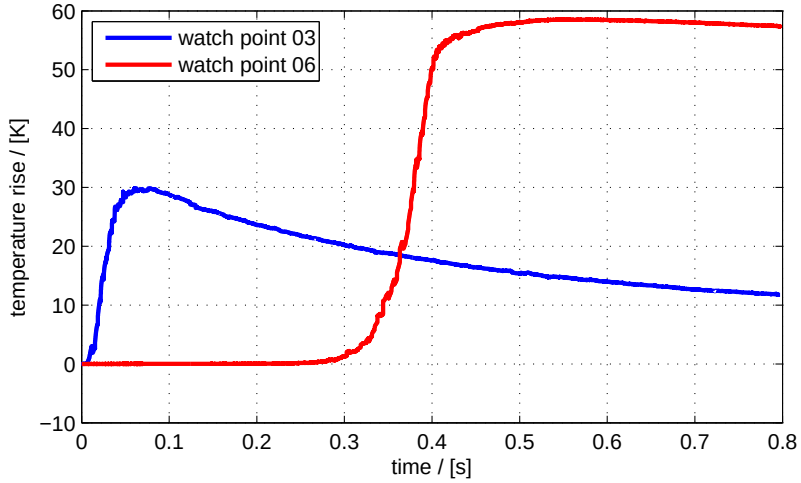

Figure 5.48: Evolution of the work piece temperature rise at watch point 3 and 6.

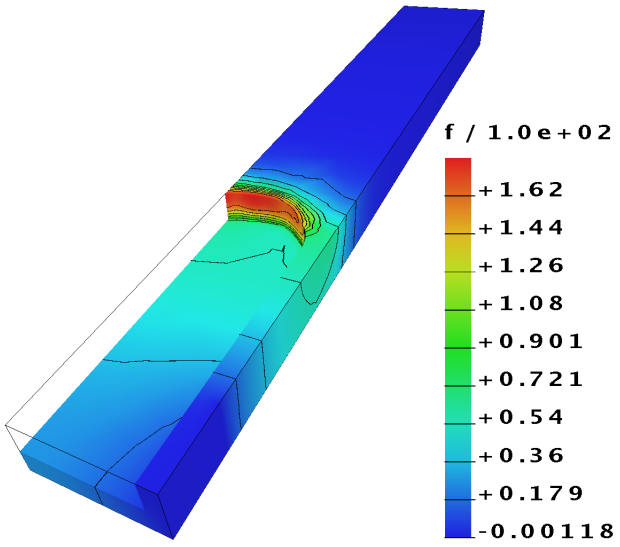

Figure 5.49: Temperature distribution in the work piece (tool is not cutting).

The maximum value of the work piece deformation illustrated in Figure 5.50 is in the range of 0.0244 mm, a small value compared to the work piece dimensions. Due to the discretisation error arising from the Dexel representation, the surface error related to the work piece deformation induced by the thermal expansion can not be simulated with the current approach. However, in case of other work piece materials and different shapes, the illustrated effects may become more important. In conclusion, it can be said, that the model properly reproduces the effects, i.e. thermal expansion and temperature distribution, related to the process heat conducted into the work piece.

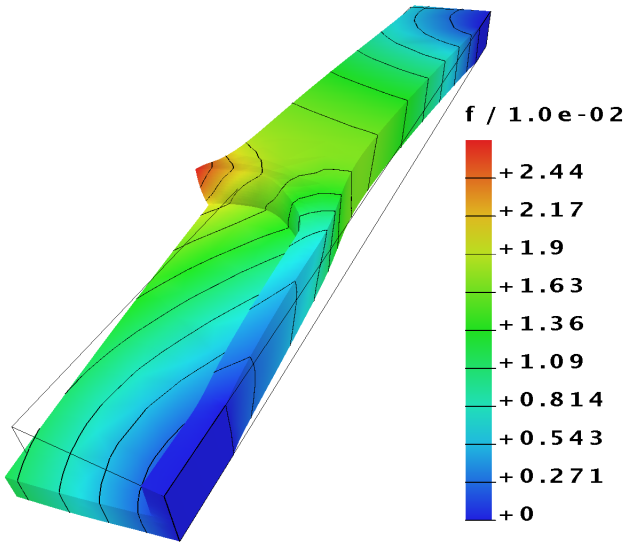

Figure 5.50: Amplified work piece deformation (factor 100) and the corresponding absolute value (colors).

Chapter 6

Experimental verification

6.1 Cooperation

The experimental studies presented in the Sections 6.2, 6.3, 6.4 and 6.5 have been performed at the Department of Production Technology and Factory Management (IWF) of Technische Universität Berlin by C. Mense and P. Rasper under the supervision of Prof. E. Uhlmann. To a large extend, the results of the experimental work have already been published in [43, 75] and [103]. The experiments related to the determination of the dynamical characteristics of the considered milling machine (Section 6.2) have been strongly supported by Prof. U. von Wagner from the Department of Applied Mechanics (Chair of Mechatronics and Machine Dynamics) of Technische Universität Berlin and his co–worker K. Theet.

The device employed for the measurement of the frequency response function discussed in Section 6.2 as well as for all cutting tests was a 5 axis milling machine from MAP Werkzeugmaschinen GmbH, Magdeburg type LPZ 500 (see Figure 6.1). For all experiments, i.e. the dynamical measurements as well as the cutting tests, a one-edge end mill high-speed steel cutter according to DIN 6535 HA with a diameter of 8 mm and a spiral angle of 23° has been used. The milling cutter was mounted in a heat shrinking tool holder with a HSK-A mounting shank according to DIN 69882-8.

6.2 Machine dynamics

As discussed in Chapter 3, the starting point for a reliable machine model is an experimental modal analysis. In milling applications, the spindle–tool system usually dominates the dynamical characteristics of the tool centre point (see e.g. [33]). As a consequence, the focus of the experimental study[1] is at first on the measurement of dynamical characteristics of the TCP.

[1] As already mentioned in Section 6.1, the measurements have been carried out at IWF by P. Rasper under supervision of Prof. E. Uhlmann, for further details see [75].

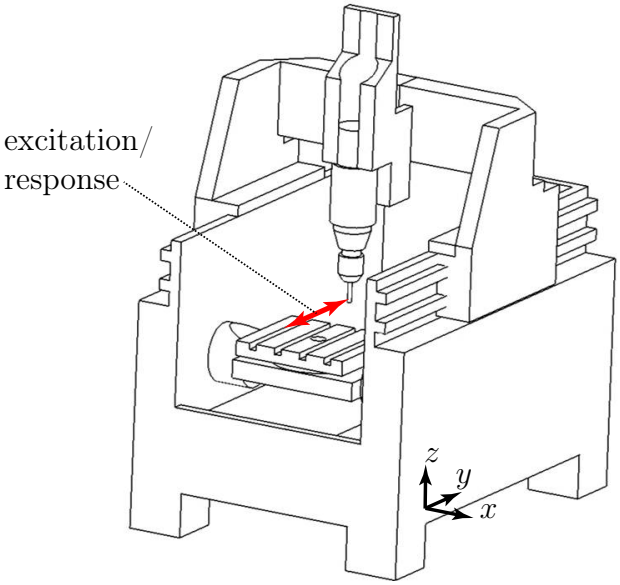

Figure 6.1: On the measurement of the mobility frequency response function[2] at the tool centre point (TCP).

In order to measure the corresponding frequency response function[2], the tool was excited in y-direction of machine reference frame (see Figure 6.1). During the measurements, the spindle–tool system was in an idle state.

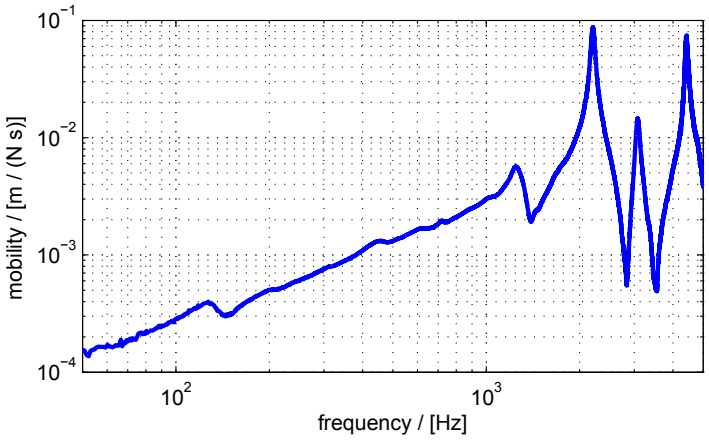

Figure 6.2: Measured mobility frequency response function[2] at the tool centre point [75].

The excitation force has been applied employing an impact hammer (Kistler 9722A500) with a steel impact tip. The corresponding bandwidth was 5000 Hz. The response in y-direction (see Figure 6.1) has been recorded using a laser vibrometer (Polytec OFV 303). In contrast to the accelerometer, the vibrometer measures the velocity

[2]As already mentioned in Section 6.1, the measurements have been carried out at IWF by P. Rasper under supervision of Prof. E. Uhlmann, for further details see [75].

of the TCP without modifying the system. The additional mass of the accelerometer attached on the TCP modifies the dynamical characteristics of the system and therefore possibly introduces measurement errors. The main result is the frequency response function corresponding to the tool centre point illustrated in Figure 6.2 (for further results and experimental issues, the reader referred to [75]). A small peak appears at about 127.3 Hz while the main peaks are located at about 1243 Hz, 2208 Hz, 3081 Hz and 4423 Hz. Due to the high frequencies, it can be concluded that the the main peaks are related to eigenmodes of the spindle tool system. Only the first peak corresponds to an eigenmode of the machine structure. Consequently, the eigenfrequencies of the machine structure, i.e. machine base, side plates, traverse plate, x-slider and headstock, can be neglected and an encompassing modal analysis is not necessary for the stability issues discussed in the present work. The focus is rather on a precise modelling of the dynamical characteristics of the spindle–tool system.

6.3 Cutting force measurements

6.3.1 Experimental setup

As outlined in Chapter 2, the first step in the stability prediction procedure is the determination of the cutting forces. In order to collect the necessary data for the identification procedure presented in Section 2.1.3, machining tests have been performed[3]. The employed work piece material was AlZnMgCu1.5, an aluminium alloy with the material number AA7075. As mentioned in Section 6.1, the device employed for the cutting tests was a 5 axis milling machine from MAP Werkzeugmaschinen GmbH, Magdeburg type LPZ 500. For the experiments a one-edge end mill high-speed steel cutter according to DIN 6535 HA with a diameter of 8 mm and a spiral angle of 23° has been used (see e.g. Figure 3.10). The milling cutter was fixed in a heat shrinking tool holder with a HSK-A mounting shank according to DIN 69882-8. A scheme of the experimental setup is shown in Figure 6.3.

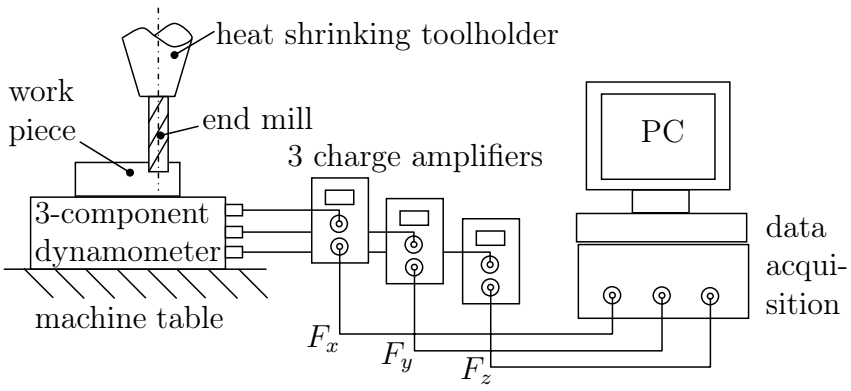

Figure 6.3: Experimental setup for determining the cutting forces (for the definition of the corresponding reference frame see Figure 6.4).

[3]As already mentioned in Section 6.1, the cutting tests have been carried out at IWF by P. Rasper under supervision of Prof. E. Uhlmann [104].

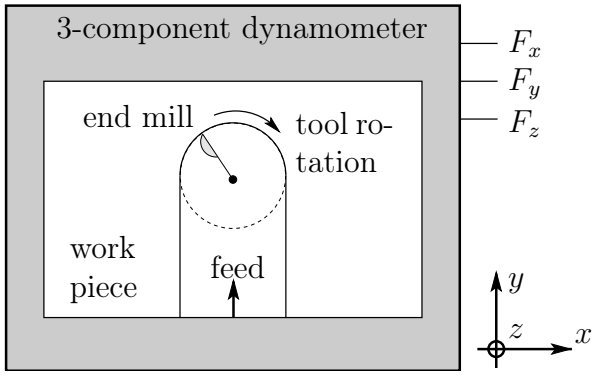

Figure 6.4: On the definition of the coordinates for the cutting force measurements.

The work piece was mounted on a 3-component dynamometer type Kistler 9257A. The dynamometer was connected to three charge amplifiers type Kistler 5011. The data acquisition has been carried out using a measuring board from National instruments with a maximum sampling rate of 500 kHz and a resolution of 16 bit. A sampling rate of 50 kHz was used for the data logging. The cutting forces acting on the work piece measured with the dynamometer are given with respect to the reference frame shown in Figure 6.4.

6.3.2 Data processing

Experiments for the determination of the cutting coefficients

For the cutting force measurements[4] described in this section, the cutting speed has

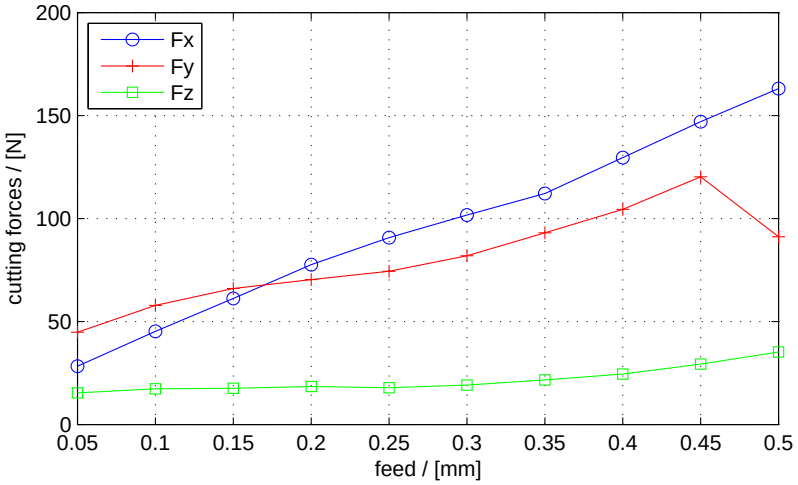

Figure 6.5: Mean values of the experimental[4] cutting forces for different feeds (coordinates are given with respect to the reference frame shown in Fig 6.4).

[4]As already mentioned in Section 6.1, the underlying cutting test data has been measured at IWF by P. Rasper under supervision of Prof. E. Uhlmann [104].

been set to 417.2 m/min, i.e. an approximate spindle speed of 16600 rpm or a tooth passing frequency of 277 Hz. The feed per tooth has been varied from 0.05 mm/tooth to 0.5 mm/tooth with increments $\Delta f_z = 0.05$ mm/tooth. In contrast to the predicted stability limits (see Section 2.3.3), in the experiments, the process was stable for an axial depth of cut $a_p = 1.5$ mm. Consequently, the value $a_p = 1.5$ mm has been chosen for all cutting tests to acquire the data for the determination of the cutting coefficients. The average values of the measured cutting forces are shown in Figure 6.5 for different values of f_z. Note that the coordinates x, y, z correspond to the directions indicated by the reference frame given in Figure 6.4. Due to the action–reaction law, the cutting forces act on the work piece as well as on the tool. The measured cutting forces can therefore be transformed in the forces acting on the tool by changing the sign only. With the additional assumption that dynamical effects arising from the dynamometer can be neglected, the measured cutting forces can be used as input data for the identification of the cutting coefficients presented in Section 2.1.3.

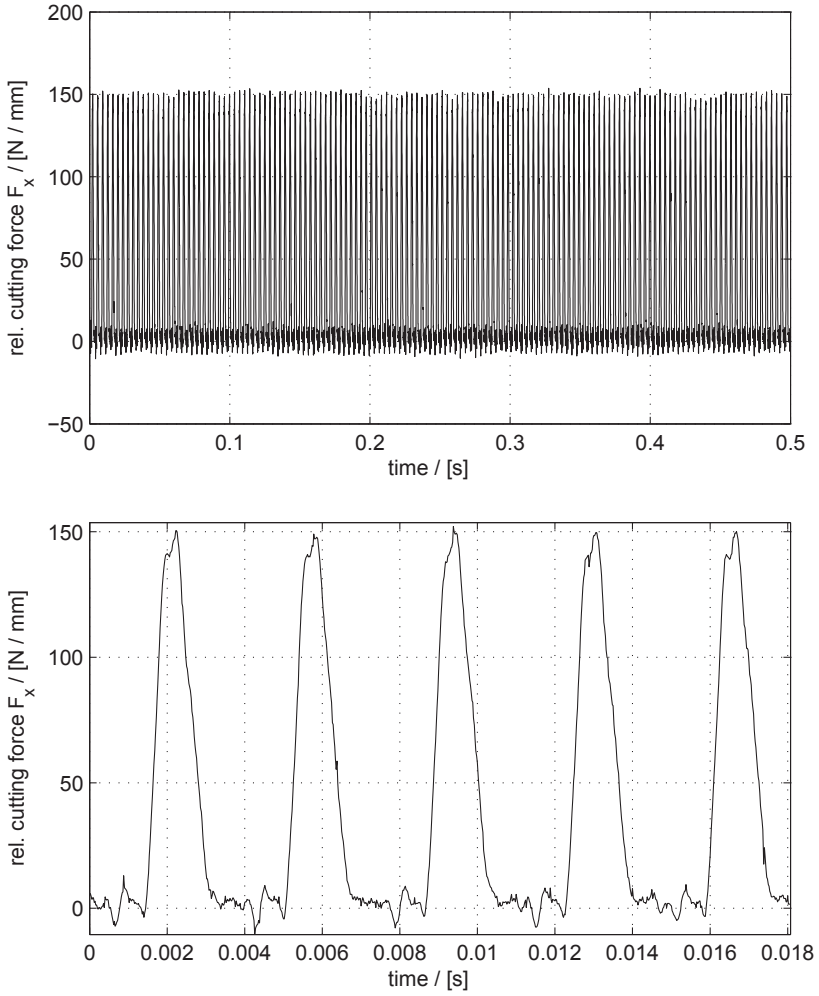

Figure 6.6: Evolution of the experimental cutting force component perpendicular to the direction of feed divided by a_p for a stable process (the corresponding measurements have been carried out by P. Rasper at IWF, see [104]).

Experimental determination of unstable processes

Cutting tests and the monitored cutting forces can also be used to identify unstable processes. In order to display the relevant effects, consider at first a stable process with $f_z = 0.2$ mm, $a_p = 1.5$ mm and cutting speed $n = 16600$ rpm, and focus on the cutting force component perpendicular to the direction of feed (for the definition of the coordinates see Figure 6.4) depicted in Figure 6.6. The corresponding frequency spectrum is illustrated in Figure 6.7 where the the red squares indicate multiples of the tooth passing frequency. Because the peak locations coincide with the frequencies marked by the red squares and no additional peaks occur in between, the corresponding process is classified as stable.

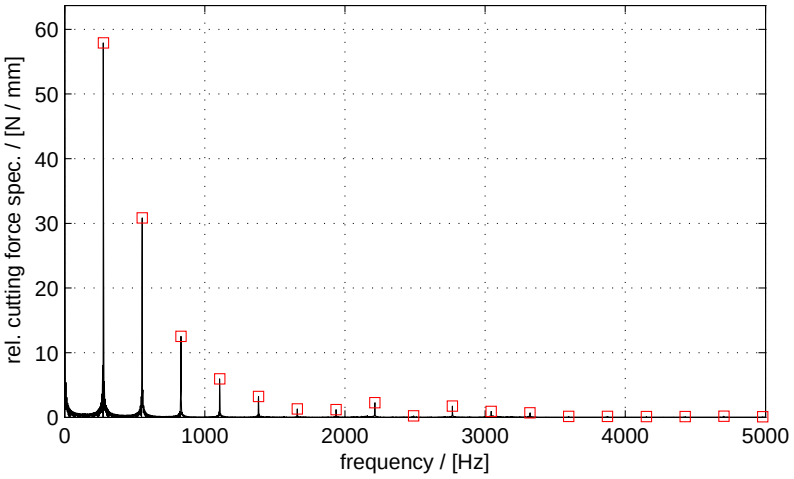

Figure 6.7: Spectrum of the relative cutting force in Figure 6.6.

Due to an increase of the axial depth of cut to $a_p = 2$ mm, the process becomes unstable. As illustrated in Figure 6.8 additional chatter vibrations are superimposed to the cutting force evolution analysed before. This observation is confirmed by the spectrum of the cutting forces illustrated in Figure 6.9. In contrast to the spectrum shown in Figure 6.7, additional peaks occur between the peaks corresponding to multiples of the tooth passing frequency. The ratio

$$\eta^{Exp} = \frac{\max\limits_{f \in \mathbb{R}^+ \setminus \mathbb{M}_{TP}} (|\hat{F}_x^{rel}(f)|)}{\max\limits_{f \in \mathbb{M}_{TP}} (|\hat{F}_x^{rel}(f)|)}, \tag{6.1}$$

with $\mathbb{M}_{TP} = \{\tau, 2\tau, \ldots\}$ denoting the set of tooth passing frequencies, can be used to define a criterion for the identification of unstable processes. The expression $F_{TP}^{max} = \max\limits_{f \in \mathbb{M}_{TP}} (|\hat{F}_x^{rel}(f)|)$ appearing in the denominator of (6.1) provides, due to the restriction $f \in \mathbb{M}_{TP}$, the maximum of the set of values obtained by evaluating the relative cutting forces spectrum $|\hat{F}_x^{rel}(f)|$ at multiples of the tooth passing frequency. The final value usually corresponds to the peak located a the the tooth passing frequency, i.e. the leftmost peak arising in the spectrum illustrated in Figure 6.7.

The expression $F_C^{max} = \max_{f \in \mathbb{R}^+ \setminus \mathbb{M}_{TP}} (|\hat{F}_x^{rel}(f)|)$ appearing in the numerator of (6.1) provides, due to the restriction $f \in \mathbb{R}^+ \setminus \mathbb{M}_{TP}$, the maximum value of the set obtained by evaluating the relative cutting force spectrum $|\hat{F}_x^{rel}(f)|$ at all frequencies different from any multiple of the tooth passing frequency.

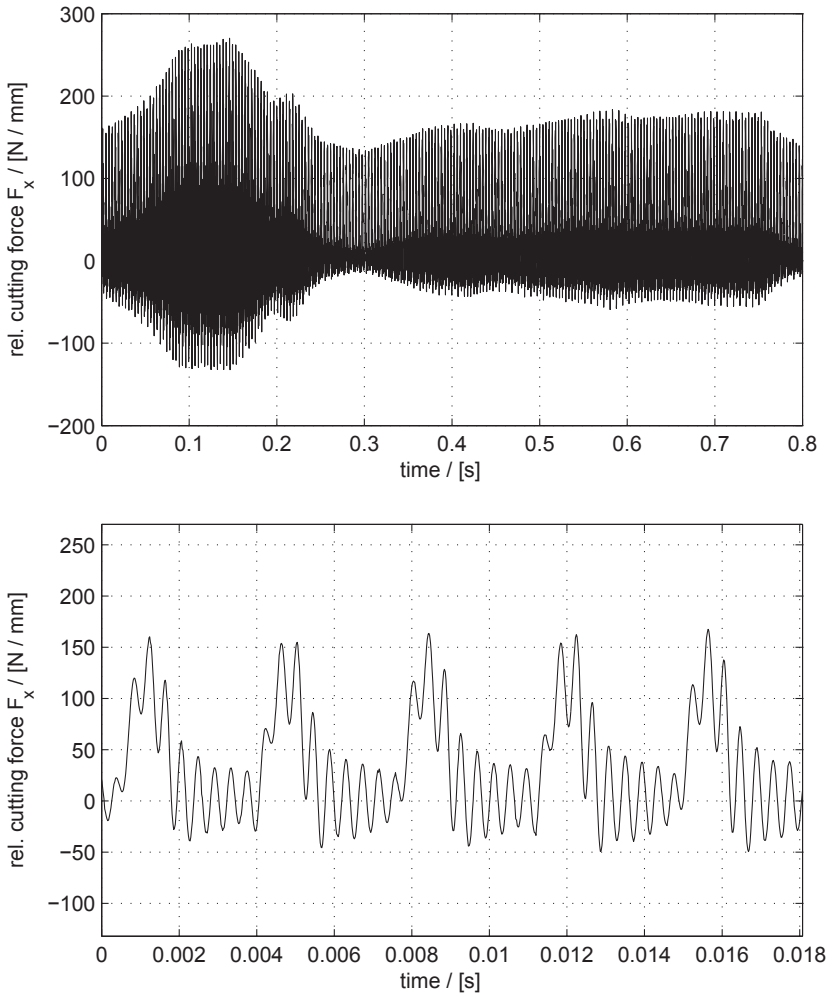

Figure 6.8: Evolution of the experimental cutting force component perpendicular to the direction of feed divided by a_p for an unstable process (the corresponding measurements have been carried out by P. Rasper at IWF, see [104]).

In case of an unstable process, the final value corresponds to the highest chatter peak, i.e. the peak located at about 2300 Hz in the spectrum illustrated in Figure 6.9. In the stable case, the value F_C^{max} is close to zero since no chatter peaks appear in the relative cutting force spectrum. Due to the periodic excitation, the value F_{TP}^{max} is always greater than zero and the ratio (6.1) approaches zero. In case of almost unstable processes, chatter vibrations occur and the value F_C^{max} increases.

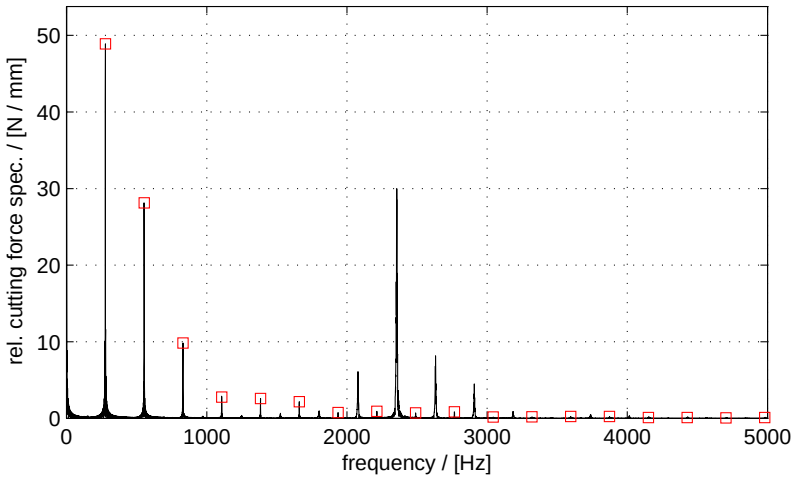

Figure 6.9: Spectrum of the relative cutting force in Figure 6.8.

As before, the periodic excitation guarantees that F_{TP}^{max} is always greater than zero and the value of the ratio (6.1) increases, due the increase of F_C^{max}, as well. If, for a given process, η^{Exp} is greater than a predefined threshold, that is, for example $\eta^{Th} = 10\%$, the process is classified as unstable.

6.4 Verification of predicted stability limits

6.4.1 Stability lobe diagram

The experimental procedure to determine a stability lobe diagram (SLD) consists of the following steps. First, choose a partition of the spindle speed range and, for each spindle speed, define a set of values for the axial depth of cut a_p. Next, perform the cutting tests for each pair of process parameters and record the corresponding cutting forces employing the dynamometer mentioned in Section 6.3.1. The chatter criterion introduced in Section 6.3.2 with a threshold $\eta^{Th} = 5\%$, finally allows to decide if the considered process is stable or not. The result of the experimental stability analysis procedure is shown in Figure 6.10 together with the SLD predicted in Section 2.3.3, Figure 2.18. The points marked with transparent squares represent stable process, while the filled circles correspond to unstable processes. The comparison illustrated in Figure 6.10 shows pronounced deviations between experiment and prediction. For the entire range of spindle speeds, the theoretical limit is below the values derived from the experiments. The predicted stability peaks are, compared to the experiments, shifted to the left, i.e. to lower spindle speeds, and, in terms of a_p, the difference between stability minimum and maximum is more pronounced for the simulated curve. For the discussion of possible reasons the reader is referred to Section 6.6 and to the considerations outlined in [75].

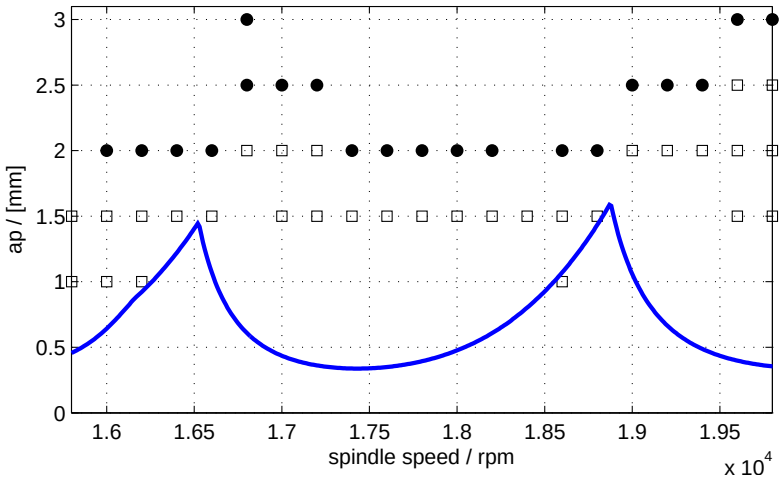

Figure 6.10: Comparison of experimental and predicted stability limit (for further details and experimental issues see [75]).

6.4.2 Chatter frequencies

The chatter frequencies corresponding to unstable processes are similar in experiment and simulation. In order to verify this observation, consider the cutting forces recorded during the simulation of the example process 3bU with stiff visco-elastic work piece (see Section 5.3.3) and the measured cutting forces corresponding to a process with parameters $n = 17800$ rpm and $a_p = 2$ mm. As shown by the relative cutting force spectrum illustrated in Figure 6.11, the three dominant chatter peaks are located at frequencies around 2500 Hz.

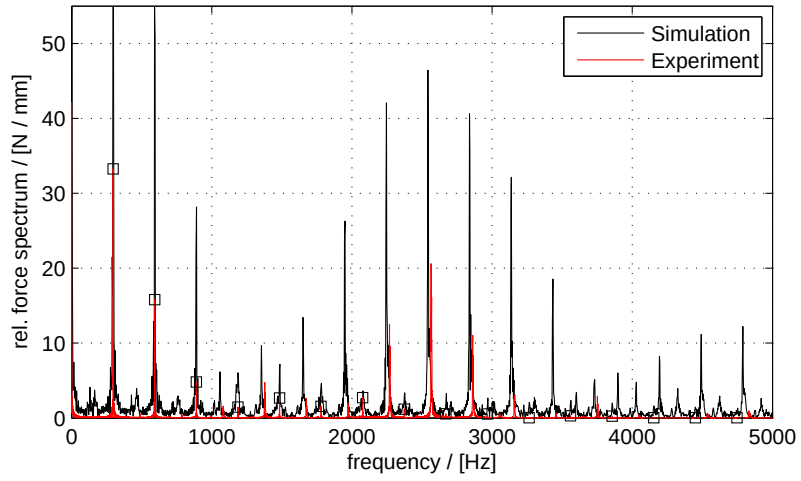

Figure 6.11: Relative cutting force spectrae for an unstable process at $n = 17800$ rpm (for further details and experimental issues see [43]).

Even though the spectrum shows pronounced deviations in the height of the peaks corresponding to experiment and simulation, the similar locations the chatter peaks indicate that the model satisfactorily reproduces the chatter frequencies. In order to compare the chatter frequencies computed in the stability prediction with the values measured in the cutting tests consider the frequencies in the interval $[0, n]$, where n denotes the spindle speed and recall that the experimental chatter frequency f_{Ch}^{Exp} is determined by

$$f_{Ch}^{Exp} = \underset{f \in \mathbb{R}^+ \setminus \mathbb{M}_{TP}}{\operatorname{argmax}} \left(|\hat{F}_x^{ref}(f)| \right), \tag{6.2}$$

with $\mathbb{M}_{TP} = \{\tau, 2\tau, \ldots\}$ denoting the set of tooth passing frequencies. The projection of the experimental chatter frequency on the interval $[0, n]$ is defined by

$$\bar{f}_{Exp}^{Ch} = \mod (f_{Exp}^{Ch}, n). \tag{6.3}$$

The projected chatter frequencies corresponding to each unstable process indicated in Figure 6.10, are depicted in Figure 6.12 together with the chatter frequencies predicted in Section 2.3.3 (see Figure 2.18). In contrast to the stability limit, the predicted chatter frequencies are in better agreement with the experimental values. The black circles indicating the experiments are located in vicinity of the lines corresponding to the predicted values. The main differences between experiment and prediction appear in the regions close to the jumps at about 16500 and 19000 rpm. The jumps in the experimental chatter frequencies are shifted to the right compared to the prediction. This effect corresponds the shifting of the peaks in the stability lobe diagram. As before, for the discussion of possible reasons the reader is referred to Section 6.6.

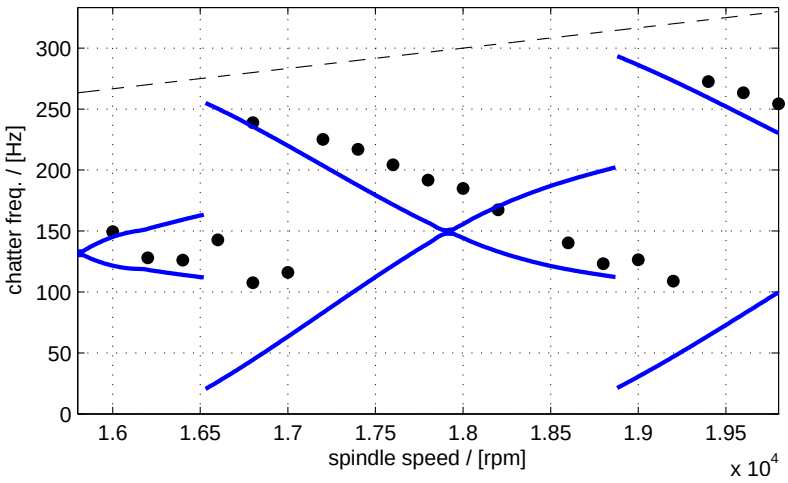

Figure 6.12: Comparison of experimental and simulated chatter frequencies (the cutting tests for the chatter frequencies and the corresponding experimental stability stability limits shown in Figure 6.10 have been carried out by P. Rasper at IWF under supervision of Prof. E. Uhlmann, see [75, 104]).

6.5 Work piece effects

The destabilising effect of a supple work piece structure discussed in Section 5.3.4, has been observed experimentally as well. The result of the cutting test employing a work piece with with the same dimensions, i.e. $100 \times 10 \times 140$ mm^3, is shown in Figure 6.13. Since the tool diameter is about 8 mm, a thin wall would remain on the left and on the right of the machined slot in the stable case. In the present example, however, the thin wall on the left of the slot has been almost entirely removed due to strong work piece oscillations. A similar effect can be observed in the simulations. While the material on the right of the tool path is still visible, the material on the left has been almost completely removed as well and the remaining surface is covered with chatter marks. Moreover, the evolution of the uncut chip thickness and the relative cutting force spectrum presented in Section 5.3.4 clearly indicate that the considered process is unstable.

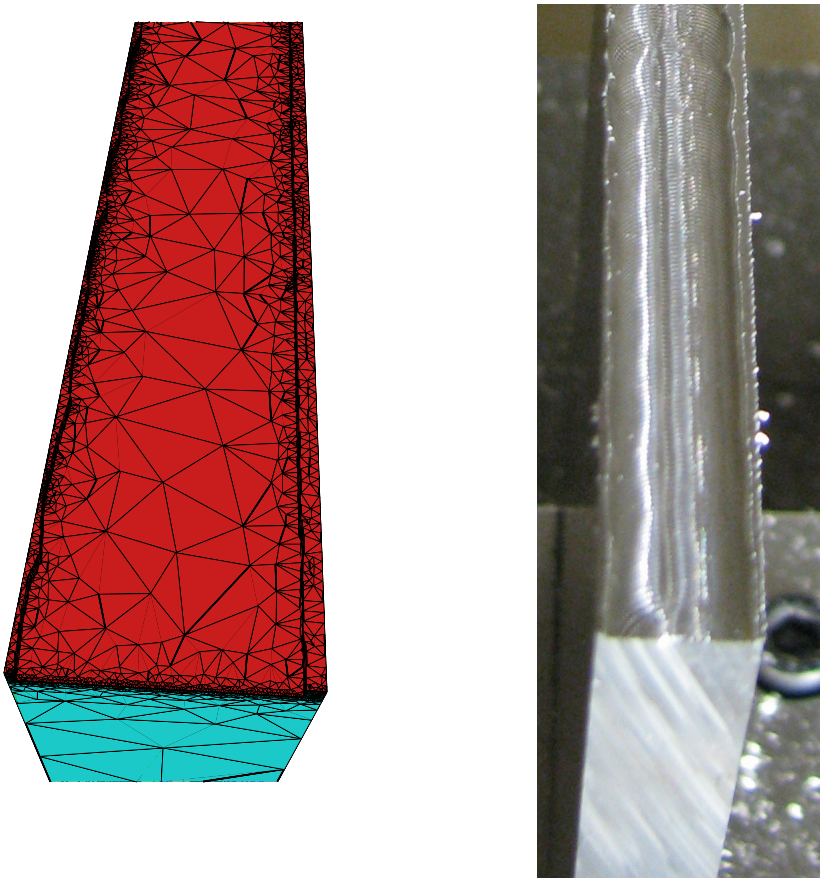

Figure 6.13: Comparison of a machined slot on top of a supple work piece (left: simulation, right: experiment[5]).

[5]The image has been kindly provided by P. Rasper from IWF (head: Prof. E. Uhlmann), TU-Berlin (see e.g. [104]).

6.6 Discussion

The comparison of simulation results and experimental data show that

- the complex model reproduces the effects of a supple work piece,
- the stability analysis method accurately predicts the chatter frequencies for large parts of the considered spindle speed range.

Moreover, the experimental observation, that a preheating of the work piece lead to an increase of the stability limits, can be reproduced with the complex model presented in this work.

However, the comparison of the stability limits reveals a large gap between experiment and simulation. Since inaccuracies due to the stability prediction method or modelling errors (the complex model presents approximately the same stability limits as the system employed for the prediction) can be excluded, the observed deviations are most probably related to measurement errors. The frequency response function measured at the tool centre point and cutting forces data recorded under stable cutting conditions are the input data for the stability prediction. As discussed for example in [75], the result of the FRF measurement changes with the excitation method and the angular position of the spindle. The observation that the peaks in the predicted stability lobe diagram and the predicted jumps of the chatter frequencies are shifted to lower spindle speeds compared to the experiments, indicate that the frequency of the main peak in the measured FRF has probably been underestimated in the experiments. The facts that the predicted stability limit lies below the experimental values and that the difference between maximum and minimum of the predicted limit curve is bigger than the corresponding experimental value are probably related to errors in magnitude and width of the main peak in the measured FRF. The dynamometer employed for the cutting force measurement is another possible source of errors. Due its structure, the dynamometer is not as rigid as, for example, an aluminium block. During the cutting tests, even in the stable case, the oscillations arising in the work piece dynamometer assembly may lead to inaccurate results. Since the cutting constants are identified from the experimental cutting force data, the measurement error is directly transferred to the cutting force model and therefore leads to inaccurate results in the stability prediction. In addition to the errors in the cutting force data, the dynamometer may directly affect the stability limit of the system under consideration. Since the oscillations and the damping effects related to the dynamometer are not included in the structure models employed for the stability prediction, the observed deviations can probably explained with the dynamometer effects. In conclusion, the problems occurred in the stability prediction could probably be solved by conducting cutting tests without the dynamometer. Alternatively, instabilities can be identified exploiting the acoustic emission of the process [7], by monitoring work piece accelerations or by recording the tool vibrations [33].

Chapter 7

Conclusions and outlook

The main objective of the present work was the development of a complex milling model to investigate the effects of machine and work piece structure on the stability of milling processes. The result of the rigorous mathematical modelling presented in Chapter 3 is a system of ordinary and partial differential equations coupled through a cutting force model. The empirical cutting force model relates the engagement conditions, i.e. basically the uncut chip thickness involving tool position and work piece deformation, to the reaction forces acting on machine and work piece. The new concept to model the work piece as a continuous thermo–elastic body, required a new strategy to formulate an analytical expression for the uncut chip thickness and a new approach to describe the effect of the cutting forces acting on the work piece. Motivated by the intention to study thermal effects, a Dexel based material removal model has been proposed in order to simulate the effect of a travelling heat source and to gain information about the final work piece shape. Since the tailored numerical algorithm presented in Chapter 4 involves a fully implicit time integration scheme, the effects arising from the coupling of machine and work piece can be accurately simulated and studied in great detail with the new milling model. Consequently, the time domain simulations in Chapter 5 clearly demonstrate that the developed model is capable of reproducing the instability effects observed in the experiments. Moreover, the simulation results document that the complex milling model reproduces the experimental observation (see [102,103]) of increasing stability limits due to a preheating of the work piece.

The objective to generate stability lobe diagrams displaying the stability limits corresponding to the new complex milling model for a wide range of process parameters, required the development of a new stability prediction method since the common solution operator discretisation methods fail due to large number of unknowns in the underlying system of equations. The new method presented in Chapter 2 for the first time allows the determination of stability limits of large DDE-systems with periodic coefficients. The main idea of the new method is to consider a numerical linear algebra approach to the characteristic roots of time-periodic delay-differential equations. In particular, a method from the field of nonlinear eigenvalue problems has been adapted to construct an iterative correction scheme. The test examples show that the new method accurately reproduces the stability limits corresponding to different milling systems and that the new method can potentially be applied to the complex milling system proposed in Chapter 3. Moreover, by means of several

examples it has been demonstrated that model reduction techniques help to drastically reduce the computational costs while maintaining a high level of accuracy.

The results are promising and open up various directions for future research. In addition to a more refined machine model and more efficient space discretisation techniques for the work piece equations, it would be desirable to have available a more flexible tri–Dexel model (see p. 89) for the material removal simulation. In order to further accelerate the time domain simulations, one could introduce an implicit time discretisation for the machine equations and consider time adaptive methods. This requires a further development of the algorithm regarding the equations of motion of the multi–body system. In addition to the implemented approach that provides the right hand side corresponding to a set of minimal coordinates, it would be desirable to have available the gradient of the right hand side with respect to minimal coordinates, too. Another issue, already discussed in [15], is to remove the requirement that the underlying system has to present a chain like structure. Based on the current model, a challenging task would be to investigate the effect of variations in the machine design to the stability of milling processes.

Finally, from application point of view an efficient numerical tool for the systematic derivation of stability diagrams is most desirable. The developed stability analysis tool is a first step in this direction. The next step would be an efficient implementation of the so called two step approach. Combining the presented iterative method and the path following approach with an efficient implementation of the operator discretisation method finally gives a tool that, on the one hand, detects unstable process parameters and, on the other hand, efficiently calculates the corresponding stability boundary in the process parameter space. Consequently, the improvement of the numerics, the further development of the employed algorithms and the consideration of work piece models involving plate or shell equations are subject to further research.

The numerical examples presented in Section 2.3.2 reveal that the computational costs related to the numerical stability analysis can be drastically reduced by means of model reduction techniques. Moreover, the examples show that replacing a part of a coupled model by the corresponding reduced system leads, from a stability analysis point of view, to a new system presenting almost the same features as the original model. The model reduction based approach therefore opens new perspectives. For the first time it is possible to treat efficiently even complex models involving, for example, a realistic 3-dimensional work piece representation.

From a mathematical point of view, a challenging task is the analysis of the employed model reduction techniques. The main difficulty is, based on the already available error estimates for the model reduction techniques, to establish error estimates for the characteristic multipliers corresponding to the reduced system.

Appendix A

Stability Definition

The stability definition utilised in the present work can be found in the book of Hale [38, p. 130]. In the following, suppose that $f : \mathbb{B} \times C([-\tau + \sigma, \sigma]) \mapsto \mathbb{R}^n$, $\tau, \sigma > 0$, is continuous and consider the retarded functional differential equation

$$\dot{x}(t) = f(t, x_t), \tag{A.1}$$

with $x_t(s) = x(t + s)$, $s \in [-\tau + \sigma, \sigma]$ and the initial condition $x_\sigma(s) = \phi(s)$, for $s \in [-\tau + \sigma, \sigma]$. Moreover suppose that f is completely continuous and that f is sufficiently smooth so that the solution $x(\sigma, \phi)(t)$ through (σ, ϕ) is continuous in (σ, ϕ, t) in the domain of the definition of the function.

Definition A.1 *Suppose $f(t, 0) = 0$ for all $t \in \mathbb{R}$. The solution $x = 0$ of* (A.1) *is said to be*

- **(Lyapunov) stable** *if for any $\sigma \in \mathbb{R}$, $\varepsilon > 0$, there is a $\delta = \delta(\sigma, \varepsilon) > 0$ such that $\phi \in \mathcal{B}(0, \delta)$ implies that $x_t(\sigma, \phi) \in \mathcal{B}(0, \varepsilon)$,*
- **asymptotically stable** *if it is stable and there is a $b_0 = b_0(\sigma) > 0$ such that $\phi \in \mathcal{B}(0, b_0)$ implies $x(\sigma, \phi)(t) \to 0$ as $t \to \infty$,*
- **uniformly stable** *if the number δ in the definition is independent of σ,*
- **uniformly asymptotically stable** *if it is uniformly stable and there is a $b_0 > 0$ such that for every $\eta > 0$, there is a $t_0(\eta) > 0$ such that $\phi \in \mathcal{B}(0, b_0)$ implies $x_t(\sigma, \phi) \in \mathcal{B}(0, \eta)$ for $t \geq \sigma + t_0(\eta)$ for every $\sigma \in \mathbb{R}$.*

Note that $\mathcal{B}(y, r)$ represents a ball around y with radius r.

Appendix B

Continuum mechanics

B.1 Material coordinates

As shown in Fig. B.1, an arbitrary body may, subjected to volume forces or stresses acting on the boundary, change its shape, orientation and position with respect to a reference configuration, i.e. a given set $\Omega_R = \Omega(t = 0) \subset \mathbb{R}^3$.

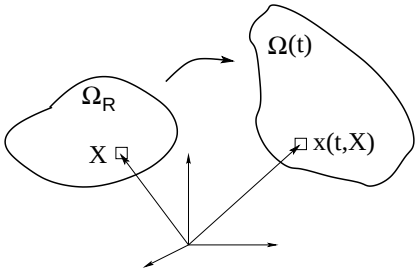

Figure B.1: Reference and current configuration.

A deformation of the reference configuration is a vector field

$$\chi(t, .) : \Omega_R \mapsto \mathbb{R}^3 \tag{B.1}$$

that shall be smooth enough, injective except possibly on the boundary of the set Ω_R and orientation preserving (see [26, pp.27]). The set $\Omega(t) = \chi(t, \Omega_R)$ is called deformed or current configuration. Since the current configuration is generated by the deformation field mentioned before, the volume enclosed by $\partial\Omega(t)$ always consists of the same material points or particles identified in the reference configuration, i.e. $\Omega(t)$ is a material volume. The derivative of the deformation field with respect to the material coordinates

$$F_{ij}(t, \mathbf{X}) = \frac{\partial \chi_i(t, \mathbf{X})}{\partial X_j}, \quad i, j = 1, 2, 3. \tag{B.2}$$

is called **deformation gradient**. Note that the subscripts characterise the vector component $(.)_i$ or the matrix element $(.)_{ij}$. The letters written in bold face refer to either the complete vector or to the complete matrix. Due to the assumptions on the

deformation field, the determinant of the deformation gradient, $J(t, \mathbf{X}) = \det(F_{ij})$ is positive for all t and $\mathbf{X} \in \Omega_R$ and there exists an inverse function

$$\chi^{-1}(t, .) : \Omega(t) \mapsto \Omega_R \tag{B.3}$$

mapping from the current to the reference configuration.

B.2 Balance of mass

The balance of mass in the current configuration reads (cf. [67, p. 93])

$$\frac{d}{dt} \int_{\Omega(t)} \varrho(t, \mathbf{x}) dx = 0. \tag{B.4}$$

Using the substitution rule for multiple dimensions [111, pp.867], the above expression can be reformulated with respect to the reference configuration

$$\int_{\Omega_0} \frac{\partial}{\partial t} \left(\hat{\varrho}(t, \mathbf{X}) J(t, \mathbf{X}) \right) dX = 0, \tag{B.5}$$

where $\varrho(t, \mathbf{x}) = \varrho(t, \chi(t, \mathbf{X})) = \hat{\varrho}(t, \mathbf{X})$. Since the reference configuration is independent of time, changing the order of differentiation and integration is possible. Moreover, (B.5) holds true for arbitrary domains Ω_0 and consequently

$$\frac{\partial}{\partial t} \left(\hat{\varrho}(t, \mathbf{X}) J(t, \mathbf{X}) \right) = 0. \tag{B.6}$$

Integrating the above equation with respect to time, using the initial condition $\hat{\varrho}(0, \mathbf{X}) = \hat{\varrho}_0(\mathbf{X})$ and exploiting the fact that $J(0, \mathbf{X}) = 1$, finally gives

$$\hat{\varrho}(t, \mathbf{X}) = \hat{\varrho}_0(\mathbf{X}) / J(t, \mathbf{X}). \tag{B.7}$$

B.3 Balance of a generic quantity

The general form of a balance equations for a generic quantity $\Psi^g(t, \mathbf{x})$ reads [68, pp. 5]

$$\frac{d}{dt} \int_{\Omega(t)} \varrho(t, \mathbf{x}) \Psi^g(t, \mathbf{x}) dx = - \int_{\partial\Omega(t)} \Phi^g_k(t, \mathbf{x}) n_k do + \int_{\Omega(t)} \varrho(t, \mathbf{x}) \xi^g(t, \mathbf{x}) dx, \tag{B.8}$$

with $\Phi^g_k(t, \mathbf{x})$ representing the flux through the boundary $\partial\Omega(t)$. The quantity $\xi^g(t, \mathbf{x})$ comprises productions and sources. An infinitesimal surface element for the current configuration do is related to a surface element in the reference configuration dO by [67, pp. 34]

$$n_k do = J(F^{-1})_{ik} N_i dO, \tag{B.9}$$

with n_j representing the normal vector in the current configuration and N_i the normal vector in the reference configuration. Applying the same strategy as shown

for the balance of mass and exploiting (B.9), (B.8) can be rewritten with respect to the reference configuration, i.e.

$$\int_{\Omega_0} \frac{\partial}{\partial t} \left[\hat{\varrho}(t, \mathbf{X}) \hat{\Psi}^g(t, \mathbf{X}) J \right] dX = - \int_{\partial \Omega_0} \Phi_k^g(t, \mathbf{x}) J (F^{-1})_{ik} N_i dO + \int_{\Omega_0} \hat{\varrho}(t, \mathbf{X}) \hat{\xi}^g(t, \mathbf{X}) J dX, \tag{B.10}$$

with $\varrho(t, \mathbf{x}) = \hat{\varrho}(t, \mathbf{X})$, $\Psi^g(t, \mathbf{x}) = \hat{\Psi}^g(t, \mathbf{X})$ and $\xi^g(t, \mathbf{x}) = \hat{\xi}^g(t, \mathbf{X})$. According to the divergence theorem, the first integral on the right hand side of (B.10) can be transformed into an integral with respect to the reference domain. Since the reference domain is arbitrary, the integrand has to be zero, i.e.

$$\frac{\partial}{\partial t} \left[\hat{\varrho}(t, \mathbf{X}) \hat{\Psi}^g(t, \mathbf{X}) J \right] + \frac{\partial}{\partial X_i} \left[\Phi_k^g(t, \mathbf{x}) J (F^{-1})_{ik} \right] = \hat{\varrho}(t, \mathbf{X}) \hat{\xi}^g(t, \mathbf{X}) J. \tag{B.11}$$

Combining the expression above with (B.5) finally gives the local balance equation for a generic field with respect to the reference configuration

$$\frac{\partial}{\partial t} \hat{\Psi}^g(t, \mathbf{X}) + \frac{1}{\hat{\varrho}_0(\mathbf{X})} \frac{\partial}{\partial X_i} \left[\Phi_k^g(t, \mathbf{x}) J (F^{-1})_{ik} \right] = \hat{\xi}^g(t, \mathbf{X}), \tag{B.12}$$

where the value $\Phi_k^g(t, \mathbf{x}) J (F^{-1})_{ik} = \hat{\Phi}_k^g(t, \mathbf{X}) J (F^{-1})_{ik} = \tilde{\Phi}_i^g(t, \mathbf{X})$ is defined as the material flux. Note that one can derive a local balance equation for a generic field with respect to the current configuration [68, p. 7] as well, i.e.

$$\frac{\partial \varrho(t, \mathbf{x}) \Psi^g(t, \mathbf{x})}{\partial t} + \frac{\partial}{\partial x_k} \left[\varrho(t, \mathbf{x}) \Psi^g(t, \mathbf{x}) v_k(t, \mathbf{x}) + \Phi_k^g(t, \mathbf{x}) \right] = \varrho(t, \mathbf{x}) \xi^g(t, \mathbf{x}). \tag{B.13}$$

As mentioned before, $\xi^g(t, \mathbf{x})$ comprises productions and sources. The expressions (B.12) and (B.8) are balance equations for generic fields. The local balance of mass for the current configuration corresponding to (B.5) follows from (B.8) choosing $\Psi^g(t, \mathbf{x}) = 1$, $\Phi_k^g(t, \mathbf{x}) = 0$ and $\xi^g(t, \mathbf{x}) = 0$, i.e

$$\frac{\partial \varrho(t, \mathbf{x})}{\partial t} + \frac{\partial}{\partial x_k} \left[\varrho(t, \mathbf{x}) v_k(t, \mathbf{x}) \right] = 0. \tag{B.14}$$

B.4 Balance of momentum

The local balance of momentum can be found setting in (B.13) $\Psi^g(t, \mathbf{x}) = v_i(t, \mathbf{x})$, $\Phi_k^g(t, \mathbf{x}) = -t_{ik}$, $\xi^g(t, \mathbf{x}) = f_i$ and reads

$$\frac{\partial \varrho(t, \mathbf{x}) v_i(t, \mathbf{x})}{\partial t} + \frac{\partial}{\partial x_k} \left[\varrho(t, \mathbf{x}) v_i(t, \mathbf{x}) v_k(t, \mathbf{x}) - t_{ik} \right] = \varrho(t, \mathbf{x}) f_i, \tag{B.15}$$

where $t_{ik} = t_{ki}$ represents the Cauchy stress tensor and f_i the external forces. With (B.12) the corresponding momentum balance in material coordinates can be written

as

$$\begin{aligned}\frac{\partial}{\partial t}\hat{v}_i(t,\mathbf{X}) &= \frac{1}{\hat{\varrho}_0}\frac{\partial}{\partial X_j}\left[t_{ik}J(F^{-1})_{jk}\right] + \hat{f}_i,\\ &= \frac{1}{\hat{\varrho}_0}\frac{\partial}{\partial X_j}\left[P_{ij}\right] + \hat{f}_i \end{aligned} \tag{B.16}$$

where $t_{ik}J(F^{-1})_{jk} = P_{ij}$ denotes the usually non symmetric 1st Piola-Kirchoff stress tensor. The 2nd Piola-Kirchoff stress tensor is related to the 1st Piola-Kirchoff stress tensor as follows

$$S_{kj} = (F^{-1})_{ki}P_{ij} \Leftrightarrow F_{lk}S_{kj} = P_{lj}. \tag{B.17}$$

Since many material laws are given in terms of the 2nd Piola-Kirchoff tensor, it is often more convenient to write instead of (B.16)

$$\frac{\partial}{\partial t}\hat{v}_i(t,\mathbf{X}) - \frac{1}{\hat{\varrho}_0}\frac{\partial}{\partial X_j}\left[F_{ik}S_{kj}\right] = \hat{f}_i. \tag{B.18}$$

B.5 Balance of internal energy

The balance of energy can be derived from (B.8) or (B.12) setting $\Psi^g(t,\mathbf{x}) = (e(t,\mathbf{x}) + v^2(t,\mathbf{x})/2)$, $\Phi^g_k(t,\mathbf{x}) = q_k - t_{jk}v_j(t,\mathbf{x})$ and $\xi^g(t,\mathbf{x}) = r + f_i v_i(t,\mathbf{x})$, i.e,

$$\frac{\partial}{\partial t}\left(\varrho\left(e + \frac{v^2}{2}\right)\right) + \frac{\partial}{\partial x_k}\left[\varrho\left(e + \frac{v^2}{2}\right)v_k + q_k - t_{jk}v_j\right] = \varrho(r + f_i v_i), \tag{B.19}$$

with r denoting the radiation, e the internal energy and q_k the heat flux. In order to get a balance equation for the internal energy only, the kinetic energy has to be removed from (B.19). To this end, multiply (B.15) with v_i and exploit (B.4) to get after some rearrangements the balance of kinetic energy, i.e,

$$\frac{\partial}{\partial t}\left(\varrho\frac{v^2}{2}\right) + \frac{\partial}{\partial x_k}\left(\varrho\frac{v^2}{2}v_k - t_{ik}v_i\right) = \varrho f_i v_i - t_{ik}\frac{\partial v_i}{\partial x_k}. \tag{B.20}$$

Subtracting the above expression from (B.19) finally leads to the balance of internal energy

$$\frac{\partial \varrho e}{\partial t} + \frac{\partial}{\partial x_k}\left[\varrho e v_k + q_k\right] = \varrho r + t_{ik}\frac{\partial v_i}{\partial x_k}, \tag{B.21}$$

An energy balance equation in material coordinates corresponding to (B.19), can be deduced setting in (B.12) $\hat{\Psi} = \hat{e} + \hat{v}^2/2$, $\Phi^g_k = q_k - t_{jk}v_j$ and $\hat{\xi}^g = \hat{r} + \hat{f}_i\hat{v}_i$, i.e,

$$\frac{\partial}{\partial t}\left(\hat{e} + \frac{\hat{v}^2}{2}\right) + \frac{1}{\hat{\varrho}_0(\mathbf{X})}\frac{\partial}{\partial X_l}\left[(q_k - t_{jk}v_j)J(F^{-1})_{lk}\right] = \hat{r} + \hat{f}_i\hat{v}_i, \tag{B.22}$$

Introducing the material heat flux $Q_l = q_k J(F^{-1})_{lk}$ and the before mentionend 1st Piola-Kirchoff stress tensor $P_{jl} = t_{jk}J(F^{-1})_{lk}$ yields

$$\frac{\partial}{\partial t}\left(\hat{e} + \frac{\hat{v}^2}{2}\right) + \frac{1}{\hat{\varrho}_0(\mathbf{X})}\frac{\partial}{\partial X_l}\left[Q_l - P_{jl}\hat{v}_j\right] = \hat{r} + \hat{f}_i\hat{v}_i. \tag{B.23}$$

Note that additionally $v_j(t,\mathbf{x})$ has been replaced by the corresponding value in material coordinates $\hat{v}_j(t,\mathbf{X})$. As before, the balance of kinetic energy in material coordinates can be derived by multiplying (B.16) with $\hat{v}_i$ which leads, after some rearrangements, to

$$\frac{\partial}{\partial t}\left(\frac{\hat{v}^2}{2}\right) = \frac{1}{\hat{\varrho}_0(\mathbf{X})}\left(\frac{\partial}{\partial X_l}(P_{il}\hat{v}_i) - P_{il}\frac{\partial \hat{v}_i}{\partial X_l}\right) + \hat{f}_i\hat{v}_i. \tag{B.24}$$

Subtracting (B.24) from (B.19) yields the balance of internal energy in material coordinates, i.e,

$$\hat{\varrho}_0\frac{\partial \hat{e}}{\partial t} + \frac{\partial Q_l}{\partial X_l} = P_{il}\frac{\partial}{\partial t}F_{il} + \hat{\varrho}_0\hat{r}, \tag{B.25}$$

with $\frac{\partial \hat{v}_i}{\partial X_l} = \frac{\partial^2 \chi_i}{\partial t \partial X_l} = \frac{\partial^2 \chi_i}{\partial X_l \partial t} = \frac{\partial}{\partial t}F_{il}$. Note that instead of the 2nd, the 1st Piola Kirchoff stress tensor appears on the right hand side of (B.25). An equivalent formula involving the 2nd Piola Kirchoff tensor can be found using the following identity

$$P_{il}\frac{\partial}{\partial t}F_{il} = F_{im}\underbrace{(F^{-1})_{mj}P_{jl}}_{S_{ml}}\frac{\partial}{\partial t}F_{il} = S_{ml}\underbrace{\left(F_{im}\frac{\partial}{\partial t}F_{il}\right)}_{(*)}. \tag{B.26}$$

Since S_{ml} is symmetric, i.e. $S_{ml} = S_{lm}$, $(*)$ can be replaced by its symmetric part, i.e.

$$S_{ml}\left(F_{im}\frac{\partial}{\partial t}F_{il}\right) = S_{ml}\frac{1}{2}\underbrace{\left(F_{im}\frac{\partial}{\partial t}F_{il} + F_{il}\frac{\partial}{\partial t}F_{im}\right)}_{(**)}. \tag{B.27}$$

Identifying $(**)$ as the time derivative of the right Cauchy Green tensor $C_{ml} = F_{im}F_{il}$, finally leads to

$$\hat{\varrho}_0\frac{\partial \hat{e}}{\partial t} + \frac{\partial Q_l}{\partial X_l} = \frac{1}{2}S_{ml}\frac{\partial}{\partial t}C_{ml} + \hat{\varrho}_0\hat{r}. \tag{B.28}$$

B.6 Balance of entropy

The balance of entropy can be recovered from (B.13) setting $\Psi^g(t,\mathbf{x}) = \eta(t,\mathbf{x})$, $\Phi^g_k(t,\mathbf{x}) = \phi_k(t,\mathbf{x})$ and $\xi^g(t,\mathbf{x}) = \sigma(t,\mathbf{x}) + \eta(t,\mathbf{x})$, i.e,

$$\frac{\partial \varrho\eta}{\partial t} + \frac{\partial}{\partial x_k}\left[\varrho\eta v_k + \phi_k\right] = \varrho\left(\sigma + s\right). \tag{B.29}$$

Again with (B.12), the entropy balance in material coordinates can be written as

$$\begin{aligned}\frac{\partial}{\partial t}\hat{\eta}(t,\mathbf{X}) &= \frac{1}{\varrho_0(\mathbf{X})}\frac{\partial}{\partial X_i}\left[\phi_k J(F^{-1})_{ik}\right] + (\hat{\sigma} + \hat{s}),\\ &= \frac{1}{\varrho_0(\mathbf{X})}\frac{\partial \Phi_i}{\partial X_i} + (\hat{\sigma} + \hat{s}),\end{aligned} \tag{B.30}$$

with $\Phi_i(t,\mathbf{X}) = \phi_k J(F^{-1})_{ik}$ denoting the material entropy flux.

Appendix C

Space discretisation of the PDE-part

C.1 Preparation

The finite dimensional spaces $V_n = \text{span}\{v_1, \ldots, v_n\}$ and $W_n = \text{span}\{\psi_1, \ldots, \psi_n\}$ arising in section 4.1.2 can be approximated with (conforming) finite elements. In order to construct the corresponding finite element matrices, recall that the functions v_i are related to the functions ψ_j by the following rule, i.e.

$$\left\{ \begin{pmatrix} \psi_1 \\ 0 \\ 0 \end{pmatrix}, \begin{pmatrix} 0 \\ \psi_1 \\ 0 \end{pmatrix}, \begin{pmatrix} 0 \\ 0 \\ \psi_1 \end{pmatrix}, \begin{pmatrix} \psi_2 \\ 0 \\ 0 \end{pmatrix}, \begin{pmatrix} 0 \\ \psi_2 \\ 0 \end{pmatrix}, \begin{pmatrix} 0 \\ 0 \\ \psi_2 \end{pmatrix}, \ldots \right\} = \{v_1, v_2, v_3, v_4, v_5, v_6, \ldots\},$$

and rewrite the representation (4.4) defined in Section 4.1.2, in a different form, i.e.

$$\begin{aligned} (u^n(\mathbf{X}, t))_b &= \sum_{k=1}^{3n} d^k(t)(v_k(\mathbf{X}))_b = \sum_{i=1}^{n} \sum_{a=1}^{3} d^{j(i,a)}(t)\delta_{ab}\psi_i(\mathbf{X}) \\ &= \sum_{i=1}^{n} d^{j(i,b)}(t)\psi_i(\mathbf{X}) = \sum_{i=1}^{n} D_b^i(t)\psi_i(\mathbf{X}) \end{aligned} \tag{C.1}$$

with the index $b = 1, 2, 3$ characterising the spatial direction, the index function $j(i, a) = 3(i - 1) + a$ and coefficients $D_b^i(t) = d^{j(i,b)}(t)$. Similarly, an arbitrary test function v can be written as a linear combination of the basis elements $v_1, v_2, \ldots, v_{3n}$, i.e.

$$\begin{aligned} (v(\mathbf{X}))_b &= \sum_{k=1}^{3n} c^k(v_k(\mathbf{X}))_b = \sum_{i=1}^{n} \sum_{a=1}^{3} c^{j(i,a)}\delta_{ab}\psi_i(\mathbf{X}) \\ &= \sum_{i=1}^{n} c^{j(i,b)}\psi_i(\mathbf{X}) = \sum_{i=1}^{n} V_b^i\psi_i(\mathbf{X}), \end{aligned} \tag{C.2}$$

again with the index $b = 1, 2, 3$ characterising the spatial direction, the index function $j(i, a) = 3(i - 1) + a$ and coefficients $V_b^i = c^{j(i,b)} = const.$

C.2 Balance of momentum

As outlined in Section 4.1.2, the weak form of the balance of momentum (4.2a) reads

$$\int_\Omega \hat{\varrho}_0 u_{tt} v d\mathbf{X} + \int_\Omega \sigma(u,\Theta) : \varepsilon(v) d\mathbf{X} = \int_\Omega \hat{\varrho}_0 s_m^e(t,z,\dot{z},u,\Theta) v d\mathbf{X}, \qquad \forall v, \tag{C.3}$$

with the stress tensor

$$\sigma = \lambda \mathrm{Tr}[\varepsilon]\mathbf{I} + 2\mu\varepsilon - 3K\alpha\Theta\mathbf{I},$$

and $2\varepsilon = \mathrm{Grad}(u) + (\mathrm{Grad}(u))^T$. Now, exploiting (C.1) and (C.2) the system matrices can be constructed for each term in the weak formulation. The first term gives

$$\begin{aligned}
\int_\Omega \hat{\varrho}_0 u_{tt} \cdot v \; d\mathbf{X} &= \int_\Omega \hat{\varrho}_0 \sum_{a=1}^{3} \left(\sum_{k=1}^{n} \psi_k(\mathbf{X}) \ddot{D}_a^k(t) \sum_{l=1}^{n} \psi_l(\mathbf{X}) V_a^l \right) \; d\mathbf{X}, \\
&= \sum_{a=1}^{3} \sum_{k,l=1}^{n} \int_\Omega \hat{\varrho}_0 \psi_k(\mathbf{X}) \psi_l(\mathbf{X}) \; d\mathbf{X} \; \ddot{D}_a^k(t) V_a^l, \\
&= \sum_{a,b=1}^{3} \sum_{k,l=1}^{n} \underbrace{\int_\Omega \hat{\varrho}_0 \psi_k(\mathbf{X}) \psi_l(\mathbf{X}) \delta_{ab} \; d\mathbf{X}}_{M_{kl}^{ab}} \; \ddot{D}_a^k(t) V_b^l,
\end{aligned} \tag{C.4}$$

where δ_{ab} represents the so called Kronecker-δ, i.e.

$$\delta_{ij} = \begin{cases} 1, & \text{if} \quad i = j, \\ 0, & \text{if} \quad i \neq j. \end{cases}$$

Inserting the definition of the stress tensor into the weak formulation yields

$$\begin{aligned}
\int_\Omega \sigma(u,\Theta) : \varepsilon(v) \; d\mathbf{X} &= \int_\Omega \Big[\lambda \mathrm{Tr}[\varepsilon(u)]\mathbf{I} + 2\mu\varepsilon(u) - 3K\alpha\Theta\mathbf{I} \Big] : \varepsilon(v) \; d\mathbf{X} \\
&= \lambda \int_\Omega \mathrm{Div}(u)\mathrm{Div}(v) d\mathbf{X} + 2\mu \int_\Omega \varepsilon(u) : \varepsilon(v) \; d\mathbf{X} \\
&\quad - 3K\alpha \int_\Omega \Theta \mathrm{Div}(v) \; d\mathbf{X}.
\end{aligned} \tag{C.5}$$

With (C.1) and (C.2), the first integral in the above equation gives

$$\begin{aligned}
\int_\Omega \lambda \mathrm{Div}(u^n)\mathrm{Div}(v) d\mathbf{X} &= \int_\Omega \lambda \sum_{a=1}^{3} \frac{\partial (u^n(t,\mathbf{X}))_a}{\partial \mathbf{X}_a} \sum_{b=1}^{3} \frac{\partial (v(\mathbf{X}))_b}{\partial \mathbf{X}_b} d\mathbf{X} \\
&= \int_\Omega \lambda \sum_{a=1}^{3} \sum_{k=1}^{n} \frac{\partial \psi_k(\mathbf{X})}{\partial \mathbf{X}_a} D_a^k(t) \sum_{b=1}^{3} \sum_{l=1}^{n} \frac{\partial \psi_l(\mathbf{X})}{\partial \mathbf{X}_b} V_b^l d\mathbf{X} \\
&= \sum_{a,b=1}^{3} \sum_{k,l=1}^{n} \int_\Omega \lambda \frac{\partial \psi_k(\mathbf{X})}{\partial \mathbf{X}_a} \frac{\partial \psi_l(\mathbf{X})}{\partial \mathbf{X}_b} d\mathbf{X} \; D_a^k(t) V_b^l.
\end{aligned} \tag{C.6}$$

The second integral reads

$$\begin{aligned}\int_\Omega 2\mu\varepsilon(u) : \varepsilon(v)\ d\mathbf{X} &= \int_\Omega 2\mu \sum_{b,c=1}^{3} \varepsilon_{bc}(u)\varepsilon_{bc}(v)\ d\mathbf{X} \\ &= \int_\Omega \mu \sum_{b,c=1}^{3} \frac{\partial(u(t,\mathbf{X}))_b}{\partial \mathbf{X}_c}\frac{\partial v_b}{\partial \mathbf{X}_c} d\mathbf{X} \\ &\quad + \int_\Omega \mu \sum_{b,c=1}^{3} \frac{\partial(u(t,\mathbf{X}))_b}{\partial \mathbf{X}_c}\frac{\partial v_c}{\partial \mathbf{X}_b}\ d\mathbf{X}. \end{aligned} \tag{C.7}$$

The integrals arising in the previous expression can be evaluated separately. While the first integral gives

$$\begin{aligned}\int_\Omega \mu \sum_{b,c=1}^{3} \frac{\partial(u^n(t,\mathbf{X}))_b}{\partial \mathbf{X}_c}\frac{\partial v_b}{\partial \mathbf{X}_c} d\mathbf{X} &= \int_\Omega \mu \sum_{b,c=1}^{3}\sum_{k=1}^{n} \frac{\partial \psi_k(\mathbf{X})}{\partial \mathbf{X}_c} D_b^k(t) \sum_{l=1}^{n} \frac{\partial \psi_l(\mathbf{X})}{\partial \mathbf{X}_c} V_b^l d\mathbf{X} \\ &= \int_\Omega \mu \sum_{a,b,c=1}^{3}\sum_{k,l=1}^{n} \frac{\partial \psi_k(\mathbf{X})}{\partial \mathbf{X}_c} D_a^k(t)\delta_{ab} \frac{\partial \psi_l(\mathbf{X})}{\partial \mathbf{X}_c} V_b^l d\mathbf{X} \\ &= \sum_{a,b=1}^{3}\sum_{k,l=1}^{n} \int_\Omega \mu \left(\sum_{c=1}^{3} \frac{\partial \psi_k(\mathbf{X})}{\partial \mathbf{X}_c}\frac{\partial \psi_l(\mathbf{X})}{\partial \mathbf{X}_c} \right) \delta_{ab}\ d\mathbf{X}\ D_a^k(t) V_b^l, \end{aligned} \tag{C.8}$$

the second integral leads to

$$\begin{aligned}\int_\Omega \mu \sum_{b,c=1}^{3} \frac{\partial(u^n(t,\mathbf{X}))_b}{\partial \mathbf{X}_c}\frac{\partial v_c}{\partial \mathbf{X}_b}\ d\mathbf{X} &= \int_\Omega \mu \sum_{a,b=1}^{3} \frac{\partial(u^n(t,\mathbf{X}))_a}{\partial \mathbf{X}_b}\frac{\partial v_b}{\partial \mathbf{X}_a}\ d\mathbf{X} \\ &= \int_\Omega \mu \sum_{a,b=1}^{3}\sum_{k=1}^{n} \frac{\partial \psi_k(\mathbf{X})}{\partial \mathbf{X}_b} D_a^k(t) \sum_{l=1}^{n} \frac{\partial \psi_l(\mathbf{X})}{\partial \mathbf{X}_a} V_b^l\ d\mathbf{X} \\ &= \sum_{a,b=1}^{3}\sum_{k,l=1}^{n} \int_\Omega \mu \frac{\partial \psi_k(\mathbf{X})}{\partial \mathbf{X}_b}\frac{\partial \psi_l(\mathbf{X})}{\partial \mathbf{X}_a} d\mathbf{X}\ D_a^k(t) V_b^l. \end{aligned} \tag{C.9}$$

Recombining (C.6), (C.8) and (C.9) with (C.5) finally yields the result

$$\begin{aligned}\int_\Omega \sigma(u^n, \Theta^n) : \varepsilon(v)\ d\mathbf{X} &= \sum_{a,b=1}^{3}\sum_{k,l=1}^{n} \left[K_{kl}^{ab}\right] D_a^k(t) V_b^l \\ &\quad - 3K\alpha \int_\Omega \Theta^n \mathrm{Div}(v)\ dx. \end{aligned} \tag{C.10}$$

with

$$\begin{aligned} K_{kl}^{ab} \quad = \quad & \int_\Omega \lambda \frac{\partial \psi_k(\mathbf{X})}{\partial \mathbf{X}_a}\frac{\partial \psi_l(\mathbf{X})}{\partial \mathbf{X}_b} d\mathbf{X} \\ & + \int_\Omega \mu \left(\sum_{c=1}^{3} \frac{\partial \psi_k(\mathbf{X})}{\partial \mathbf{X}_c}\frac{\partial \psi_l(\mathbf{X})}{\partial \mathbf{X}_c} \right) \delta_{ab} d\mathbf{X} \\ & + \int_\Omega \mu \frac{\partial \psi_k(\mathbf{X})}{\partial \mathbf{X}_b}\frac{\partial \psi_l(\mathbf{X})}{\partial \mathbf{X}_a} d\mathbf{X}. \end{aligned} \tag{C.11}$$

representing the stiffness matrix. The last integral in (C.5) assumes the form

$$\begin{aligned}\int_\Omega 3K\alpha\Theta^n \mathrm{Div}(v)\, d\mathbf{X} &= \int_\Omega 3K\alpha\Theta^n \sum_{b=1}^{3} \frac{\partial v_b}{\partial \mathbf{X}_b}\, d\mathbf{X} \\ &= \int_\Omega 3K\alpha \sum_{k=1}^{n} \psi_k(\mathbf{X})\gamma^k(t) \sum_{b=1}^{3}\sum_{l=1}^{n} \frac{\partial \psi_l(\mathbf{X})}{\partial \mathbf{X}_b} V_b^l\, d\mathbf{X} \\ &= \sum_{b=1}^{3}\sum_{k,l=1}^{n} \int_\Omega 3K\alpha\psi_k(\mathbf{X}) \frac{\partial \psi_l(\mathbf{X})}{\partial \mathbf{X}_b}\, d\mathbf{X}\gamma^k(t) V_b^l \\ &= \sum_{b=1}^{3}\sum_{k,l=1}^{n} C_{kl}^b\, \gamma^k(t) V_b^l, \end{aligned} \tag{C.12}$$

with

$$C_{kl}^b = \int_\Omega 3K\alpha\psi_k(\mathbf{X}) \frac{\partial \psi_l(\mathbf{X})}{\partial \mathbf{X}_b}\, d\mathbf{X}, \tag{C.13}$$

denoting the coupling matrix. The discretisation of the right hand side in (4.2a) reads

$$\begin{aligned}\int_\Omega \hat{\varrho}_0 s_m^e v d\mathbf{X} &= \int_\Omega \hat{\varrho}_0 \sum_{b=1}^{3} (s_m^e)_b v_b d\mathbf{X} = \int_\Omega \hat{\varrho}_0 \sum_{b=1}^{3} (s_m^e)_b \sum_{l=1}^{n} \psi_l(\mathbf{X}) V_b^l d\mathbf{X} \\ &= \sum_{b=1}^{3}\sum_{l=1}^{n} \int_\Omega \hat{\varrho}_0 (s_m^e)_b \psi_l(\mathbf{X}) d\mathbf{X}\, V_b^l \\ &= \sum_{b=1}^{3}\sum_{l=1}^{n} R_l^b V_b^l, \end{aligned} \tag{C.14}$$

with $R_l^b = \int_\Omega \hat{\varrho}_0 (s_m^e)_b \psi_l(\mathbf{X}) d\mathbf{X}$. Inserting the discrete expressions (C.12) into (C.10) and combining the result together with (C.14) and (C.4) with (C.3), leads to

$$\begin{aligned} 0 = &\sum_{a,b=1}^{3}\sum_{k,l=1}^{n} \left[M_{kl}^{ab}\right] \ddot{D}_a^k(t) V_b^l + \sum_{a,b=1}^{3}\sum_{k,l=1}^{n} \left[K_{kl}^{ab}\right] D_a^k(t) V_b^l \\ &- \sum_{b=1}^{3}\sum_{k,l=1}^{n} C_{kl}^b\, \gamma^k(t) V_b^l - \sum_{b=1}^{3}\sum_{l=1}^{n} R_l^b V_b^l, \\ = &\sum_{b=1}^{3}\sum_{l=1}^{n} \Bigg[\sum_{a=1}^{3}\sum_{k=1}^{n} M_{kl}^{ab} \ddot{D}_k^a(t) + \sum_{a=1}^{3}\sum_{k=1}^{n} K_{kl}^{ab}\, D_a^k(t) \\ &- \sum_{k=1}^{n} C_b^{kl} \gamma^k(t) - R_l^b \Bigg] V_b^l. \end{aligned}$$

Since (C.3) has to be fulfilled for all test functions $v \in V_n$ and in particular for $(v)_b = \sum_{l=1}^{n} \psi_l V_b^l$ with arbitrary V_b^l, the expression in the square brackets has to

vanish. Thus, for all $l = 1, \ldots, n$ and $b = 1, 2, 3$, the finite dimensional balance of momentum reads

$$\sum_{a=1}^{3}\sum_{k=1}^{n} M_{kl}^{ab}\ddot{D}_a^k(t) + \sum_{a=1}^{3}\sum_{k=1}^{n} K_{kl}^{ab}\ D_a^k(t) = \sum_{k=1}^{n} C_{kl}^{b}\gamma^k(t) + R_b^l. \tag{C.15}$$

Rewriting the above equation in matrix/vector notation finally gives

$$\mathbf{M}\left[\ddot{d}^j(t)\right] + \mathbf{K}\left[d^j(t)\right] = \mathbf{C}\left[\gamma^k(t)\right] + \mathbf{R}, \tag{C.16}$$

where $d^j(t) = d^{j(k,b)} = D_b^k(t)$ and $j = 1, \ldots, 3n$ and $k = 1, \ldots, n$.

C.2.1 Energy balance

The finite dimensional energy balance can be directly derived from (4.2b) and the representation (4.4), i.e. $\Theta^n(\mathbf{X}, t) = \sum_{k=1}^{n} \gamma^k(t)\psi_k(\mathbf{X})$, choosing $w = \psi_l$. The result reads

$$\begin{aligned}\sum_{i=1}^{n} \dot{\gamma}^i(t) \int_\Omega \varrho c_D \psi_i \psi_l d\mathbf{X} + \sum_{i=1}^{n} \gamma^i(t) \int_\Omega \kappa \mathrm{Grad}(\psi_i)\mathrm{Grad}(\psi_l) d\mathbf{X} \\ + \int_\Omega 3K\alpha T_0 \mathrm{Div}(u_t^n(t, \mathbf{X}))\psi_l d\mathbf{X} = \int_\Omega s_e^e \psi_l d\mathbf{X},\end{aligned} \tag{C.17}$$

with mass matrix

$$m_{il} = \int_\Omega \varrho c_D \psi_i \psi_l d\mathbf{X}, \qquad i, l = 1, \ldots, n,$$

stiffness matrix

$$k_{il} = \int_\Omega \kappa \mathrm{Grad}(\psi_i)\mathrm{Grad}(\psi_l) d\mathbf{X}, \qquad i, l = 1, \ldots, n,$$

and right hand side

$$r_l = \int_\Omega s_e^e \psi_l d\mathbf{X}, \qquad l = 1, \ldots, n.$$

The coupling term can be further evaluated by introducing the previously mentioned notation of the displacement field, i.e.

$$\begin{aligned}\int_\Omega 3K\alpha T_0 \mathrm{Div}(u_t^n(t, \mathbf{X}))\psi_l d\mathbf{X} &= \int_\Omega 3K\alpha T_0 \sum_{a=1}^{3} \frac{\partial (u_t^n(t, \mathbf{X}))_a}{\partial \mathbf{X}_a} \psi_l d\mathbf{X} \\ &= \int_\Omega 3K\alpha T_0 \sum_{a=1}^{3}\sum_{k=1}^{n} \frac{\partial \psi_k}{\partial \mathbf{X}_a} \dot{D}_a^k(t) \psi_l d\mathbf{X} \\ &= \sum_{a=1}^{3}\sum_{k=1}^{n} \int_\Omega 3K\alpha T_0 \frac{\partial \psi_k}{\partial \mathbf{X}_a} \psi_l d\mathbf{X}\ \dot{D}_a^k(t) \\ &= \sum_{a=1}^{3}\sum_{k=1}^{n} c_a^{kl}\ \dot{D}_a^k(t),\end{aligned} \tag{C.18}$$

with c_a^{kl} denoting the second coupling matrix. With the abbreviations introduced above, the finite dimensional energy balance reads for all $l = 1, \ldots, n$

$$\sum_{i=1}^{n} \dot{\gamma}^i(t) m_{il} + \sum_{i=1}^{n} \gamma^i(t) k_{il} + \sum_{a=1}^{3} \sum_{k=1}^{n} c_a^{kl} \dot{D}_a^k(t) = r_l. \tag{C.19}$$

In matrix/vector notation, the above equation reads

$$\mathbf{m}\left[\dot{\gamma}^k(t)\right] + \mathbf{k}[\gamma^k(t)] + \mathbf{c}\left[\dot{d}^j(t)\right] = \mathbf{r}. \tag{C.20}$$

where $\dot{d}^j(t) = \dot{d}^{j(k,a)} = \dot{D}_a^k(t)$ and $j = 1, \ldots, 3n$.

C.3 Initial conditions

C.3.1 Balance of momentum

In order to compute the finite dimensional representation $d^j(0)$, with $j = 1, \ldots, 3n$, of an initial condition $u_0 \in V$, consider the variational formulation

$$\int_\Omega v u^n(0, \mathbf{X}) d\mathbf{X} = \int_\Omega v u_0 d\mathbf{X}, \qquad \forall\, v \in V.$$

$$\Leftrightarrow \qquad \int_\Omega \sum_{a=1}^{3} (v)_a (u^n(0, \mathbf{X}))_a d\mathbf{X} = \int_\Omega \sum_{a=1}^{3} (v)_a (u_0)_a d\mathbf{X}, \qquad \forall\, v \in V.$$

Inserting the representations (C.1) and (C.2) into the left hand side leads to

$$\begin{aligned} \int_\Omega \sum_{a=1}^{3} (v)_a (u^n(0, \mathbf{X}))_a d\mathbf{X} &= \int_\Omega \sum_{a=1}^{3} \sum_{l=1}^{n} V_a^l \psi_l(\mathbf{X}) \sum_{k=1}^{n} D_a^k(0) \psi_k(\mathbf{X}) d\mathbf{X} \\ &= \sum_{a,b=1}^{3} \sum_{k,l=1}^{n} \int_\Omega \psi_l(\mathbf{X}) \psi_k(\mathbf{X}) \delta_{ab}\, d\mathbf{X}\, D_a^k(0) V_b^l. \end{aligned}$$

Similarly, the left hand side reads

$$\begin{aligned} \int_\Omega \sum_{a=1}^{3} (v)_a (u_0)_a d\mathbf{X} &= \int_\Omega \sum_{b=1}^{3} \sum_{l=1}^{n} V_b^l \psi_l(\mathbf{X}) (u_0)_b d\mathbf{X} \\ &= \sum_{b=1}^{3} \sum_{l=1}^{n} \int_\Omega \psi_l(\mathbf{X}) (u_0)_b d\mathbf{X} V_b^l. \end{aligned}$$

Combining both expressions gives the variational equation

$$0 = \sum_{b=1}^{3} \sum_{l=1}^{n} \left(\sum_{a=1}^{3} \sum_{k=1}^{n} \int_\Omega \psi_l(\mathbf{X}) \psi_k(\mathbf{X}) \delta_{ab}\, d\mathbf{X} D_a^k(0) - \int_\Omega \psi_l(\mathbf{X}) (u_0)_b d\mathbf{X} \right) V_b^l, \qquad \forall\, V_b^l.$$

Since V_b^l is arbitrary, the above condition holds if and only if

$$\sum_{a=1}^{3} \sum_{k=1}^{n} \int_\Omega \psi_l(\mathbf{X}) \psi_k(\mathbf{X}) \delta_{ab} d\mathbf{X} D_a^k(0) = \int_\Omega \psi_l(\mathbf{X}) (u_0)_b d\mathbf{X}.$$

In matrix/vector notation and with the identity $d^j(0) = d^{j(k,a)}(0) = D_a^k(0)$, the above equations reads

$$\mathbf{M}\left[d^j(0)\right] = \mathbf{R}^0(u_0), \tag{C.21}$$

where $\mathbf{M}$ denotes the previously introduced mass matrix and $(\mathbf{R}(u_0))_{lc} = \int_\Omega \hat{\varrho}_0 \psi_l(\mathbf{X})(u_0)_c d\mathbf{X}$. Similarly, the finite dimensional representation $\dot{d}^j(0)$, with $j = 1, \ldots, 3n$, of the initial condition for the velocity field $v_0 \in V$ can be computed solving the linear system

$$\mathbf{M}\left[\dot{d}^j(0)\right] = \mathbf{R}^0(v_0). \tag{C.22}$$

C.3.2 Balance of internal energy

The finite dimensional representation $\gamma^k(0)$, $k = 1, \ldots, n$, of an initial condition $\Theta_0 \in W$ can be computed from the variational formulation

$$\int_\Omega w\Theta^n(0, \mathbf{X}) d\mathbf{X} = \int_\Omega w\Theta_0(\mathbf{X}) d\mathbf{X}, \qquad \forall w \in W.$$

Inserting the definition $\Theta^n(0,t) = \sum_{k=1}^n \gamma^k(0)\psi_k(\mathbf{X})$ and choosing $w = \psi_l(\mathbf{X})$ leads to

$$\sum_{k=1}^n \int_\Omega \psi_l(\mathbf{X})\psi_k(\mathbf{X}) d\mathbf{X}\gamma^k(0) = \int_\Omega \psi_l(\mathbf{X})\Theta_0(\mathbf{X}) d\mathbf{X},$$

for all $l = 1, \ldots, n$. In matrix/vector notation the condition reads

$$\mathbf{m}\left[\gamma^k(0)\right] = \mathbf{r}^0(\Theta_0), \tag{C.23}$$

where $\mathbf{m}$ denotes the previously introduced mass matrix and $(\mathbf{r}^0(\Theta_0))_l = \int_\Omega \hat{\varrho}_0 c_D \psi_l(\mathbf{X})\Theta_0(\mathbf{X}) d\mathbf{X}$.

Appendix D

Material damping models (viscoelasticity)

D.1 Uni-axial stress and strain

D.1.1 Review of linear damping models

As outlined by Lazan [57], the damping capacity of a material can be measured with the loss coefficient η being defined as

$$\eta = \frac{D}{2\pi U}. \tag{D.1}$$

The damping D is defined as the area enclosed by the hysteretic loop shown in Figure D.1. For a cyclic strain with amplitude ε_a and frequency ω, the damping is given by

$$D = \int_0^{\frac{2\pi}{\omega}} \sigma \frac{d\varepsilon}{dt} dt. \tag{D.2}$$

For a nonlinear stress strain relation the strain energy U can be defined in several ways [57]. Among them, the definition based on the mid stress (see Figure D.1), seems to be a quite general concept. Thus, following the arguments of Lazan [57], the strain energy reads

$$U = \int_0^{\varepsilon_a} \sigma_{mid}(\varepsilon)\, d\varepsilon = \frac{1}{2} \int_0^{\varepsilon_a} \sigma_{dec}(\varepsilon) + \sigma_{inc}(\varepsilon)\, d\varepsilon. \tag{D.3}$$

The loss coefficient introduced above can be used to classify different linear and non linear damping models. The material law and the loss coefficient corresponding to the Maxwell model illustrated in Figure D.2 read

$$\dot{\sigma} + \frac{k_1}{\mu_1}\sigma = k_1 \dot{\varepsilon}, \tag{D.4}$$

$$\eta_{mw} = \frac{k_1}{\omega \mu_1}, \tag{D.5}$$

with k_1 and μ_1 representing material constants. The form of the loss coefficient (D.5)

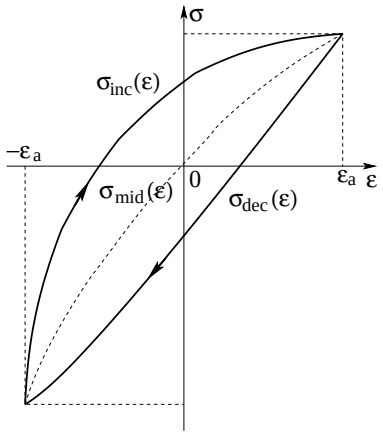

Figure D.1: Stress-strain relation for an arbitrary nonlinear visco-elastic body under cyclic load.

Figure D.2: Maxwell and Kelvin-Voigt model for uni-axial stress and strain.

indicates that the Maxwell material law provides large damping for small frequencies which becomes smaller and finally tends to zero for increasing frequencies ω. The Kelvin-Voigt material model illustrated in Figure D.2 provides the opposite damping characteristic. The material law and loss coefficient, i.e.

$$\sigma = k_1 \varepsilon + \mu_1 \dot{\varepsilon}, \tag{D.6}$$

$$\eta_{kv} = \omega \frac{\mu_1}{k_1}, \tag{D.7}$$

with material constants k_1 and μ_1, reveal that the damping corresponding to the Kelvin-Voigt material model is small for low frequencies, increases with increasing frequencies. The standard linear solid model shown in Figure D.3 is a combination of the Maxwell and the Kelvin-Voigt model. The configurations illustrated in Figure D.3 are equivalent, i.e. both models lead to similar material laws that can be

Figure D.3: Equivalent standard linear solid models for uni-axial stress and strain.

converted into each other by an appropriate choice of the material constants. The corresponding material laws read

$$\dot{\sigma} + \frac{k_a}{\mu_a}\sigma = \frac{k_a k_b}{\mu_a}\varepsilon + (k_a + k_b)\dot{\varepsilon} \tag{D.8}$$

$$\Leftrightarrow \dot{\sigma} + \frac{k_1 + k_2}{\mu_1}\sigma = \frac{k_1 k_2}{\mu_1}\varepsilon + k_2\dot{\varepsilon}. \tag{D.9}$$

The model (D.9) can be derived from (D.8) by choosing the material constants as

$$k_a = \frac{(k_2)^2}{k_1 + k_2},$$
$$k_b = \frac{k_1 k_2}{k_1 + k_2},$$
$$\mu_a = \frac{\mu_1 (k_2)^2}{(k_1 + k_2)^2}.$$

The material models presented before can be interpreted as special cases of the standard linear solid (D.9). Taking the limit $k_1 \to 0$ leads to the Maxwell model. The Kelvin-Voigt model can be derived from (D.9) considering the limit $k_2 \to \infty$. The loss coefficient corresponding to (D.9) reads

$$\eta_{sls} = \frac{\mu_1 k_2 \omega}{k_1(k_1 + k_2) + (\mu_1)^2\omega^2} = C_{sls}\frac{\tau_r \omega}{1 + \tau_r^2\omega^2}, \tag{D.10}$$

with a constant $C_{sls} = k_2(\sqrt{k_1(k_1 + k_2)})^{-1}$ and the relaxation time

$$\tau_r^2 = \frac{(\mu_1)^2}{k_1(k_2 + k_2)}.$$

The loss coefficient (D.10) also depends on the input frequency. The material provides for a frequency $\omega_{max} = 1/\tau_r$ the highest damping capacity $\eta_{sls}^{max} = C_{sls}/2$. If the frequency tends to zero or to infinity, the loss coefficient and thus the damping capacity converges to zero. In the frequency range corresponding to milling processes, grain boundary (for polycristalline aluminium) and macro– and micro–thermo–elasticity effects are sources of material damping (see [57]). The damping characteristic induced by these effects can qualitatively be reproduced by the standard linear solid model (D.9).

For a given $\varepsilon(t)$ sufficiently smooth, (D.8) can be solved analytically using the variation of constants formula, i.e.

$$\sigma(t) = \sigma(0)e^{-\frac{k_a}{\mu_a}t} + e^{-\frac{k_a}{\mu_a}t}\int_0^t e^{\frac{k_a}{\mu_a}s}\left(\frac{k_a k_b}{\mu_a}\varepsilon(s) + (k_a + k_b)\dot{\varepsilon}(s)\right)ds. \tag{D.11}$$

For $\sigma(0) = 0$ and $\varepsilon(0) = 0$, (D.11) can be written in a more compact form (see [30], [40]). By means of integration by parts and some rearrangements one can show that

$$\sigma(t) = \int_0^t R(t - s)\dot{\varepsilon}(s)ds, \tag{D.12}$$

with the so called *relaxation function*

$$R(s) = \left[k_b + k_a \exp\left(-\frac{k_a}{\mu_a} s \right) \right]. \tag{D.13}$$

An alternative formulation of (D.12) can be derived by means of integration by parts and exploiting the condition $\varepsilon(0) = 0$, i.e.

$$\sigma(t) = R(0)\varepsilon(t) + \int_0^t R'(t-s)\varepsilon(t)ds, \tag{D.14}$$

Because the effect of any previous strains decays with time, it is mathematically convenient to imagine that the material has existed forever and the origin of behaviour is at $t_{or} = -\infty$ (cf. [30]). The constitutive relation can then be written as

$$\sigma(t) = R(0)\varepsilon(t) + \int_{-\infty}^t R'(t-s)\varepsilon(t)ds. \tag{D.15}$$

The corresponding constitutive equation presented in [40] can be recovered from (D.15) using the substitution rule, i.e.

$$\sigma(t) = R(\infty)\varepsilon(t) + \int_0^\infty R'(s)\varepsilon_d^t(s)ds, \tag{D.16}$$

with the relative strain history $\varepsilon_d^t(s) = \varepsilon(t-s) - \varepsilon(t)$. Note that the material laws defined by (D.12) and (D.14) are different formulations of a constitutive law describing linear visco-elastic bodies for uniaxial stress and strain. Supposing an infinite strain history leads to similar formulations given by (D.15) and (D.16). For the strain jumping from zero to ε_0, i.e

$$\bar{\varepsilon}(t) = \begin{cases} 0 & \text{for} \quad t \leq 0, \\ \varepsilon_0 & \text{otherwise}, \end{cases} \tag{D.17}$$

the integral in (D.16) reads

$$\int_0^\infty R'(s)[\bar{\varepsilon}(t-s) - \bar{\varepsilon}(t)]ds = \varepsilon_0(R(t) - R(\infty)) \tag{D.18}$$

and thus converges to zero for $t \to \infty$. Consequently, passing to the limit in (D.16) gives

$$\lim_{t\to\infty} \sigma(t) = \sigma_{eq} = R(\infty)\varepsilon_0 = E_{eq}\varepsilon_0 = k_b\varepsilon_0. \tag{D.19}$$

Since E_{eq} represents the **ersatz** stiffness of the standard linear solid model illustrated in Figure D.3, $R(\infty)$ is called equilibrium modulus and σ_{eq} equilibrium stress [40].

However, real metals do not have a fixed size or character in their microconstituents. The size, shape, and environment of grains and the grain boundary properties all vary form point to point. Thus, macroscopic behaviour depends on the distribution of the important features of the microstructure. Under load the response of these visco-elastic materials includes both short-time and long-time reordering characteristics. These characteristics of real materials can usually only be simulated

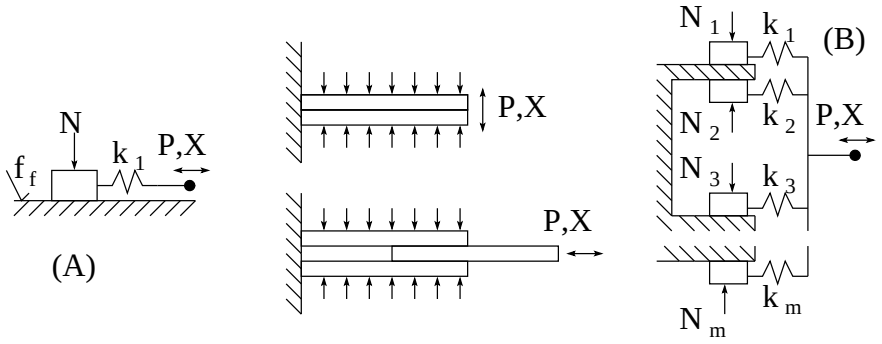

Figure D.4: Biparameter elasto-slide (A) and general elasto-slip (B) model.

in models by use of multiple relaxation times (see [57]). Such models correspond to a spring and N Maxwell elements in parallel arrangement. As shown in [40], the corresponding constitutive equations can be constructed by replacing the simple relaxation function (D.13) with

$$R(s) = E_{eq} + \sum_{j=1}^{N} k_j \exp\left(-\frac{k_j}{\mu_j} t\right) \tag{D.20}$$

or with a continuous relaxation spectrum, i.e.

$$R(s) = E_{eq} + \int_0^{\infty} k(z) \exp\left(-\frac{t}{z}\right) dz. \tag{D.21}$$

Note that the parameters k_j, μ_j and the function $k(z)$ have to be determined experimentally.

D.1.2 Review of nonlinear and rate independent damping effects

Another important source of damping is friction between joint interfaces. A simple model to describe the damping effects arising from joint interfaces is illustrated in Figure D.4. The loss coefficient corresponding to the biparameter elasto-slide-model reads

$$\eta_s = \begin{cases} 0 & \text{if} \quad X_a < f_f N/k_1, \\ \frac{4}{\pi}\left(\frac{X_a k_1}{f_f N} - 1\right) & \text{otherwise.} \end{cases} \tag{D.22}$$

The value X_a denotes the amplitude of the imposed displacement $X(t)$. Analysing the form of the loss coefficient (D.22) reveals that the elasto-slide damping does not depend on the frequency but on the amplitude of the input displacement. Consequently, the elasto-slide effects have to be classified as rate independent and nonlinear damping phenomena. However, the general case of damping due to interface friction is more difficult. Vibrating elastic bodies connected to each other by a joint interface, only induce a relative motion on the contact zone if the shear stress on

the interface exceeds the yield stress given by normal stress and frictional coefficient. Since the distribution of normal and shear stress changes in time due to the oscillation of the elastic bodies, the elasto-slide effects occur non uniformly and progressively. This kind of friction damping effect is often called elasto-slip and can be modelled combining several elasto-slide elements with different normal forces N_i and elastic constants k_i (see [57]). Figure D.4 illustrates different contact conditions and a scheme representing the elasto-slip model. Since the dissipation mechanism is similar to the elasto-slide case, the elasto-slip damping effects are also nonlinear and rate independent.

D.2 Review of linear damping models for multi-axial stress and strain

The constitutive equations in the multi-axial case are similar to the formulae presented in section D.1.1. The constitutive law corresponding to (D.12) given by [40] reads

$$\sigma(t) = \int_0^t K(t-s)\mathrm{Tr}[\varepsilon'(s)]\mathbf{I} + 2\mu(t-s)\langle\varepsilon'(s)\rangle ds, \tag{D.23}$$

with $K(.)$ denoting the bulk modulus and $\mu(.)$ the shear modulus respectively. While $\langle\varepsilon'(s)\rangle$ represents the deviatoric part, $\mathrm{Tr}[\varepsilon'(s)]$ provides the trace of $\varepsilon'(s)$. Dill [30] presents an alternative formulation to (D.23), i.e.

$$\sigma(t) = C(0) : \varepsilon(t) + \int_0^\infty C'(s) : \varepsilon(t-s) ds, \tag{D.24}$$

with $C(.)$ denoting a forth order constitutive function. Exploiting the identity

$$C(0) : \varepsilon(t) = C(\infty) : \varepsilon(t) - \int_0^\infty C'(s) : \varepsilon(t) ds$$

leads to the multi-axial constitutive law corresponding to (D.16) for non isotropic materials, i.e.

$$\sigma(t) = C(\infty) : \varepsilon(t) + \int_0^\infty C'(s) : \underbrace{[\varepsilon(t-s) - \varepsilon(t)]}_{\varepsilon_d^t(s)} ds. \tag{D.25}$$

Exploiting that $\varepsilon(.)$ is symmetric and the fact that for isotropic material the constitutive function reads

$$C_{ijkl}(.) = \lambda(.)\delta_{ij}\delta_{kl} + 2\mu(.)(\delta_{jl}\delta_{ik} + \delta_{il}\delta_{jk}), \tag{D.26}$$

leads together with (D.25) to

$$\begin{aligned}\sigma(t) &= \lambda(\infty)\mathrm{Tr}[\varepsilon(t)]\mathbf{I} + 2\mu(\infty)\varepsilon(t) + \\ &\quad + \int_0^\infty \lambda'(s)\mathrm{Tr}\left[\varepsilon_d^t(s)\right]\mathbf{I} + 2\mu'(s)\varepsilon_d^t(s) ds. \\ &= K(\infty)\mathrm{Tr}[\varepsilon(t)]\mathbf{I} + 2\mu(\infty)\langle\varepsilon(t)\rangle \\ &\quad + \int_0^\infty K'(s)\mathrm{Tr}\left[\varepsilon_d^t(s)\right]\mathbf{I} + 2\mu'(s)\langle\varepsilon_d^t(s)\rangle ds,\end{aligned} \tag{D.27}$$

Note that the above equation is the extension of (D.16) for multi-axial stress and strain and can also be found in the book of Haupt [40]. The material laws corresponding to the uni-axial case can be derived choosing special relaxation functions. The standard linear solid model given in [30], i.e.

$$\dot{\sigma} + \frac{\mu_1 + \mu_2}{\eta}\sigma = 2\mu_1\dot{\varepsilon} + \left(K - \frac{2}{3}\mu_1\right)\mathrm{Tr}[\dot{\varepsilon}]\mathbf{I} + \frac{2\mu_1\mu_2}{\eta}\varepsilon + \left(\frac{\mu_1 + \mu_2}{\eta}K - \frac{2\mu_1\mu_2}{3\eta}\right)\mathrm{Tr}[\varepsilon]\mathbf{I},$$

can be derived from (D.23) or (D.27) respectively, choosing the constitutive functions as

$$\begin{aligned}\mu(s) &= \frac{\mu_1\mu_2}{\mu_1 + \mu_2} + \frac{(\mu_1)^2}{\mu_1 + \mu_2}e^{-\frac{\mu_1+\mu_2}{\eta}t},\\ K(s) &= K = const.\end{aligned}$$

The Maxwell model for multi-axial stress and strain, i.e.

$$\dot{\sigma} + \frac{\mu_1}{\eta}\sigma = 2\mu_1\dot{\varepsilon} + \left(K - \frac{2}{3}\mu_1\right)\mathrm{Tr}[\dot{\varepsilon}]\mathbf{I} + \frac{\mu_1}{\eta}K\mathrm{Tr}[\varepsilon]\mathbf{I},$$

can be recovered from (D.23) or (D.27) respectively, choosing the constitutive functions as

$$\begin{aligned}\mu(s) &= \mu_1 e^{-\frac{\mu_1}{\eta}t},\\ K(s) &= K = const.\end{aligned}$$

However, the Kelvin-Voigt model presented in [30], i.e

$$\sigma = 2\mu\varepsilon + \left(K - \frac{2}{3}\mu\right)\mathrm{Tr}[\varepsilon]\mathbf{I} + 2\eta\dot{\varepsilon} + \left(\zeta - \frac{2}{3}\eta\right)\mathrm{Tr}[\dot{\varepsilon}]\mathbf{I}.$$

can only be recovered from (D.23) because the constitutive function contains a Dirac-delta-distribution $\delta(.)$, i.e.

$$\begin{aligned}\mu(s) &= \mu + \eta\delta(s),\\ K(s) &= K + \zeta\delta(s).\end{aligned}$$

Due to the parallel arrangement of spring and dashpot the Kelvin-Voigt model does not allow a jump in the strain which leads in turn to the infinite stress.

Bibliography

[1] S. Alan, E. Budak, and H.N. Özgüven. Analytical prediction of part dynamics for machining stability analysis. *International Journal of Automation Technology*, 4(3):259–267, 2010.

[2] E.L. Allgower and K. Georg. *Numerical Continuation Methods*. Springer-Verlag, 1990.

[3] Y. Altintas. *Manufacturing Automation*. Cambridge University Press, 2000.

[4] Y. Altintas and E. Budak. Analytical prediction of stability lobes in milling. *Ann. of the CIRP*, 44/1:357–362, 1995.

[5] Y. Altintas, M. Eynian, and H. Onozuka. Identifcation of dynamic cutting force coefficients and chatter stability with process damping. *CIRP Annals - Manufacturing Technology*, 57:371–374, 2008.

[6] Y. Altintas and P. Lee. Mechanics and Dynamics of Ball End Milling. *Transactions of the ASME*, 120:684–692, 1998.

[7] A. Archenti and Nicolescu C.M. Model-based Identifcation of Dynamic Stability of Machining Systems. In B. Denkena, editor, *Proceedings, 1st International Conference on Process Machine Interactions*, pages 41–52. PZH Produktionstechnisches Zentrum GmbH, Hannover-Garbsen, September 3–4 2008.

[8] S. Atlar, E. Budak, and H. N. Özgüven. Modeling part dynamics and chatter stability in machining considering material removal. In B. Denkena, editor, *Proceedings, 1st International Conference on Process Machine Interactions*, pages 61–72. PZH Produktionstechnisches Zentrum GmbH, Hannover-Garbsen, September 3–4 2008.

[9] P.V. Bayly, J.E. Halley, B.P. Mann, and M.A. Davies. Stability of Interrupted Cutting by Temporal Finite Element Analysis. *Transactions of the ASME*, 125:220–225, 2003.

[10] D. Biermann, H. Blum, T. Jansen, A. Rademacher, A. Scheidler, A. Schröder, and K. Weinert. Space adaptive finite element methods for dynamic signorini problems in the simulation of the nc-shape grinding process. In B. Denkena, editor, *Proceedings, 1st International Conference on Process Machine Interactions*, pages 309–317. PZH Produktionstechnisches Zentrum GmbH, Hannover-Garbsen, September, 3–4 2008.

[11] D. Biermann, H. Blum, A. Rademacher, and A. Scheidler. Simulation of thermal effects in NC–Shape grinding of free formed surfaces using toroid grinding wheels. part II: Modeling and FE–Discretization. In Y. Altintas, editor, *Proceedings, CIRP 2nd International Conference Process Machine Interactions*, 2010.

[12] U. Bravo, O. Altuzarra, L.N. López de Lacalle, J.A. Sánchez, and F.J. Campa. Stability limits of milling considering the flexibility of the workpiece and the machine. *International Journal for Machine Tools and Manufacture*, 45:1669–1680, 2005.

[13] D. Breda, S. Maset, and R. Vermiglio. Pseudospectral differencing methods for characteristic roots of delay differential equations. *SIAM J. Sci. Comput.*, 27(2):482–495, 2005.

[14] D. Breda, S. Maset, and R. Vermiglio. Numerical computation of characteristic multipliers for linear time periodic coefficients delay differential equations. In *Proceedings of the Sixth IFAC Workshop on Time-Delay Systems, L'Aquila, Italy*, 2006.

[15] H. Bremer and F. Pfeiffer. *Elastische Mehrkörpersysteme*. B. G. Teubner, Stuttgart, 1992.

[16] R. Britz and H. Ulbrich. Lathe: Modeling and coupling of process and structure. In B. Denkena, editor, *Proceedings, 1st International Conference on Process Machine Interactions*, pages 231–238. PZH Produktionstechnisches Zentrum GmbH, Hannover-Garbsen, September 3–4 2008.

[17] E. Budak and Y. Altintas. Anlytical Prediction of Chatter Stability in Milling–part I: General Formulation. *Journal of Dynamic Systems, Measurement and Control*, 120:22–30, 1998.

[18] E. Budak and Y. Altintas. Anlytical Prediction of Chatter Stability in Milling–Part II: Application of the General Formulation to Common Milling Systems. *Journal of Dynamic Systems, Measurement and Control*, 120:31–36, 1998.

[19] E. Budak and L. T. Tunc. A new method for identification and modeling of process damping in machining. In B. Denkena, editor, *Proceedings, 1st International Conference on Process Machine Interactions*, pages 113–122. PZH Produktionstechnisches Zentrum GmbH, Hannover-Garbsen, September 3-4 2008.

[20] E. Bueler. Error bounds for approximate eigenvalues of periodic-coefficient linear delay-differential equations. *SIAM J. Numer. Anal.*, 45/6:2510–2536, 2007.

[21] E. A. Butcher, H. Ma, E. Bueler, V. Averina, and Z. Szabo. Stability of linear time-periodic delay-differential equations via Chebyshev polynomials. *Int. J. Numer. Methods Eng.*, 59:895–922, 2004.

[22] E.A. Butcher, P. Nindujarla, and E. Bueler. Stability of up- and down-milling using Chebyshev collocation method. In *Proceedings of IDETC/CIE 2005*, 2005.

[23] M. L. Campomanes and Y. Altintas. An improved time doman simulation for dynamic milling at small radial immersions. *Journal of Manufacturing Science and Engineering*, 2003.

[24] K. Chelminski, D. Hömberg, and O. Rott. On a thermomechanical milling model. *Nonlinear Analysis Real World Applications*, 12:615–632, 2010.

[25] H. N. Christiansen and T. W. Seeberg. Conversion of Complex Contour Line Definitions Into Polygonal Element Mosaics. In *Proceedings of 5th Annual Conference on Computer Graphics and Interactive Techiques*, pages 187–192. ACM Press, New York, 1978.

[26] P.G. Ciarlet. *Mathematical Elasticity*, volume 1: Three-dimensional elasiticity. NORTH-HOLLAND, 1988.

[27] C. Cordes and M. Putti. Accuracy of Galerkin finite elements for groundwater fow simulations in two and three-dimensional triangulations. *International Journal for Numerical Methods in Engineering*, 52:371–387, 2001.

[28] B. Denkena, D. Hömberg, and E. Uhlmann. Mathematics for Machine Tools and Factory Automation. In Martin Grötschel, Klaus Lucas, and Volker Mehrmann, editors, *Production Factor Mathematics*, pages 231–247. Springer Berlin Heidelberg, 2010. ISBN 978-3-642-11248-5. URL `http://dx.doi.org/10.1007/978-3-642-11248-5_12`.

[29] O. Diekmann, S. A. van Gils, S. M. Verduyn Lunel, and H.-O. Walther. *Delay equations. Functional-, complex-, and nonlinear analysis*. Applied Mathematical Sciences. 110. New York, NY: Springer-Verlag, 1995.

[30] E.H. Dill. *Continuum mechanics*. CRC Press, 2006.

[31] K. Engelborghs, T. Luzyanina, and D. Roose. Numerical bifurcation analysis of delay differential equations using DDE-BIFTOOL. *ACM Transactions on Mathematical Software*, 28(1):1–24, 2002.

[32] D.J. Ewins. *Modal Testing: Theory and Practice*. Res. Stud. Press LTD, 1986.

[33] R. P. H. Faassen, N. van de Wouw, J.A.J. Oosterling, and H. Nijmeijer. Prediction of regenerative chatter by modelling and analysis of high-speed milling. *International Journal of Machine Tools and Manufacture*, 2003.

[34] M. Fiedler. *Special matrices and their applications in numerical mathematics*. Martinus Nijhoff Publishers, Dordrecht/Boston/Lancaster, 1986.

[35] K. Großmann, A. Mühl, and M. Löser. Prognose von Stabilitätsgrenzen für das Fräsen. *Zeitschrift für wirtschaftlichen Fabrikbetrieb*, 101(7/8):416–421, 2006.

[36] S. Gumussoy and W. Michiels. Computing $\mathcal{H}_\infty$ norms of time-delay systems. In *Proceedings of the 48th IEEE Conference on Decision and Control*, 2009.

[37] E. Hairer, S.P. Nørsett, and G. Wanner. *Solving Ordinary Differential Equations I.* Springer, 1987.

[38] J.K. Hale. *Theory of Functional Differential Equations.* Springer-Verlag, 1977.

[39] A. Hannukainen, S. Korotov, and T. Vejchodsk. Discrete maximum principle for 3D-FE solutions of the diffusion-reaction problem on prismatic meshes. *Preprint, Institute of Mathematics, AS CR, Prague.*, 2008.

[40] P. Haupt. *Continuum Mechanics and Theory of Materials.* Advanced texts in physics. Springer, Berlin Heidelberg, 2000.

[41] C. Henninger and P. Eberhard. An investigation of pose-dependent regenerative chatter for a parallel kinematic milling machine. In *Proceedings (CD-ROM) of the 12th IFToMM World Congress, Besancon, France*, 2007.

[42] D. Hömberg and O. Rott. Modelling, analysis and stability of milling processes including workpiece effects. In A.D. Fitt, J. Norbury, H. Ockendon, and E Wilson, editors, *Progress in Industrial Mathematics at ECMI 2008*, page 1050. Springer-Verlag, May 2010.

[43] D. Hömberg, E. Uhlmann, O. Rott, and P. Rasper. Development of a stability prediction tool for the identification of stable milling processes. *WIAS Preprint*, (1588), 2011.

[44] D. Hömberg and W. Weiss. Pid-control of laser surface hardening of steel. *IEEE Trans. Control Syst. Technol.*, 14:896–904, 2006.

[45] T. J. R. Hughes. *The finite element method.* Dover Publications, New York, 2000.

[46] T. Insperger. *Stability Analysis of Periodic Delay-Differential Equations Modeling Machine Tool Chatter.* PhD thesis, Budapest University of Technology and Economics, 2002.

[47] T. Insperger, B.P. Mann, T. Surmann, and G. Stépán. On the chatter frequencies of milling processes with runout. *International Journal of Machine Tools and Manufacturing*, 48:1081–1089, 2008.

[48] T. Insperger and G. Stépán. Stability of the milling process. *Periodica Polytechnica Service Mechanical Engineering*, 1999.

[49] T. Insperger and G. Stépán. Semi-discretization method for delayed systems. *Int. J. Numer. Methods Eng.*, 55(5):503–518, 2002.

[50] T. Insperger and G. Stépán. Stability chart for the delayed Mathieu equation. *Proc. R. Soc. Lond., Ser. A, Math. Phys. Eng. Sci.*, 458(2024):1989–1998, 2002.

[51] T. Insperger and G. Stépán. Updated semi-discretization method for periodic delay-differential equations with discrete delay. *International Journal for Numerical Methods in Engineering*, 2004.

[52] E. Jarlebing. Convergence factors of Newton methods for nonlinear eigenvalue problems. *Elsevier (submitted)*, 2010.

[53] E. Jarlebring. *The spectrum of delay-differential equations: numerical methods, stability and perturbation.* PhD thesis, Inst. Comp. Math, TU Braunschweig, 2008.

[54] D. W. Jordan and P. Smith. *Nonlinear ordinary differential equations*. Clarendon Press, Oxford, 1987.

[55] J. Karandikar and T. L. Schmitz. An investigation of stability dependence on tool wear. In Y. Altintas, editor, *Proceedings, CIRP 2nd International Conference Process Machine Interactions*, 2010.

[56] F. Klocke, S. Kratz, and D. Veselovac. FEM simulation and experimental evaluation of a thin walled components dynamic behaviour. In Y. Altintas, editor, *Proceedings, CIRP 2nd International Conference Process Machine Interactions*, 2010.

[57] B. J. Lazan. *Damping of Materials and Members in Structural Mechanics*. Pergamon Press, 1st edition, 1968.

[58] R. B. Lehoucq, D. C. Sorensen, and C. Yang. *ARPACK Users' Guide: Solution of Large-Scale Eigenvalue Problems with Implicitly Restarted Arnoldi Methods*. SIAM, 1998.

[59] H. Li and Li X. Modelling and simulation of chatter in milling using a predictive force model. *International Journal for Machine Tools and Manufacture*, 40:2047–2017, 2000.

[60] H. Z. Li, X. P. Li, and X. Q. Chen. A novel chatter stability criterion for the modelling and simulation of the dynamic milling process in the time domain. *International Journal of Advanced Manufacturing Technologies*, 2003.

[61] H. Z. Li, W.B. Zhang, and Li X.P. Modelling of cutting forces in helical end milling using a predictive machining theory. *International Journal of Mechanical Sciences*, 43:1711–1730, 2001.

[62] R. Löhner. *Applied Computational Fluid Dynamics Techniques*. John Wiley & Sons, Ltd, 2nd edition, 2008.

[63] B. Mann, T. Insperger, P.V. Bayly, and G. Stépán. Stability of up-milling and down-milling, part 2: experimental verification. *International Journal of Machine Tools and Manufacture*, 43:35–40, 2003.

[64] B. Mann, T. Insperger, P.V. Bayly, G. Stépán, T.L. Schmitz, and D.A. Peters. Effects of radial immersion and cutting direction on chatter stability in end-milling. In N.N., editor, *Proceedings of IMECE02*, 2002.

[65] V. Mehrmann and H. Voss. Nonlinear eigenvalue problems: A challenge for modern eigenvalue methods. *Mitteilungen der Gesellschaft für Angewandte Mathematik und Mechanik*, 27:121–151, 2005.

[66] M. E. Merchant. Mechanics of the Cutting Process. *Journal of Applied Physics*, 16:318–324, 1945.

[67] I. Müller. *Thermodynamics*. Pitman Publishing, 1985.

[68] I. Müller. *Grundzüge der Thermodynamik*. Springer, 2001.

[69] A. Neumaier. Residual inverse iteration for the nonlinear eigenvalue problem. *SIAM J. Numer. Anal.*, 22:914–923, 1985.

[70] P. L. B. Oxley. *The mechanics of machining*. Ellis Horwood series in mechanical engineering, 1977.

[71] H. Özgüven. Structural modifications using frequency response functions. *Mechanical Systems and Signal Processing*, 4(1):53–63, 1990.

[72] E. Ozturk and Budak E. Modeling Dynamics of Parallel Milling Processes in Time-Domain. In Y. Altintas, editor, *Proceedings, CIRP 2nd International Conference Process Machine Interactions*, 2010.

[73] X. Peng and W. Zhang. A Virtual Sculpting System Based on Triple Dexel Models with Haptics. *Computer-Aided Design and Applications*, 6:645–659, 2009.

[74] K. M. Popp, M. Kröger, M. Deichmueller, and B. Denkena. Analysis of the machine structure and dynamic response of a tool grinding machine. In B. Denkena, editor, *Proceedings, 1st International Conference on Process Machine Interactions*, pages 299–308. PZH Produktionstechnisches Zentrum GmbH, Hannover-Garbsen, September 3–4 2008.

[75] P. Rasper, O. Rott, D. Hömberg, and E. Uhlmann. Analysis of uncertainties in the stability prediction for milling processes. In Y. Altintas, editor, *Proceedings, CIRP 2nd International Conference Process Machine Interactions*, 2010.

[76] T. Reis and T. Stykel. Stability analysis and model order reduction of coupled systems. *Math. Comput. Model. Dyn. Syst.*, 13:413–436, 2007.

[77] T. Reis and T. Stykel. Balanced truncation model reduction of second-order systems. *Math. Comput. Model. Dyn. Syst.*, 5:391–406, 2008.

[78] T. Reis and T. Stykel. A survey on model reduction of coupled systems. In W.H.A. Schilders, H.A. van der Vorst, and J.Rommes, editors, *Model Order Reduction: Theory, Research Aspects and Applications*, volume 13 of *Mathematics in Industry*, pages 133–155. Springer-Verlag, 2008.

[79] O. Rott, D. Hömberg, and C. Mense. A comparison of analytical cutting force models. *WIAS Preprint No. 1151*, 2006.

[80] O. Rott and E. Jarlebring. An iterative method for the multipliers of periodic delay-differential equations and the analysis of a pde milling model. In T. Vyhlidal, editor, *Proceedings of the 9th IFAC Workshop on Time Delay Systems*. Prague, 2010.

[81] O. Rott, P. Rasper, D. Hömberg, and E. Uhlmann. A milling model with thermal effects including the dynamics of machine and work piece. In B. Denkena, editor, *Proceedings, 1st International Conference on Process Machine Interactions*, pages 369–378. PZH Produktionstechnisches Zentrum GmbH, Hannover-Garbsen, September 3–4 2008.

[82] A. Ruhe. Algorithms for the nonlinear eigenvalue problem. *SIAM J. Numer. Anal.*, 10:674–689, 1973.

[83] G. Samaey, K. Engelborghs, and D. Roose. Numerical computation of connecting orbits in delay differential equations. *Numer. Algorithms*, 30:335–352, 2002.

[84] K. Schittkowski. *Numerical Data Fitting in Dynamical Systems*. Kluwer Academic Publilshers, 2002.

[85] L. F. Shampine and M. K. Gordon. *Computer Solution of Ordinary Differential Equations*. W. H. Freeman, SanFrancisco, 1975.

[86] L. F. Shampine and S. Thompson. Solving ddes in matlab. *Applied Numerical Mathematics*, 2001.

[87] M.C. Shaw. *Metal Cutting Principles*. Oxford University Press, 2nd edition, 2005.

[88] Y. Shi, F. Mahr, U. von Wagner, and E. Uhlmann. A spatial multiple degree of freedom machine tool model for micro milling simulation. In Y. Altintas, editor, *Proceedings, CIRP 2nd International Conference Process Machine Interactions*, 2010.

[89] H. Si. TetGen – A Quality Tetrahedral Mesh Generator and Three-Dimensional Delauny Triangulator Version 1.3 User's Manual. Technical report, Weierstrass Institute for Applied Analysis and Stochastics, 2004.

[90] H. Si, J. Fuhrmann, and K. Gärtner. Boundary conforming delaunay mesh generation. *Computational Mathematics and Mathematical Physics*, 50:38–53, 2010.

[91] N. D. Sims. The self-excitation damping ratio: a chatter criterion for time-domain milling simulations. *Journal of Manufacturing Science and Engineering*, 2005.

[92] S. Smith and J. Tlusty. Efficient Simulation Programs for Chatter in Milling. *Annals of the CIRP*, 42/1:463–466, 1993.

[93] G. Stépán. *Retarded dynamical systems: stability and characterisitc functions.* Pitman Research Notes in Mathematics Series, 1989.

[94] S. Stifter. Simulation of NC Machining Based on the Dexel Model: A Critical Analysis. *The International Journal of Advanced Manufacturing Technology*, 10:140–157, 1995.

[95] T. Suhrmann, M. Kalveram, and K. Weinert. Simulation of cutting tool vibrations for the milling of free formed surfaces. In *Proceedings of the 8th CIRP International Workshop on Modeling of Machining Operations*, pages 175–182, 2005.

[96] R. Szalai, G. Stépán, and J. Hogan. Continuation of bifurcations in periodic delay-differential equations using characteristic matrices. *SIAM J. Sci. Comput.*, 28(4):1301–1317, 2006.

[97] J. Tlusty. Self-Excited Vibrations in Cutting Metals (german). *Acta Technica Ac Sc Hungaricae*, VIII:319–360, 1954.

[98] J. Tlusty and M. Polacek. Stability of Machine Tools Angainst Self-Excited Vibration in Machining. In *Proceedings ASME Prod. Eng. Res. Conf.* Pittsburgh, 1963.

[99] S. A. Tobias. *Schwingungen an Werkzeugmaschinen.* Carl Hanser Verlag München, 1961.

[100] S. A. Tobias and W. Fishwick. The vibrations of radial drilling machines und test and working conditions. In *Proceedings of the Institution of Mechanical Engineers 1847-1996*, volume 170, pages 232–264, 1956.

[101] H. K. Tönshoff and B. Denkena. *Spanen.* Springer, 2004.

[102] E. Uhlmann and P. Rasper. Temperaturabhängiges Stabilitätsverhalten - Untersuchung des Temperatureinflusses auf das Stabilitätsverhalten beim Umfangsstirnfräsen. *wt Werkstattstechnik online*, 7/8:464–469, 2009.

[103] E. Uhlmann and P. Rasper. Influences on specific cutting forces and their impact on the stability behaviour of milling processes. *Prod. Eng. Res. Devel.*, 5:175–181, 2011.

[104] E. Uhlmann, P. Rasper, and C. Mense. Unpublished Experimental Data, Department of Production Technology and Factory Management (IWF), Technische Universität Berlin. 2005-2011.

[105] M. Weck and K. Teipel. *Dynamisches Verhalten spanender Werkzeugmaschinen.* Springer Berlin Heidelberg New York, 1977.

[106] K. Weinert, H. Blum, T. Jansen, and A. Rademacher. Simulation based optimization of the NC-shape grinding process with toroid grinding wheels. *Prod. Eng. Res. Devel.*, 1:245—-252, 2007.

[107] K. Weinert and S. Grünert. Thermische Simulation des Bohrprozesses – FEM-Simulation der thermischen Bauteilbelastung beim Bohren. *wt Werkstattstechnik online*, 97:30–34, 2007.

[108] K. Weinert and A. Loichinger. Prozessoptimierung thermisch bedingter Bauteildeformation – Einfluss der Bearbeitungswärme auf die Bauteilqualität – Analyse und Prozessoptimierung. *wt Werkstattstechnik online*, 92:259–263, 2002.

[109] K. Weinert and T. Surmann. Geometric simulation of the milling process for free formed surfaces. In K. Weinert, editor, *Simulation Aided Offline Process Design and Optimization in Manufacturing Sculptured Surfaces*. Witten, 2003.

[110] R. J. Wood and M. J. O'Neill. A faster algorithm for identification of an m-matrix. In Rob May and A. J. Roberts, editors, *Proc. of 12th Computational Techniques and Applications Conference CTAC-2004*, volume 46, pages C732–C743, 2005.

[111] R. Wüst. *Mathematik für Physiker und Mathematiker*, volume Band 2. Wiley-VCH, 2002.

[112] W. Zang and C. L. Ming. Surface Reconstruction Using Dexel Data from Three Sets of Orthogonal Rays. *Journal of Computing and Information Science in Engineering*, 9, 2009.

[113] M. Zatarain, J. Munoa, G. Peigné, and T. Insperger. Analysis of the influence of mill helix angle on chatter stability. *Annals of the CIRP*, 55/1, 2006.

[114] W. Zhang, X. Peng, M.C. Leu, and W. Zhang. A novel contour generation algorithm for surface reconstruction from dexel data. *Journal of Computing and Information Science in Engineering*, 7:203–210, 2007.